SISSA
Scuola
Internazionale
Superiore di
Studi Avanzati

Physics Area - PhD course in
Theory and Numerical Simulations
of Condensed Matter

Probing and detecting entanglement in synthetic quantum matter

Candidate:
Vittorio Vitale

Advisors:
Dr. Marcello Dalmonte
Prof. Giuseppe Santoro

Academic Year 2021-22


Is this a pigeon?
百科事典

Preface

In the past decades, rapid advances in the experimental control of quantum systems have opened up unparalleled capabilities of engineering exotic quantum states. Nowadays, we may consider ourselves witnesses of a *second quantum revolution* [1, 2] as strongly correlated quantum matter is regularly created, on a daily basis, within the most diverse platforms, e.g. arrays of Rydberg atoms [3–5], ultra-cold atoms in optical lattices [6, 7], superconducting qubits [8, 9], trapped ions [10, 11], and quantum dots [12]. In this era, dubbed Noisy-Intermediate Scale Quantum [13] (NISQ) era, the effort in pursuing research for realizing quantum technologies with practical purposes, such as quantum computing [14, 15], simulations [16], communication [17] and metrology [18], has greatly accelerated, and we are just starting to experience the immense progress that could be achieved.

The remarkable breakthrough we are facing builds upon seminal theoretical and experimental advances in quantum physics. The key achievements in atomic, molecular, and optical (AMO) physics have opened up the possibility of controlling, trapping, and measuring single atoms, one by one, with high accuracy and reliability [19–21]. In parallel, from a theoretical point of view, the study of quantum entanglement and correlations has bridged AMO physics and quantum information with crucial proposals for the realization of universal quantum computers [22, 23]. In this context, entanglement has emerged as one of the key tools to characterize and to exploit quantum many-body systems for quantum information purposes [15, 24].

Entanglement is the intrinsic expression of the *non-locality* of quantum mechanics and has generated a lot of questions since its foundation. The interest in quantum entanglement is interdisciplinary, as it spans in several communities, ranging from quantum information and computation [15, 24] to condensed matter [25, 26], high energy physics, and cosmology [27–31]. Since entanglement is intimately related to the complexity of many-body quantum states and our capability of representing them efficiently, it has served as a tool to probe quantum phases of matter [25, 26], benchmark experimental platforms [32, 33], and develop advanced numerical techniques such as tensor network methods [34, 35].

In this thesis, we will study quantum entanglement in several scenarios to investigate and probe complex quantum many-body systems. We will consider examples ranging from generic mixed states in equilibrium to out-of-equilibrium dynamics, with and without dissipation, and topologically non-trivial systems. The leitmotif of this work will be how entanglement and correlations can be exploited to characterize the many-body quantum state describing a physical system and

how entanglement can be detected in an experimentally efficient manner. We will proceed by asking ourselves the following questions: *i)* how is it possible to detect entanglement in mixed states, in such a way that it is experimentally feasible in nowadays quantum platforms? *ii)* how the role of symmetry intertwines with entanglement both in- and out-of-equilibrium? *iii)* can entanglement serve as a probe to characterize topological features of quantum matter?
For the sake of clarity, we divide the thesis into four parts. Each one is self-contained to give a complete picture of the topic studied. We provide a short introduction, which summarizes the notation we use and briefly introduces some technical aspects, in Part I. We divide the work as follows:

In Part I we give an overview on entanglement measures for pure and mixed states. We discuss the generalization of entanglement in case the system has a $U(1)$ symmetry, introducing the notion of symmetry resolved entanglement and reviewing its study in previous works. Furthermore, we describe an experimental protocol to measure observables on state-of-the-art quantum platforms, named *randomized measurement protocol* [36]. This protocol has been extensively used and improved in the past years and has been exploited in this thesis to post-process the published data of Ref. [11], for estimating several quantities that will be discussed in the respective chapters.

In Part II we tackle the problem of mixed state entanglement from different points of view. First, we attempt a characterization of entanglement in terms of operator properties which goes beyond the well known one for entanglement Hamiltonians [37, 38]. We discuss the idea of *negativity Hamiltonian* for the partial transpose of a reduced density matrix and propose a quasi-local structure for it. Then, we focus on entanglement detection via the partial transpose moments of a reduced density matrix, intending to devise experimentally efficient entanglement criteria. We employ the moments of the partial transpose and symmetry resolved entanglement to go beyond the standard PPT-criterion [39, 40], we observe that exploiting symmetry is extremely useful to extend the capability of witnessing many-body entanglement, both experimentally and theoretically.

In Part III we study the entanglement evolution in open quantum dynamics when the unitary dynamics preserves an additive conserved charge. We unveil a new effect, supported by experimental evidence, that we name *dynamical purification*. It is due to the interplay between coherent and incoherent dynamics, and it is remarkably general and observable only if symmetry resolved entanglement is investigated. Then, we study the *operator entanglement*, observing the so-called *entanglement barrier* [41–44] and uncovering two interesting physical effects: a time delay for the onset of the growth of symmetry-resolved operator entanglement and an effective equipartition between charge sectors.

In Part IV we study entanglement in topologically non-trivial 1D systems. We build an entanglement based topological invariant, similar to the one discussed in Ref. [45, 46], for detecting

symmetry-protected topological order, and apply it to two prototypical models: the interacting Kitaev model and the Su-Schrieffer-Heeger chain.

Bibliography

[1] J. P. Dowling and G. J. Milburn, Philosophical Transactions of the Royal Society of London. Series A: Mathematical, Physical and Engineering Sciences **361**, 1655 (2003).

[2] I. H. Deutsch, PRX Quantum **1**, 020101 (2020).

[3] D. Jaksch, J. I. Cirac, P. Zoller, S. L. Rolston, R. Côté, and M. D. Lukin, Phys. Rev. Lett. **85**, 2208 (2000).

[4] M. Saffman, T. G. Walker, and K. Mølmer, Rev. Mod. Phys. **82**, 2313 (2010).

[5] H. Levine, A. Keesling, G. Semeghini, A. Omran, T. T. Wang, S. Ebadi, H. Bernien, M. Greiner, V. Vuletić, H. Pichler, and M. D. Lukin, Phys. Rev. Lett. **123**, 170503 (2019).

[6] D. Jaksch, H.-J. Briegel, J. I. Cirac, C. W. Gardiner, and P. Zoller, Phys. Rev. Lett. **82**, 1975 (1999).

[7] S. Murmann, A. Bergschneider, V. M. Klinkhamer, G. Zürn, T. Lompe, and S. Jochim, Phys. Rev. Lett. **114**, 080402 (2015).

[8] J. Clarke and F. K. Wilhelm, Nature **453**, 1031 (2008).

[9] M. Kjaergaard, M. E. Schwartz, J. Braumüller, P. Krantz, J. I.-J. Wang, S. Gustavsson, and W. D. Oliver, arXiv preprint arXiv:1905.13641 (2019).

[10] N. Friis, O. Marty, C. Maier, C. Hempel, M. Holzäpfel, P. Jurcevic, M. B. Plenio, M. Huber, C. Roos, R. Blatt, and B. Lanyon, Phys. Rev. X **8**, 021012 (2018).

[11] T. Brydges, A. Elben, P. Jurcevic, B. Vermersch, C. Maier, B. P. Lanyon, P. Zoller, R. Blatt, and C. F. Roos, Science **364**, 260 (2019).

[12] Y. He, S. Gorman, D. Keith, L. Kranz, J. Keizer, and M. Simmons, Nature **571**, 371 (2019).

[13] J. Preskill, Quantum **2**, 79 (2018).

[14] D. P. DiVincenzo, Science **270**, 255 (1995).

[15] M. A. Nielsen and I. L. Chuang, *Quantum Computation and Quantum Information* (Cambridge University Press, 2009).

[16] J. I. Cirac and P. Zoller, Nature Physics **8**, 264 (2012).

[17] N. Gisin and R. Thew, Nature Photonics **1**, 165 (2007).

[18] C. L. Degen, F. Reinhard, and P. Cappellaro, Rev. Mod. Phys. **89**, 035002 (2017).

[19] T. H. Maiman, Nature **187**, 493 (1960).

[20] P. A. Franken, A. E. Hill, C. W. Peters, and G. Weinreich, Phys. Rev. Lett. **7**, 118 (1961).

[21] C. Gardiner and P. Zoller, *The Quantum World of Ultra-Cold Atoms and Light Book I: Foundations of Quantum Optics* (IMPERIAL COLLEGE PRESS, 2014).

[22] J. I. Cirac and P. Zoller, Phys. Rev. Lett. **74**, 4091 (1995).

[23] K. Mølmer and A. Sørensen, Phys. Rev. Lett. **82**, 1835 (1999).

[24] G. Benenti, G. Casati, and G. Strini, *Principles of Quantum Computation and Information* (WORLD SCIENTIFIC, 2004).

[25] L. Amico, R. Fazio, A. Osterloh, and V. Vedral, Rev. Mod. Phys. **80**, 517 (2008).

[26] N. Laflorencie, Physics Reports **646**, 1 (2016).

[27] M. Srednicki, Phys. Rev. Lett. **71**, 666 (1993).

[28] X. Dong, Nature Comm. **7**, 12472 (2016).

[29] S. Ryu and T. Takayanagi, Phys. Rev. Lett. **96**, 181602 (2006).

[30] M. Van Raamsdonk, Gen. Rel. and Grav. **42**, 2323 (2010).

[31] J. Maldacena and L. Susskind, Fortschr. Phys. **61**, 781–811 (2013).

[32] A. Elben, R. Kueng, H.-Y. R. Huang, R. van Bijnen, C. Kokail, M. Dalmonte, P. Calabrese, B. Kraus, J. Preskill, P. Zoller, and B. Vermersch, Physical Review Letters **125**, 200501 (2020).

[33] J. Eisert, D. Hangleiter, N. Walk, I. Roth, D. Markham, R. Parekh, U. Chabaud, and E. Kashefi, Nature Reviews Physics **2**, 382 (2020).

[34] F. Verstraete, M. M. Wolf, and J. Ignacio Cirac, Nature Physics **5**, 633 (2009).

[35] U. Schollwöck, Annals of Physics **326**, 96 (2011).

[36] A. Elben, S. T. Flammia, H.-Y. Huang, R. Kueng, J. Preskill, B. Vermersch, and P. Zoller, arXiv:2203.11374 (2022).

[37] H. Casini, Classical and Quantum Gravity **21**, 2351 (2004).

[38] J. J. Bisognano and E. H. Wichmann, Journal of Mathematical Physics **17**, 303 (1976).

[39] A. Peres, Physical Review Letters **77**, 1413 (1996).

[40] M. Horodecki, P. Horodecki, and R. Horodecki, Physics Letters A **223**, 1 (1996).

[41] P. Zanardi, C. Zalka, and L. Faoro, Physical Review A **62**, 030301 (2000).

[42] P. Zanardi, Physical Review A **63**, 040304 (2001).

[43] T. Prosen and I. Pižorn, Physical Review A **76**, 032316 (2007).

[44] I. Pižorn and T. Prosen, Physical Review B **79**, 184416 (2009).

[45] A. Kitaev and J. Preskill, Physical Review Letters **96**, 110404 (2006).

[46] B. Zeng, X. Chen, D.-L. Zhou, and X.-G. Wen, *Quantum Information Meets Quantum Matter* (Springer New York, 2019).

List of publications

In this thesis:

- S. Murciano*, **V. Vitale***, M. Dalmonte, P. Calabrese, *The Negativity Hamiltonian: An operator characterization of mixed-state entanglement*, Physical Review Letters 128, 140502 (2022) [Chap. 4];
- A. Neven, J. Carrasco, **V. Vitale**, C. Kokail, A. Elben, M. Dalmonte, P. Calabrese, P. Zoller, B. Vermersch, R. Kueng, B. Kraus, *Symmetry-resolved entanglement detection using partial transpose moments*, npj Quantum Inf 7, 152 (2021) [Chap. 5];
- **V. Vitale***, A. Elben*, R. Kueng, A. Neven, J. Carrasco, B. Kraus, P. Zoller, P. Calabrese, B. Vermersch, M. Dalmonte, *Symmetry-resolved dynamical purification in synthetic quantum matter*, SciPost Physics 12 (3), 106 (2022) [Chap. 6];
- A. Rath*, **V. Vitale***, S. Murciano*, M. Votto, J. Dubail, R. Kueng, C. Branciard, P. Calabrese, B. Vermersch, *Entanglement barrier and its symmetry resolution: theory and experiment*, arXiv:2209.04393 (2022) [Chap. 7];
- P. Fromholz, G. Magnifico, **V. Vitale**, T. Mendes-Santos, M. Dalmonte, *Entanglement topological invariants for one-dimensional topological superconductors*, Physical Review B 101 (8), 085136 (2020) [Chap. 8];
- T. Micallo, **V. Vitale**, M. Dalmonte, P. Fromholz, *Topological entanglement properties of disconnected partitions in the Su-Schrieffer-Heeger model*, SciPost Phys. Core 3, 012 (2020) [Chap. 9].

Other publications:

- A. Santini, **V. Vitale**, *Experimental violations of Leggett-Garg's inequalities on a quantum computer*, Physical Review A 105 (3), 032610 (2022);
- **V. Vitale**, G. De Filippis, A. de Candia, A. Tagliacozzo, V. Cataudella, P. Lucignano, *Assessing the quantumness of the annealing dynamics via Leggett Garg's inequalities: a weak measurement approach*, Scientific Reports volume 9, 13624 (2019).

*the authors contributed equally to this work.

Contents

I

Introduction

1 Entanglement

1.1 Introduction

Entanglement has been a central concept in quantum mechanics since its foundation, being the key feature distinguishing between classical and quantum mechanics [1–4]. It has gained renewed interest, in the early 2000s, thanks to the development of quantum information science [1] and, subsequently, as a promising - and potentially revolutionary - tool in other areas of physics such as statistical mechanics and quantum field theory [5]. It has been used to characterize quantum phases of matter and dynamics of many-body quantum systems [6–12], exploited as a resource to allow quantum platforms to outperform their classical counterparts [13–15], and employed as a benchmark tool for gauging the performances of today available NISQ devices [6, 9]. The problem of quantifying and computing entanglement is already very difficult for simple few-body systems. However, a lot has been understood thanks to the efforts coming from disparate and disconnected communities. For example, entanglement has been observed to play an important role in the physics of phase transitions where it is often used as a tool to probe criticality [16, 17]: the investigation of entanglement can be employed to distinguish if the system is in a gapped or gapless phase and is known to display universal features in critical systems. Entanglement can provide more detailed information about the order of a quantum state, e.g. if the system has non-trivial topological order [18]. In fact, it has been observed to contain a sub-leading constant term indicating the existence of a long-range structure that originates from the topological nature of the system. In a generic quantum system with non-zero correlation length, the calculation of this topological term may not be straightforward, as it can be hard to separate from the leading one and various other non-universal contributions.

Concerning out of equilibrium phenomena, an important and well-established result is the *quasi-*

particle picture for entanglement spreading in a system after a global quantum quench [19]. This idea is based on a simple semi-classical argument. Imagine to perform a homogeneous quantum quench such to bring the system out-of-equilibrium at time $t = 0^+$. From the perspective of the post-quench Hamiltonian, the system lays in a highly excited state, and one can depict such a state as a collection of excitations, that start to spread in the system[1]. Thus, one can say that the traveling particles are responsible of the entanglement (and correlation) spreading. In the original formulation of Ref. [19], quasi-particles are assumed to be produced in pairs of opposite momenta and spreading in opposite directions. This is the simplest assumption which respects translational invariance, and it is the common situation in most quench protocols and in exactly solvable quenches in integrable models.
Finally, let us close this introduction by touching on a problem that is of recent interest, thanks to the development of efficient quantum simulators, that is the detection of entanglement in mixtures of quantum states, i.e. systems described by density matrices. It is well established that the only necessary and sufficient condition for the separability of a density matrix known so far, i.e. the Peres' criterion (or PPT), requires the full spectral resolution of it and it is not affordable in real world devices. Going beyond this particular issue is still a vivid topic of study in the quantum information community, since it is of present interest for the realization of commercial quantum computers.

1.2 Entanglement measures

Entanglement is conventionally defined via its opposite: separability. A pure quantum state $|\psi\rangle$ is called separable when it can be written as a tensor product:

$$|\psi\rangle = |\psi_A\rangle \otimes |\psi_B\rangle \,, \tag{1.1}$$

where $|\psi_X\rangle$ lives in the Hilbert space H_X ($X = A, B$). Conversely, any state that is not separable is called *entangled* and cannot be created via local operations aided by classical communication (LOCC) [2]. The same can be phrased for mixtures of pure quantum states, i.e. density matrices ρ. To rule out the possibility that a state (both pure or mixed) is entangled, it is necessary to define *entanglement witnesses*. An entanglement witness is a tool that can be used to figure out whether a state is separable or not. In formulas one could say that a state is entangled if an Hermitian operator W exists such that

$$\begin{aligned} &\mathrm{tr}(W\rho) \ll 0 \quad \text{if } \rho \text{ is entangled,} \\ &\mathrm{tr}(W\rho) \geq 0 \quad \text{if } \rho \text{ is separable.} \end{aligned} \tag{1.2}$$

[1] In the case the post-quench Hamiltonian is described by a conformal field theory or is an integrable model, these excitations undergo a ballistic motion and are stable. Conversely, if the state evolves under a non-integrable dynamics, the quasi-particle acquire a finite life-time.

The operator W is then called entanglement witness. While an entanglement witness gives information about a quantum state being entangled or not, an observable that is able to quantify the amount of entanglement present in a given quantum state is called *entanglement measure*. A good entanglement measure $\mathcal{E}$ is defined by the following properties:

1. $\mathcal{E}(\rho)$ is a map from density matrices to positive real numbers, $\rho \to \mathcal{E}(\rho) \in \mathbb{R}^+$, where ρ is an arbitrary state of a bipartite quantum system. The measure is normalized such $\mathcal{E}(|\phi_d^+\rangle) = \log(d)$ for maximally entangled state, e.g. $|\phi_d^+\rangle = \frac{1}{\sqrt{d}} \sum_{i=0}^{d-1} |ii\rangle$, where d is the Hilbert space dimension and $|ii\rangle$ denotes the quantum state of a bipartite system, where each subsystem is in the same physical state $|i\rangle$.

2. $\mathcal{E}(\rho) = 0$ for a separable quantum state.

3. Entanglement cannot increase under LOCC: $\mathcal{E}(\mathcal{M}_{LOCC}(\rho)) \leq E(\rho)$, with $\mathcal{M}_{LOCC}$ some local operations performed on the system or nonlocal classical communication.

4. *Convexity*. $\mathcal{E}\left(\sum_j p_j \rho_j\right) \leq \sum_j p_j \mathcal{E}(\rho_j)$, where $p_j > 0$ and $\sum_j p_j = 1$.

5. *Additivity*. Given n identical copies of ρ, the amount of entanglement of the whole ensemble is n times the entanglement of a single copy: $\mathcal{E}(\rho^{\otimes n}) = n\mathcal{E}(\rho)$. This condition can be also be satisfied asymptotically
$$\mathcal{E}^{\infty}(\rho) = \lim_{n\to\infty} \frac{\mathcal{E}(\rho^{\otimes n})}{n} .$$

6. *Subadditivity*. For any pair of states ρ_1 and ρ_2, one can write $\mathcal{E}(\rho_1 \otimes \rho_2) \leq \mathcal{E}(\rho_1) + \mathcal{E}(\rho_2)$.

Any function satisfying the first three conditions is called entanglement monotone [2]. In the following sections we will introduce the entanglement measures, monotones, witnesses which are used to characterize many-body quantum states and that we use throughout this thesis. We also comment on how and in which contexts they have been successfully employed to investigate quantum matter.

1.3 Entanglement entropies

In most cases, one is interested in bipartite systems, with a partition $A \cup B$. In the case of a many-body pure state, the bipartite entanglement between A and B is fully encoded in the reduced density matrix $\rho_A = \mathrm{tr}_B \rho$ of the given subsystem A, and is characterized via n-order Rényi entropies, defined as
$$S_A^{(n)} = \frac{1}{1-n} \log \mathrm{tr}\{\rho_A^n\}. \tag{1.3}$$
Bipartite entanglement being symmetric: $S_A^{(n)} = S_B^{(n)}$. For $n \to 1$, these reduce to the renowned von Neumann entanglement entropy
$$S(\rho_A) \equiv \lim_{n\to 1} S_A^{(n)} = -\,\mathrm{tr}_A\left(\rho_A \log \rho_A\right). \tag{1.4}$$

The von Neumann entropy of the reduced density operator is a rigorous entanglement measure for pure states, and the corresponding Rényi entropies with $n > 1$ provide rigorous lower bounds. Both Rényi and von Neumann entropies have found widespread applications in the realm of many-body physics, from the characterization of topological matter, to dynamics out of equilibrium, to the understanding of tensor network methods - see, e.g., Ref. [4] for a review.

1.4 Symmetry-resolved Renyi entropies

For a quantum system whose Hamiltonian dynamics preserves an additive conserved charge, it is possible to identify and compute the contributions to the entanglement related to each symmetry sector [20–23]. Here, we focus on global symmetries.

Let Q denote such a conserved charge ($Q = Q_A \otimes \mathbb{1}_B + \mathbb{1}_A \otimes Q_B$). Then, the reduced density matrix ρ_A is necessarily block diagonal and each block corresponds to an eigenvalue q of Q_A. One can thus introduce Π_q, the projector into the eigenspace related to eigenvalue q, and the associated density matrix $\rho_A(q)$

$$\rho_A(q) \equiv \frac{\Pi_q \rho_A \Pi_q}{\mathrm{tr}\{\rho_A \Pi_q\}}, \quad \mathrm{tr}\{\rho_A(q)\} = 1, \tag{1.5}$$

so that

$$\rho_A = \oplus_q \, p(q)\, \rho_A(q) \tag{1.6}$$

with $p(q) = \mathrm{tr}\{\rho_A \Pi_q\}$ the probability of being in charge sector q. We introduce the symmetry-resolved purity

$$\mathcal{P}_A(q) \equiv \mathrm{tr}\Big\{\rho_A(q)^2\Big\}. \tag{1.7}$$

It quantifies how mixed the state is in a given symmetry sector. $\mathcal{P}_A(q)$ ranges in $[2^{-\dim(\mathcal{H}_A(q))}, 1]$, where $\dim(\mathcal{H}_A(q))$ is the dimension of the Hilbert space associated to the symmetry sector q of subsystem A.

The symmetry-resolved Rényi entropies are a straightforward extension of this concept:

$$S_A^{(n)}(q) \equiv \frac{1}{1-n} \log \mathrm{tr}\{\rho_A(q)^n\} \, . \tag{1.8}$$

Computing $\mathrm{tr}\{\rho_A(q)^n\}$ (in cases when a direct application of projectors in not feasible) requires the knowledge of the spectral resolution in Q_A of ρ_A. As pointed out in Refs. [22, 23], for some of the computations below, it will be more convenient to study the charged moments $Z_n(\alpha)$,

$$Z_n(\alpha) \equiv \mathrm{tr}\Big\{\rho_A^n e^{i\alpha Q_A}\Big\}, \tag{1.9}$$

since those do not directly require spectral resolution to start with. The charged moments have been calculated in several cases [22–38]. Starting from the computation of $Z_n(\alpha)$, it is possible to

obtain $\mathrm{tr}\{\rho_A^n \Pi_q\}$ by means of a Fourier transform:

$$\mathrm{tr}\{\rho_A^n \Pi_q\} = \int_{-\pi}^{\pi} \frac{\mathrm{d}\alpha}{2\pi} Z_n(\alpha) \mathrm{e}^{-i\alpha q}. \tag{1.10}$$

We will exploit this last route for the simulations of free fermions in Sec. 6.5.

Recent studies have discussed the basic properties of these symmetry-resolved contributions both in-[22–26, 28–36, 39] and out-of-equilibrium [27, 37], in presence of disorder [38], and in the context of gauge theories [20–23, 27, 40]. In most cases, it has been shown that symmetry-resolved Rényi entropies of large subsystems exhibits entanglement equipartition at long times (namely all symmetry-resolved Rényi entropies are equal) for the most relevant and populated symmetry sectors. The non equilibrium dynamics of symmetry-resolved Rényi entropies has been considered for isolated systems, both after a local [37] and a global [27] quantum quench, and has revealed the presence of a universal time delay for the activation of a given sector [27]. The investigation of symmetry-resolved Rényi entropies is far from complete and the characterization of its behavior in the presence of dissipation is one of the topic we will focus on in this thesis.

1.5 Entanglement negativity

In the case the system $\mathcal{S}$ is in a mixed state, the entropies of the reduced density matrix are no longer proper measures of bipartite entanglement, as they are also sensitive to classical correlations, although they still provide useful information. A more appropriate and commonly used quantity to witness entanglement in these cases is the negativity [41].

Considering $A = A_1 \cup A_2$, according to Peres' criterion [42], also called positive partial transpose (PPT) criterion, a necessary condition for separablity is that the eigenvalues λ_i of its partial transpose ρ^{T_1} (with respect to subsystem A_1) are exclusively non-negative ($\lambda_i \geq 0$).

For a bosonic system, the partial transpose of the reduced density matrix ρ^{T_1} with respect to A_1 is defined by performing a standard transposition in $\mathcal{H}_{A_1}$, i.e. exchanging the matrix elements in A_1,

$$\rho_A^{T_1} = (T_{A_1} \otimes \mathbb{1}_{A_2}) \rho_A = = \sum_{i,j,k,l} \left\langle e_k^{A_1}, e_j^{A_2} \right| \rho_A \left| e_i^{A_1}, e_l^{A_2} \right\rangle \left| e_i^{A_1}, e_j^{A_2} \right\rangle \left\langle e_k^{A_1}, e_l^{A_2} \right|. \tag{1.11}$$

The partial transposition has also an interpretation in terms of a time-reversal transformation or mirror reflection in phase space [43]. Namely, considering the one-to-one correspondence between density matrices and Wigner distribution functions $W(q,p)$ then

$$\rho_A \to \rho_A^T \iff W(q,p) \to W(q,-p).$$

This can be conveniently observed starting from a bosonic density matrix written in a coherent state basis, since time-reversal transformation ($\mathcal{T}$) can be identified with the complex conjuga-

tion [44]. Taking $|\alpha\rangle$, a bosonic coherent state, one has

$$(|\alpha\rangle\langle\alpha^*|) \xrightarrow{\mathcal{T}} |\alpha^*\rangle\langle\alpha| = (|\alpha\rangle\langle\alpha^*|)^T. \tag{1.12}$$

Starting from the partial transposition one can define the entanglement negativity written as

$$\mathcal{N} \equiv \sum_i \max\{0, -\lambda_i\} = \tfrac{1}{2}\left(\mathrm{tr}\left\{|\rho_A^{T_1}|\right\} - 1\right) \tag{1.13}$$

that quantifies the degree to which $\rho_A^{T_1}$ fails to be positive semidefinite. So, a non-zero negativity implies the presence of entanglement between A_1 and A_2.

To construct the partial transpose for fermionic systems one has to observe that Eq.(1.12) does not hold anymore. Let us start by writing the density matrix of a fermionic system in terms of Majorana operators c_j, which are defined in terms of the fermionic operators a_j obeying $\{a_k^\dagger, a_j\} = \delta_{kj}$ as

$$\begin{cases} c_{2j-1} = a_j + a_j^\dagger, \\ c_{2j} = i(a_j - a_j^\dagger). \end{cases} \tag{1.14}$$

We consider a system $A = A_1 \cup A_2$ and denote with the subscripts $\{m_1, \ldots, m_{l_1}\}$ the operators in the subset A_1 and with $\{n_1, \ldots, n_{l_2}\}$ the ones in the subset A_2; here $l_1(l_2)$ corresponds to the number of sites in subsystem $A_1(A_2)$. One can write [45]:

$$\rho_A = \sum_{\boldsymbol{\kappa},\boldsymbol{\tau}} w_{\boldsymbol{\kappa},\boldsymbol{\tau}} c_{m_1}^{\kappa_1} \ldots c_{m_{2l_1}}^{\kappa_{2l_1}} c_{n_1}^{\tau_1} \ldots c_{n_{2l_2}}^{\tau_{2l_2}} \tag{1.15}$$

where we defined $\boldsymbol{\kappa} = (\kappa_1, \ldots, \kappa_{2l_1})$ and $\boldsymbol{\tau} = (\tau_1, \ldots, \tau_{2l_2})$ with $\kappa_j, \tau_j = 0, 1$. We also set $|\kappa| = \sum_{j=1}^{2l_1} \kappa_j$ and $|\boldsymbol{\tau}| = \sum_{j=1}^{2l_2} \tau_j$. Since the physical fermionic states must commute with the parity operator one has that the sum of the moduli of $\boldsymbol{\kappa}$ and $\boldsymbol{\tau}$ must be even. The partial transpose (1.11) leaves unaltered the state in A_2 and exchanges the states in A_1 as

$$\rho_A^{T_1} = \sum_{\boldsymbol{\kappa},\boldsymbol{\tau}} (-1)^{f(\boldsymbol{\kappa})} w_{\boldsymbol{\kappa},\boldsymbol{\tau}} c_{m_1}^{\kappa_1} \ldots c_{m_{2l_1}}^{\kappa_{2l_1}} c_{n_1}^{\tau_1} \ldots c_{n_{2l_2}}^{\tau_{2l_2}} \tag{1.16}$$

where

$$(-1)^{f(\boldsymbol{\kappa})} = \begin{cases} 0 & |\boldsymbol{\kappa}| \bmod 4 \in \{0, 3\} \\ 1 & |\boldsymbol{\kappa}| \bmod 4 \in \{1, 2\} \end{cases}. \tag{1.17}$$

The easiest way to see this is to perform the partial transpose in the occupation number basis and then write the density matrix in terms of Majorana operators.

As a prototypical example, let us now consider a Gaussian state that can be written in the form

$$\rho_A = \frac{1}{Z} e^{\frac{1}{4}\sum_{kl} W_{kl} c_k c_l}, \tag{1.18}$$

where c_k are fermionic Majorana operators and W is a $2\ell \times 2\ell$ matrix (ℓ size of the system described by ρ), with eigenvalues $\in \mathbb{R}$. The latter is related to the correlation matrix Γ (i.e. the matrix with elements $\Gamma_{i,j} = \frac{1}{2}\langle [c_i, c_j] \rangle$) by the relation

$$\Gamma = \tanh \frac{W}{2}. \tag{1.19}$$

Here Γ has eigenvalues between $[-1, 1]$. It is convenient to introduce the block structure of Γ as

$$\Gamma = \begin{pmatrix} \Gamma_{A_1 A_1} & \Gamma_{A_1 A_2} \\ \Gamma_{A_2 A_1} & \Gamma_{A_2 A_2} \end{pmatrix}. \tag{1.20}$$

Using Eq. (1.16) it can be shown that [45]

$$\rho_A^{T_1} = \frac{1-i}{2} O_+ + \frac{1+i}{2} O_- \tag{1.21}$$

where $O_\pm = \sum_{\boldsymbol{\kappa},\boldsymbol{\tau}} o^\pm_{\boldsymbol{\kappa},\boldsymbol{\tau}} c^{\kappa_1}_{m_1} \dots c^{\kappa_{2l_1}}_{m_{2l_1}} c^{\tau_1}_{n_1} \dots c^{\tau_{2l_2}}_{n_{2l_2}}$ with

$$o^\pm_{\boldsymbol{\kappa},\boldsymbol{\tau}} = \begin{cases} \pm i (-1)^{\frac{|\boldsymbol{\kappa}|-1}{2}} w_{\boldsymbol{\kappa},\boldsymbol{\tau}} & |\boldsymbol{\kappa}| \text{ odd} \\ i (-1)^{\frac{|\boldsymbol{\kappa}|}{2}} w_{\boldsymbol{\kappa},\boldsymbol{\tau}} & |\boldsymbol{\kappa}| \text{ even.} \end{cases} \tag{1.22}$$

The operators $O_\pm$ are Gaussian and can be written as

$$O_+ = O_-^\dagger = \frac{1}{Z} e^{\frac{1}{4}\sum_{kl} (N_A)_{kl} c_k c_l} \tag{1.23}$$

where N_A is related (as in Eq. (1.19)) to the correlation matrix Γ_+ defined according to the following equation:

$$\Gamma_+ = \begin{pmatrix} -\Gamma_{A_1 A_1} & i\Gamma_{A_1 A_2} \\ i\Gamma_{A_2 A_1} & \Gamma_{A_2 A_2} \end{pmatrix}. \tag{1.24}$$

It is clear that the partially transposed reduced density matrix (1.21) is not a Gaussian operator, but rather the sum of two of them. Even more troubling, the density matrix defined starting from Eq. (1.21) does not satisfy additivity nor subadditivity and fails to capture, for this reason, some topological features of fermionic Majorana systems such as the entanglement due to zero-energy modes in Kitaev's chain [44].

For all the above reasons, a different partial transpose has been introduced for fermionic systems starting from the analogy with the time-reversal transformation [44, 46, 47]. In a coherent

state basis the reduced density matrix of a fermionic system reads [44, 45, 47, 48]

$$\rho_A = \frac{1}{Z}\int \mathrm{d}[\xi]\mathrm{d}[\bar{\xi}]\mathrm{e}^{-\sum_j \bar{\xi}_j\xi_j}\left\langle\{\xi_j\}\right|\rho_A\left|\{\bar{\xi}_j\}\right\rangle\left|\{\xi_j\}\right\rangle\left\langle\{\bar{\xi}_j\}\right|. \tag{1.25}$$

Here $\xi,\bar{\xi}$ are Grassman variables and $|\xi\rangle = \mathrm{e}^{-\xi a^\dagger}|0\rangle$,$|\bar{\xi}\rangle = \langle 0|\,\mathrm{e}^{-a^\dagger\bar{\xi}}$ are the related fermionic coherent states. The partial time reversal, analog of Eq. (1.12), is [44]

$$|\xi\rangle\langle\bar{\xi}| \xrightarrow{\mathcal{T}} |i\bar{\xi}\rangle\langle i\xi| \tag{1.26}$$

This definition can be readily generalized to multi-particle states. Considering a system $A = A_1 \cup A_2$ one has

$$\left(\left|\{\xi_j\}_{j\in A_1}\{\xi_j\}_{j\in A_2}\right\rangle\left\langle\{\bar{\chi}_j\}_{j\in A_1}\{\bar{\chi}_j\}_{j\in A_2}\right|\right)^{R_1} = \left|\{i\bar{\chi}_j\}_{j\in A_1}\{\xi_j\}_{j\in A_2}\right\rangle\left\langle\{i\xi_j\}_{j\in A_1}\{\bar{\chi}_j\}_{j\in A_2}\right|, \tag{1.27}$$

where $\{\xi_j\}_{j\in A_X}$,$\{\chi_j\}_{j\in A_X}$ are Grassman variables on sites $j \in A_X$. In the occupation number basis, the above equation reads [44]

$$\begin{aligned}&\left(\left|\{n_j\}_{j\in A_1}\{n_j\}_{j\in A_2}\right\rangle\left\langle\{\bar{n}_j\}_{j\in A_1}\{\bar{n}_j\}_{j\in A_2}\right|\right)^{R_1} = \\ &= (-1)^{\phi(\{n_j,\bar{n}_j\})}\times\left|\{\bar{n}_j\}_{j\in A_1}\{n_j\}_{j\in A_2}\right\rangle\left\langle\{n_j\}_{j\in A_1}\{\bar{n}_j\}_{j\in A_2}\right|.\end{aligned} \tag{1.28}$$

Here the term $\phi(\{n_j,\bar{n}_j\})$ is a phase factor depending on the occupation number

$$\begin{aligned}\phi(\{n_j,\bar{n}_j\}) = \frac{\tau_{A_1}(\tau_{A_1}+2)}{2} + \frac{\bar{\tau}_{A_1}(\bar{\tau}_{A_1}+2)}{2} + \tau_{A_2}\bar{\tau}_{A_2} + \\ + \tau_{A_1}\tau_{A_2} + \bar{\tau}_{A_1}\bar{\tau}_{A_2} + (\bar{\tau}_{A_1}+\bar{\tau}_{A_2})(\tau_{A_1}+\tau_{A_2}),\end{aligned} \tag{1.29}$$

with $\tau_{A_1} = \sum_{j\in A_1} n_j$ ($\tau_{A_2} = \sum_{j\in A_2} n_j$) and $\bar{\tau}_{A_1} = \sum_{j\in A_1}\bar{n}_j$ ($\bar{\tau}_{A_2} = \sum_{j\in A_2}\bar{n}_j$). Hence the definition in Eq. (1.28) is equivalent to a standard partial transposition up to phase factor depending on the parity of the two subsystems, as in Eq. (1.29). In terms of Majorana operators, the transformation in Eq. (1.28) can be rewritten as

$$\rho_A^{R_1} = \sum_{|\boldsymbol{\kappa}|+|\boldsymbol{\tau}|even} w_{\boldsymbol{\kappa},\boldsymbol{\tau}} i^{|\boldsymbol{\kappa}|} c_{m_1}^{\kappa_{m_1}}\cdots c_{m_{2l_1}}^{\kappa_{m_{2l_1}}} c_{n_1}^{\tau_{n_1}}\cdots c_{n_{2l_2}}^{\tau_{n_{2l_2}}} \tag{1.30}$$

where we used the notation $c_x^0 = \mathbb{1}$, $c_x^1 = c_x$. The matrix $\rho_A^{R_1}$ satisfies three necessary properties for a partial transposition:

1. $(\rho_A^{R_1})^{R_2} = \rho_A^R$,
2. $(\rho_A^{R_1})^{R_1} = \rho_A$,
3. $(\rho_1\otimes\rho_2\cdots\rho_n)^{R_1} = \left(\rho_1^{R_1}\otimes\rho_2^{R_1}\otimes\cdots\otimes\rho_n^{R_1}\right)$.

This density operator $\rho_A^{R_1}$ is not Hermitian and, in general, has complex eigenvalues. Nevertheless, one can still define a fermionic logarithmic negativity as [44]

$$\mathcal{E} = \log \mathrm{tr} \sqrt{(\rho_A^{R_1})^\dagger \rho_A^{R_1}} \tag{1.31}$$

where the object $(\rho_A^{R_1})^\dagger \rho_A^{R_1}$ is Hermitian and its spectrum is positive. In spite of the name, the fermionic negativity has nothing to do with the negativeness of the spectrum of $\rho_A^{R_1}$. However It can be proved that it is a proper entanglement monotone [49] and it has been shown that it can detect entanglement when the standard negativity fails [44]. In [46] it has also been shown that, in general, there is a freedom in the definition of the partial transpose operation. This leads to an alternative definition for the fermionic negativity (1.31) given by

$$\mathcal{E} = \log \mathrm{tr} |\rho_A^{\tilde{R}_1}|. \tag{1.32}$$

with

$$\rho_A^{\tilde{R}_1} = \rho_A^{R_1} (-1)^{F_{A_1}}, \tag{1.33}$$

where $F_{A_1} = \sum_{j \in A_1} n_j$ is the number of fermions in the subsystem A_1. Given that the spectrum of $\rho_A^{\tilde{R}_1}$ is real, the fermionic negativity is a measure of the negativeness of the eigenvalues of the latter.

Notice that $\rho_A^{R_1}$ for fermionic gaussian systems is nothing but O_+ in Eq. (1.21). Furthermore, in the case of Gaussian states the relation between $\rho_A^{\tilde{R}_1}$ and $\rho_A^{R_1}$ simplifies and one can write

$$\mathrm{e}^{\tilde{N}_A} = \frac{\mathbb{1} + \Gamma_+}{\mathbb{1} - \Gamma_+} U_{A_1}, \tag{1.34}$$

where the matrix $U_A = -\mathbb{1}_{A_1} \oplus \mathbb{1}_{A_2}$ is related to the transformation $(-1)^{F_{A_1}}$. A last comment concerns the structure of the spectrum of $\rho_A^{\tilde{R}_1}$. The eigenvalues of $\tilde{\Gamma}$ are of the form $\pm \tilde{\nu}_j$. In terms of these, the density matrix $\rho_A^{\tilde{R}_1}$ can be brought into a diagonal form

$$\rho_A^{\tilde{R}_1} = \frac{1}{Z} \prod_{j=1}^{\ell_1+\ell_2} \frac{1 + i\tilde{\nu}_j d_{2j} d_{2j-1}}{2}, \tag{1.35}$$

where d_j are a set of real fermionic operators. Since the eigenvalues of $d_{2j} d_{2j-1}$ are $\pm i$, the 2^ℓ eigenvalues of $\rho_A^{\tilde{R}_1}$ are given by all possible products of $\frac{1 \pm \tilde{\nu}_j}{2}$. Hence, in order to have negative eigenvalues a necessary conditions is that some ν_j are larger than 1. Focusing now, for practical reasons, to the case of two intervals of length ℓ_1 and ℓ_2 respectively, we anticipated in the main text that the eigenvalues of $\tilde{N}_A$ are either real or real $+i\pi$. To be more precise, the spectrum of $\tilde{N}_A$ is of the form $\{\lambda_j + i\pi\}, \lambda_j \in \mathbb{R}$ for $j = 1, \cdots, 2\ell_1$ and $\{\lambda_j\}, \lambda_j \in \mathbb{R}$ for $j = 2\ell_1 + 1, \cdots, 2(\ell_1 + \ell_2)$. The presence of the terms $i\pi$ is what determines the negative eigenvalues in the spectrum of $\rho_A^{\tilde{R}_1}$.

Indeed, using the relation

$$\tilde{\Gamma} = \tanh \frac{\tilde{N}_A}{2}, \tag{1.36}$$

if the eigenvalues are $\lambda_j + i\pi$, then $\nu_j = \tanh(\lambda_j/2 + i\pi/2) = \coth(\lambda_j/2)$, and so $\nu_j = \coth(\lambda_j/2) > 1$.

We finally mention that the fermionic logarithmic negativity in Eq. (1.32) can be computed as

$$\mathcal{E} = \sum_{j=1}^{\ell_1+\ell_2} \log\left[\left|\frac{1-\tilde{\nu}_j}{2}\right| + \left|\frac{1+\tilde{\nu}_j}{2}\right|\right] + \log \mathrm{tr}(\rho_A^{\tilde{R}_1}), \tag{1.37}$$

where $\mathrm{tr}(\rho_A^{\tilde{R}_1}) = \sqrt{\det \Gamma_{A_1 A_1}}$. Note that the sum is over half of the eigenvalues of $\tilde{\Gamma}$.

In recent years, the negativity has been extensively studied in a large variety of physical situation, including critical [50–54] and disordered systems [55, 56], topological phases [57–61], and out of equilibrium [62–68]. The same holds for the fermionic counterpart of the negativity which has been investigated to characterise the entanglement in fermionic mixed states [44–46, 48, 69–72].

1.6 Symmetry-resolved entanglement negativity

In analogy to entanglement entropy, one can consider the negativity for a system, with a partition $A \cup B$, possessing some additive conserved charge $Q = Q_A \otimes \mathbb{1}_B + \mathbb{1}_A \otimes Q_B$. Interestingly, ρ^{T_A} admits a block diagonal form in the quantum numbers of the *charge imbalance*, that is, the difference of charge between A and B, $\tilde{Q} = Q_A - Q_B^{T_A}$ [73]. Let $\Pi_{\tilde{q}}$ denote the projector onto the eigenspace of $\tilde{Q}$ associated with eigenvalue $\tilde{q}$. We define the normalized symmetry-resolved partially transposed density matrix [73, 74]

$$\rho^{T_A}(\tilde{q}) \equiv \frac{\Pi_{\tilde{q}} \rho^{T_A} \Pi_{\tilde{q}}}{\mathrm{tr}\{\rho^{T_A} \Pi_{\tilde{q}}\}}, \quad \mathrm{tr}\Big\{\rho^{T_A}(\tilde{q})\Big\} = 1, \tag{1.38}$$

such that

$$\rho^{T_A} = \oplus_{\tilde{q}}\, p(\tilde{q}) \rho^{T_A}(\tilde{q}) \tag{1.39}$$

with $p(\tilde{q}) = \mathrm{tr}\{\rho^{T_A} \Pi_{\tilde{q}}\} \geq 0$ the probability of being in charge imbalance sector $\tilde{q}$. We can thus define the symmetry-resolved negativity as

$$\mathcal{N}(\tilde{q}) \equiv \frac{\mathrm{tr}\{|\rho^{T_A}(\tilde{q})|\} - 1}{2} \tag{1.40}$$

with $\mathcal{N} = \sum_{\tilde{q}} \tilde{p}(\tilde{q}) \mathcal{N}(\tilde{q})$. To compute the symmetry-resolved negativity, one needs the spectral resolution of ρ^{T_A} as in the previous case. Beyond the case of exact simulations, this challenging calculation is performed in two steps. We first focus on the moments $\mathrm{tr}\{(\rho^{T_A}(\tilde{q}))^n\}$, from which

the negativity is obtained from a replica trick [51]. Then we consider the charged moments [46, 73]

$$R_n(\alpha) \equiv \mathrm{tr}\Big\{ \left(\rho^{T_A}\right)^n \mathrm{e}^{i\alpha\tilde{Q}_A} \Big\} \tag{1.41}$$

and performing a Fourier transform we get the desired $\mathrm{tr}\big\{(\rho^{T_A}(\tilde{q}))^n\big\}$. This way of performing the calculation is very powerful when combined with $1+1$D CFTs [51, 73], which also provided exact results for the time evolution of the symmetry-resolved negativity after a local quantum quench [37]. The extension of symmetry resolved negativity for fermionic systems (i.e. fermionic partial transpose) is not discussed in this work; the reader could refer to Ref.[74] and references therein for more information.

1.7 Operator entanglement

In this section we introduce the operator entanglement (OE) of a reduced density matrix and discuss its symmetry resolution in the presence of an additive global conserved charge.

1.7.1 Definition of operator entanglement

Let us formally consider the OE of a density matrix ρ_{AB} of a bipartite system $A \cup B$. Despite we restrict to this choice, all the definitions of this section hold for a generic operator O acting on a bipartite system. In Ref.[75] several examples are discussed. We observe that it admits a Schmidt decomposition:

$$\frac{\rho_{AB}}{\sqrt{\mathrm{Tr}(O^\dagger O)}} = \sum_{i=1}^{\mathrm{srank}(O)} \lambda_i O_{A,i} \otimes O_{B,i}. \tag{1.42}$$

It has the property that all expansion coefficients λ_i are positive and the associated operators $O_{A,i}, O_{B,i}$ are Hermitian and orthonormal with respect to the Hilbert-Schmidt inner product

$$\mathrm{Tr}(O_{A,i}^\dagger O_{A,j}) = \mathrm{Tr}(O_{B,i}^\dagger O_{B,j}) = \delta_{i,j}.$$

Normalization on the lhs of Eq. (1.42) moreover ensures that the expansion coefficients obey $\sum_i \lambda_i^2 = 1$, i.e. the set $\{\lambda_i^2\}$ forms a probability distribution of (squared) Schmidt value. The smallest summation range for which Eq. (1.42) is possible is called the operator Schmidt rank $\mathrm{srank}(O)$ of ρ_{AB}, see e.g. [76]. From this decomposition, we can quantify the operator entanglement properties of ρ_{AB} through the Rényi α-OE

$$S^{(\alpha)}(\rho_{AB}) := \frac{1}{1-\alpha} \log \sum_i \lambda_i^{2\alpha} \quad \text{for } \alpha > 1. \tag{1.43}$$

The limit $\alpha \to 1$ gives the OE

$$S(\rho_{AB}) := \sum_i -\lambda_i^2 \log \lambda_i^2. \tag{1.44}$$

We have presented the OE in terms of 'operator Schmidt decompositions', Eqs. (1.42), but it is equivalent to apply the standard Schmidt decomposition —of a pure state— to the vectorization of the density matrix ρ_{AB}. The vectorization is nothing but the mapping (known as Choi–Jamiołkowski isomorphism)

$$\rho_{AB} = \sum_{ij} (\rho_{AB})_{ij} \, |i\rangle \langle j| \to |\rho_{AB}\rangle = \sum_{ij} (\rho_{AB})_{ij} \, |i\rangle \, |j\rangle \,, \tag{1.45}$$

where $|i\rangle$ is an arbitrary basis in the Hibert space of AB. It follows that the Schmidt decomposition of $|\rho_{AB}\rangle$ is equivalent to (the vectorization of) Eq. (1.42)

1.8 Symmetry resolved operator entanglement

In the presence of a global symmetry, the OE of the operator ρ_{AB} can be split into different charge sectors, similarly to the state entanglement [77, 78].

This happens in particular for global U(1) symmetry, when the U(1) charge operator acting on $A \cup B$ is a sum of the two charge operators acting on subsystems A and B, $Q_{AB} = Q_A \otimes \mathbb{I}_B + \mathbb{I}_A \otimes Q_B$. If density matrix ρ_{AB} commutes with Q_{AB}, then it is possible to organize the terms in the Schmidt decomposition according to their charge q,

$$\frac{\rho_{AB}}{\sqrt{\mathrm{Tr}[\rho_{AB}^2]}} = \sum_q \sum_j \lambda_j^{(q)} O_{A,j}^{(q)} \otimes O_{B,j}^{(-q)}, \tag{1.46}$$

where

$$[Q_A, O_{A,j}^{(q)}] = q \, O_{A,j}^{(q)}, \quad [Q_B, O_{B,j}^{(-q)}] = -q \, O_{B,j}^{(-q)}, \tag{1.47}$$

so that

$$[Q_A \otimes \mathbb{I}_B + \mathbb{I}_A \otimes Q_B, O_{A,j}^{(q)} \otimes O_{B,j}^{(-q)}] = 0.$$

As above, the operators $O_{A,j}^{(q)}$ and $O_{B,j}^{(q)}$ in the decomposition (1.46) are orthonormal sets,

$$\mathrm{Tr}[O_{A,j_1}^{(q_1)} O_{A,j_2}^{(q_2)}] \; = \; \mathrm{Tr}[O_{B,j_1}^{(q_1)} O_{B,j_2}^{(q_2)}] \; = \; \delta_{q_1,q_2} \delta_{j_1,j_2}.$$

We can define the total weight of the terms at fixed q,

$$p(q) := \sum_j (\lambda_j^{(q)})^2. \tag{1.48}$$

This weight satisfies $\sum_q p(q) = 1$, so it is a probability distribution on the different charge sectors. In terms of that probability distribution, the OE (1.44) reads

$$S(\rho_{AB}) \; = \; \sum_q p(q) S_q(\rho_{AB}) \; + \; \sum_q -p(q) \log p(q), \tag{1.49}$$

where the 'symmetry-resolved operator entanglement' (SROE) of ρ_{AB} in the charge sector q is

$$S_q(\rho_{AB}) := \sum_j -\frac{(\lambda_j^{(q)})^2}{p(q)} \log \frac{(\lambda_j^{(q)})^2}{p(q)}. \tag{1.50}$$

Similarly, for a generic Rényi index α, the Rényi-α SROE is defined as

$$S_q^{(\alpha)}(\rho_{AB}) := \frac{1}{1-\alpha} \log \sum_j \frac{(\lambda_j^{(q)})^{2\alpha}}{p(q)^\alpha}. \tag{1.51}$$

Again, the same result can be derived applying the standard Schmidt decomposition to the vectorization of the density matrix ρ_{AB}. The charge 'superoperator' $\mathcal{Q}_{AB}$ which acts on the vectorized density matrix $|\rho_{AB}\rangle$ reads

$$\mathcal{Q}_{AB} = Q_{AB} \otimes \mathbb{1} - \mathbb{1} \otimes Q_{AB}^T, \tag{1.52}$$

so that

$$\mathcal{Q}_{AB} |\rho_{AB}\rangle = |Q_{AB}\rho_{AB}\rangle - |\rho_{AB} Q_{AB}\rangle = |[Q_{AB}, \rho_{AB}]\rangle . \tag{1.53}$$

Similarly, the charge superoperators acting only on subsytems A and B are defined as $\mathcal{Q}_A = Q_A \otimes \mathbb{1} - \mathbb{1} \otimes Q_A^T$ and $\mathcal{Q}_B = Q_B \otimes \mathbb{1} - \mathbb{1} \otimes Q_B^T$. The terms in the Schmidt decomposition of $|\rho_{AB}\rangle$ can be organized according to the eigenvalue of the charge superoperators $\mathcal{Q}_A$ $(= -\mathcal{Q}_B)$ and this is equivalent to (the vectorization of) Eq. (1.46).

Importantly, in Chap. 7 we focus on a density matrix that is the reduced density matrix of the subsystem $A \cup B$, obtained after tracing out degrees of freedom in C in a tripartite system $A \cup B \cup C$. It turns out this naturally yields an operator ρ_{AB} which commutes with the U(1) charge operator in $A \cup B$,

$$[Q_{AB}, \rho_{AB}] = 0. \tag{1.54}$$

To understand how this happens, let us look at a minimal illustrative example: a 3-qubits system, whose qubits are labeled A, B and C, in a state of the form $(|\alpha|^2 + |\beta|^2 + |\gamma|^2 = 1)$

$$|\psi\rangle_{ABC} = \alpha |100\rangle + \beta |010\rangle + \gamma |001\rangle . \tag{1.55}$$

This is an eigenstate of the total charge operator $Q_{ABC} = \sum_{j=A,B,C} |1\rangle_j \langle 1|_j$. The reduced density matrix of the subsystem AB is

$$\rho_{AB} = (\alpha |10\rangle + \beta |01\rangle)(\alpha^* \langle 10| + \beta^* \langle 01|) + |\gamma|^2 |00\rangle \langle 00| , \tag{1.56}$$

which commutes with $Q_A \otimes \mathbb{I}_B + \mathbb{I}_A \otimes Q_B$. Therefore the above definitions can be applied and it makes sense to study the SROE of the reduced density matrix ρ_{AB} in this minimal example.

Let us proceed vectorizing the reduced density matrix ρ_{AB}:

$$\begin{aligned} |\rho_{AB}\rangle = |\gamma|^2 |00\rangle_A |00\rangle_B + |\beta|^2 |00\rangle_A |11\rangle_B + |\alpha|^2 |11\rangle_A |00\rangle_B \\ + \beta\alpha^* |01\rangle_A |10\rangle_B + \beta^*\alpha |10\rangle_A |01\rangle_B . \end{aligned} \tag{1.57}$$

From this, we can build the object $|\rho_{AB}\rangle \langle\rho_{AB}|$ and take the trace over the subsystem over B. This gives

$$\begin{aligned} \mathrm{Tr}_{B\otimes B} |\rho_{AB}\rangle \langle\rho_{AB}| = |\beta|^4 |00\rangle \langle 00| \\ + |\beta|^2|\alpha|^2(|01\rangle \langle 01| + |10\rangle \langle 10|) \\ + (|\gamma|^2 |00\rangle + |\alpha|^2 |11\rangle)(|\gamma|^2 \langle 00| + |\alpha|^2 \langle 11|). \end{aligned} \tag{1.58}$$

By reshuffling the elements of the basis, we find out that the matrix has a block-diagonal decomposition as

$$\mathrm{Tr}_{B\otimes B} |\rho_{AB}\rangle \langle\rho_{AB}| \cong \left(|\alpha|^2|\beta|^2\right)_{q=-1} \oplus \begin{pmatrix} |\beta|^4 + |\gamma|^4 & |\alpha|^2|\gamma|^2 \\ |\alpha|^2|\gamma|^2 & |\alpha|^4 \end{pmatrix}_{q=0} \oplus \left(|\beta|^2|\alpha|^2\right)_{q=1} . \tag{1.59}$$

The eigenvalues of each block correspond to the $\lambda_j^{(q)}$'s in Eq. (1.46). From this expression, is clear that each block is labelled by the imbalance between the charge in A and in its copy, coming from the vectorization of ρ_{AB}, or equivalently from the difference between the charge Q_A acting from the left and from the right, as formally stated in Eq. (1.47).

2

Randomized measurements

2.1 Introduction

In the era of noisy intermediate-scale quantum devices, experimentalists and theorists are working together on developing and employing effective tools to investigate and characterize the features of many-qubit quantum states prepared in the laboratory. Usually, the most naive way of tackling this problem consists of preparing and measuring the same quantum state multiple times, such that, collecting enough information it is possible to completely reconstruct an N-qubit state: this is denoted as full state tomography [79–83]. This approach is inefficient and hopelessly applicable on large systems, as it requires a number of repetitions of the experiments which scales exponentially in N (system size), and classical post-processing which would be a daunting challenge even for the most powerful super-computers.

In the past years, it has been shown that the number of experiments and the subsequent post-processing may be profitably optimized, for most of the properties of quantum states need a far less complete description to be efficiently estimated. This comes at the expense of a small statistical uncertainty on the observable at stake, whose upper bound can be estimated analytically [84, 85]. The main idea, which goes under the umbrella of *randomized measurements protocol*, is that global properties of quantum states can be computed using a modest number of measurement repetitions. Before performing the measurements, one can act with random unitary operations such that the single qubits are actually measured in a random basis in the Hilbert space. This protocol effectively translates the quantum information of the system in a classical representation of the states in terms of unitary operations and classical bit-strings. As a result, a lot of information is discarded, but many relevant features of the quantum state can still be extracted through classical

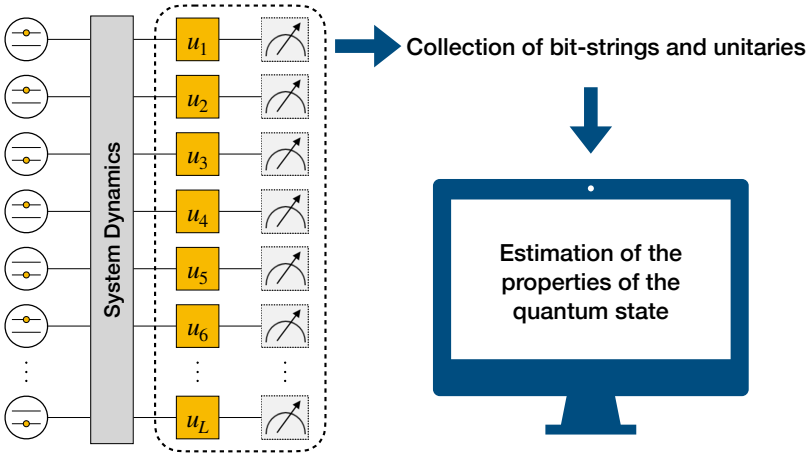

Figure 2.1: Sketch of randomized measurement protocol. A N qubits quantum state ρ is prepared and undergoes a given dynamics. A set of random unitaries sampled from a suitable ensemble $\{u_1, \ldots, u_N\}$ (e.g Clifford group or CUE) is applied on it. The state is then measured in the computational basis and bit strings are collected $s = \{s_1, \ldots, s_N\}$. Via classical post-processing of bit-strings and unitaries it is possible to estimate many non-linear functions of the density matrix ρ.

post-processing of the data. In the following section we review a particular randomized measurement scheme that employs single-qubit measurements to construct a, so-called, *classical shadow* of a quantum state. Here we describe the standard protocol of randomized measurements. We consider a quantum system consisting of n qubits with associated Hilbert space $\mathbb{C}_2^{\otimes n}$. A randomized measurement, schematically depicted in Fig.2.1, consists in the following steps:

(i) the quantum many-body state ρ of interest is prepared in the laboratory;

(ii) a unitary operation U, selected at random from a suitable ensemble of unitary operations, is applied to ρ. Often it is considered the case when U consists of n local unitaries $U = u_1 \otimes \cdots \otimes u_n$. The individual single-qubit rotations are sampled from suitable ensembles of single-qubit unitary operations, e.g. the Clifford group or the Circular Unitary Ensemble (CUE);

(iii) a projective measurement in the computational basis is performed, collecting the bit-string $s = \{s_1, ..., s_n\}$ with $s_j \in 0, 1$ for $j = 1, \ldots, n$.

These steps are repeated $N_m \cdot N_u$ times in total. N_u counts the number of different unitary sets considered and N_m the number of repetitions for each unitary set. After completing the experiment, the obtained data can be used to extract information about the underlying many-body system with full classical post-processing.

2.2 Classical shadows

Here we consider the particular case of randomized measurements which consists in collecting classical snapshots of the quantum state taken into account, i.e. *classical shadows*.
We are interested in quantum systems comprised of n qubits. Suppose furthermore, that we can perform certain unitary transformations $U \in \mathcal{E}$ (ensemble), as well as a measurement in the computational basis:

$$\{|b\rangle\langle b| : b \in \{0,1\}^n\}\,.$$

It is instructive to analyze the quantum-to-classical channel that arises from first performing a randomly selected unitary transformation $\rho \mapsto U\rho U^\dagger$ followed by a computational basis measurement:

$$\begin{aligned}\mathcal{M}_{\mathcal{E}}(\rho) &= \int_{\mathcal{E}} \sum_{b\in\{0,1\}^n} \Pr\big[\hat{b} = b|U\rho U^\dagger\big] U^\dagger|b\rangle\langle b|U \mathrm{d}U \\ &= \int_{\mathcal{E}} \mathrm{d}U \sum_{b\in\{0,1\}^n} \langle b|U\rho U^\dagger|b\rangle U^\dagger|b\rangle\langle b|U. \end{aligned} \tag{2.1}$$

The integral over $\mathcal{E}$ is an average over all possible classically randomized measurement settings. The summation over b averages over quantum randomness associated with measurement outcomes (Born's rule). It is easy to check that $\mathcal{M}_{\mathcal{E}}(\cdot)$ is always a quantum channel, i.e. a completely positive and trace-preserving map.

Viewed as a linear operator, this channel is also invertible if the underlying ensemble $\mathcal{E}$ is sufficiently expressive. More precisely, we require that the complete family $\{U^\dagger|b\rangle\langle b|U :\ U \in \mathcal{E}\}$ of admissible basis measurements is *tomographically complete* [84]. That is, for all $\rho \neq \sigma$, there exists a $U \in \mathcal{E}$ and a outcome $b \in \{0,1\}^n$ such that $\langle b|U\rho U^\dagger|b\rangle \neq \langle b|U\sigma U^\dagger|b\rangle$.

Therefore, assuming that $\{U^\dagger|b\rangle\langle b|U :\ U \in \mathcal{E}, b \in \{0,1\}^n\}$ is a tomographically complete family of basis measurements, $\mathcal{M}_{\mathcal{E}}$ has a well-defined and unique inverse $\mathcal{M}_{\mathcal{E}}^{-1}(\cdot)$. From now on, we will always assume that we are dealing with tomographically complete families of basis measurements.

Classical shadow estimation with randomized measurements is based on the following basic routine:

1. *state preparation:* prepare a copy of the unknown quantum state ρ;

2. *randomized single-shot measurement:* sample $U \sim \mathcal{E}$ at random, transform $\rho \mapsto U\rho U^\dagger$ and measure in the computational basis;

3. *construct a classical snapshot:* upon receiving outcome $\hat{b} \in \{0,1\}^n$, compute

$$\hat{\rho} = \mathcal{M}_{\mathcal{E}}^{-1}\left(U^\dagger|\hat{b}\rangle\langle\hat{b}|U\right). \tag{2.2}$$

By construction, each snapshot is a random matrix that exactly reproduces the true underlying state ρ in expectation (over both the classical choice of transformation and the quantum randomness in the basis outcome). That is,

$$\begin{aligned}\mathbb{E}\left[\hat{\rho}\right] =& \mathcal{M}_{\mathcal{E}}^{-1}\left(\mathbb{E}_{U\sim\mathcal{E}}\mathbb{E}_{\hat{b}\in\{0,1\}^n}U^\dagger|\hat{b}\rangle\langle\hat{b}|U\right)\\ =& \mathcal{M}_{\mathcal{E}}^{-1}\left(\mathcal{M}_{\mathcal{E}}(\rho)\right) = \rho.\end{aligned}$$

Statistically speaking, $\hat{\rho}$ is an unbiased estimator of the underlying quantum state ρ. But a single snapshot is only a very poor estimator. This situation changes if we have access to multiple independent snapshots $\{\hat{\rho}_1, \ldots, \hat{\rho}_N\}$. We call such a collection a *classical shadow* of ρ with size N. Forming the empirical average of snapshots within a classical shadow produces ever more accurate approximations of the true underlying state:

$$\frac{1}{N}\sum_{i=1}^{N}\hat{\rho}_i \overset{N\to\infty}{\longrightarrow} \frac{1}{N}\sum_{i=1}^{N}\mathbb{E}\left[\hat{\rho}_i\right] = \rho. \tag{2.3}$$

The main results in Ref. [84] highlight that classical shadows of moderate size already allow joint estimation of many interesting state properties. More precisely, the classical shadow formalism allows for computing powerful a-priori bounds on the convergence behavior of such estimators.

Before moving on, it is worthwhile to emphasize implicit assumptions within the classical shadows model. It turns out that almost all of them can be relaxed without threatening statistical guarantees like error bounds or confidence intervals.

Perfect/noiseless measurements: the original randomized measurement framework is contingent on perfect knowledge of the average quantum-to-classical channel (2.1). Erroneous executions of the ensemble rotation U, or noisy executions of the subsequent computational basis measurement can thwart this assumption. However, recent results [86, 87] highlight that a suitably extended shadow formalism can handle such imperfections. The key idea is to adjust the inversion formula (2.2) appropriately. Ref. [87] achieves such an adjustment by assuming explicit knowledge of the (average) noise channel, while Ref. [86] actually goes a step further and proposes a tractable calibration protocol that reveals sufficient information to appropriately correct Eq. (2.2).

Independent and identically distributed state copies: because quantum measurements are typically destructive, most estimation protocols assume access to a perfect source that produces independent and identically distributed (*iid*) copies of the underlying quantum state ρ. Formally,

N queries of such a perfect *iid* state source produce the state $\rho^{\otimes N}$ and we subsequently proceed to measure independent copies sequentially. This particular tensor product structure is a strong assumption that combines stochastic independence (individual state copies are completely uncorrelated) with identical distribution (all state copies are identical). This second assumption is often violated in concrete experimental architectures. Small fluctuations within the device can lead to state copies that, although uncorrelated, vary in time ("drifting source"). N state copies produced by such drifting (but independent) sources can be modelled by a sequence $\{\rho_i\}_{i=1}^N$ of non-identical quantum states.

The classical shadow formalism can readily handle drifting (but independent) sources. Each snapshot $\hat{\rho}_i$ will have a different expectation value and Eq. (2.3) needs to be adjusted accordingly:

$$\frac{1}{N}\sum_{i=1}^{N}\hat{\rho}_i \longrightarrow \frac{1}{N}\sum_{i=1}^{N}\mathbb{E}\hat{\rho}_i = \frac{1}{N}\sum_{i=1}^{N}\rho_i =: \rho_{\text{avg}}. \tag{2.4}$$

Hence, empirical averages of classical shadows are well-suited for approximating linear properties of the average source state ρ_{avg}. We will show below that this desirable feature extends to the shadow estimation of polynomials as well.

In order to handle drifting sources, we will also assume access to trusted classical randomness that allows us to randomly select unitary transformations $U \in \mathcal{E}$. Mild by comparison, this assumption also features as an explicit (or implicit) assumption in other statistically sound treatments of entanglement detection, see e.g. [88] and references therein.

Finally, we point out that assuming access to independent state copies (tensor product structure) is not a mild assumption. But, the classical shadow estimators below are invariant under permuting individual state copies. Permutation invariance suggests that strong proof techniques from quantum cryptography – like the quantum de Finetti theorem, see e.g. [89, Chapter 7] and references therein – may be applicable and allow for relaxing the independence assumption as well.

2.3 Predicting linear functions with classical shadows

We are now ready to discuss the simplest use-case of classical shadows: estimate a linear function, say $\text{tr}(O\rho)$, based on N randomized measurements of *independent* (but not necessarily identical) states. We can achieve this by simply replacing the unknown quantum state ρ by an empirical average of snapshots within a classical shadow:

$$\begin{aligned}\hat{o}_{(N)} =& \frac{1}{N}\sum_{i=1}^{N}\text{tr}\left(O\hat{\rho}_i\right) \quad \text{obeys} \\ \mathbb{E}\hat{o} =& \text{tr}\left(O\frac{1}{N}\sum_{i=1}^{N}\mathbb{E}\hat{\rho}_i\right) = \text{tr}\left(O\frac{1}{N}\sum_{i=1}^{N}\rho_i\right) = \text{tr}\left(O\rho_{\text{avg}}\right).\end{aligned} \tag{2.5}$$

Independence ensures that the individual snapshots $\hat{\rho}_i$ are stochastically independent random matrices. This in turn implies that each $\mathrm{tr}(O\hat{\rho}_i)$ is a stochastically independent random variable. Empirical averages of independent random variables tend to concentrate sharply around their expectation value – regardless of the underlying distribution. The *variance* is an important parameter that can control the rate of convergence. Chebyshev's inequality, for instance, implies for $\epsilon > 0$

$$\begin{aligned}\Pr\left[\left|\hat{o}_{(N)} - \mathrm{tr}\left(O\rho_{\mathrm{avg}}\right)\right| \geq \epsilon\right] &\leq \tfrac{1}{\epsilon^2}\mathrm{Var}\left[\hat{o}_{(N)}\right] \\ &= \tfrac{1}{N\epsilon^2}\left(\tfrac{1}{N}\sum_{i=1}^{N}\mathrm{Var}\left[\mathrm{tr}\left(O\hat{\rho}_i\right)\right]\right). \end{aligned} \tag{2.6}$$

This tail bound is a consequence of independence alone. The remaining average variance does depend on the ensemble $\mathcal{E}$. Different ensemble give rise to different variance contributions [84, 90]. Here, we focus on the practically most relevant case: randomized, *single-qubit measurements*. Each qubit is measured in either the X-, the Y-, or the Z-basis. More formally, the ensemble $\mathcal{E}$ subsumes random single qubit Clifford rotations. That is $U = u_1 \otimes \cdots \otimes u_n$ with $u_1, \ldots, u_n \overset{iid}{\sim} \mathrm{Cl}(2)$ and $\mathrm{Cl}(2)$ denotes the single-qubit Clifford group, i.e., the finite group generated by Hadamard and phase gates. More generic single-qubit ensembles (like Haar-random unitaries) are also an option – what matters is that the single qubit ensemble forms a 3-design [91, 92]. The (single- and multi-qubit) Clifford group is one ensemble with this feature [93–95]. As demonstrated in Ref. [84], the 3-design assumption allows us to compute the measurement channel (2.1), as well as its inverse. Let $\mathcal{D}_{1/3}(X) = 1/3\,(X + \mathrm{tr}(X)\mathbb{I})$ denote the single-qubit depolarizing channel with parameter $1/3$. Then,

$$\begin{aligned}\mathcal{M}\left(\bigotimes_{k=1}^{n} X_k\right) &= \bigotimes_{k=1}^{n}\mathcal{D}_{1/3}(X_k) = 3^{-n}\bigotimes_{k=1}^{3}\left(X_k + \mathrm{tr}(X_k)\mathbb{I}\right), \\ \mathcal{M}^{-1}\left(\bigotimes_{k=1}^{n} X_k\right) &= \bigotimes_{k=1}^{n}\mathcal{D}_{1/3}^{-1}(X_k) = \bigotimes_{k=1}^{n}\left(3X_k - \mathrm{tr}(X_k)\mathbb{I}\right), \end{aligned}$$

and we refer to [84, Supplementary Information, Section C] for details. We see that the measurement channel (and its inverse) factorizes nicely into a tensor product of single-qubit operations. This is also true for snapshots (2.2) within a classical shadow:

$$\hat{\rho} = \bigotimes_{k=1}^{n}\left(3u_k^\dagger|\hat{b}_k\rangle\langle\hat{b}_k|u_k - \mathbb{I}\right). \tag{2.7}$$

This explicit formulation allows for deriving powerful and useful variance bounds, see [84, Supplementary Information, proof of Proposition S3].

If we fix an observable O and suppose that $\hat{\rho}_i$ is the snapshot (2.7) of an unknown quantum

state, then

$$\mathrm{Var}\left[\mathrm{tr}(O\hat{\rho}_i)\right] \leq 2^{\mathrm{w}(O)}\mathrm{tr}(O^2), \tag{2.8}$$

where $\mathrm{w}(O)$ denotes the observable's weight; that is, the number of qubits on which it acts non-trivially.

We can combine Eq. (2.8) with Eq. (2.6) to obtain

$$\Pr\left[\left|\hat{o}_{(N)} - \mathrm{tr}\left(O\rho_{\mathrm{avg}}\right)\right| \geq \epsilon\right] \leq \frac{2^{\mathrm{w}(O)}\mathrm{tr}(O^2)}{N\epsilon^2}. \tag{2.9}$$

There are different ways to capitalize on this tail bound. Firstly, we can fix a desired approximation accuracy ϵ, as well as a desired (maximal) failure probability δ. Eq. (2.9) then provides us with a lower bound on the number of measurements N required to achieve these values.

Fix $\epsilon, \delta \in (0,1)$ and a linear observable O. Suppose that we perform

$$N \geq \frac{2^{\mathrm{w}(O)}\mathrm{tr}(O^2)}{\epsilon^2\delta}$$

randomized single-qubit measurements on independent states. Then, the associated classical shadow suffices to ϵ-approximate the expectation value of the average source state:

$$\left|\hat{o}_{(N)} - \mathrm{tr}\left(O\rho_{\mathrm{avg}}\right)\right| \leq \epsilon \quad \text{with prob. (at least) } 1-\delta.$$

Alternatively, we can fix a confidence level α and a total measurement budget N. In this case, Eq. (2.9) provides us with a bound on the accuracy of the approximation we made. Together with the empirical average $\hat{o}_{(N)}$ itself, this provides a statistically sound confidence interval.

Fix an observable O, a confidence level $\alpha \in (0,1)$, as well as a measurement budget N (comprised of independent states). Then, the true observable average $\mathrm{tr}(O\rho_{\mathrm{avg}})$ is contained in the interval

$$\left[\hat{o}_{(N)} - \epsilon, \hat{o}_{(N)} + \epsilon\right] \quad \text{with} \quad \epsilon = \sqrt{\frac{2^{\mathrm{w}(O)}\mathrm{tr}(O^2)}{N(1-\alpha)}}$$

with probability (at least) α.

These statements tell us that the measurement budget N (required number of independent state copies) should scale with $2^{\mathrm{w}(O)}\mathrm{tr}(O^2)$ and the approximation error decays as $1/\sqrt{N}$. This is asymptotically optimal because of the central limit theorem, (as the sample size N gets larger, the central limit theorem implies that $\sqrt{N}\left(\hat{o}_{(N)} - o_{(N)}\right)$) but the scaling in $1/(1-\alpha)$ is extremely poor. More sophisticated estimation techniques – like median of means instead of empirical averages [84] – improve this dependence exponentially from $1/(1-\alpha)$ to const $\times \log(1/(1-\alpha))$.

2.4 Predicting quadratic functions with classical shadows

2.4.1 U-statistics estimator

The linear prediction ideas from above do extend to higher order polynomials. But in contrast to before, independent, but not identical, state copies ("drifting sources") do require extra attention. Here, we restrict our attention to quadratic polynomials [84]. An extension to higher order polynomials is conceptually straightforward, but can become somewhat tedious to analyze [96]. Recall that we can rewrite any quadratic function in ρ as a linear function in the tensor product $\rho \otimes \rho$:

$$q(\rho) = \mathrm{tr}\left(Q\rho \otimes \rho\right).$$

We can approximate this function by replacing each exact copy of the unknown state with distinct classical snapshots (say $\hat{\rho}_i$ and $\hat{\rho}_j$, with $i \neq j$). Independence of the underlying states ensures stochastic independence of the classical snapshots and we conclude

$$\mathrm{tr}\left(Q\hat{\rho}_i \otimes \hat{\rho}_j\right) \quad \text{obeys} \quad \mathbb{E}\mathrm{tr}\left(Q\hat{\rho}_i \otimes \hat{\rho}_j\right) = \mathrm{tr}\left(Q\rho_i \otimes \rho_j\right).$$

This is not a good estimator (yet). We can improve approximation accuracy by empirically averaging over all *distinct* pairs of N classical shadows $\hat{\rho}_1, \ldots, \hat{\rho}_N$:

$$\hat{q}_{(N)} = \frac{1}{N(N-1)} \sum_{i \neq j} \mathrm{tr}\left(Q\hat{\rho}_i \otimes \hat{\rho}_j\right). \tag{2.10}$$

This is the simplest example of a *U-statistics estimator* [97]. It is invariant under permuting the individual snapshots $\hat{\rho}_i$ and $\hat{\rho}_j$. This invariance allows us to also symmetrize the quadratic observable. We can without loss assume $\mathrm{tr}(QX \otimes Y) = \mathrm{tr}\left(QY \otimes X\right)$ for all matrices X, Y with compatible dimension. Such a symmetry will simplify our derivations considerably.

2.4.2 Deterministic bias

The estimator average (2.10) exactly reproduces $q\left(\rho_{\mathrm{avg}}\right) = \mathrm{tr}(Q\rho_{\mathrm{avg}} \otimes \rho_{\mathrm{avg}})$ if and only if the underlying states are identical ($\rho_1 = \cdots = \rho_N = \rho$). If this is not the case, the expectation values of individual classical shadows can be distinct from each other. This can introduce a bias when attempting to estimate the average behavior of a quadratic function. Fortunately, any such bias is suppressed by $1/N$ and approaches zero once the number of measurements gets sufficiently large. This is the content of the following statement. Let $\|\cdot\|_1$ and $\|\cdot\|_\infty$ denote the trace and operator norm, respectively.

Let $\{\hat{\rho}_1, \ldots, \hat{\rho}_N\}$ be a classical shadow that arise from measuring independent states $\rho_1, \ldots, \rho_N$. Set $\rho_{\mathrm{avg}} = \frac{1}{N}\sum_{i=1}^N \rho_i$ and consider a quadratic function $q(\sigma) = \mathrm{tr}(Q\sigma \otimes \sigma)$. Then, the associated

U-statistics estimator (2.10) obeys

$$\mathbb{E}\hat{q}_{(N)} = q(\rho_{\text{avg}}) + \tfrac{\Delta}{N-1} \text{ with } |\Delta| \leq \max_{1\leq k\leq N} \|\rho_{\text{avg}} - \rho_k\|_1 \|Q\|_\infty.$$

Note that the bias term Δ vanishes if all states are identically distributed ($\rho_i = \rho_j$ for all $1 \leq i, j \leq N$) and can never be too large either:

$$|\Delta| \leq 2\|Q\|_\infty,$$

as the trace norm difference between two quantum states is at most two. Many quadratic functions, which are particularly relevant in entanglement detection, also obey $\|Q\|_\infty \leq 1$.

The previous result can be proved as in the following. Apply $\mathbb{E}\left[\hat{\rho}_i \otimes \hat{\rho}_j\right] = \rho_i \otimes \rho_j$ (independence) and elementary reformulations to conclude

$$\begin{aligned}
\Delta =& (N-1)\left(q\left(\rho_{\text{avg}}\right) - \mathbb{E}\hat{q}_N\right) \\
=& \tfrac{1}{N}\left(\tfrac{N-1}{N}\sum_{i,j=1}^{N} \operatorname{tr}\left(Q\rho_i \otimes \rho_j\right) - \sum_{i\neq j} \operatorname{tr}\mathbb{E}\left(Q\hat{\rho}_i \otimes \hat{\rho}_j\right)\right) \\
=& \tfrac{1}{N}\left(\sum_{i=1}^{N} \operatorname{tr}\left(Q\rho_i \otimes \rho_i\right) - \tfrac{1}{N}\sum_{i,j=1}^{N} \operatorname{tr}\left(Q\rho_i \otimes \rho_j\right)\right) \\
=& \tfrac{1}{N}\sum_{i=1}^{N} \operatorname{tr}\left(Q\rho_i \otimes \left(\rho_i - \rho_{\text{avg}}\right)\right).
\end{aligned}$$

Apply matrix Hoelder to this reformulation to obtain a slightly stronger version of the advertised bound:

$$\begin{aligned}
|\Delta| \leq& \tfrac{1}{N}\sum_{i=1}^{N} \|Q\|_\infty \|\rho_i \otimes (\rho_i - \rho_{\text{avg}})\|_1 \\
=& \|Q\|_\infty \tfrac{1}{N}\sum_{i=1}^{N} \|\rho_i - \rho_{\text{avg}}\|_1,
\end{aligned}$$

because the trace norm is multiplicative under tensor products and quantum states ρ_i satisfy $\|\rho_i\|_1 = 1$.

2.4.3 Variance bounds

In analogy to the linear estimator (2.5) (empirical average), the U-statistics estimator (2.10) converges to its expectation value $\mathbb{E}\left[\hat{q}_{(N)}\right]$. The variance, which we compute in the following, provides a useful summary parameter for the rate of this convergence. Use $\mathbb{E}\left[\hat{\rho}_i \otimes \hat{\rho}_j\right] = \rho_i \otimes \rho_j$ to

rewrite the U-statistics variance as

$$\begin{aligned}\mathrm{Var}\left[\hat{q}_{(N)}\right] =& \mathbb{E}\left[\left(\tfrac{1}{N(N-1)}\sum_{i\neq j}\mathrm{tr}\left(Q\left(\hat{\rho}_i\otimes\hat{\rho}_j-\rho_i\otimes\rho_j\right)\right)\right)^2\right]\\ =&\tfrac{1}{N^2(N-1)^2}\sum_{i\neq j}\sum_{k\neq l}\mathbb{E}\left[\mathrm{tr}\left(Q\left(\hat{\rho}_i\otimes\hat{\rho}_j-\rho_i\otimes\rho_j\right)\right)\ \mathrm{tr}\left(Q\left(\hat{\rho}_k\otimes\hat{\rho}_l-\rho_k\otimes\rho_l\right)\right)\right].\end{aligned}$$

We can now analyze these contributions separately. And, owing to stochastic independence, most of them vanish identically. It is at this point, where the assumption of independent state copies (and access to independent randomness for selecting measurements) matters the most. For instance, if all indices i,j,k,l are distinct, the expectation value factorizes and produces a zero contribution. As detailed in [96, Supplemental Material] the only exceptions are contributions where at least two indices coincide. Together with symmetry of the observable ($\mathrm{tr}\left(QX\otimes Y\right)=\mathrm{tr}\left(QY\otimes X\right)$) and the AM-GM inequality ($X_jX_k\leq|X_j||X_k|\leq\frac{1}{2}\left(|X_j|^2+|X_k|^2\right)=\frac{1}{2}\left(X_j^2+X_k^2\right)$), we obtain

$$\begin{aligned}\mathrm{Var}\left[\hat{q}_{(N)}\right]\leq&\tfrac{4(N-2)}{N^2(N-1)^2}\sum_{i\neq j}\mathbb{E}\left[\mathrm{tr}\left(Q\left(\hat{\rho}_i-\rho_i\right)\otimes\rho_j\right)^2\right]+\tfrac{2}{N^2(N-1)^2}\sum_{i\neq j}\mathbb{E}\left[\mathrm{tr}\left(Q\left(\hat{\rho}_i\otimes\hat{\rho}_j-\rho_i\otimes\rho_j\right)\right)^2\right]\\ \leq&\tfrac{4(N-2)}{N^2(N-1)^2}\sum_{i\neq j}\mathrm{Var}\left[\mathrm{tr}\left(\mathrm{tr}_2\left(Q\mathbb{I}\otimes\rho_j\right)\hat{\rho}_i\right)\right]+\tfrac{2}{N^2(N-1)^2}\sum_{i\neq j}\mathrm{Var}\left[\mathrm{tr}\left(Q\hat{\rho}_i\otimes\hat{\rho}_j\right)\right].\end{aligned}$$

The final reformulation allows us to re-use the linear variance bound from Lemma 2.8. For $1\leq j\leq N$, we define the effective single-copy observable

$$Q_j=\mathrm{tr}_2\left(Q\mathbb{I}\otimes\rho_j\right) \tag{2.11}$$

to recognize simple linear variance terms within the first sum.

$$\begin{aligned}\mathrm{Var}\left[\hat{q}_{(N)}\right]\leq&\tfrac{4(N-2)}{N^2(N-1)^2}\sum_{i\neq j}2^{\mathrm{w}(Q_j)}\mathrm{tr}\left(Q_j^2\right)+\tfrac{2}{N^2(N-1)^2}\sum_{i\neq j}2^{\mathrm{w}(Q)}\mathrm{tr}(Q^2)\\ \leq&\tfrac{2}{N}\left(2\max_{1\leq i\leq N}2^{\mathrm{w}(Q_i)}\mathrm{tr}(Q_i^2)+\tfrac{1}{N-1}2^{\mathrm{w}(Q)}\mathrm{tr}(Q^2)\right).\end{aligned} \tag{2.12}$$

Clearly, this upper bound becomes smaller as the measurement budget N increases.

2.4.4 Error bound and confidence interval

Having derived bounds on deterministic bias and variance allows us to deduce a general error bound. Markov's inequality implies

$$\begin{aligned}
&\Pr\left[\left|\hat{q}_{(N)} - q\left(\rho_{\text{avg}}\right)\right| \geq \epsilon\right] = \Pr\left[\left(\hat{q}_{(N)} - q(\rho_{\text{avg}})\right)^2 \geq \epsilon^2\right] \\
\leq & \tfrac{1}{\epsilon^2}\mathbb{E}\left[\left(\hat{q}_{(N)} - \mathbb{E}\left[\hat{q}_{(N)}\right] + \mathbb{E}\left[\hat{q}_{(N)}\right] - q\left(\rho_{\text{avg}}\right)\right)^2\right] \\
= & \tfrac{1}{\epsilon^2}\left(\mathbb{E}\left[\left(\hat{q}_{(N)} - \mathbb{E}\left[\hat{q}_{(N)}\right]\right)^2\right] + \left(\mathbb{E}\left[\hat{q}_{(N)}\right] - q\left(\rho_{\text{avg}}\right)\right)^2\right) \\
= & \tfrac{1}{\epsilon^2}\left(\text{Var}\left[\hat{q}_{(N)}\right] + \frac{\Delta^2}{(N-1)^2}\right),
\end{aligned}$$

where we have isolated statistical fluctuations from the underlying deterministic bias. Inserting the bounds from Eq. (2.12) and Lemma 2.4.2 renders this bound more explicit:

$$\Pr\left[\left|\hat{q}_{(N)} - q\left(\rho_{\text{avg}}\right)\right| \geq \epsilon\right] \leq 4 \max_{1\leq i\leq N} \frac{2^{\text{w}(Q_i)}\text{tr}(Q_i^2)}{\epsilon^2 N} + 2\frac{2^{\text{w}(Q)}\text{tr}(Q^2)}{N(N-1)\epsilon^2} + 4\frac{\|Q\|_\infty^2}{(N-1)^2\epsilon^2}.$$

Term two and three have a comparable scaling in N and ϵ. The first term is different and starts to dominate as N increases. Recall that $Q(\rho_i) = \text{tr}\left(Q\mathbb{I} \otimes \rho_i\right)$ denotes an effectively linear function on a single copy of AB. This is the power of U-statistics. Asymptotically, it is an effectively linear scaling term that dominates the statistical convergence rate of a quadratic estimator. The other terms, however, can dominate in the small-N regime.

3

Experimental platform and simulations

During this thesis we will discuss several experimental results obtained from analyzing the data of the experiment described in Ref. [98]. In this chapter we give the basics for understanding the setup and the modeling of the latter.
We want to emphasize here that, thanks to the protocol described in the previous chapter, it has been possible to post-process the randomized measurements of [98] several years after the experiment has been done, leading to new experimental observations. Indeed a fundamental asset of randomized measurements is that they are based on a unifying experimental recipe to acquire data, which is then openly available to the community (see also the paragraph on 'measure first, ask questions later' in Ref. [99]).

3.1 Experiment and modeling of the evolution

The experimental platform in [98] is realized with trapped $^{40}Ca^{+}$ atoms, each one encoding a single qubit. Coupling all ions off-resonantly with a laser beam subjects the ions to realize long-range Ising model in presence of a transverse field, whose effective Hamiltonian writes:

$$H = \hbar \sum_{i<j} J_{ij} \sigma_i^x \sigma_j^x + \hbar B \sum_i \sigma_i, \tag{3.1}$$

with $i, j = 1, \ldots, N$ and N is the total system size. To model the experiment using numerical simulations, we approximate the interaction matrix J_{ij} as a power-law $J_{ij} = J_0/|i-j|^{\alpha}$, where the values of J_0 and α depend on the specifics of each experimental realization. For the experiments conducted with strings of 10 ions, $\alpha = 1.24$ and $J_0 = 420\ s^{-1}$. For those experiments with 20 ions, $\alpha = 1.01$ and $J_0 = 370\ s^{-1}$. The effective magnetic field B is considered much larger than the

interaction term ($B \simeq 22J_0$) such that terms that would break the conservation of the total magnetization, i.e. $\sigma_i^+\sigma_j^+ + h.c.$ are energetically suppressed. The effects of decoherence on the system are taken into account considering the time evolution subject to local spin-flips and spin excitation loss. The full system dynamics is described according to a Gorini-Kossakowski-Sudarshan-Lindblad (GKSL) master equation whose $2N$ local jump operators are written as $C_i = \sqrt{\gamma_x}\sigma_i^x$ (spin flip), $C_{i+L} = \sqrt{\gamma_-}\sigma_i^-$ (excitation loss), $i = 1, \ldots, L$, with rates γ_x, γ_m. Furthermore, the experimentally prepared state is not pure. As such, it can be written as the following mixed product state $\rho_0 = \bigotimes_i \left(p_i \left|\uparrow\right\rangle \left\langle\uparrow\right| + (1 - p_i) \left|\downarrow\right\rangle \left\langle\downarrow\right|\right)$ with $p_i \approx 0.004$ for i even and $p_i \approx 0.995$ for i odd.

In the case of the 10-ions experiment, the evolution described by the GKSL master equation is solved via exact diagonalization, utilizing the QuTiP toolbox [100]. In the case of the 20-ions experiment, the numerical simulations are done using tensor network algorithms. For the unitary part of the dynamics we approximate the interaction matrix J_{ij} as a sum of 3 exponentially decaying terms which can efficiently be represented as MPOs. To treat the decoherence we use quantum trajectories [101], applying the quantum jumps C_i, to the state approximated as an MPS. The latter is evolved according to the Time-Dependent Variational Principle (TDVP) [102]. Before calculating the observables we are interested in, we average our results on 1500 trajectories, reconstructing the full density matrix of the system.
In Sec. 3.3 we comment on the use of quantum trajectories and why building the full density matrix is convenient in our cases with respect to the stochastic average of the estimation of the observables on independent trajectories.

3.2 Measurement protocol

To build a classical snapshot of the quantum state of the experiment, randomized measurements were performed through individual rotations of each qubit by a random unitary U_i, sampled from the Circular Unitary Ensemble (CUE), followed by a state measurement in the z basis. The random unitary is decomposed as a product of three rotations $U_i = R_z(\theta_1)R_y(\theta_2)R_z(\theta_3)$. To make the drawing of random unitaries from the CUE more robust against miscalibration or drift of experimental control parameters, two random unitaries are concatenated to obtain a random unitary with a distribution that is closer to the ideal one. The projective measurement in the logical z basis is realized through spatially resolved fluorescence. The procedure is repeated $N_U = 500$ times and for each application of a unitary set $U_1 \otimes \cdots \otimes U_N$, where N is the total number of qubits, $N_m = 150$ measurements are performed. This same procedure is applied both to the $N = 10$ and $N = 20$ experiments we will discuss in this thesis. During the application of the local random unitary, local depolarizing noise is acting on the system. From the point of view of

simulations, we modify the density matrix obtained via our numerical algorithms as

$$\rho(\bar{t}) \to (1 - p_{DP}N)\rho(\bar{t}) + p_{DP}\sum_i \mathrm{Tr}_i[\rho(\bar{t})] \otimes \frac{\mathbb{I}_i}{2}, \tag{3.2}$$

to take into account this effect. We consider $p_{DP} \approx 0.02$ and $\bar{t}$ denoting the time at which the measurement is performed.

3.3 Master equation and quantum trajectories

In Sec. 3 we have anticipated that the open evolution of the experimental system is described according to a GKSL master equation

$$\dot{\rho} = -\frac{\mathrm{i}}{\hbar}[H, \rho] + \sum_k \left[L_k \rho L_k^\dagger - \frac{1}{2}\{L_k^\dagger L_k, \rho\} \right] \tag{3.3}$$

where ρ is the density matrix describing the system, H is the Hamiltonian ruling the coherent part of the dynamics and L_k are local jump operators describing the dissipative effects due to the environment. The assumptions needed to adopt this description are well satisfied in any state-of-the-art experimental platform [101], as well as in the trapped ion quantum simulator taken into account in this thesis. In Chap. 6 we will directly work on the master equation to derive the behaviour at early times of $\rho(t)$ at first order in perturbation theory.
Here, we believe it is necessary to comment on the fact that the numerical simulations describing the experiment in the following chapters consider a different approach to model the decoherence term, namely *quantum trajectories*.

Quantum trajectories have been introduced in the 90s, to avoid the need to propagate a full density matrix in time [103–106]. In fact, this is often numerically prohibitive even with state-of-the-art numerical technique. This approach involves replacing the complexity of the simulation of the full density matrix with stochastic sampling, hence rewriting the master equation as a stochastic average over individual trajectories, which can be evolved in time numerically as pure states. The simplest realization of quantum trajectories is obtained evolving the pure state coherently under the effective Hamiltonian, for a time step dt, and follow with the action of a quantum jump, stochastically sampled according to a probability distribution dependent on the particular physical scenario.
In this way, one can see that taking a stochastic average over trajectories is equivalent to the master equation in Eq. 3.3. In order to compute a particular quantity at time t, one can compute the expectation value for each of the stochastically propagated trajectories, and take the average of this quantity over all of them. Evidently, if the observable is non-linear this is not equivalent to estimating an observable on the density matrix evolved according to the master equation. For

this reason, to compare the results obtained describing the system with the quantum trajectories or with the GKSL equation, in this work we will always average the quantum trajectories to compute the full density matrix before estimating any observable and we will use the newfound ρ to calculate the observable at stake.

Bibliography

[1] M. A. Nielsen and I. L. Chuang, *Quantum Computation and Quantum Information* (Cambridge University Press, 2009).

[2] G. Benenti, G. Casati, and G. Strini, *Principles of Quantum Computation and Information* (WORLD SCIENTIFIC, 2004).

[3] L. Amico, R. Fazio, A. Osterloh, and V. Vedral, Rev. Mod. Phys. **80**, 517 (2008).

[4] N. Laflorencie, Physics Reports **646**, 1 (2016).

[5] J. Preskill, Journal of Modern Optics **47**, 127 (2000).

[6] T. Brydges, A. Elben, P. Jurcevic, B. Vermersch, C. Maier, B. P. Lanyon, P. Zoller, R. Blatt, and C. F. Roos, Science **364**, 260 (2019).

[7] V. Vitale, A. Elben, R. Kueng, A. Neven, J. Carrasco, B. Kraus, P. Zoller, P. Calabrese, B. Vermersch, and M. Dalmonte, SciPost Phys. **12**, 106 (2022).

[8] A. Elben, R. Kueng, H.-Y. R. Huang, R. van Bijnen, C. Kokail, M. Dalmonte, P. Calabrese, B. Kraus, J. Preskill, P. Zoller, and B. Vermersch, Physical Review Letters **125**, 200501 (2020).

[9] A. Neven, J. Carrasco, V. Vitale, C. Kokail, A. Elben, M. Dalmonte, P. Calabrese, P. Zoller, B. Vermersch, R. Kueng, and B. Kraus, npj Quantum Inf **7**, 152 (2021).

[10] A. M. Kaufman, M. E. Tai, A. Lukin, M. Rispoli, R. Schittko, P. M. Preiss, and M. Greiner, Science **353**, 794 (2016).

[11] A. Lukin, M. Rispoli, R. Schittko, M. E. Tai, A. M. Kaufman, S. Choi, V. Khemani, J. Léonard, and M. Greiner, Science **364**, 256–260 (2019).

[12] R. Islam, R. Ma, P. M. Preiss, M. Eric Tai, A. Lukin, M. Rispoli, and M. Greiner, Nature **528**, 77 (2015).

[13] J. I. Cirac and P. Zoller, Nature Physics **8**, 264 (2012).

[14] I. Buluta, S. Ashhab, and F. Nori, Reports on Progress in Physics **74**, 104401 (2011).

[15] F. Arute, K. Arya, R. Babbush, D. Bacon, J. C. Bardin, R. Barends, R. Biswas, S. Boixo, F. G. S. L. Brandao, D. A. Buell, B. Burkett, Y. Chen, Z. Chen, B. Chiaro, R. Collins, W. Courtney, Dunsworth, *et al.*, Nature **574**, 505–510 (2019).

[16] G. Vidal, J. I. Latorre, E. Rico, and A. Kitaev, Physical review letters **90**, 227902 (2003).

[17] P. Calabrese and J. Cardy, J. Physics A: Math. Theor. **42**, 504005 (2009).

[18] B. Zeng, X. Chen, D.-L. Zhou, and X.-G. Wen, *Quantum Information Meets Quantum Matter* (Springer New York, 2019).

[19] P. Calabrese and J. Cardy, Journal of Statistical Mechanics: Theory and Experiment **2005**, P04010 (2005).

[20] P. Buividovich and M. Polikarpov, Physics Letters B **670**, 141 (2008).

[21] H. Casini, M. Huerta, and J. A. Rosabal, Physical Review D **89**, 085012 (2014).

[22] M. Goldstein and E. Sela, Physical Review Letters **120**, 200602 (2018).

[23] J. C. Xavier, F. C. Alcaraz, and G. Sierra, Physical Review B **98**, 041106 (2018).

[24] L. Capizzi, P. Ruggiero, and P. Calabrese, Journal of Statistical Mechanics: Theory and Experiment **2020**, 073101 (2020).

[25] M. T. Tan and S. Ryu, Physical Review B **101**, 235169 (2020).

[26] S. Fraenkel and M. Goldstein, Journal of Statistical Mechanics: Theory and Experiment **2020**, 033106 (2020).

[27] G. Parez, R. Bonsignori, and P. Calabrese, Phys. Rev. B **103**, L041104 (2021).

[28] R. Bonsignori, P. Ruggiero, and P. Calabrese, Journal of Physics A: Mathematical and Theoretical **52**, 475302 (2019).

[29] S. Murciano, G. Di Giulio, and P. Calabrese, Journal of High Energy Physics **2020**, 1 (2020).

[30] S. Murciano, G. D. Giulio, and P. Calabrese, SciPost Physics **8**, 46 (2020).

[31] P. Calabrese, M. Collura, G. Di Giulio, and S. Murciano, Europhysics Letters **129**, 60007 (2020).

[32] S. Murciano, P. Ruggiero, and P. Calabrese, Journal of Statistical Mechanics: Theory and Experiment **2020**, 083102 (2020).

[33] E. Cornfeld, L. A. Landau, K. Shtengel, and E. Sela, Physical Review B **99**, 115429 (2019).

[34] D. X. Horváth and P. Calabrese, Journal of High Energy Physics **2020**, 1 (2020).

[35] D. Azses and E. Sela, Physical Review B **102**, 235157 (2020).

[36] R. Bonsignori and P. Calabrese, Journal of Physics A: Mathematical and Theoretical **54**, 015005 (2020).

[37] N. Feldman and M. Goldstein, Physical Review B **100**, 235146 (2019).

[38] X. Turkeshi, P. Ruggiero, V. Alba, and P. Calabrese, Physical Review B **102**, 014455 (2020).

[39] B. Estienne, Y. Ikhlef, and A. Morin-Duchesne, SciPost Phys. **10**, 54 (2021).

[40] N. Laflorencie and S. Rachel, Journal of Statistical Mechanics: Theory and Experiment **2014**, P11013 (2014).

[41] G. Vidal and R. F. Werner, Physical Review A **65**, 032314 (2002).

[42] A. Peres, Physical Review Letters **77**, 1413 (1996).

[43] R. Simon, Phys. Rev. Lett. **84**, 2726 (2000).

[44] H. Shapourian, K. Shiozaki, and S. Ryu, Physical Review B **95**, 165101 (2017).

[45] V. Eisler and Z. Zimborás, New Journal of Physics **17**, 053048 (2015).

[46] H. Shapourian, P. Ruggiero, S. Ryu, and P. Calabrese, SciPost Physics **7**, 37 (2019).

[47] H. Shapourian, K. Shiozaki, and S. Ryu, Phys. Rev. Lett. **118**, 216402 (2017).

[48] J. Eisert, V. Eisler, and Z. Zimborás, Physical Review B **97**, 1 (2018).

[49] H. Shapourian and S. Ryu, Phys. Rev. A **99**, 022310 (2019).

[50] P. Ruggiero, V. Alba, and P. Calabrese, Physical Review B **94**, 195121 (2016).

[51] P. Calabrese, J. Cardy, and E. Tonni, Physical Review Letters **109**, 130502 (2012).

[52] P. Calabrese, L. Tagliacozzo, and E. Tonni, Journal of Statistical Mechanics: Theory and Experiment **2013**, P05002 (2013).

[53] P. Calabrese, J. Cardy, and E. Tonni, Journal of Physics A: Mathematical and Theoretical **48**, 015006 (2014).

[54] O. Blondeau-Fournier, O. A. Castro-Alvaredo, and B. Doyon, Journal of Physics A: Mathematical and Theoretical **49**, 125401 (2016).

[55] P. Ruggiero, V. Alba, and P. Calabrese, Physical Review B **94**, 035152 (2016).

[56] X. Turkeshi, P. Ruggiero, and P. Calabrese, Phys. Rev. B **101** (2020).

[57] X. Wen, P.-Y. Chang, and S. Ryu, Journal of High Energy Physics **2016**, 12 (2016).

[58] C. Castelnovo, Physical Review A **88**, 042319 (2013).

[59] O. Hart and C. Castelnovo, Physical Review B **97**, 144410 (2018).

[60] Y. A. Lee and G. Vidal, Physical Review A **88**, 042318 (2013).

[61] T.-C. Lu, T. H. Hsieh, and T. Grover, Physical Review Letters **125**, 116801 (2020).

[62] A. Coser, E. Tonni, and P. Calabrese, Journal of Statistical Mechanics: Theory and Experiment **2014**, P12017 (2014).

[63] V. Eisler and Z. Zimborás, New Journal of Physics **16**, 123020 (2014).

[64] V. Alba and P. Calabrese, Europhysics Letters **126**, 60001 (2019).

[65] M. Hoogeveen and B. Doyon, Nuclear Physics B **898**, 78 (2015).

[66] X. Wen, P.-Y. Chang, and S. Ryu, Physical Review B **92**, 075109 (2015).

[67] M. J. Gullans and D. A. Huse, Physical Review X **9**, 021007 (2019).

[68] J. Kudler-Flam, M. Nozaki, S. Ryu, and M. T. Tan, Journal of High Energy Physics **2020**, 31 (2020).

[69] C. P. Herzog and Y. Wang, Journal of Statistical Mechanics: Theory and Experiment **2016**, 073102 (2016).

[70] H. Shapourian and S. Ryu, Journal of Statistical Mechanics: Theory and Experiment **2019**, 043106 (2019).

[71] A. Coser, E. Tonni, and P. Calabrese, Journal of Statistical Mechanics: Theory and Experiment **2016**, 033116 (2016).

[72] H. Shapourian and S. Ryu, Physical Review A **99**, 022310 (2019).

[73] E. Cornfeld, M. Goldstein, and E. Sela, Physical Review A **98**, 032302 (2018).

[74] S. Murciano, R. Bonsignori, , and P. Calabrese, SciPost Phys. **10**, 111 (2021).

[75] A. Rath, V. Vitale, S. Murciano, M. Votto, J. Dubail, R. Kueng, C. Branciard, P. Calabrese, and B. Vermersch, arXiv:2209.04393 (2022).

[76] O. Gühne and G. Tóth, Physics Reports **474**, 1 (2009).

[77] J. C. Xavier, F. C. Alcaraz, and G. Sierra, Physical Review B **98**, 041106 (2018).

[78] M. Goldstein and E. Sela, Physical Review Letters **120**, 200602 (2018).

[79] D. Gross, Y.-K. Liu, S. T. Flammia, S. Becker, and J. Eisert, Phys. Rev. Lett. **105**, 150401 (2010).

[80] R. Kueng, H. Rauhut, and U. Terstiege, Appl. Comput. Harmon. Anal. **42**, 88 (2017).

[81] R. O'Donnell and J. Wright, in *STOC'16—Proceedings of the 48th Annual ACM SIGACT Symposium on Theory of Computing* (ACM, New York, 2016) pp. 899–912.

[82] J. Haah, A. W. Harrow, Z. Ji, X. Wu, and N. Yu, IEEE Trans. Inf. Theory **63**, 5628 (2017).

[83] M. Guţă, J. Kahn, R. Kueng, and J. A. Tropp, J. Phys. A **53**, 204001 (2020).

[84] H.-Y. Huang, R. Kueng, and J. Preskill, Nature Physics , 1050 (2020).

[85] A. Rath, R. van Bijnen, A. Elben, P. Zoller, and B. Vermersch, arXiv:2102.13524 .

[86] S. Chen, W. Yu, P. Zeng, and S. T. Flammia, PRX Quantum **2**, 030348 (2021).

[87] D. E. Koh and S. Grewal, arXiv:2011.11580 .

[88] B. Dirkse, M. Pompili, R. Hanson, M. Walter, and S. Wehner, Quantum Sci. and Technol. **5**, 035007 (2020).

[89] J. Watrous, *The Theory of Quantum Information* (Cambridge University Press, 2018).

[90] M. Paini and A. Kalev, (2019), arXiv:1910.10543 .

[91] C. Dankert, R. Cleve, J. Emerson, and E. Livine, Physical Review A **80**, 012304 (2009).

[92] D. Gross, K. Audenaert, and J. Eisert, Journal of Mathematical Physics **48**, 052104 (2007).

[93] H. Zhu, Phys. Rev. A **96**, 062336 (2017).

[94] Z. Webb, Quantum Inf. Comput. **16**, 1379 (2016).

[95] R. Kueng and D. Gross, arXiv:1510.02767 .

[96] A. Elben, B. Vermersch, R. van Bijnen, C. Kokail, T. Brydges, C. Maier, M. K. Joshi, R. Blatt, C. F. Roos, and P. Zoller, Physical Review Letters **124**, 010504 (2020).

[97] W. Hoeffding, in *Breakthroughs in Statistics* (Springer, 1992) pp. 308–334.

[98] T. Brydges, A. Elben, P. Jurcevic, B. Vermersch, C. Maier, B. P. Lanyon, P. Zoller, R. Blatt, and C. F. Roos, Science **364**, 260 (2019).

[99] A. Elben, S. T. Flammia, H.-Y. Huang, R. Kueng, J. Preskill, B. Vermersch, and P. Zoller, arXiv:2203.11374 (2022).

[100] J. Johansson, P. Nation, and F. Nori, Computer Physics Communications **184**, 1234 (2013).

[101] A. J. Daley, Advances in Physics **63**, 77 (2014).

[102] J. Haegeman, J. I. Cirac, T. J. Osborne, I. Pižorn, H. Verschelde, and F. Verstraete, Physical review letters **107**, 070601 (2011).

[103] R. Dum, P. Zoller, and H. Ritsch, Phys. Rev. A **45**, 4879 (1992).

[104] J. Dalibard, Y. Castin, and K. Mølmer, Phys. Rev. Lett. **68**, 580 (1992).

[105] M. B. Plenio and P. L. Knight, Rev. Mod. Phys. **70**, 101 (1998).

[106] H. J. Carmichael, Phys. Rev. Lett. **70**, 2273 (1993).

II

Mixed-state entanglement and entanglement detection

This part is based on the following publications:

[1] *Negativity Hamiltonian: An Operator Characterization of Mixed-State Entanglement*, S. Murciano*, V. Vitale*, M. Dalmonte, P. Calabrese, Physical Review Letters 128, 140502 (2022)

[2] *Symmetry-resolved entanglement detection using partial transpose moments*. A. Neven, J. Carrasco, V. Vitale, C. Kokail, A. Elben, M. Dalmonte, P. Calabrese, P. Zoller, B. Vermersch, R. Kueng, B. Kraus, npj Quantum Information 7 (1), 1-12 (2021)

4

Negativity Hamiltonian

4.1 Introduction

Over the past two decades, entanglement has been a central concept in many branches of quantum physics ranging from quantum information [1, 2] to condensed matter theory [3, 4] and high-energy physics [5–9]. In particular, it has been successfully utilized to characterize quantum many-body systems both theoretically and experimentally [10–16]. The main object which enters in its quantification is the reduced density matrix (RDM). For a given state ρ, the RDM of a region A, ρ_A, is obtained by tracing ρ over the complement of A, B, that is:

$$\rho_A = \mathrm{tr}_B \rho = \frac{\mathrm{e}^{-H_A}}{Z_A}, \quad Z_A = \mathrm{tr}\mathrm{e}^{-H_A}, \tag{4.1}$$

where the operator H_A is the entanglement (or modular) Hamiltonian (EH).

From a many-body viewpoint, the entanglement properties of pure states can be construed in a hierarchical manner. Firstly, there exists a characterization of its entanglement properties via entanglement entropies. Those are uniquely dependent on the spectrum of H_A - also known as entanglement spectrum. Secondly, it is possible to characterize the properties of the RDM directly at the operator level, via the full characterization of the EH - a paradigmatic example being the Li-Haldane conjecture in the context of topological matter [17].

The EH fully characterizes the "local" properties of entanglement in a many-body system - that is, it allows to understand whether the RDM can be interpreted as the exponential of a local operator composed solely of few-body local terms. In the context of quantum field theory, this principle of locality is an established pillar - the Bisognano-Wichmann (BW) theorem [18, 19]. Such locality is at the heart of several physical phenomena - from topological order, to the nature of area

laws in gapped systems-, and is the key element at the basis of theory and experiments aimed at large-scale reconstructions of the RDM [20–22]. However, it is presently unknown whether it is possible to associate locality and entanglement in a similar way for the case of mixed-state entanglement, that encompasses a variety of scenarios of key experimental and theoretical relevance - from mixed states, to correlations between partitions in pure states.

Here, we introduce and investigate the negativity Hamiltonian - an operator that allows us to cast the relation between locality and entanglement (in particular, that related to Peres-Horodecki criterion) for general mixed states. Our work is directly motivated by a series of recent results that have emphasized the importance of the entanglement negativity in a variety of settings, including harmonic oscillator chains [23–29], quantum spin models [30–38], free-fermionic systems [39–44], (1+1)d conformal and integrable field theories [45–55], out-of-equilibrium settings [56–64], and topological order [65–70]. Importantly, the negativity is directly linked to the partial transpose $\rho_A^{T_1}$ of the RDM - and, as such, does lend itself naturally to an interpretation based on statistical mechanics. For the case of a subpartition of $A = A_1 \cup A_2$, we define the *negativity Hamiltonian* $\mathcal{N}_A$ as

$$\rho_A^{T_1} = Z_A^{-1} \mathrm{e}^{-\mathcal{N}_A}. \tag{4.2}$$

Clearly $\mathcal{N}_A$ is non-hermitian because negative eigenvalues of $\rho_A^{T_1}$ are the signature of mixed-state entanglement. Nevertheless, it is still natural to wonder about the locality properties of $\mathcal{N}_A$ and about the location of its eigenvalues in the complex plane.

After discussing the definition of $\mathcal{N}_A$ for both bosonic (spin) and fermionic systems, we unveil the operator structure of $\mathcal{N}_A$ for two relevant cases: (1+1)-d fermionic conformal field theory and a tight-binding model of spinless fermions on a chain. Both cases show a characteristic quasi-local (in a sense to be specified below) structure - a first demonstration of the relation between entanglement and locality at the operator level beyond the case of complementary partitions. On top of its conceptual relevance, and similarly to what has been discussed in the context of pure states for the case of local EHs, this fact enables some immediate consequences: i) interpreting the negativity spectrum, i.e. the analog of the pure-state entanglement spectrum for mixed states [38, 50], ii) simulating this object in nowadays available quantum platforms [10] iii) applying well-established statistical mechanics tools such as tensor networks [71, 72] and quantum Monte Carlo [73] to access the entire partial transpose $\rho_A^{T_1}$.

4.2 The Negativity Hamiltonian and its quasi-local structure

To introduce the concept of the negativity Hamiltonian, the first step is to discuss the partial transpose for bosonic and fermionic systems. We already introduced it in Sec.1.5; here we elaborate again on the definitions and set the notation that will be used in the following. Let us start

considering a bosonic system $A = A_1 \cup A_2$ described by

$$\rho_A = \sum_{i,j,k,l} \left\langle e_i^{A_1}, e_j^{A_2} \right| \rho_A \left| e_k^{A_1}, e_l^{A_2} \right\rangle \left| e_i^{A_1}, e_j^{A_2} \right\rangle \left\langle e_k^{A_1}, e_l^{A_2} \right|, \tag{4.3}$$

where $\left|e_i^{A_1}\right\rangle, \left|e_j^{A_2}\right\rangle$ denote orthonormal bases in the Hilbert spaces $\mathcal{H}_{A_1}$ and $\mathcal{H}_{A_2}$ corresponding to subsystems A_1 and A_2. The partial transpose of the reduced density matrix $\rho_A^{T_1}$ with respect to the system A_1 is defined performing a standard transposition in $\mathcal{H}_{A_1}$, i.e. exchanging the matrix elements in A_1, $\rho_A^{T_1} = (T_{A_1} \otimes \mathbb{1}_{A_2})\rho_A$. The presence of negative eigenvalues of $\rho_A^{T_1}$ is a signature of mixed state entanglement [74], which can be quantified by the logarithmic negativity $\mathcal{E} = \log \mathrm{tr}|\rho_A^{T_1}|$ [75, 76].

The partial transposition has also an interpretation in terms of a time-reversal transformation or mirror reflection in phase space [77]. Namely, considering the one-to-one correspondence between density matrices and Wigner distribution functions $W(q,p)$ then

$$\rho_A \to \rho_A^T \Longleftrightarrow W(q,p) \to W(q,-p). \tag{4.4}$$

This can be conveniently observed starting from a bosonic density matrix written in a coherent state basis, since time-reversal transformation ($\mathcal{T}$) can be identified with the complex conjugation [39]. Taking $|\alpha\rangle$, a bosonic coherent state, one has

$$(|\alpha\rangle \langle\alpha^*|) \xrightarrow{\mathcal{T}} |\alpha^*\rangle \langle\alpha| = (|\alpha\rangle \langle\alpha^*|)^T. \tag{4.5}$$

In the case of fermionic systems, the equivalence above does not hold and the definition of partial transposition differs when looking at the density matrix or at the Wigner distribution function. In a coherent state basis the RDM reads [39, 44, 78, 79]

$$\rho_A = \frac{1}{Z} \int \mathrm{d}[\xi]\mathrm{d}[\bar{\xi}] \mathrm{e}^{-\sum_j \bar{\xi}_j \xi_j} \left\langle \{\xi_j\} \right| \rho_A \left| \{\bar{\xi}_j\} \right\rangle \left| \{\xi_j\} \right\rangle \left\langle \{\bar{\xi}_j\} \right|. \tag{4.6}$$

Here $\xi, \bar{\xi}$ are Grassman variables and $|\xi\rangle = \mathrm{e}^{-\xi a^\dagger} |0\rangle, \langle\bar{\xi}| = \langle 0| \mathrm{e}^{-a^\dagger \bar{\xi}}$ are the related fermionic coherent states. The partial time reversal, analog of Eq. (4.5), is [39]

$$|\xi\rangle \langle\bar{\xi}| \xrightarrow{\mathcal{T}} |i\bar{\xi}\rangle \langle i\xi| \tag{4.7}$$

The partial time reversal $\rho_A^{R_1}$, obtained by acting with (4.7) in (4.6) only in A_1, provides the fermionic negativity as

$$\mathcal{E} = \log \mathrm{Tr}|\rho_A^{R_1}|, \tag{4.8}$$

although its spectrum is not real in general [40]. To have a more transparent interpretation of the fermionic negativity, an alternative partial transpose, called twisted fermionic partial transpose,

has been defined as [40]

$$\rho_A^{\tilde{R}_1} = \rho_A^{R_1}(-1)^{F_{A_1}}, \tag{4.9}$$

where $F_{A_1} = \sum_{j\in A_1} n_j$ is the number of fermions in the subsystem A_1. This new object has only real eigenvalues and the logarithmic negativity

$$\mathcal{E} = \log \mathrm{tr}|\rho_A^{\tilde{R}_1}|. \tag{4.10}$$

is a measure of the negativeness of the eigenvalues, exactly as for the bosonic partial transpose. We define the negativity Hamiltonian related to $\rho_A^{R_1}$ as $\mathcal{N}_A$ and the one related to $\rho_A^{\tilde{R}_1}$ as $\tilde{\mathcal{N}}_A$.

The BW theorem gives a general structure for the entanglement Hamiltonian of the ground state of a relativistic invariant quantum field theory with Hamiltonian density $H(\mathbf{x})$, when considering a bipartition between two half spaces of an infinite system. In formulas, considering a d-dimensional system, $\mathbf{x} = \{x_1, \ldots, x_d\}$, and a partition $A = \{\mathbf{x}|x_1 > 0\}$, the EH of the ground state is

$$H_A = 2\pi \int_{\mathbf{x}\in A} \mathrm{d}\mathbf{x}\; x_1 H(\mathbf{x}) + c, \tag{4.11}$$

where c is a normalization constant that guarantees the trace of the density matrix to be set to unity. This result does not depend on the dimensionality of the system or on any apriori knowledge of the ground state and can be applied to a large variety of systems and quantum phases. For conformal invariant theories, the BW theorem is easily generalized to some different geometries by conformal mappings [80–83]. This equivalence does not hold when A is the union of two disjoint intervals, but, nevertheless, the EH for this geometry is known for $1+1$-dimensional free Dirac fermions [84]. In this case, it is possible to identify a local part in the entanglement Hamiltonian proportional to the energy density and a quasi-local part quadratic in the fermionic field. We will make explicit use of this example in the following. We will also check our analytical prediction against lattice simulations. In fact, the BW theorem can be used to construct approximate entanglement Hamiltonians for lattice models. This has been extensively investigated both for one- and two-dimensional models and it has been shown that the approximation provided by BW theorem allows to build entanglement Hamiltonians that encode all the relevant entanglement properties of the ground states [85–87].

To build the negativity Hamiltonian, we should first recall the path integral construction of the (bosonic) partial transpose [46, 47]. The partial transposition corresponds to the exchange of row and column indices in A_1 which naturally leads to a space inversion within A_1. On a fundamental level, this fact can be deduced from CPT theorem. Indeed, the partial transposition is equivalent to a partial time reversal that, by CPT, is the same as a parity operation in the worldsheet combined with a charge conjugation. This second construction holds true also for $\rho_A^{R_1}$ in fermionic systems.

Therefore, starting from the entanglement hamiltonian for two disjoint intervals and doing a

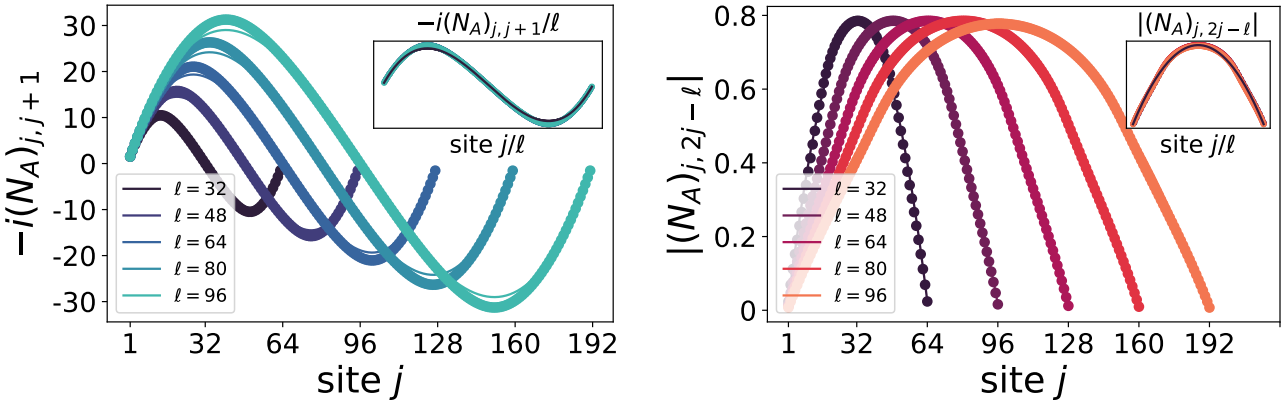

Figure 4.1: Benchmark of the analitycal prediction for the Negativity Hamiltonian of a real fermion. We consider $A_1 = [1, \ell], A_2 = [\ell + 1, 2\ell]$ embedded in the infinite line. The symbols correspond to numerical data, while the solid lines to the discretized form of Eq. (4.12). Upper panel: $N_{A,\mathrm{loc}}$. Lower panel: $|N_{A,\mathrm{q-loc}}|$. Inset: data collapse

spatial inversion of the interval $A_1 = [a_1, b_1]$, one obtains the partial time reversal of the density matrix. Although this procedure is fully general, the entanglement hamiltonians of disjoint intervals are known only in few cases [84, 88–94]. In particular, starting from the EH for the massless real (Majorana) fermion $\Psi(x)$ [84], $\Psi(x) = \begin{pmatrix} \psi_1(x) \\ \psi_2(x) \end{pmatrix}$, and performing this inversion, we get after simple algebra

$$\begin{aligned} \mathcal{N}_A &= \mathcal{N}_{A,\mathrm{loc}} + i\mathcal{N}_{A,\mathrm{q-loc}}, \\ \mathcal{N}_{A,\mathrm{loc}} &= 2\pi \int_A \beta^R_{\mathrm{loc}}(x) T_{tt}(0,x) dx, \\ \mathcal{N}_{A,\mathrm{q-loc}} &= 2\pi \int_A \beta^R_{\mathrm{q-loc}}(x) T_{\mathrm{q-loc}}(x, \bar{x}^R(x)) dx, \end{aligned} \tag{4.12}$$

where

$$\beta^R_{\mathrm{loc}}(x) = \frac{1}{w^{R\prime}(x)}, \qquad \beta^R_{\mathrm{q-loc}}(x) = \frac{\beta^R_{\mathrm{loc}}(\bar{x}^R(x))}{x - \bar{x}^R(x)}, \tag{4.13}$$

with

$$\begin{aligned} w^R(x) &= \log\left[-\frac{(x-b_1)(x-a_2)}{(x-a_1)(x-b_2)}\right], \\ \bar{x}^R(x) &= \frac{(a_1 b_2 - b_1 a_2)x + (a_1 + b_2)b_1 a_2 - (b_1 + a_2)a_1 b_2}{(a_1 - b_1 + b_2 - a_2)x + b_1 a_2 - a_1 b_2}. \end{aligned} \tag{4.14}$$

Here $T_{tt}(0,x)$ is the energy density operator of the theory while $T_{\mathrm{q-loc}}(x,\bar{x})$ is a bilinear of the real fermionic fields, with $x \in A_1$ and $\bar{x} \in A_2$ (and viceversa), i.e.

$$T_{\mathrm{q-loc}}(x,y) \equiv i : (\psi_1(x)\psi_1(y) + \psi_2(x)\psi_2(y)) : . \tag{4.15}$$

The structure of Eq. (4.12) is very suggestive: it consists of a local term proportional to the energy density and an additional non local part given by a quadratic expression in the fermionic

field. The latter, however, has a mild non-locality: each point $x \in A_1$ is coupled to only a specific $y = \bar{x}^R \in A_2$ (that is a consequence of the mirror symmetry for equal intervals). Thus, following [84], we refer to $\mathcal{N}_{A,\mathrm{q-loc}}$ as a quasi-local operator. Its existence is the reason of the imaginary components in the spectrum of $\mathcal{N}_A$, which is one characteristic treat of $\rho_A^{R_1}$. The shape of $|\mathcal{N}_{A,\mathrm{q-loc}}|$ (see also Fig. 4.1) is compatible with the results of the negativity contour [42] suggesting that the largest contribution to the negativity comes from the boundary region between A_1 and A_2.

To test the validity of Eq. (4.12), we consider a lattice discretization of the Hamiltonian of free real fermions. Because of the gaussianity of $\rho_A^{R_1}$ [39], the numerical evaluation of the negativity Hamiltonian amounts to compute the single particle operator N_A defined as

$$\mathcal{N}_{\mathcal{A}} = \sum_{ij} (N_A)_{i,j} \psi_j \psi_i, \tag{4.16}$$

related to the covariance matrix [95, 96]. We focus on two equal adjacent intervals $A = A_1 \cup A_2$ made up of ℓ sites labelled by $1 \leq j \leq 2\ell$. In this case, the point $\bar{x}^R$ in Eq. (4.14) is just $\bar{x}^R = 2\ell - x$ and so the quasi-local term lies entirely on the antidiagonal. As a consequence, in Fig. 4.1 we show only the subdiagonal $(N_A)_{j,j+1}$ (a similar behaviour can be found for $(N_A)_{j+1,j}$) and the antidiagonal $(N_A)_{j,2\ell-j}$ which correspond, respectively, to the local and to the quasi-local parts of N_A. The agreement between lattice exact and field-theoretical discretized N_A is remarkable over the all parameter regime, and even for modest system sizes. Small discrepancies up to a few percent are present far from the boundaries: those have very little effects on the negativity, as they affect only very small (in absolute value) eigenvalues of the partial transpose. We verified that the other matrix elements of N_A are negligible, in the sense that they are subleading as $\ell \to \infty$ (in the same sense as subleading terms in the EH are negligible, see Refs. [85–87, 97–101]).

We have also studied the structure of negativity Hamiltonian $\tilde{\mathcal{N}}_A$ for two adjacent intervals of equal length, $\ell_1 = \ell_2 = \ell$. We remind that $\rho_A^{\tilde{R}_1} = Z_A^{-1} e^{-\tilde{\mathcal{N}}}$, where $\rho_A^{\tilde{R}_1}$ is defined in Eq. (4.9). The advantage in the analysis of this operator is that it is Hermitian, so the logarithmic negativity recovers its original meaning of measure of the negativeness of the eigenvalues, as we are going to show by discussing the spectrum of this operator. Although we did not manage to derive its form explicitly, we provide a conjecture that very accurately matches numerical data on the lattice. It reads $\tilde{\mathcal{N}}_A = \tilde{\mathcal{N}}_{A,\mathrm{diag}} + \tilde{\mathcal{N}}_{A,\mathrm{loc}} + \tilde{\mathcal{N}}_{A,\mathrm{qloc}}$, with

$$\begin{aligned}
\tilde{\mathcal{N}}_{A,\mathrm{diag}} &= 2\pi i \int_A \tilde{\beta}_{\mathrm{diag}}(x) dx, \\
\tilde{\mathcal{N}}_{A,\mathrm{loc}} &= 2\pi \int_A \tilde{\beta}_{\mathrm{loc}}(x) dx T_{tt}(0,x), \\
\tilde{\mathcal{N}}_{A,\mathrm{q-loc}} &= 2\pi \int_A \tilde{\beta}_{\mathrm{q-loc}}(x) T_{\mathrm{q-loc}}(x, \bar{x}^R) dx,
\end{aligned} \tag{4.17}$$

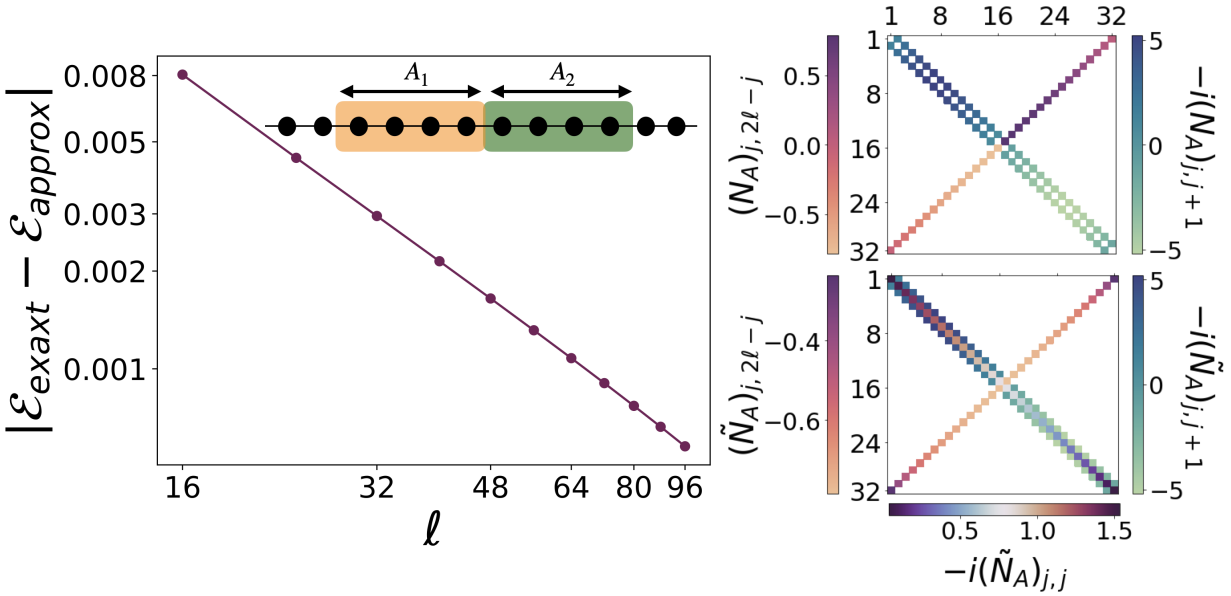

Figure 4.2: Summary of our results for adjacent intervals of equal length ℓ on the infinite line for lattice free fermions (geometry in the inset). The one-particle negativity hamiltonians N_A and $\tilde{N}_A$ are dominated by quasi-local terms appearing close to the diagonal and on the antidiagonal (see the right panels for $\ell = 8$). Left panel: Comparison of the exact logarithmic negativity with the approximate one coming from field theoretical $\tilde{N}_A$, see text.

where

$$\begin{aligned}
\tilde{\beta}_{\text{diag}}(x) &= \frac{1}{2} - \frac{x}{8\ell}, \\
\tilde{\beta}_{\text{loc}} &= -\frac{x(8\ell^2 - 6\ell x + x^2)}{8\ell^2}, \\
\tilde{\beta}_{\text{q-loc}}(x) &= 4\left(\frac{x - 2\ell - \frac{1}{2}}{4\ell}\right)^4 + \frac{1}{2}\left(\frac{x - 2\ell - \frac{1}{2}}{4\ell}\right)^2 - \frac{1}{2},
\end{aligned} \tag{4.18}$$

Let us observe that by choosing $a_1 = 0, b_1 = a_2 = \ell, b_2 = 2\ell$, $\tilde{\mathcal{N}}_{A,loc}$ and $\mathcal{N}_{A,loc}$ coincide, while $\tilde{\mathcal{N}}_{A,non-loc}$ and $\mathcal{N}_{A,non-loc}$ are different because the former is a quartic function of x, while the latter is quadratic. As a non-trivial test for the accuracy of this conjecture, we verified that it provides a logarithmic negativity that, as ℓ increases, approaches the exact numerical value (see Fig. 4.2). We also benchmarked the analytical predictions from Eq. (4.17) for free real fermions on the lattice, as shown in Fig. 4.3, for the one-particle NH, i.e. $\tilde{\mathcal{N}}_A = \sum_{ij}(\tilde{N}_A)_{i,j}\psi_j\psi_i$. Remarkably, the formulas above are in good agreement with simulations and, as already observed, the small discrepancies do not affect sizeably the logarithmic negativity approximation. The inset illustrates how results from different partition sizes collapse onto a single functional form, signaling scale invariance.

A final comment concerns the spectrum of $\tilde{N}_A$: it consists of two parts $\{\lambda_j + i\pi\}, \lambda_j \in \mathbb{R}$ for $j = 1, \cdots, 2\ell$ and $\{\lambda_j\}, \lambda_j \in \mathbb{R}$ for $j = 2\ell + 1, \cdots, 4\ell$. By simple exponentiation, we get the eigenvalues of $\rho_A^{\tilde{R}_1}$, see SM. We can then trace back the appearance of negative eigenvalues in the spectrum of $\rho_A^{\tilde{R}_1}$ (and, as a consequence, of a non-zero negativity) to the presence of the factors $i\pi$

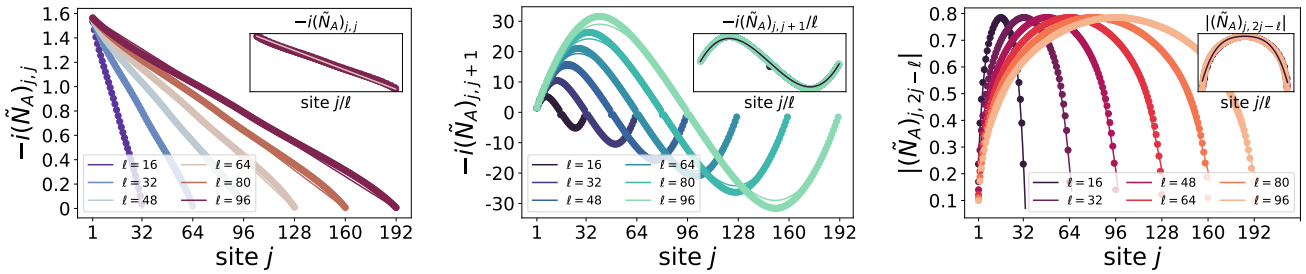

Figure 4.3: Benchmark of the analytic prediction for the Negativity Hamiltonian $\tilde{N}_A$. The symbols correspond to numerical data, while the solid lines correspond to the discretized form of Eq. (4.17) for two adjacent intervals of length ℓ. Comparison of $\tilde{N}_{A,\mathrm{loc}}$, $\tilde{N}_{A,\mathrm{q-loc}}$ and $\tilde{N}_{A,\mathrm{q-loc}}$ with exact lattice simulations. Insets: Data collapse

in $\tilde{N}_A$.

Other tests of the analytic formulas for the negativity hamiltonian N_A, including different and disjoint intervals, are reported in Sec.4.4.

4.3 From the Entanglement Hamiltonian and Bisognano Wichmann theorem to the Negativity Hamiltonian in field theory

The calculation of the exact entanglement Hamiltonian is in general a very difficult task. However, for conformal invariant field theories (CFTs) it is possible to generalize the Bisognano Wichmann (BW) result for a bipartition between two half spaces of an infinite system to different geometries [80–83].

Let us consider the vacuum state of a d-dimensional Hamiltonian of a relativistic quantum field theory,

$$H = \int_{\mathbb{R}^d} d^d x\, h(x) \tag{4.19}$$

and a subsystem A which consists of the degrees of freedom in a half-space, $x_1 > 0$. The BW theorem guarantees that the entanglement Hamiltonian H_A can be expressed as an integral of the Hamiltonian density $h(x)$

$$H_A = \frac{2\pi}{v} \int_A d^{d-1}x\, x_1\, h(x), \tag{4.20}$$

where, from now on, we fix the velocity $v = 1$. There are other examples in the ground-state of a 1+1 dimensional CFT in which H_A can be written as a local integral over the Hamiltonian density. They include the case of a single interval $A = (0, \ell)$ in an infinite system, and its generalizations to finite size or finite temperature [83]. In these cases, H_A takes the form

$$H_A = 2\pi \int_A dx \frac{h(x)}{f'(x)}, \tag{4.21}$$

where $f'(x)$ is the conformal mapping from the Euclidean space-time to a rectangle with height

2π and width $2\log(\ell/\epsilon)$, ϵ UV cutoff. More concretely, some mappings are

- finite interval in an infinite system:

$$f(x) = \log \frac{x}{\ell - x};$$

- finite interval in a finite system:

$$f(x) = \log \frac{e^{2\pi i x/L} - 1}{e^{2\pi i \ell/L} - e^{2\pi i x/L}}.$$

Despite the result of Bisognano and Wichmann and the conformal symmetry allow to compute the aforementioned modular Hamiltonians, in general it is not an easy task to get analytic expressions, even in CFTs. One of these examples is the modular Hamiltonian for the ground state of the free $1+1$ dimensional massless Dirac fermion for several disjoint intervals on the infinite line [84, 89, 90]. We have already discussed its peculiar structure in the main text and here we report the explicit analytical expression. The massless $1+1$ dimensional Dirac field $\psi(t,x)$ is a doublet made by the two complex fields

$$\psi(t,x) = \begin{pmatrix} \psi_1(t,x) \\ \psi_2(t,x) \end{pmatrix}. \tag{4.22}$$

The normal ordered component of the energy-momentum tensor of the Dirac field corresponding to the energy density reads

$$T_{tt}(t,x) \equiv \frac{i}{2} : [((\partial_x \psi_1^*)\psi_1 - \psi_1^* \partial_x \psi_1)(x+t) - ((\partial_x \psi_2^*)\psi_2 - \psi_2^* \partial_x \psi_2)(x-t)] : . \tag{4.23}$$

The modular Hamiltonian for two disjoint intervals $A \equiv [a_1, b_1] \cup [a_2, b_2]$ on the line can be written as the sum $H_A = H_{\rm loc} + H_{\rm q-loc}$, where the local term $H_{\rm loc}$ and the quasi-local term $H_{\rm q-loc}$ are defined respectively as

$$\begin{aligned} H_{\rm loc} &= 2\pi \int_A \beta_{\rm loc}(x) T_{tt}(0,x) dx, \\ H_{\rm q-loc} &= 2\pi \int_A \beta_{\rm q-loc}(x) T_{\rm q-loc}(0,x,\bar{x}) dx, \end{aligned} \tag{4.24}$$

with $T_{tt}(0,x)$ the energy density in Eq. (4.23), while $T_{\rm q-loc}(0,x,y)$ is given by

$$\begin{aligned} T_{\rm q-loc}(t,x,y) \equiv \frac{i}{2} : [&(\psi_1^*(x+t)\psi_1(y+t) - \psi_1^*(y+t)\psi_1(x+t)) + \\ &(\psi_2^*(x-t)\psi_2(y-t) - \psi_2^*(y-t)\psi_2(x-t))] : . \end{aligned} \tag{4.25}$$

Here the asterisk denotes the Hermitian conjugation. The other functions in Eq. (4.24) can be written as

$$\beta_{\rm loc}(x) = \frac{1}{w'(x)} \qquad \beta_{\rm q-loc}(x) = \frac{\beta_{\rm loc}(\bar{x}(x))}{x - \bar{x}(x)}, \tag{4.26}$$

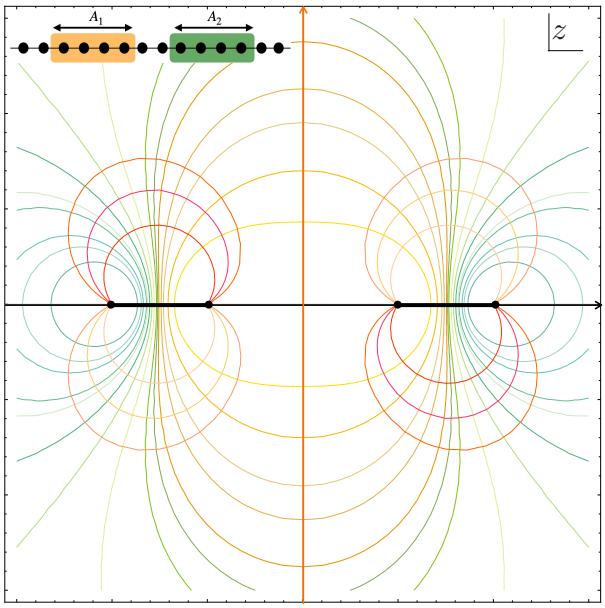

Figure 4.4: Contour plot of the conformal mapping $w^R(z)$ defined in Eq. (4.14), where $z = x + iy$. Here A consists of two disjoint intervals whose endpoints are the black dots on the horizontal axis. The absence of singular points along the imaginary axis is the main difference with respect to the conformal mapping $w(z)$ in Eq. (4.27).

with

$$\begin{aligned} w(x) &= \log\left[-\frac{(x-a_1)(x-a_2)}{(x-b_1)(x-b_2)}\right], \\ \bar{x}(x) &= \frac{(b_1b_2 - a_1a_2)x + (b_1+b_2)a_1a_2 - (a_1+a_2)b_1b_2}{(b_1 - a_1 + b_2 - a_2)x + a_1a_2 - b_1b_2}. \end{aligned} \tag{4.27}$$

Here x and $\bar{x}(x)$ belong to different intervals in A (if $x \in A_1$ then $\bar{x} \in A_2$ and viceversa). In the limit $b_1 \to a_2$ we get back a single interval and so the quasi-local part vanishes and we recover the result in Eq. (4.21), where now $A = [a_1, b_2]$.

The entanglement Hamiltonian in Eq. (4.24) is the starting point to obtain an analytical expression for the negativity Hamiltonian $\mathcal{N}_A$. As explained in the main text, in the path integral representation the partial transposition has the net effect to perform a spatial inversion within A_1 plus a charge conjugation. This implies that the negativity Hamiltonian $\mathcal{N}_A$ can be obtained from the entanglement Hamiltonian H_A by inverting the endpoints $a_1 \leftrightarrow b_1$ in the expression for H_A, Eq. (4.24). Furthermore, since under partial time reversal $\psi(x) \to i\psi(x)$ if $x \in A_1$, the term $T_{\mathrm{q-loc}}(0, x, \bar{x})$ defined in Eq. (4.25) gets an i prefactor, because if $x \in A_1$ then $\bar{x} \in A_2$ (and viceversa). To sum up, we get the following expression for the negativity Hamiltonian of a Dirac field

$$\begin{aligned} \mathcal{N}_A &= \mathcal{N}_{A,\mathrm{loc}} + i\mathcal{N}_{A,\mathrm{q-loc}}, \\ \mathcal{N}_{A,\mathrm{loc}} &= 2\pi \int_A \beta^R_{\mathrm{loc}}(x) T_{tt}(0,x)dx, \\ \mathcal{N}_{A,\mathrm{q-loc}} &= 2\pi \int_A \beta^R_{\mathrm{q-loc}}(x) T_{\mathrm{q-loc}}(0, x, \bar{x}^R(x))dx, \end{aligned} \tag{4.28}$$

where $\beta^R_{\mathrm{loc}}, \beta^R_{\mathrm{q-loc}}, \bar{x}^R(x)$ are given in Eq. (10)-(11) of the main text and they are obtained by

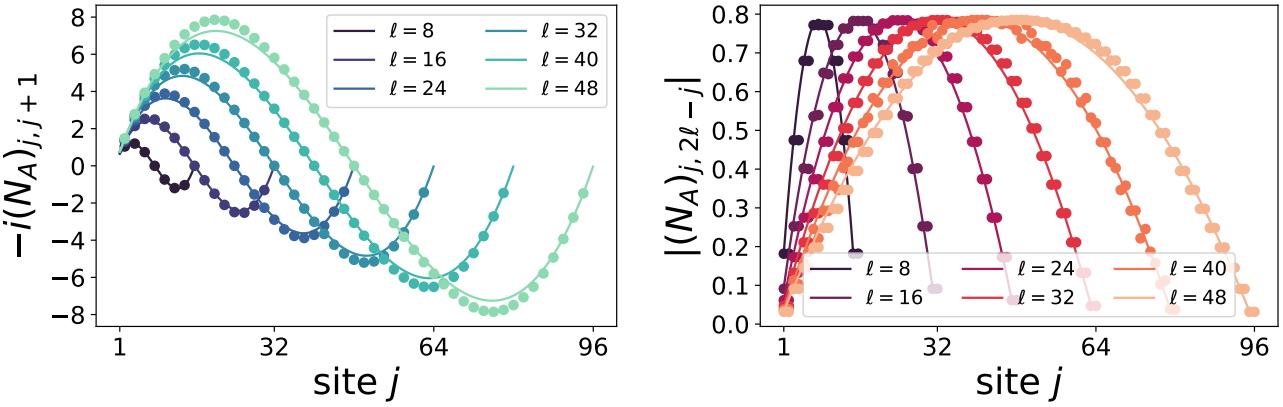

Figure 4.5: Negativity Hamiltonian corresponding to $\rho_A^{R_1}$ for complex fermions on two adjacent intervals of equal length ℓ on the infinite line. The symbols correspond to numerical data, while the solid lines correspond to the discretized form of Eq. (4.28). The right panel is $N_{A,\mathrm{loc}}$, while the left one is $|N_{A,\mathrm{q-loc}}|$. Using the notation of Eq. (11) of the main text, here we have $a_1 = 0, b_1 = \ell = a_2, b_2 = 2\ell$.

switching a_1 and b_1 in the definitions of $\beta_{\mathrm{loc}}, \beta_{\mathrm{q-loc}}, \bar{x}(x)$ given above. In Fig. 4.4, we show a contour plot of the real and imaginary part of $w^R(x)$. The curves $\mathrm{Im}(w^R(x))$ do not exhibit singular points for which the mapping fails to be conformal, contrarily to what happens for $\mathrm{Im}(w(x))$ and showed in Fig. 9 of [83]. The presence of this singularity prevents from applying the BW theorem with a conformal mapping given by $w(x)$ [83]. The operators $T_{tt}, T_{\mathrm{q-loc}}$ are the ones in Eq. (4.23), (4.25), respectively.

At this point, the result for real (Majorana) fermions can be obtained without any further effort. Indeed, the Dirac spinor in Eq. (4.22) can be written in terms of two Majorana spinors (real fermions). Rewriting the negativity (entanglement) hamiltonian in terms of these components, the mixed term cancel and $\mathcal{N}_A$ (H_A) is the sum of the two negativity (entanglement) hamiltonians for each real component of the complex field. As a consequence Eq. (4.24) is valid also for real massless fermions in 1+1 dimensions with $T_{tt}(0,x)$ the energy density of the real fermions and $T_{\mathrm{q-loc}}(0,x,y)$ given by Eq. (12) of the main text. There, we have explicitly reported only the expression of $\mathcal{N}_A$ and $\tilde{\mathcal{N}}_A$ for Majorana, while in Eq. (4.28) we report the explicit expression of $\mathcal{N}_A$ for Dirac. The functional form of $\beta^R_{\mathrm{loc}}, \beta^R_{\mathrm{q-loc}}, \bar{x}^R(x)$ is the same and only the definition of $T_{tt}(0,x)$ and $T_{\mathrm{q-loc}}(t,x,y)$ in terms of a real or complex fermionic field change.

4.4 Lattice Negativity Hamiltonian and numerical checks

In this section we review the numerical procedure that we used to benchmark our analytical results. We consider lattice systems described by the quadratic Hamiltonian

$$H(\lambda,\gamma) = \frac{i}{2}\sum_{l=-\infty}^{\infty}\Big(\frac{1+\gamma}{2}c_{2l}c_{2l+1} - \frac{1-\gamma}{2}c_{2l-1}c_{2l+2} + \lambda c_{2l-1}c_{2l}\Big). \tag{4.29}$$

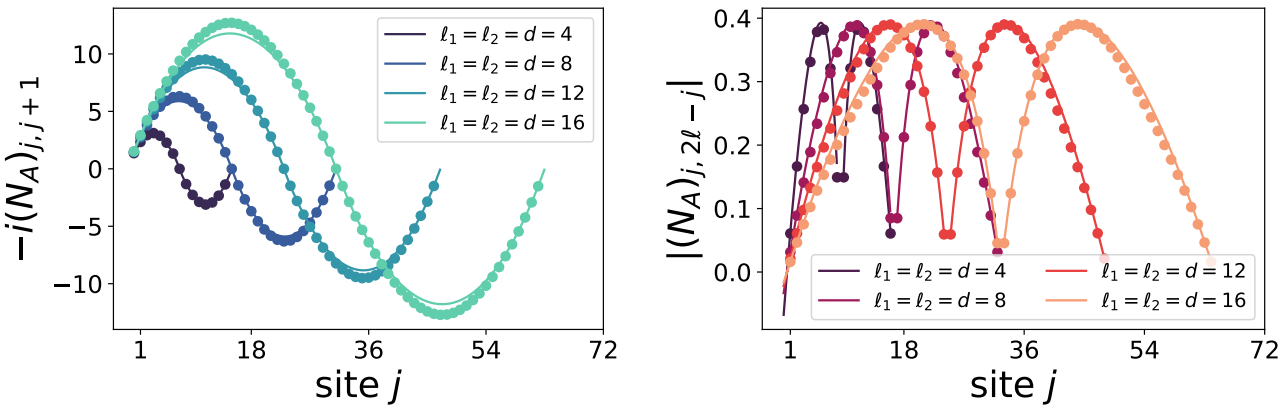

Figure 4.6: Negativity Hamiltonian for a real free fermion and for the geometry of two disjoint intervals of equal length ℓ on the infinite line. The symbols correspond to numerical data, while the solid lines correspond to the discretized form of N_A (Eq. (9) of the main text), both the local part (left panel) and the quasi-local one (right panel).

The one-particle energy levels are

$$\Lambda_k = \sqrt{(\lambda - \cos k)^2 + \gamma^2 \sin^2 k} \tag{4.30}$$

where $k \in [-\pi, \pi]$ is the physical momentum. For $(\lambda, \gamma) = (1,1)$ or $(\lambda, \gamma) = (0,0)$ the system is critical and Lorentz invariant at low energy. In the former case, the critical behavior is described by the conformal field theory of a free massless real fermion with central charge equal to $1/2$ (Majorana) while in the latter case the critical behavior is described by a free massless complex fermion with central charge equal to 1 (Dirac). Thus, the Hamiltonian (4.29), $H(0,0)$ or $H(1,1)$, is the ideal setting to compute the lattice negativity Hamiltonian $\mathcal{N}_A$ and benchmark the analytical expression in Eq. (9) of the main text (real fermion) and in Eq. (4.28) here (complex fermions).

Let us now consider the ground state of the Hamiltonian (4.29). For free complex fermions ($H(0,0)$), the covariance matrix Γ is given as

$$\Gamma_{2j_1-1,2j_2} = -\Gamma_{2j_2-1,2j_1} = i(2C_{j_1,j_2} - \delta_{j_1,j_2}), \tag{4.31}$$

with $C_{ij} = f_{j-i}$ and f_j

$$f_j = \frac{1}{\pi j} \sin \frac{\pi j}{2}, \quad f_0 = \frac{1}{2}. \tag{4.32}$$

For real fermions ($H(1,1)$), the elements of the covariance matrix are instead

$$\Gamma_{2j_1-1,2j_2} = -\Gamma_{2j_2,2j_1-1} = g_{j_2-j_1}, \tag{4.33}$$

where

$$g_j = -\frac{i}{\pi} \frac{1}{j + \frac{1}{2}}. \tag{4.34}$$

If now we focus on two intervals $A = A_1 \cup A_2$, adjacent or disjoint and of arbitrary lengths, the correlation matrix Γ_A is obtained from the Γ above simply restricting to the subsystem of interest and leading to the block structure of Eq. (1.20). If the total length of A is $\ell_1 + \ell_2$, the covariance matrix has dimension $2(\ell_1 + \ell_2) \times 2(\ell_1 + \ell_2)$. From this, the covariance matrix Γ^+ corresponding to the fermionic partial transpose is obtained by building Eq. (1.24). As a consequence, the numerical evaluation of the single particle negativity Hamiltonian corresponding to $\rho_A^{R_1}$, which is a Gaussian operator, just amounts to compute $N_A = \log \frac{1+\Gamma_+}{1-\Gamma_+}$. The case of two adjacent intervals of equal length for the real fermion has been reported in the main text finding small discrepancies up to a few percent between field theory and numerics. Here we substantiate our findings by displaying further tests of our predictions.

4.4.1 Intervals of equal length $\ell_1 = \ell_2$

We start from Fig. 4.5 reporting the case of two equal adjacent intervals for a complex fermion ($H(0,0)$). As in the main text, the agreement between numerics and field theory is remarkable. There are small deviations (up to $\sim 6\%$) between the theoretical curves and the numerical computation that however, as also motivated in the main text, they do not affect the lower part of the negativity spectrum and hence any universal aspect of the negativity Hamiltonian, as also found for the entanglement Hamiltonian, see e.g. [98, 99].

We observe that the data in the right panel of Fig. 4.5 show also some parity (in ℓ) effects that were not present for the real fermions. Such oscillations are well known finite ℓ effects [102, 103] and disappear as $\ell \to \infty$.

We now move to another geometry starting from real fermions. In Fig. 4.6 we report the case of two equal disjoint intervals at distance d and we benchmark once again our analytical result found in Eq. 9 of the main text. The curves again show a good agreement with the numerical computation, since the discrepancy is at most $\sim 6\%$.

4.4.2 Intervals of different length $\ell_1 \neq \ell_2$

Finally, we analyze in Fig. 4.7 the case of two disjoint intervals of different length, $\ell_1 \neq \ell_2$ for a real fermion. In this case, the reflected point $\bar{x}^R$ (Eq. (11) main text) is not on the antidiagonal and does not correspond to an integer number. Consequently its contributions "spreads" to the neighbouring integer. Such an effect is well shown in the right panel of 4.7 in which it is clear that the largest terms of the quasi-local parts of the negativity Hamiltonian are centered around $\bar{x}^R$. A more quantitative analysis of the quasilocal terms would require a weighted sum of the nearby elements to get the correct continuum limit, a procedure similar to the one exploited for the entanglement Hamiltonian in Refs. [19, 100, 101, 104, 105]. Such analysis is beyond our scope and for this reason we focus on the local term which instead is easily discretized. This is shown in the left panel of Fig. 4.7. Also in this case, the field theory prediction correctly matches the numerics, with small deviations that are at most $\sim 6\%$ for the system sizes considered.

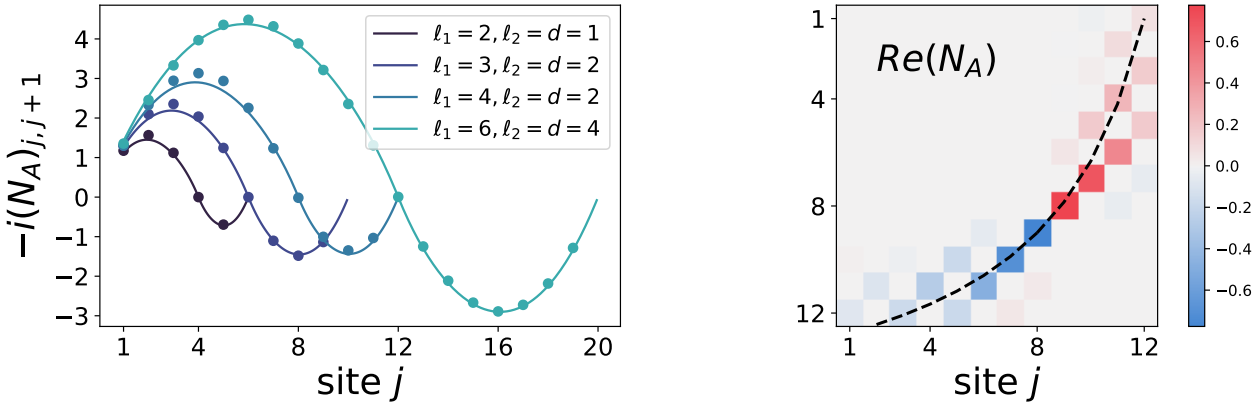

Figure 4.7: Negativity Hamiltonian for a real free fermion and for two disjoint intervals of different length $\ell_1 \neq \ell_2$. In this case, the discretized form of N_A correctly reproduces the local behavior of the negativity Hamiltonian (left panel). However, the reflected point $\bar{x}^R$ is not an integer living on the antidiagonal, as in the case of two intervals of equal length. Therefore, we only plot the location of $\bar{x}^R$, Eq. (11) main text, in order to show that its shape is compatible with the structure of the quasi-local part of N_A. Here we fix $\ell_1 = 2\ell_2 = 2d = 4$ (right panel).

4.5 Discussion and outlook

In the previous sections we initiated the study of the negativity Hamiltonian in many-body quantum systems. Although our field theoretical construction in terms of the EH of disjoint intervals is very general, its applicability relies crucially on the exact knowledge of the latter, that is not always available. We stress that the knowledge of the negativity Hamiltonian encodes the entire information content about the entanglement in the mixed states. This is remarkable with respect to the scalar quantities used to compute the entanglement (e.g. the negativity), which do not allow to reconstruct the whole partial transpose reduced density matrix. We expect that the quasi-local structure of the negativity Hamiltonian can be generalised to other contexts, at least for free fermions, such as a single interval in an infinite system at finite temperature [83], or two disjoint intervals in the presence of a point-like defect [91]. At present, it is unclear whether this quasi-local structure survives to finite interaction strengths and in higher dimensions.

Having established an explicit approximate functional form for the negativity Hamiltonian that is quasi-local opens up several possible applications. First, one could design experiments aimed at a direct realization of N_A: since the corresponding operators have simple functional form, this could be done by combining local tuning with tailor-engineered long-distance couplings similarly to what has already been proposed in the context of quantum chemistry simulations [106]. Second, the local structure of N_A paves the way for a direct reconstruction of partial transposes in experiments, utilizing, e.g., Hamiltonian reconstruction methods that have already been combined with the BW theorem [21]. Both of these applications would allow a direct measurement of the negativity spectrum, something that is presently unachievable by any method other than full state tomography. Thirdly, it may be possible to design efficient classical or hybrid classical-quantum algorithms for the *ab initio* determination of N_A, similarly to what has been

done for the EH following a BW inspired ansatz [20, 22, 107]. Having an explicit functional form could enable computations that are then not available otherwise - one example being quantum Monte Carlo algorithms aimed at computing the negativity utilizing meta-dynamics, similarly to what has been done in the context of the EH [108].

5

Entanglement-detection via partial transpose moments

5.1 Introduction

In the past years, considerable effort led to the building of larger and larger NISQ devices [109, 110]. For the benchmarking of such devices comes the need for more scalable tools in order to characterize the underlying many-body quantum state (see e.g. [111] and references therein). For instance, characterizing the entanglement properties of these quantum states is, besides the intrinsic theoretical interest, essential to gauge the performance and verify the proper working of the NISQ devices.

As a first prominent example among the tools to characterize entanglement, there is the concept of entanglement witness [112, 113]. As we have discussed in Chap.1, an entanglement witness is a functional of the quantum density matrix that separates a specific entangled state from the set of all separable states [1] (for specific examples of entanglement witnesses in various types of systems, see e.g. Ref. [114] and references therein). By contrast we shall focus on a superset of the set of separable states: the set of states with positive partial transpose. In other words, we will focus on sufficient conditions for entanglement (equivalently, necessary conditions for separability).

From the numerous theoretical sufficient conditions for entanglement that have been developed in the literature, many cannot be straightforwardly implemented experimentally, mainly because they require the (exponentially expensive) knowledge of the full density matrix [115, 116].

[1] When this functional is linear, it can be identified with an observable whose expectation value can be used to decide whether the target state is entangled or not.

This is for instance the case of the celebrated PPT condition [74, 112], which states that a separable state ρ always has a positive semi-definite (PSD) partial transpose (PT) ρ^{Γ}[2] for any bipartite splitting of its subsystems. Thus, if ρ^{Γ} has (at least) a single negative eigenvalue, then ρ is entangled. The negativity, which resulted from this condition, is the most renowned entanglement measure for mixed states [75, 117, 118].

This powerful entanglement condition, which found many applications in theoretical works [34, 50, 66, 69, 119–122], is difficult to apply in experimental conditions as the PT spectrum is difficult to access. To overcome this challenge, it was shown in Ref. [12] that valuable information about the PT spectrum can be obtained from a few PT moments $\mathrm{tr}(\rho^{\Gamma})^k$ only. Using the first three PT moments, an entanglement condition, called p_3-PPT, was proposed and shown to be useful for detecting entangled states in several different contexts. Moments $\mathrm{tr}(\rho^{\Gamma})^k$ have the advantage that they can be estimated using shadow tomography [12] in a more efficient way than if one had to reconstruct ρ via full quantum state tomography.

Indeed, the k-th order PT moment of a state ρ can be expressed as the expectation value of some k-copy permutation operator O [12], i.e. $\mathrm{tr}(\rho^{\Gamma})^k = \mathrm{tr}\left(O\rho^{\otimes k}\right)$. As shown in Ref. [123], the classical shadow formalism allows to estimate such an expectation value from independent classical snapshots $\hat{\rho}_1, \ldots, \hat{\rho}_k$ (which can each be obtained from post-processing single-qubit measurement outcomes) through the U-statistics estimator $\hat{o}_k = \mathrm{tr}\left(O\hat{\rho}_1 \otimes \cdots \otimes \hat{\rho}_k\right)$. Therefore, as in other randomized measurements protocols probing entanglement [10, 12, 123–131], the classical shadows formalism only requires (randomized) single-qubit measurements in experiments realizing the single-copy state ρ. Here, we follow this idea of using PT moments to build experimentally computable entanglement conditions, and extend the p_3-PPT condition in two directions.

On the one hand, we propose different entanglement detection strategies depending on how many PT moments can be estimated. Starting from the third order moment, we show that the estimation of each higher order moment gives access to an independent entanglement condition. Interestingly, if all the PT moments can be estimated, this set of conditions is then necessary and sufficient for the state to be PPT (i.e. to have a positive semi-definite partial transpose). Of course, the higher the moment, the larger the number of experimental runs needed. In case higher order moments cannot be accessed, we show how to obtain an optimal entanglement condition using PT moments of order up to three.

On the other hand, we investigate the effect of symmetries on this entanglement detection method. As shown in Ref. [11] for the case of dynamical purification[3], taking symmetries into account to define symmetry-resolved (SR) versions of the tools usually used to characterize quantum states can enable a finer characterization of some quantum features and even reveal phenomena that cannot be observed without symmetry-resolution. For states preserving an extensive quantity, we define SR versions of the PT-moment inequalities mentioned previously and show that these are indeed better suited to detect the entanglement of such states. Furthermore, we also

[2] ρ^{Γ} is used to define the PT with no particular reference to given system geometries.
[3] This will be described in details in Chap.6.

show that these SR inequalities provide a sufficient entanglement condition for states that do not possess any symmetry.

The conditions derived here are particularly interesting from an experimental (and numerical) point of view, as low moments of (partially transposed) density operators are accessible. We show how source drifts in an experiment can be taken into account and how the quantities which are of interest here can be accurately estimated via local measurements on single copies of the state.

The chapter is structured as follows. In Sec. 5.2, we summarize our results. Our methods to obtain entanglement conditions from PT-moments are presented in Sec. 5.3. In Sec. 5.5 we study the effect of symmetries and show how to obtain a SR version of these PT-moment inequalities. In Sec. 5.7, we apply these inequalities to a variety of physical systems and compare their efficiency for detecting entanglement. Finally, we conclude and give some outlook in Sec. 5.8.

5.2 Definitions and summary of results

In this section, we introduce the basic definitions needed for the entanglement detection criteria below, and summarize in a succinct manner our main results. Given a bipartite state $\rho = \rho_{AB}$, we denote by ρ^Γ its partial transpose with respect to subsystem B. We say that ρ is PPT if ρ^Γ is positive semi-definite, and NPT otherwise. All NPT states are entangled, however there are entangled states, known as bound-entangled states, that are not NPT. We focus here on the detection of NPT entangled states.

We denote the k-th order moment of a matrix M by

$$p_k(M) \equiv \mathrm{tr} M^k. \tag{5.1}$$

We will mostly consider moments of ρ^Γ, and sometimes use the short-hand notation $p_k \equiv p_k(\rho^\Gamma)$. In the presence of symmetries, the partial transpose can be cast in block diagonal form: we denote as $\rho^\Gamma_{(q)}$ the resulting blocks, where q indicates a quantum number, and define the corresponding moments $p_k(\rho^\Gamma_{(q)})$ as from Eq. (5.1).

We start by recalling the p_3-PPT condition of Ref. [12], i.e. that any PPT state satisfies

$$p_3(\rho^\Gamma) p_1(\rho^\Gamma) \geq (p_2(\rho^\Gamma))^2 . \tag{5.2}$$

Any state violating this condition is NPT and therefore entangled. The p_3-PPT condition will serve as a reference point below in accessing the predictive power of the new relations.

i) the first set of conditions, that we dub D_n conditions, also contains polynomial inequalities in the moments p_k of order up to $k \leq n$. The first non-trivial such a condition is D_3, and reads:

$$p_3(\rho^\Gamma) \geq -\frac{1}{2}(p_1(\rho^\Gamma))^3 + \frac{3}{2} p_1(\rho^\Gamma) p_2(\rho^\Gamma). \tag{5.3}$$

Knowing only the first three moments $p_1(\rho^\Gamma), p_2(\rho^\Gamma)$ and $p_3(\rho^\Gamma)$, this condition is optimal for

detecting entanglement if $1/2 \leq p_2(\rho^\Gamma) \leq 1$. Knowing moments of order up to the dimension of ρ^Γ, the set of D_n conditions provides a necessary and sufficient condition for NPT entanglement;

ii) the second set of conditions, dubbed Stieltjes$_n$, involves inequalities among the moments p_k of order up to n. The condition Stieltjes$_3$ is equivalent to p_3-PPT, while Stieltjes$_5$ reads:

$$\det \begin{pmatrix} p_1 & p_2 & p_3 \\ p_2 & p_3 & p_4 \\ p_3 & p_4 & p_5 \end{pmatrix} \geq 0 \tag{5.4}$$

and similar conditions are obtained including higher moments;

iii) in case high-order moments are difficult or too expensive to access, we also show how to obtain an optimized, necessary condition for PPT using only PT moments of order up to three. We call this condition D_3^{opt};

iv) all of the above conditions can be cast in terms of $\rho^\Gamma_{(q)}$, in which case we add the prefix SR (for symmetry-resolved). For instance, the SR-p_3-PPT condition for sector q reads

$$p_3(\rho^\Gamma_{(q)})p_1(\rho^\Gamma_{(q)}) \geq (p_2(\rho^\Gamma_{(q)}))^2. \tag{5.5}$$

Since these conditions are sensitive to the presence of negative eigenvalues in a specific symmetry sector, they are typically much more sensitive than their non-SR counterparts, as illustrated in Fig. 5.1.

In the SR case, it is worth mentioning that also the SR-D_2 condition,

$$p_2(\rho^\Gamma_{(q)}) \leq (p_1(\rho^\Gamma_{(q)}))^2\,, \tag{5.6}$$

is non-trivial;

v) we show how SR conditions can, in fact, be applied to arbitrary states, via application of a proper transformation on the density matrix of interest. In practice, this transformation is effectively carried out in the post-processing step of the classical shadows;

vi) as illustrated in Fig. 5.1, the uncertainty in estimating the moments can be bounded, in principle, using the classical shadows formalism. Here, we show how to combine those bounds to provide rigorous confidence intervals for SR-D_2, which considerably strengthen the impact of our results in real experiments.

5.3 Entanglement detection from partial transpose moments

In this section, we present entanglement conditions based on PT moments. We extend the idea behind the p_3-PPT condition (c.f. Eq. (5.2)) of Ref. [12] in two directions. On the one hand, we present a set of inequalities involving all the PT moments which provides a necessary and sufficient condition for the underlying state to be PPT. In addition, each condition of this set is itself

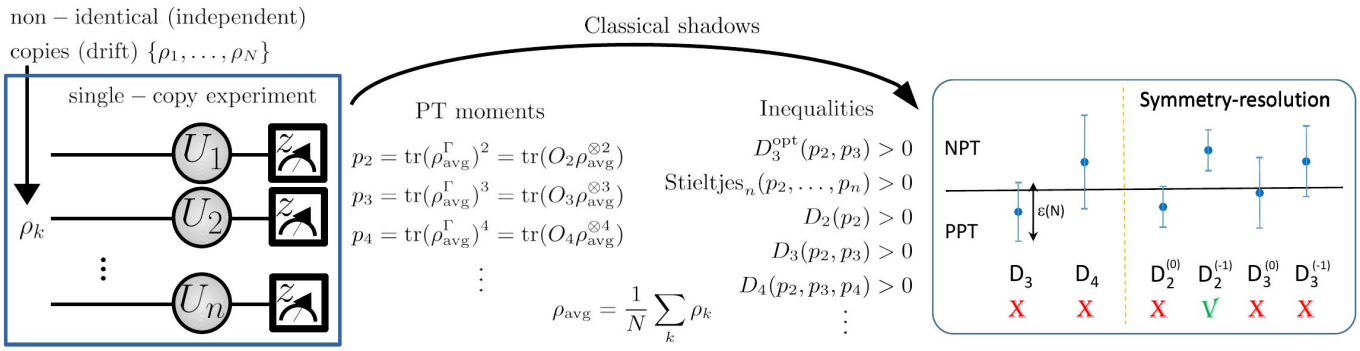

Figure 5.1: An illustration of the proposed method for entanglement detection. We assume the experimentally relevant situation of a source producing non-identical but independent copies $\{\rho_1, \ldots, \rho_N\}$ ("drift"). Randomly-chosen unitaries U_i are applied to the qubits of each copy and then measured in the standard basis. Using classical shadows [123], these measurement outcomes are post-processed to obtain the moments $p_j = \mathrm{tr}(\rho_{\mathrm{avg}}^{\Gamma})^j$. As explained in the main text, we combine those moments to derive inequalities whose violation implies that the state ρ_{avg} is NPT, thus showing that at least one of the states ρ_k produced by the source is entangled. We also show how symmetry-resolution techniques can be used to enhance the entanglement detection capabilities.

a necessary PPT condition. On the other hand, we show how to optimize such entanglement conditions when only few low-order PT moments are accessible.

The idea behind this set of conditions is to use Descartes' rule of signs on the characteristic polynomial of a Hermitian matrix to obtain a set of moment inequalities that has to be satisfied by any PSD matrix. Applied to the partially transposed matrix ρ^{Γ}, such conditions can then be used to detect the entanglement of NPT quantum states. More precisely, using the definition of the elementary symmetric polynomials on d variables,

$$e_i(x_1, \ldots, x_d) = \sum_{1 \leq j_1 < \cdots < j_i \leq d} x_{j_1} \cdots x_{j_i}, \tag{5.7}$$

for $i = 1, \ldots, d$, and $e_0(x_1, \ldots, x_d) = 1$, we derive in Appendix A.1 the following lemma.

Lemma 1. *A Hermitian matrix A of dimension d is PSD if and only if $e_i(\lambda_1, \ldots, \lambda_d) \geq 0$ for all $i = 1, \ldots, d$, where $\lambda_1, \ldots, \lambda_d$ are the eigenvalues of A, and e_i denote the elementary symmetric polynomials (Eq. (5.7)).*

Using Newton's identities, which relate the elementary symmetric polynomials, e_k, in the eigenvalues of A to the moments of A through the recursive formula

$$k e_k = \sum_{i=1}^{k} (-1)^{i-1} e_{k-i}\, p_i(A), \tag{5.8}$$

each inequality $e_i \geq 0$ can be transformed into an inequality involving moments of A of order up

to i. We denote by D_i these moments inequalities. As an illustration, the conditions D_1 to D_4 read

$$p_1(A) \geq 0, \tag{5.9}$$
$$p_2(A) \leq (p_1(A))^2, \tag{5.10}$$
$$p_3(A) \geq -\frac{1}{2}(p_1(A))^3 + \frac{3}{2}p_1(A)p_2(A), \tag{5.11}$$
$$p_4(A) \leq \frac{1}{2}\left((p_1(A))^2 - p_2(A)\right)^2 - \frac{1}{3}(p_1(A))^4 + \frac{4}{3}p_1(A)p_3(A), \tag{5.12}$$

respectively. One has $p_1(\rho^\Gamma) = 1$ for any quantum state ρ, implying that D_1 is trivially satisfied. Similarly, since $p_2(\rho^\Gamma)$ is equal to $p_2(\rho)$ (i.e., to the purity of ρ) for any quantum state ρ, the inequality D_2 is also trivially satisfied. Therefore, when ρ is a quantum state, the first non-trivial inequality for ρ^Γ is D_3. As will be shown in the next section, it is sometimes more efficient (in order to detect entanglement) to apply these inequalities to projections of ρ^Γ onto specific subspaces, rather than to ρ^Γ itself. We would like to stress here that, in that case, the argument above does not hold, so that the inequality D_2 is not trivially satisfied and can already reveal the presence of entanglement (see Sec. 5.5).

When applied to ρ^Γ, Lemma 1 and Newton's identities (5.8) can thus be used to detect NPT entangled states from PT moments only. From an experimental point of view, this is an important aspect of this entanglement detection scheme, as PT moments are experimentally more affordable to estimate than, for instance, the whole spectrum of ρ^Γ. As PT moments are more expensive to be estimated the higher the order, these inequalities should be considered starting from those involving the lowest moment orders. Even though showing that a state is NPT with this method can in principle require the knowledge of all the PT moments, we will provide many experimentally relevant instances where entanglement can be effectively detected from low-order moments even in the presence of errors.

Similarly, let us mention here that necessary and sufficient conditions for a matrix to be PSD can be expressed as different sets of polynomial inequalities in its moments. One of such sets can be deduced from the well-known (truncated) *Stieltjes moment problem* (see Appendix A.2). In Sec. 5.7, we illustrate the usefulness of these inequalities by applying them to the entanglement detection of the ground state of the XXZ model (c.f. Fig 5.5). Let us finally also mention that, from a few moments of a Hermitian matrix, one can also obtain bounds on the distance between this matrix and the PSD cone [132].

5.4 Optimized condition for low-order moments

Due to (experimental) constraints, it might not be possible to determine all, but only a few, PT moments. This is why, we show here how to optimize necessary PPT conditions using only PT moments of order up to three. From the previous sections, we already have two examples of such conditions, namely the p_3-PPT and D_3 conditions. As illustrated in Fig. 5.2, the p_3-PPT (D_3)

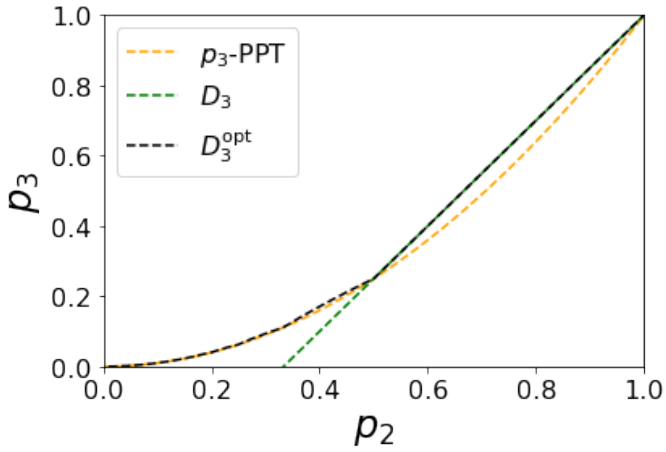

Figure 5.2: Plot of the value of the third moment p_3 saturating the p_3-PPT (dashed orange curve), the D_3 (dashed green line) and the optimal D_3^{opt} (dashed black curve) conditions as a function of the second moment p_2 for a normalized Hermitian matrix. According to the p_3-PPT condition, any state ρ with a value of $p_3(\rho^\Gamma)$ below the dashed orange curve is entangled. Similarly, the condition D_3 shows that any state ρ with a value of $p_3(\rho^\Gamma)$ below the dashed green line is entangled. From this plot, it is clear that, for $p_2(\rho^\Gamma) > 1/2$, all entangled states detected by the p_3-PPT condition are also detected by D_3, which coincides with D_3^{opt} in this case. When $p_2(\rho^\Gamma) < 1/2$, the p_3-PPT condition is then *stronger* than D_3, and D_3^{opt} represents a slight improvement over the p_3-PPT condition.

condition is tighter than D_3 (p_3-PPT) for states with purity larger (smaller) than $1/2$, respectively. As the low-order moments are easier to access experimentally, we now address the question about the optimal inequality involving PT moments of order up to three.

To answer this question, we use the following approach. For fixed values p_1 and p_2 of the first two moments, we determine the minimal value $p_3^{\min}$ that the third moment can reach for any PSD matrix [4]. From this bound, we know that any Hermitian matrix with a smaller third moment is necessarily not PSD. Naturally, we restirc ourselves to values of p_1 and p_2 which are compatible with a PSD matrix, and therefore satisfy Eqs. (5.9) and (5.10) [5].

Given a $d \times d$ PSD matrix A, with non-zero eigenvalues $\lambda_1, \ldots, \lambda_r$, for some $r \in [1, d]$, this optimization can be performed with the help of Lagrange multipliers. As shown in Appendix A.3, this leads to solutions with only two distinct eigenvalues λ_a, λ_b with multiplicity $r_a, r - r_a$, respectively, for $r_a \in [1, r]$. Assuming, without loss of generality, that $\lambda_a \geq \lambda_b$, the optimization of p_3 leads then to $r_a = r - 1$. For each value of r, the optimal value of p_3 can be easily determined in the interval $[1/r, 1/(r-1)]$. For $r = 2$ this leads to D_3 whereas for $r > 2$ one obtains an optimal value of p_3 which is slightly better than p_3-PPT. Observe that $p_3^{\min}(p_2)$ is a piece-wise function and the derivative $\partial p_3^{\min}/\partial p_2$ is discontinuous at points $p_2 = 1/r$ (see Fig. 5.2).

[4] Note that we want here to minimize p_3 because it is an odd moment (for which negative eigenvalues would have the tendency to decrease the value of the moment). For an even moment, we would instead maximize the value of this moment over PSD matrices. This is also reflected in the D_n conditions (5.10)–(5.12), where the inequality sign alternates between even and odd values of n.

[5] Recall that for the partial transpose of a density operator this is always fulfilled.

5.5 Symmetry-resolved entanglement detection

Symmetries, as they often occur in physical situations, can be exploited to observe relevant phenomena (see e.g. Refs. [11, 133–143]). Here, we use symmetries to ease the detection of entanglement. More precisely, we apply the previously developed tools to symmetric states, which will lead to conditions of entanglement involving much lower moments of the partial transpose projected onto certain subspaces. Despite the fact that these quantities differ significantly from the moments of ρ^Γ, we will show later on that they can nevertheless be estimated using the framework of classical shadows.

We consider a bipartite state $\rho = \rho_{AB}$, with subsystems A and B containing n and m qubits, respectively. We assume that this state commutes with $\sum_{i=1}^{n+m} Z_i$, or similarly with the total number operator $\mathcal{N} = \mathcal{N}_A + \mathcal{N}_B$. Here and in the following, we denote by X, Y, Z the Pauli operators. Obviously, such a state has a block diagonal form, i.e.,

$$\rho = \bigoplus_{q=0}^{n+m} \rho_{(q)} = \sum_q Q_q \rho Q_q, \tag{5.13}$$

where each block (or sector) is labeled by an eigenvalue $q \in \{0, 1, \ldots, n+m\}$ of the operator $\mathcal{N}$ and has support in the corresponding eigenspace. Here,

$$Q_q = \sum_{a+b=q} \Pi_a(A) \otimes \Pi_b(B),$$

with

$$\Pi_k(A) = \sum_{i_1+\cdots+i_n=k} |i_1 \cdots i_n\rangle \langle i_1 \cdots i_n|$$

and similarly for B. It has been shown [144] that, for this type of symmetry, the partial transpose ρ^Γ is also block diagonal, but in a different basis. In fact, $\rho^\Gamma = \oplus_{q=-m}^{n} \rho^\Gamma_{(q)} = \sum_q P_q \rho^\Gamma P_q$, where P_q is the projector onto the eigenspace of $\mathcal{N}_A - \mathcal{N}_B$ with eigenvalue $q \in \{-m, -m+1, \ldots, n\}$ [6], i.e.

$$P_q = \sum_{a-b=q} \Pi_a(A) \otimes \Pi_b(B). \tag{5.14}$$

The size of the sector corresponding to the eigenvalue q in the block-decomposition of ρ^Γ is given by

$$\mathrm{tr} P_q = \sum_{a-b=q} \binom{n}{a}\binom{m}{b} = \binom{n+m}{q+m}.$$

[6] This can be easily seen as follows. Consider a matrix element $\rho_{ab,a'b'} |ab\rangle \langle a'b'|$ of ρ with eigenvalue i of $\mathcal{N}_A + \mathcal{N}_B$. Precisely, let us write $\mathcal{N}_A |a\rangle = n_a |a\rangle$, $\mathcal{N}_A |a'\rangle = n_{a'} |a'\rangle$, $\mathcal{N}_B |b\rangle = n_b |b\rangle$, and $\mathcal{N}_B |b'\rangle = n_{b'} |b'\rangle$ with $n_a + n_b = n_{a'} + n_{b'} = i$. After partial transposition, $\rho_{ab,a'b'} |ab\rangle \langle a'b'| \mapsto \rho_{ab,a'b'} |ab'\rangle \langle a'b|$. For our particular case, $\mathcal{N}_B = \mathcal{N}_B^\Gamma$ and one can see that $(\mathcal{N}_A - \mathcal{N}_B) |ab'\rangle = (n_a - n_{b'}) |ab'\rangle$ and $(\mathcal{N}_A - \mathcal{N}_B) |a'b\rangle = (n_{a'} - n_b) |a'b\rangle$ with $n_a - n_{b'} = n_{a'} - n_b$. This shows that matrix elements within a block of ρ are mapped, via partial transposition, to matrix elements within a block of ρ^Γ.

When the partial transpose of a density matrix has a block structure, it is naturally PSD iff each block is itself a PSD matrix. Therefore, one can apply the conditions of the previous section directly to the blocks $\rho^\Gamma_{(q)}$ of the partial transpose. For the p_3-PPT condition, the corresponding symmetry-resolved (SR) inequalities are simply

$$p_3(\rho^\Gamma_{(q)})p_1(\rho^\Gamma_{(q)}) \geq (p_2(\rho^\Gamma_{(q)}))^2$$

for all $q = -m, -m+1, \ldots, n$. Any violation of a PSD condition in one of the blocks is then sufficient to show that ρ^Γ has at least one negative eigenvalue and that ρ is therefore entangled.

When using the D_i conditions, symmetry-resolution can be a significant advantage (see e.g. Sec. 5.7). First, the necessary and sufficient PSD conditions involve moments of order at most equal to the dimension of the largest block, that is $\binom{n+m}{\lfloor (n+m)/2 \rfloor}$, which is necessarily smaller than the dimension of the density matrix itself. Second, since a block $\rho^\Gamma_{(q)}$ of ρ^Γ is (in general) not the partial transpose of any positive matrix [7], the inequality:

$$p_2(\rho^\Gamma_{(q)}) \leq (p_1(\rho^\Gamma_{(q)}))^2 \tag{5.15}$$

is not necessarily satisfied. This implies that moments of order two can already be sufficient to detect entanglement.

As stressed in the introduction, using PT-moment inequalities to detect entanglement is particularly interesting from an experimental point of view, because such PT moments can be estimated, for instance using shadow tomography [12]. As we show in the following lemma, the shadow tomography protocol used in Ref. [12] can also be used to estimate moments of blocks of the partial transpose (which differ significantly from the PT moments) by slightly modifying the non-linear observable that has to be measured.

Lemma 2. *Given a symmetric state $\rho = \sum_i Q_i \rho Q_i$, for each eigenvalue i of $\mathcal{N}_A - \mathcal{N}_B$, it holds that*

$$\mathrm{tr}(P_i \rho^\Gamma P_i)^k = \mathrm{tr}(L_i^{(k)} \rho^{\otimes k})$$

where the operators $L_i^{(k)}$ are given by

$$L_i^{(k)} = \left(\sum_{a-b=i} \Pi_a(A_1) \otimes 1 \otimes \cdots \otimes 1 \otimes \Pi_b(B_k) \right) \cdot \tilde{S}(A_1, \ldots, A_k) \otimes S(B_1, \ldots, B_k) \tag{5.16}$$

with

$$\tilde{S}(A_1, \ldots, A_k) = \sum_{a_1} \cdots \sum_{a_k} |a_k a_1 \cdots a_{k-1}\rangle \langle a_1 \cdots a_k| \,,$$
$$S(B_1, \ldots, B_k) = \sum_{b_1} \cdots \sum_{b_k} |b_2 \cdots b_k b_1\rangle \langle b_1 \cdots b_k| \,.$$

[7] This is, there could be no $\sigma > 0$ such that $\rho^\Gamma_{(q)} = \sigma^\Gamma$.

Here, the sum over each a_i (b_i) runs from 1 to 2^n (2^m) respectively.

Proof. Denoting by $\rho_{ab,a'b'}$ the entries of the operator and using that $\rho_{ab,a'b'} = \rho^{\Gamma}_{ab',a'b}$, it is straightforward to see that

$$\mathrm{tr}_{\setminus A_1 B_k}\left(\tilde{S}(A_1,\ldots,A_k)\otimes S(B_1,\ldots,B_k)\rho^{\otimes k}\right) = ((\rho^{\Gamma})^k)^{\Gamma}\,. \tag{5.17}$$

Then, we have that

$$\mathrm{tr}(L_i^{(k)}\rho^{\otimes k}) = \mathrm{tr}\left(P_i\,((\rho^{\Gamma})^k)^{\Gamma}\right) = \mathrm{tr}\left(P_i^{\Gamma}\,(\rho^{\Gamma})^k\right) = \mathrm{tr}\left(P_i\,(\rho^{\Gamma})^k\right).$$

Here, the first equality follows from the definition of $L_i^{(k)}$ and Eq. (5.17); the second, from $\mathrm{tr}(RS^{\Gamma}) = \mathrm{tr}(R^{\Gamma}S)$ for any two matrices R, S; and the third, from $P_i^{\Gamma} = P_i$. Finally, using that $P_i = P_i^2$ are orthogonal projectors, the cyclic property of the trace, and the block structure of ρ^{Γ}, we have

$$\mathrm{tr}\left(P_i\,(\rho^{\Gamma})^k\right) = \mathrm{tr}\left(P_i\,(\rho^{\Gamma})^k P_i\right) = \mathrm{tr}\left(P_i\,\rho^{\Gamma}P_i\right)^k,$$

which completes the proof.

□

5.6 SR inequalities applied to states without symmetries

SR inequalities can also be used to detect the entanglement of arbitrary states, including those that do not have any symmetry.

The reason for that is that there exists a local channel $\mathcal{C}$ that transforms any state ρ into a state $\sigma \equiv \mathcal{C}(\rho)$ that has the desired block structure. The channel can be realized with local operations assisted by classical communication, and can thus not generate entanglement. Therefore, the initial state ρ must be at least as entangled as the final block diagonal state σ. This statement holds for any entanglement measure. As a consequence, if entanglement is detected in σ (which can be investigated using the symmetry-resolved tools), then ρ is necessarily also entangled. In other words, looking at the entanglement of σ, the "block-diagonalized" version of ρ, provides a sufficient condition of entanglement for ρ. This condition is not necessary as it could be that the channel $\mathcal{C}$ destroys all the entanglement of ρ.

The local channel that can be used for this approach is the following:

$$\mathcal{C} : \rho \to \mathcal{C}(\rho) = \frac{1}{2^k}\sum_{i=0}^{2^k-1} U_i^{\otimes(n+m)}\rho\,(U_i^{\dagger})^{\otimes(n+m)} \tag{5.18}$$

where $k = \lfloor \log(n+m) \rfloor + 1$ and $U_i = Z^{i/2^k}$. The fact that this channel maps ρ to a state σ that is block-diagonal in the number-of-excitations basis can easily be seen as follows. First, observe

that for any $j \in \{0, \ldots, 2^{(n+m)} - 1\}$, the computational basis state $|j\rangle$ is an eigenvector of U_i, associated to an eigenvalue, $(-1)^{|j|i/2^k}$, that essentially depends on $|j|$, the number of excitations of $|j\rangle$. Therefore, we have

$$\sigma = \frac{1}{2^k} \sum_{j,j'=0}^{2^{(m+n)}-1} \sum_{i=0}^{2^k-1} (-1)^{\frac{i(|j|-|j'|)}{2^k}} \rho_{j,j'} |j\rangle\langle j'|. \tag{5.19}$$

For any j and j' having different number of excitations, i.e. such that $|j| \neq |j'|$, the sum over i in Eq. (5.19) vanishes, explaining why σ is diagonal in the number-of-excitations basis.

As can be seen from the argument above, the non-zero elements of σ are all equal to the corresponding elements of ρ. This implies that the channel can effectively be replaced by a sum of projectors onto all the number-of-excitations sectors. From an experimental point of view, the practical implementation of this channel can thus be circumvented by using the observables of Lemma 2 in the post-processing of the classical shadows.

5.7 Applications

In this section, we apply and compare the entanglement conditions presented in the previous sections on various physical systems. For the systems possessing a symmetry as discussed in Sec. 5.5, we highlight some of the advantages that can result from considering symmetry-resolved entanglement detection tools.

5.7.1 Entanglement detection in quench dynamics

We begin by considering the situation of quench dynamics, where entanglement emerges from the dynamics of a many-body Hamiltonian. We consider the model presented in Ref. [11], where the interplay between coherent dynamics with $U(1)$ symmetry and dissipation leads to a dynamics of 'purification'. Here, we will use the same formalism to show how entanglement is generated at short times, and can be detected via the symmetry-resolved versions of the D_2 and p_3-PPT conditions. In the next section, we will consider an analogous experimental situation obtained with trapped ions [10].

Our model is described by a master equation

$$\partial_t \rho = -\frac{i}{\hbar}[H_{XY}, \rho] + \sum_j \gamma \left[\sigma_j^- \rho \sigma_j^+ - \frac{1}{2}\{\sigma_j^+ \sigma_j^-, \rho\}\right], \tag{5.20}$$

with the lowering and raising operators $\sigma_j^- = (X_j - iY_j)/2$, $\sigma_j^+ = (X_j + iY_j)/2$, and the Hamiltonian

$$H_{XY} = \frac{\hbar}{2} \sum_{i<j} J_{ij}(X_i X_j + Y_i Y_j) \tag{5.21}$$

and where γ is the spontaneous emission rate. Here, we consider open boundary conditions. The hopping between spins i and j is described by the coefficient J_{ij} and we consider this section nearest-neighbor hopping $J_{ij} = J\delta_{i+1,j}$ with strength J. The initial state is the Néel state $\rho(0) = |\psi(0)\rangle\langle\psi(0)|$, with $|\psi(0)\rangle = |\downarrow\uparrow\rangle^{\otimes N/2}$. As shown in Ref. [11], the time evolved state $\rho(t)$ of the N spin system has the block diagonal form of Eq. (5.13). Moreover, the partially transposed matrix w.r.t a partition A, ρ^Γ is also block diagonal with blocks $\rho^\Gamma_{(q)}$. Here, the index q represents the difference between the number of spin excitations in A and the one in the complement partition B (see also Sec. 5.5).

As we are interested in short time dynamics, we can solve Eq. (5.20) in first order in perturbation theory, which is valid for $t \ll 1/J, 1/\gamma$. Considering for concreteness a half-partition A, made of the first N_A sites, we obtain a block with a negative eigenvalue [11]. Assuming for simplicity $N_A = N/2$, N_A even, we obtain

$$\rho^\Gamma_{(-1)}(t) = \gamma t \sum_{m=1}^{N_A/2} \sigma^-_{2m}\rho(0)\sigma^+_{2m} + Jt\left(-i\sigma^+_{N_A+1}\rho(0)\sigma^+_{N_A} + \text{h.c}\right). \tag{5.22}$$

The presence of a negative eigenvalue in this sector can be detected from the value of the moments

$$p_1(\rho^\Gamma_{(-1)}(t)) = \frac{\gamma N_A t}{2}, \tag{5.23}$$
$$p_2(\rho^\Gamma_{(-1)}(t)) = 2J^2t^2, \tag{5.24}$$
$$p_3(\rho^\Gamma_{(-1)}(t)) = 3\gamma J^2 t^3, \tag{5.25}$$

in leading order in $J \gg \gamma N_A$. In particular, the p_3-PPT ratio

$$\frac{p_3(\rho^\Gamma_{(-1)}(t))p_1(\rho^\Gamma_{(-1)}(t))}{p_2(\rho^\Gamma_{(-1)}(t))^2} = \frac{3\gamma^2 N_A}{8J^2} \ll 1, \tag{5.26}$$

and the D_2 condition

$$\frac{p_1(\rho^\Gamma_{(-1)}(t))^2}{p_2(\rho^\Gamma_{(-1)}(t))} = \frac{\gamma^2 N_A^2}{8J^2} \ll 1, \tag{5.27}$$

can be used to reveal the presence of entanglement at short times. We show in Fig. 5.3 a numerical confirmation of these results for various values of γ/J and $N = 8$, which was obtained by simulating Eq. (5.20). We note that, in the present context, utilizing symmetry-resolution is fundamental to detect entanglement: this is due to the fact that the negative eigenvalues in ρ^Γ appear in sectors that are not macroscopically populated [11], so that moments without symmetry resolution would not be able to detect them.

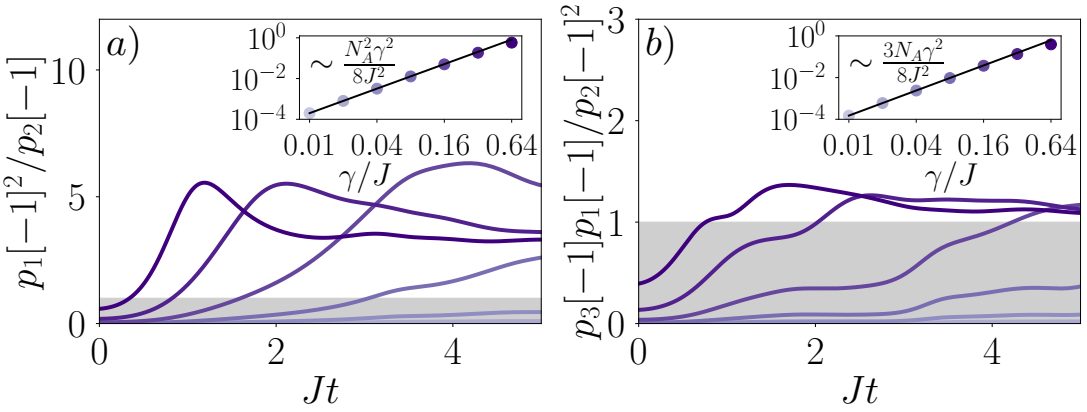

Figure 5.3: Symmetry resolved entanglement detection in quench dynamics with spin excitation loss. We study SR-entanglement in quench dynamics in a system consisting of $N = 8$ spins initialized in a Néel state $|{\downarrow\uparrow}\rangle^{\otimes N/2}$ and evolved with H_{XX} subject to spin excitation loss with various rates γ (γ/J increases with the darkness of the color, see insets). We take $A = [1,2,3,4]$ and $B = [5,6,7,8]$. In panels a) and b), the D_2 ratio and p_3-PPT ratio of sector $q = -1$ are shown, respectively. Entanglement is detected for values below unity in the shaded gray areas. The insets in a) and b) show the early time value at $t = 0^+$ of the D_2-ratio a) and p_3-PPT ratio b), respectively, as function of the decoherence rate γ/J. Black lines are the perturbation theory results displayed in Eqs. (5.27) and (5.26).

5.7.2 Experimental demonstration in a trapped-ion quantum simulator

In the previous section, we showed in an idealized theoretical setting that entanglement is generated –and can be revealed via SR-entanglement conditions– at early times after a quantum quench. Here, we demonstrate this effect experimentally via the measurement of the SR-D_2 and SR-p_3-ppT condition using randomized measurement data taken at early times after quantum quench in a trapped ion quantum simulator (c.f. Ref. [10]). In particular, we show that the SR-D_2 condition and SR-p_3-PPT condition allow for a fine-grained detection of bipartite entanglement, in regimes where the corresponding global conditions [12] and conditions relying on the purities of different subsystems [10] are not conclusive.

In the experiment reported in Ref. [10], a one-dimensional spin-1/2-chain, consisting of $N = 10$ spins, was initialized in the Néel state $|{\uparrow\downarrow}\rangle^{\otimes 5}$ and time-evolved with the Hamiltonian H_{XY} [Eq. (5.21)] where the coupling parameter J_{ij} follows the approximate power-law decay $J_{ij} \approx J_0/|i-j|^\alpha$, with $\alpha \approx 1.24$, $J_0 = 420\text{s}^{-1}$. The Hamiltonian evolution exhibits a global $U(1)$-symmetry conserving the total magnetization of the system (i.e., $[H, \sum_i Z_i] = 0$). Symmetry-breaking terms (such as $\sigma_i^+\sigma_j^+ + \text{h.c.}$) are strongly suppressed due to a large effective magnetic field [10]. As detailed in Refs. [10, 11] weak decoherence effects are present in the experiment, including imperfect initial state preparation, local spin-flips and spontaneous emission during the dynamics, and measurement errors model as local depolarization. Note that coherent spin-flips do not preserve the global magnetization and block-diagonal form of the (reduced) density matrix. On the timescales accessed in the experiment, these effects are however very weak (causing in numerical simulations including the above decoherence model a purity mismatch of the order of 10^{-5} of the full 10-spin density matrix ρ vs. the projected one $\rho_Q = \sum_q Q_q \rho Q_q$ at $t = 5\text{ms}$).

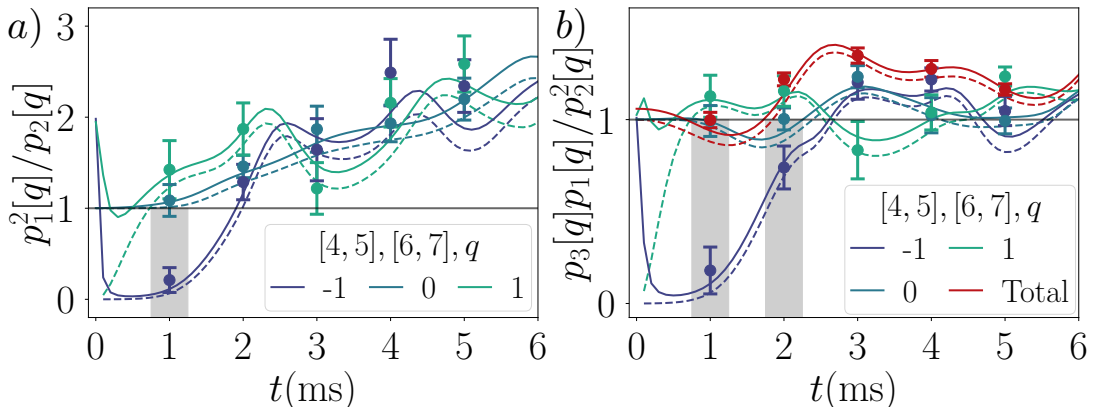

Figure 5.4: Experimental SR-entanglement detection in a trapped ion quantum simulator using data obtained in Ref. [10]. For a total system of $N = 10$ spins and subsystem $A, B = [4,5], [6,7]$, we present in a) the SR-D_2 ratio and b) SR-p_3-PPT ratio as a function of time for various symmetry sectors . In both panels, entanglement is detected in regimes where the corresponding global conditions do not reveal entanglement, as indicated in the shaded grey areas (values below unity). The points with error bars correspond to the values and uncertainties extracted from the experimental data from Ref. [10], whereas the dashed (solid) lines are theoretical simulations of unitary dynamics (taking decoherence effects into account), as detailed in Refs. [10, 11].

In Ref. [10] randomized measurements were performed at various times ($t = 0\text{ms}, \ldots, 5\text{ms}$) after the quantum quench. As described in detail in Ref. [11] (see also Chap. 6), we can use this data to estimate SR-PT moments and the SR entanglement conditions via classical shadow formalism [123]. In Fig. 5.4, we present the SR D_2 and p_3-PPT conditions in the different sectors, for a subsystem consisting of the neighbouring spins $A, B = [4,5], [6,7]$ and where the partial transpose is taken in the subsystem $A = [4,5]$. Similar to the results of the previous section, both conditions detect entanglement at short times in the sector $q = -1$. The corresponding global conditions, in particular the global p_3-PPT condition, do not reveal the presence of entanglement in this regime [see Fig. 5.4 b)].

The fact that the SR-D_2 condition can reveal the presence of entanglement is particularly interesting from an experimental point of view as it implies that entanglement can be detected from the estimation of only two moments of the partial transpose (in a sector). For the shadow estimation of $D_2(-1)$, it can be proven (Ref.[13]) $\sim 1.3 \times 10^6$ measurements would be sufficient to guarantee entanglement detection with a probability of 95%. While this represents an upper bound, valid irrespective of the quantum state in question, for the specific states in the experiment only 8×10^5 have been performed. The errorbars of the experimental are then drawn at 1.96σ where the standard error of the mean σ has been estimated for each data point using Jackknife resampling [8].

While the SR-D_2 condition requires only the estimation of first and second PT-moment, the third order SR-p_3-PPT condition [panel b)], allows to detect entanglement in an even wider time

[8] For normally distributed data with empirical mean μ, $\mu \pm 1.96\sigma$ defines a 95% confidence interval. While normal distribution is here not guaranteed a priori, we checked through additional numerical simulations of many experiments (with fixed number of runs per experiment) that errorbars of length 1.96σ indeed approximate a confidence interval with confidence level 95%.

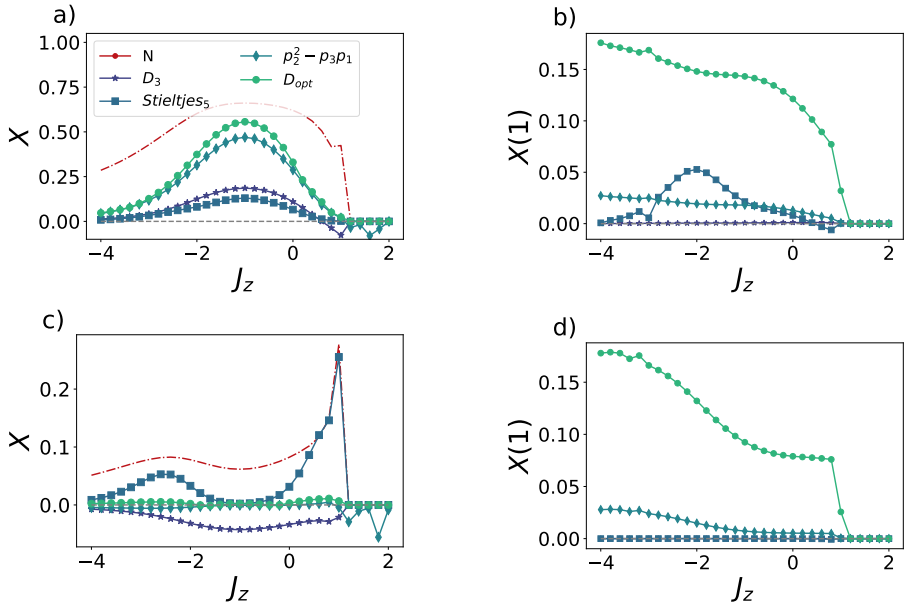

Figure 5.5: Entanglement conditions on the ground state of XXZ model. With $X \in [D_3, D_3^{\text{opt}}, Stieltjes_5, p_2^2 - p_3 p_1, N]$ we denote the conditions computed on ρ_A and with $X(1)$ the ones on $\rho_A(q=1)$. Chain length $L = 14$, subsystem length $\ell = 10$. We consider in a)-b) a connected subsystem A of length ℓ at the center of the chain; in c)-d) a disjoint interval A consisting of $\ell/2$ sites at the beginning and $\ell/2$ sites at the end of the chain. We set the sign of the inequalities such that a positive value indicates the violation of a PPT condition, and thus the presence of entanglement. To compare data of different magnitude we multiply the $Stieltjes_5$ condition by 10^2 in a), 10^5 in b), 10^4 in c), 10^5 in d).

window. In comparison to the global p_3-PPT condition [red curve in panel b)], this clearly demonstrates the benefit of taking symmetry-resolution into account.

5.7.3 Entanglement detection in the ground state of the XXZ model

The XXZ spin chain is a generalization of the Heisenberg chain including an anisotropy in the interaction along the z direction, whose Hamiltonian reads:

$$H = -J\left(\sum_i X_i X_{i+1} + \sum_i Y_i Y_{i+1} + J_z \sum_i Z_i Z_{i+1}\right). \tag{5.28}$$

We will fix $J = 1$ as energy unit: J_z sets the strength of the anisotropy along the z-axis. The phase diagram at zero temperature is known [145]: the system hosts an antiferromagnetic phase when $J_z < -1$, a Luttinger liquid for $J_z \in [-1, 1]$, and a ferromagnetic one for $J_z > 1$. We might expect that the entanglement conditions we described in the previous sections will detect that the state is not PPT in the range $J_z \in]-\infty, -1]$. Since the XXZ spin chain exhibits a $U(1)$ symmetry related to magnetization conservation, we can exploit the symmetry-resolved counterpart of the D_k conditions, the p_3-PPT and their optimized version D_3^{opt}.

The simulation results are shown in Fig. 5.5. We consider the ground state of an open chain of $L = 14$ sites. In a) and b), we select $\ell = 10$ sites in the middle as subsystem A and divide it in

two parts $A = A_1 \cup A_2$. We use the negativity as a reference to benchmark the efficiency of some entanglement conditions to detect entanglement between A_1 and A_2.

In Fig. 5.5a), we calculate the p_3-PPT, the D_3, the optimal D_3^{opt} condition and the Stieltjes condition using moments up to order five (see Appendix A.2). The convention we choose in the plot is that entanglement is detected whenever the value is positive. All the conditions work in most of the interval $J_z \in [-4, 1]$, where we expect entanglement to be sizeable, except for D_3 failing in the vicinity of $J_z = 1$. The presence of entanglement is confirmed by the calculation of the negativity (red line).

In Fig. 5.5b) we focus on the $q = 1$ sector. In this case, we observe that all conditions indicate the presence of at least a negative eigenvalue in the sector $\rho_A^{\Gamma}(q = 1)$ - that is, they are informative about which sector for the reduced density matrix contributes to violating PPT. In this specific instance, SR is however not fundamental in detecting entanglement beyond what non-SR conditions can.

In Fig. 5.5c) and d), we carry out the same analysis for disconnected partitions. We consider $A = A_1 \cup A_2$, where A_1 consists of the first $l/2$ sites and A_2 of the last $l/2$, and $L = 14, l = 10$. In Fig. 5.5c) for $J_z \sim -1.9$ all the quantities except $Stieltjes_5$ are below zero, thus not revealing entanglement even though the negativity is positive. In this plot, one can also see that, for $J_z < -2$, the optimized condition D_3^{opt} detects entanglement whereas both p_3-PPT and D_3 fail. This illustrates that the slight improvement obtained from the optimization in Sec. 5.4 (see Fig. 5.2) can be decisive to detect the entanglement of physically relevant states from the first three moments only.

5.7.4 Entanglement detection under constrained dynamics

As a third example, we study the detection of mixed-state entanglement in subsystems of constrained spin models after a global quantum quench. Such models have been realized experimentally with neutral atoms in optical tweezer arrays coupled to Rydberg states [146, 147]. Below we simulate an experiment, in which moments of the partially transposed density matrix are obtained from a classical shadow involving global random unitaries available in current experimental setups. In particular we demonstrate that periodic revivals of mixed state entanglement can be detected from the conditions D_3 and D_4 (Eqs. (5.11) and (5.12)) requiring only a small number of experimental runs.

We consider the Fibonacci chain with open boundary conditions described by the Hamiltonian

$$H = \Omega \sum_i \mathcal{P}_{i-1} X_i \mathcal{P}_{i+1} \,, \tag{5.29}$$

where $\mathcal{P}_i = |0\rangle_i \langle 0|$ are local projectors. As can be seen from (5.29), each spin undergoes independent Rabi-oscillations as long as the neighbouring spins are in their ground state $|0\rangle$. This constraint breaks the tensor product structure of the Hilbert space (as it the case in a lattice gauge

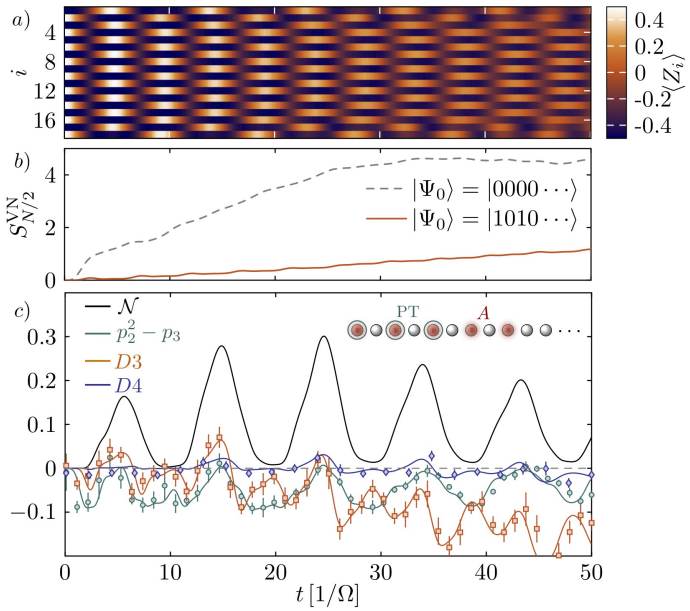

Figure 5.6: a) Coherent oscillations of the Z_i-expectation values in a quench with a 18-site Fibonacci chain from a staggered initial state: $|\Psi_0\rangle = |1010\ldots\rangle$. b) Von Neumann entropy of half partition of the chain as a function of time. c) Entanglement detection in a subsystem of 5 spins (corresponding to the red dots in the inset), with partial transpose taken with respect to the first three. All plotted curves are tuned so that positive values indicate entanglement. Revivals indicate periodic entangling and disentangling of spins. The points are obtained from a classical shadow consisting of 5000 global random unitaries. Error bars are obtained by repeating the procedure 20 times and estimating the standard error.

theory [148]). The model effectively resembles the experimental situation in [146] if the Rydberg atoms are driven close to resonance and neighbouring atoms cannot be simultaneously in the state $|1\rangle$ due to the Rydberg blockade mechanism. The Hamiltonian (5.29) has recently attracted great interest in the context of quantum many-body scarring [149, 150]. In particular, performing a quantum quench on special unentangled product states results in long-lived periodic revivals which have been attributed to the existence of quantum scarred eigenstates in the many-body spectrum [149].

In the following we study the conditions given in Eqs. (5.11) and (5.12), when a quench is performed from a product state that leads to kinetically constrained dynamics. To this end, the initial state $|\Psi_0\rangle = |10\rangle^{\otimes N/2}$ is time evolved with the Hamiltonian ((5.29)) up to $t = 50/\Omega$. Fig. 5.6 a) shows the local Z_i-expectation values exhibiting long-lived persistent oscillations. This striking departure from a thermalizing behaviour is also reflected in the slow growth of entanglement entropy (Panel b). We now analyse the time resolved behaviour of mixed state entanglement for a subsystem depicted in the inset of Fig. 5.6 c). The revivals in the negativity indicate that spins in the subsystem get periodically entangled and disentangled with each other. Interestingly, the p_3-PPT condition is unable to detect the revivals, while D_3 yields positive values at the first 3 peaks in the negativity. At later times, the D_3 fails to detect the entanglement present in the system, but this entanglement is still captured by D_4.

Finally, we investigate the required number of experimental runs in order to measure the con-

ditions up to given error bar. The classical shadow is constructed by sampling bit strings from the quantum state after applying a global random unitary on the subsystem A. At each point in Fig. 5.6 c), we collect 5000 bit strings in different random basis. Note that global random unitaries in Rydberg systems can be implemented via random quenches with local disorder potentials [151]. The entire estimation of the conditions is repeated 20 times in order to obtain statistical uncertainties. Note that statistical covariances among the measured moments $\mathrm{tr}(\rho^\Gamma)^n$ can give rise to nonuniform sizes for the error bars. In Fig. 5.6 c) we depict the 2σ error bars, showing that entanglement can be detected with a moderate experimental effort.

5.8 Conclusions and outlook

The study of entanglement has a long and prominent history in a variety of disciplines. And with the advent of serious quantum technologies, reliable entanglement generation is more important than ever. We provided a novel and principled approach to reliably detect bipartite entanglement between subsystem A and subsystem B. We have presented a set of inequality conditions D_k ($1 \leq k \leq 2^{|AB|}$). Each D_k is an inequality that involves the first k moments of the partially transposed density operator. Violation of a single inequality implies that the underlying density operator cannot have a PSD partial transpose. This in turn implies that the state must be entangled. Conversely, if the underlying state is not PPT, then, there must exist at least one D_k that is violated. This motivates a sequence of one-sided entanglement tests. Start with D_3 – the lowest non-trivial condition – and check whether it is violated. If this is the case, we are done. If not, we move on to the next higher condition (D_4) and repeat until we find a violation. For states having an extensive conserved quantity (such as total magnetization, in the case of spin systems), both the density matrix and its partial transpose have a block-diagonal structure [144]. In this case, it is advisable to apply these conditions directly to individual symmetry sectors of the partial transpose. The resulting sequence of symmetry-resolved conditions is stronger in the sense that lower order moments (of blocks of the partial transpose) suffice to detect entanglement. Importantly, this approach is not only conceptually sound, but also tractable from an experimental perspective. The classical shadows formalism [123] allows for reliably estimating moments of the partial transpose from randomized single-qubit measurements. We demonstrated how to include the experimentally relevant situation of non identical (however independent) copies in the analysis.For a derivation on error bounds and confidence intervals for D_2, with a natural extension to quantities involving higher order moments, the reader could refer to Ref. [13]. Empirical evaluations complement our theoretical findings. Applications to several theoretical models, as well as experimental data, demonstrate both tractability and viability of our approach.

The results provided in this chapter may open up several interesting future research directions. Firstly, the sequence of D_k's is designed to detect bipartite entanglement in a reliable and experimentally accessible fashion. A natural next step is to try to extend similar ideas to multipartite entanglement detection, e.g. using non–linear entanglement witnesses [152, 153]. Secondly,

the complete sequence of D_k's is used to answer a binary question: is the partial transpose negative or not? Entanglement measures, like the negativity, address entanglement in a quantitative fashion, but are also harder to estimate. Is it possible to use moments (or other density matrix functionals) to define entanglement measures that are experimentally tractable?

Another promising direction of research would be to try to detect and characterize phase transitions in quantum mechanical Hamiltonians at finite (non-zero) temperature. Quantum phase transitions at zero temperature originate from quantum fluctuations, whereas quantum phase transitions at finite temperature are due to thermal fluctuations. Following Ref. [154], quantum phase transitions at finite temperature can be studied using the negativity. It would be interesting to investigate whether low-order PT moments, intimately related to the negativity, can also be used to this end.

A

Additional information on entanglement detection conditions

A.1 Descartes' rule of signs

Let A be a Hermitian matrix of dimension d. Its eigenvalues $\lambda_1, \ldots, \lambda_d$ are the roots of the characteristic polynomial

$$P(t) = \det(A - t\,\mathbb{1}) = \prod_{i=1}^{d} (\lambda_i - t).$$

For convenience, let us now consider the polynomial $P(-t)$, which effectively replaces the positive eigenvalues of A by negative ones and vice versa. The coefficients of this polynomial can be expressed using the elementary symmetric polynomials in its roots, $e_i(\lambda_1, \ldots, \lambda_d)$, defined as

$$e_i(\lambda_1, \ldots, \lambda_d) = \sum_{1 \leq j_1 < \cdots < j_i \leq d} \lambda_{j_1} \ldots \lambda_{j_i},$$

for $i = 1, \ldots, d$ and with $e_0(\lambda_1, \ldots, \lambda_d) = 1$. This yields

$$P(-t) = \sum_{i=0}^{d} e_i(\lambda_1, \ldots, \lambda_d)\, t^{d-i}.$$

For a polynomial with real roots (as it is the case here), Descartes' rule of sign states that the number of positive roots is given by the number of sign changes between consecutive elements in the ordered list of its non-zero coefficients (see Ref. [155] and references therein). The matrix A is PSD iff $P(-t)$ has only negative roots, which by Descartes' rule is the case iff there is no sign change in the ordered list of its non-zero coefficients, i.e., iff $e_i(\lambda_1, \ldots, \lambda_d) \geq 0$ for all $i = 1, \ldots, d$,

since $e_0(\lambda_1, \ldots, \lambda_d) = 1$.

A.2 Stieltjes moment problem

Given a sequence of moments, $(m_n)_{n=0}^d$, the (truncated) Stieltjes moment problem consists in finding necessary and sufficient conditions for the existence [1] of a measure μ on the half-line $[0, \infty)$ such that

$$m_n = \int_0^\infty x^n \mathrm{d}\mu(x), \; \forall n \in \{0, \ldots, d\}. \tag{A.1}$$

Defining the matrices

$$A(n) = \begin{pmatrix} m_0 & m_1 & m_2 & \cdots & m_n \\ m_1 & m_2 & m_3 & \cdots & m_{n+1} \\ m_2 & m_3 & m_4 & \cdots & m_{n+2} \\ \vdots & \vdots & \vdots & \ddots & \vdots \\ m_n & m_{n+1} & m_{n+2} & \cdots & m_{2n} \end{pmatrix} \tag{A.2}$$

and

$$B(n) = \begin{pmatrix} m_1 & m_2 & m_3 & \cdots & m_{n+1} \\ m_2 & m_3 & m_4 & \cdots & m_{n+2} \\ m_3 & m_4 & m_5 & \cdots & m_{n+3} \\ \vdots & \vdots & \vdots & \ddots & \vdots \\ m_{n+1} & m_{n+2} & m_{n+3} & \cdots & m_{2n+1} \end{pmatrix}, \tag{A.3}$$

a solution to this problem can be stated as follows [156]. If d is odd – such that $d = 2k + 1$ for some integer k – there exists such a measure μ if and only if

$$A(k) \geq 0, \; B(k) \geq 0 \text{ and } (m_k, \ldots, m_{2k+1})^T \in \mathcal{R}[A(k)], \tag{A.4}$$

where, given a matrix M, the notation $M \geq 0$ indicates that M is PSD and $\mathcal{R}(M)$ denotes the range of M. If d is even – such that $d = 2k$ for some integer k – there exists such a measure μ if and only if

$$A(k) \geq 0, \; B(k-1) \geq 0 \text{ and } (m_{k+1}, \ldots, m_{2k})^T \in \mathcal{R}[B(k-1)]. \tag{A.5}$$

These solutions to the Stiltjes moment problem can be used to obtain entanglement conditions. Given $\lambda_1, \ldots, \lambda_r$ the eigenvalues of ρ^Γ for some density matrix ρ, let us define the (atomic) eigenvalue distribution function

$$\mathrm{d}\mu(x) = \sum_{i=1}^r \delta(x - \lambda_i),$$

where δ is the Dirac delta distribution. If ρ is PPT, this density function has support on $[0, \infty)$ and

[1] If such a measure exists, one may wonder whether it is unique or not. For our purposes, it will be enough to discuss only its existence.

reproduces the moments of ρ^Γ, as

$$m_n = \int_0^\infty x^n \mathrm{d}\mu(x) = p_n(\rho^\Gamma).$$

Therefore, according to the solution of the Stieltjes moment problem mentioned above, the moments of any PPT state necessary satisfy either condition (A.4) or (A.5), depending on the value of r. The violation of any of these conditions for a set of PT moments thus reveals that the corresponding state must be entangled. The range condition may require the knowledge of all the moments to be checked, but the PSD conditions can be broken into sets of simpler conditions. And some of them only involve low order moments. Indeed, it is well known (see e.g. [157]) that a matrix is PSD if and only if all its principal minors are non-negative. For instance, looking at the principal minor at the intersection of the first two rows and columns of $B(k)$, one obtains the condition $m_1 m_3 - (m_2)^2 \geq 0$. This condition is nothing but the p_3-PPT condition (which we know is useful to detect entanglement [12]). Extending this principal minor to the third row and column, one gets another PPT condition:

$$\det \begin{pmatrix} m_1 & m_2 & m_3 \\ m_2 & m_3 & m_4 \\ m_3 & m_4 & m_5 \end{pmatrix} \geq 0. \tag{A.6}$$

We call this condition Stieltjes$_5$. We illustrate in Sec. 5.7 (c.f. Fig 5.5) that this condition is also useful for entanglement. Numerical computations suggest that this condition is a powerful tool to detect the entanglement of random mixed states, in the sense that it detects more random entangled states than either p_3^{opt} or D_5. Not all Stieltjes moment conditions are this powerful, though. For instance, the principal minor condition for the first two rows and columns of $A(k)$ is trivial.

Note that, because we consider here an atomic density function, we have $m_0 = r$. We could naturally renormalize the density function so that $m_0 = 1$, but it would imply a re-scaling of the first moment, i.e., the trace of ρ^Γ, would be $1/r$. Since the partial transpose and the density function cannot be normalized at the same time, we chose to keep normalized partial transposes.

A.3 Optimizing conditions involving moments up to degree three

Given a PSD matrix A, with non-zero eigenvalues $\lambda_1, \ldots, \lambda_r$, for some $r \in [1, \dim A]$, consider the Lagrangian function

$$L(\lambda_1, \ldots, \lambda_r, C_1, C_2) \sum_{i=1}^r \lambda_i^3 + C_1 \left(\sum_{i=1}^r \lambda_i^2 - p_2 \right) + C_2 \left(\sum_{i=1}^r \lambda_i - p_1 \right), \tag{A.7}$$

where C_1 and C_2 are Lagrange multipliers.

Here we show that, for all $1 \leq r \leq \dim A$, the stationary points $(\lambda_1, \ldots, \lambda_r)$ of the Lagrangian function (A.7) are such that the variables λ_i can take at most two distinct values. These stationary points, for which the derivatives of the Lagrangian (A.7) with respect to each variable vanish, satisfy the set of equations

$$3\lambda_i^2 + 2C_1\lambda_i + C_2 = 0\,, \qquad i = 1, \ldots, r \tag{A.8}$$

$$\sum_{i=1}^{r} \lambda_i^2 = p_2\,, \tag{A.9}$$

$$\sum_{i=1}^{r} \lambda_i = p_1\,. \tag{A.10}$$

We first sum up Eq. (A.8) for all values of i and then insert Eqs.(A.9) and (A.10) into it. This yields

$$C_2 = \frac{-2C_1 p_1 - 3p_2}{r}.$$

Inserting this relation into Eq. (A.8) and considering this equation for two distinct values of i, say 1 and $k \neq 1$, one can eliminate the variable C_1 to get a relation between λ_1 and λ_k. After some algebra, one finds

$$\lambda_k = \lambda_1 \text{ or } \lambda_k = \frac{\lambda_1 p_1 - p_2}{\lambda_1 r - p_1}.$$

Since this argument holds for any $k \neq 1$, it must hold that the eigenvalues λ_i are either all equal or can only take two distinct values. In the first case, in which all the eigenvalues are equal, one obtains the isolated points $(p_2, p_3) = (1/r, 1/r^2)$ in Fig. 5.2 in the main text. In the second case, the rank r PSD matrices corresponding to the stationary points of the Lagrangian (A.7) have a spectrum with r_a degenerate eigenvalues λ_a and $r - r_a$ eigenvalues λ_b. Assuming, without loss of generality, $\lambda_a > \lambda_b$, one can show that the minimal value of the third moment is obtained when $r_a = r - 1$.

Bibliography

[1] M. A. Nielsen and I. L. Chuang, *Quantum Computation and Quantum Information* (Cambridge University Press, 2009).

[2] G. Benenti, G. Casati, and G. Strini, *Principles of Quantum Computation and Information* (WORLD SCIENTIFIC, 2004).

[3] L. Amico, R. Fazio, A. Osterloh, and V. Vedral, Rev. Mod. Phys. **80**, 517 (2008).

[4] N. Laflorencie, Physics Reports **646**, 1 (2016).

[5] M. Srednicki, Phys. Rev. Lett. **71**, 666 (1993).

[6] X. Dong, Nature Comm. **7**, 12472 (2016).

[7] S. Ryu and T. Takayanagi, Phys. Rev. Lett. **96**, 181602 (2006).

[8] M. Van Raamsdonk, Gen. Rel. and Grav. **42**, 2323 (2010).

[9] J. Maldacena and L. Susskind, Fortschr. Phys. **61**, 781–811 (2013).

[10] T. Brydges, A. Elben, P. Jurcevic, B. Vermersch, C. Maier, B. P. Lanyon, P. Zoller, R. Blatt, and C. F. Roos, Science **364**, 260 (2019).

[11] V. Vitale, A. Elben, R. Kueng, A. Neven, J. Carrasco, B. Kraus, P. Zoller, P. Calabrese, B. Vermersch, and M. Dalmonte, SciPost Phys. **12**, 106 (2022).

[12] A. Elben, R. Kueng, H.-Y. R. Huang, R. van Bijnen, C. Kokail, M. Dalmonte, P. Calabrese, B. Kraus, J. Preskill, P. Zoller, and B. Vermersch, Physical Review Letters **125**, 200501 (2020).

[13] A. Neven, J. Carrasco, V. Vitale, C. Kokail, A. Elben, M. Dalmonte, P. Calabrese, P. Zoller, B. Vermersch, R. Kueng, and B. Kraus, npj Quantum Inf **7**, 152 (2021).

[14] A. M. Kaufman, M. E. Tai, A. Lukin, M. Rispoli, R. Schittko, P. M. Preiss, and M. Greiner, Science **353**, 794 (2016).

[15] A. Lukin, M. Rispoli, R. Schittko, M. E. Tai, A. M. Kaufman, S. Choi, V. Khemani, J. Léonard, and M. Greiner, Science **364**, 256–260 (2019).

[16] R. Islam, R. Ma, P. M. Preiss, M. Eric Tai, A. Lukin, M. Rispoli, and M. Greiner, Nature **528**, 77 (2015).

[17] H. Li and F. D. M. Haldane, Phys. Rev. Lett. **101**, 010504 (2008).

[18] J. J. Bisognano and E. H. Wichmann, Journal of Mathematical Physics **17**, 303 (1976).

[19] R. E. Arias, D. D. Blanco, H. Casini, and M. Huerta, Phys. Rev. D **95**, 065005 (2017).

[20] C. Kokail, B. Sundar, T. V. Zache, A. Elben, B. Vermersch, M. Dalmonte, R. van Bijnen, and P. Zoller, Phys. Rev. Lett. **127**, 170501 (2021).

[21] C. Kokail, R. van Bijnen, A. Elben, B. Vermersch, and P. Zoller, Nature Physics **17** (2021).

[22] W. Zhu, Z. Huang, and Y.-C. He, Phys. Rev. B **99**, 235109 (2019).

[23] K. Audenaert, J. Eisert, M. B. Plenio, and R. F. Werner, Phys. Rev. A **66** (2002).

[24] A. Ferraro, D. Cavalcanti, A. García-Saez, and A. Acín, Phys. Rev. Lett. **100** (2008).

[25] D. Cavalcanti, A. Ferraro, A. García-Saez, and A. Acín, Phys. Rev. A **78** (2008).

[26] S. Marcovitch, A. Retzker, M. B. Plenio, and B. Reznik, Phys. Rev. A **80** (2009).

[27] V. Eisler and Z. Zimborás, New J. Phys. **16**, 123020 (2014).

[28] N. E. Sherman, T. Devakul, M. B. Hastings, and R. R. P. Singh, Phys. Rev. E **93** (2016).

[29] C. De Nobili, A. Coser, and E. Tonni, J. Stat. Mech. **2016**, 083102 (2016).

[30] H. Wichterich, J. Molina-Vilaplana, and S. Bose, Phys. Rev. A **80** (2009).

[31] A. Bayat, S. Bose, and P. Sodano, Phys. Rev. Lett. **105** (2010).

[32] A. Bayat, S. Bose, P. Sodano, and H. Johannesson, Phys. Rev. Lett. **109** (2012).

[33] T.-C. Lu and T. Grover, Phys. Rev. B **99**, 075157 (2019).

[34] P. Ruggiero, V. Alba, and P. Calabrese, Physical Review B **94**, 035152 (2016).

[35] X. Turkeshi, P. Ruggiero, and P. Calabrese, Phys. Rev. B **101** (2020).

[36] G. B. Mbeng, V. Alba, and P. Calabrese, J. Phys. A **50**, 194001 (2017).

[37] S. Wald, R. Arias, and V. Alba, J. Stat. Mech. **2020**, 033105 (2020).

[38] H. Shapourian, S. Liu, J. Kudler-Flam, and A. Vishwanath, PRX Quantum **2**, 030347 (2021).

[39] H. Shapourian, K. Shiozaki, and S. Ryu, Physical Review B **95**, 165101 (2017).

[40] H. Shapourian, P. Ruggiero, S. Ryu, and P. Calabrese, SciPost Physics **7**, 37 (2019).

[41] K. Shiozaki, H. Shapourian, and S. Ryu, Phys. Rev. B **95**, 205139 (2017).

[42] J. Kudler-Flam, H. Shapourian, and S. Ryu, SciPost Phys. **8** (2020).

[43] V. Eisler and Z. Zimborás, Physical Review B **93** (2016).

[44] V. Eisler and Z. Zimborás, New Journal of Physics **17**, 053048 (2015).

[45] E. Cornfeld, E. Sela, and M. Goldstein, Phys. Rev. A **99** (2019).

[46] P. Calabrese, J. Cardy, and E. Tonni, Physical Review Letters **109**, 130502 (2012).

[47] P. Calabrese, J. Cardy, and E. Tonni, Journal of Statistical Mechanics: Theory and Experiment **2013**, P02008 (2013).

[48] P. Calabrese, L. Tagliacozzo, and E. Tonni, J. Stat. Mech. **2013**, P05002 (2013).

[49] P. Calabrese, J. Cardy, and E. Tonni, Journal of Physics A: Mathematical and Theoretical **48**, 015006 (2014).

[50] P. Ruggiero, V. Alba, and P. Calabrese, Physical Review B **94**, 195121 (2016).

[51] O. Blondeau-Fournier, O. A. Castro-Alvaredo, and B. Doyon, J. Phys. A **49**, 125401 (2016).

[52] D. Bianchini and O. A. Castro-Alvaredo, Nucl. Phys. B **913**, 879–911 (2016).

[53] O. A. Castro-Alvaredo, C. De Fazio, B. Doyon, and I. M. Szécsényi, JHEP **2019** (2019).

[54] O. A. Castro-Alvaredo, C. De Fazio, B. Doyon, and I. M. Szécsényi, J. Math. Phys. **60**, 082301 (2019).

[55] F. Ares, R. Santachiara, and J. Viti, JHEP **2021** (2021).

[56] V. Eisler and Z. Zimborás, New J. Phys. **16**, 123020 (2014).

[57] M. J. Gullans and D. A. Huse, Phys. Rev. X **9**, 021007 (2019).

[58] J. Kudler-Flam, Y. Kusuki, and S. Ryu, JHEP **2020** (2020).

[59] M. Hoogeveen and B. Doyon, Nucl. Phys. B **898**, 78–112 (2015).

[60] B. Shi, X. Dai, and Y.-M. Lu, (2021), arXiv:2012.00040 .

[61] V. Alba and P. Calabrese, EPL **126**, 60001 (2019).

[62] A. Coser, E. Tonni, and P. Calabrese, J. Stat. Mech. **2014**, P12017 (2014).

[63] X. Wen, P.-Y. Chang, and S. Ryu, Phys. Rev. B **92** (2015).

[64] S. Murciano, V. Alba, and P. Calabrese, (2021), arXiv:2110.14589 .

[65] T.-C. Lu, T. H. Hsieh, and T. Grover, Physical Review Letters **125**, 116801 (2020).

[66] C. Castelnovo, Physical Review A **88**, 042319 (2013).

[67] O. Hart and C. Castelnovo, Phys. Rev. B **97** (2018).

[68] Y. A. Lee and G. Vidal, Phys. Rev. A **88** (2013).

[69] X. Wen, P.-Y. Chang, and S. Ryu, Journal of High Energy Physics **2016**, 12 (2016).

[70] X. Wen, S. Matsuura, and S. Ryu, Phys. Rev. B **93** (2016).

[71] U. Schollwöck, Ann. of Phys. **326**, 96 (2011).

[72] S. R. White, Phys. Rev. Lett. **69**, 2863 (1992).

[73] A. W. Sandvik and J. Kurkijärvi, Phys. Rev. B **43**, 5950 (1991).

[74] A. Peres, Physical Review Letters **77**, 1413 (1996).

[75] G. Vidal and R. F. Werner, Physical Review A **65**, 032314 (2002).

[76] M. B. Plenio, Phys. Rev. Lett. **95** (2005).

[77] R. Simon, Phys. Rev. Lett. **84**, 2726 (2000).

[78] H. Shapourian, K. Shiozaki, and S. Ryu, Phys. Rev. Lett. **118**, 216402 (2017).

[79] J. Eisert, V. Eisler, and Z. Zimborás, Physical Review B **97**, 1 (2018).

[80] H. J. Borchers and J. Yngvason, Journal of Mathematical Physics **40**, 601–624 (1999).

[81] H. Casini, M. Huerta, and R. C. Myers, Journal of High Energy Physics **2011** (2011).

[82] G. Wong, I. Klich, L. A. P. Zayas, and D. Vaman, Journal of High Energy Physics **2013** (2013), 10.1007/jhep12(2013)020.

[83] J. Cardy and E. Tonni, Journal of Statistical Mechanics: Theory and Experiment **2016**, 123103 (2016).

[84] H. Casini and M. Huerta, Class. Quant. Grav. **26**, 185005 (2009).

[85] M. Dalmonte, B. Vermersch, and P. Zoller, Nature Physics **14**, 827 (2018).

[86] G. Giudici, T. Mendes-Santos, P. Calabrese, and M. Dalmonte, Phys. Rev. B **98**, 134403 (2018).

[87] J. Zhang, P. Calabrese, M. Dalmonte, and M. A. Rajabpour, SciPost Phys. Core **2**, 7 (2020).

[88] R. Longo, P. Martinetti, and K.-H. Rehren, Rev. Math. Phys. **22** (2010).

[89] R. E. Arias, H. Casini, M. Huerta, and D. Pontello, Phys. Rev. D **98**, 125008 (2018).

[90] M. Mintchev and E. Tonni, JHEP **2021**, 204 (2021).

[91] M. Mintchev and E. Tonni, JHEP **2021** (2021).

[92] S. Hollands, (2019), arXiv:1904.08201 .

[93] I. Klich, D. Vaman, and G. Wong, Phys. Rev. Lett. **119** (2017).

[94] P. Fries and I. A. Reyes, Phys. Rev. Lett. **123** (2019).

[95] I. Peschel, Journal of Physics A: Mathematical and General **36**, L205 (2003).

[96] I. Peschel and V. Eisler, Journal of Physics A: Mathematical and Theoretical **42**, 504003 (2009).

[97] I. Peschel and M.-C. Chung, J. Phys. A **32** (1999).

[98] V. Eisler and I. Peschel, J. Phys. A **50**, 284003 (2017).

[99] V. Eisler and I. Peschel, J. Stat. Mech. **2018**, 104001 (2018).

[100] V. Eisler, G. Di Giulio, E. Tonni, and I. Peschel, J. Stat. Mech. **2020** (2020).

[101] G. Di Giulio and E. Tonni, J. Stat. Mech. **2020** (2020).

[102] P. Calabrese and F. H. L. Essler, J. Stat. Mech. **2010**, P08029 (2010).

[103] P. Calabrese, M. Campostrini, F. Essler, and B. Nienhuis, Phys. Rev. Lett. **104** (2010).

[104] V. Eisler, E. Tonni, and I. Peschel, J. Stat. Mech. **2019** (2019).

[105] G. Di Giulio, R. Arias, and E. Tonni, J. Stat. Mech. **2019** (2019).

[106] J. Argüello-Luengo, A. González-Tudela, T. Shi, P. Zoller, and J. I. Cirac, Nature **574** (2019).

[107] F. Parisen Toldin and F. F. Assaad, Phys. Rev. Lett. **121** (2018).

[108] T. Mendes-Santos, G. Giudici, R. Fazio, and M. Dalmonte, New J. Phys. **22**, 013044 (2020).

[109] I. H. Deutsch, PRX Quantum **1**, 020101 (2020).

[110] J. Preskill, Quantum **2**, 79 (2018).

[111] J. Eisert, D. Hangleiter, N. Walk, I. Roth, D. Markham, R. Parekh, U. Chabaud, and E. Kashefi, Nature Reviews Physics **2**, 382 (2020).

[112] M. Horodecki, P. Horodecki, and R. Horodecki, Physics Letters A **223**, 1 (1996).

[113] B. M. Terhal, Physics Letters A **271**, 319 (2000).

[114] N. Friis, G. Vitagliano, M. Malik, and M. Huber, Nature Reviews Physics **1**, 72 (2019).

[115] R. Horodecki, P. Horodecki, M. Horodecki, and K. Horodecki, Rev. Mod. Phys. **81**, 865 (2009).

[116] O. Gühne and G. Tóth, Physics Reports **474**, 1 (2009).

[117] K. Życzkowski, P. Horodecki, A. Sanpera, and M. Lewenstein, Phys. Rev. A **58**, 883 (1998).

[118] M. B. Plenio, Phys. Rev. Lett. **95**, 090503 (2005).

[119] P. Calabrese, J. Cardy, and E. Tonni, Phys. Rev. Lett. **109**, 130502 (2012).

[120] P. Calabrese, J. Cardy, and E. Tonni, Journal of Statistical Mechanics: Theory and Experiment **2013**, P02008 (2013).

[121] V. Eisler and Z. Zimborás, New Journal of Physics **16**, 123020 (2014).

[122] O. Blondeau-Fournier, O. A. Castro-Alvaredo, and B. Doyon, Journal of Physics A: Mathematical and Theoretical **49**, 125401 (2016).

[123] H.-Y. Huang, R. Kueng, and J. Preskill, Nature Physics , 1050 (2020).

[124] S. J. van Enk and C. W. J. Beenakker, Physical Review Letters **108**, 110503 (2012).

[125] A. Elben, B. Vermersch, M. Dalmonte, J. I. Cirac, and P. Zoller, Physical Review Letters **120**, 050406 (2018).

[126] A. Elben, B. Vermersch, C. F. Roos, and P. Zoller, Physical Review A **99**, 052323 (2019).

[127] L. Knips, J. Dziewior, W. Kłobus, W. Laskowski, T. Paterek, P. J. Shadbolt, H. Weinfurter, and J. D. A. Meinecke, npj Quantum Information **6** (2020), 10.1038/s41534-020-0281-5.

[128] A. Ketterer, N. Wyderka, and O. Gühne, Physical Review Letters **122**, 120505 (2019).

[129] Y. Zhou, P. Zeng, and Z. Liu, Physical Review Letters **125**, 200502 (2020).

[130] A. Ketterer, N. Wyderka, and O. Gühne, Quantum **4**, 325 (2020).

[131] A. Ketterer, S. Imai, N. Wyderka, and O. Gühne, arXiv:2012.12176 .

[132] G. De las Cuevas, T. Fritz, and T. Netzer, Communications in Mathematical Physics **375**, 105 (2020).

[133] M. Goldstein and E. Sela, Physical Review Letters **120**, 200602 (2018).

[134] J. C. Xavier, F. C. Alcaraz, and G. Sierra, Physical Review B **98**, 041106 (2018).

[135] N. Feldman and M. Goldstein, Physical Review B **100**, 235146 (2019).

[136] R. Bonsignori, P. Ruggiero, and P. Calabrese, Journal of Physics A: Mathematical and Theoretical **52**, 475302 (2019).

[137] M. T. Tan and S. Ryu, Physical Review B **101**, 235169 (2020).

[138] S. Fraenkel and M. Goldstein, Journal of Statistical Mechanics: Theory and Experiment **2020**, 033106 (2020).

[139] S. Murciano, G. D. Giulio, and P. Calabrese, SciPost Phys. **8**, 46 (2020).

[140] D. Azses and E. Sela, Physical Review B **102**, 235157 (2020).

[141] X. Turkeshi, P. Ruggiero, V. Alba, and P. Calabrese, Physical Review B **102**, 014455 (2020).

[142] S. Murciano, R. Bonsignori, , and P. Calabrese, SciPost Phys. **10**, 111 (2021).

[143] G. Parez, R. Bonsignori, and P. Calabrese, Phys. Rev. B **103**, L041104 (2021).

[144] E. Cornfeld, M. Goldstein, and E. Sela, Physical Review A **98**, 032302 (2018).

[145] A. O. Gogolin, A. A. Nersesyan, and A. M. Tsvelik, *Bosonization and Strongly Correlated Systems* (Cambridge Univ. Press, Cambridge, 2004).

[146] H. Bernien, S. Schwartz, A. Keesling, H. Levine, A. Omran, H. Pichler, S. Choi, A. S. Zibrov, M. Endres, M. Greiner, V. Vuletić, and M. D. Lukin, Nature **551**, 579 (2017).

[147] S. Ebadi, T. T. Wang, H. Levine, A. Keesling, G. Semeghini, A. Omran, D. Bluvstein, R. Samajdar, H. Pichler, W. W. Ho, *et al.*, Nature **595**, 227 (2021).

[148] F. M. Surace, P. P. Mazza, G. Giudici, A. Lerose, A. Gambassi, and M. Dalmonte, Phys. Rev. X **10**, 021041 (2020).

[149] C. J. Turner, A. A. Michailidis, D. A. Abanin, M. Serbyn, and Z. Papić, Nature Physics **14**, 745 (2018).

[150] W. W. Ho, S. Choi, H. Pichler, and M. D. Lukin, Phys. Rev. Lett. **122**, 040603 (2019).

[151] B. Vermersch, A. Elben, M. Dalmonte, J. I. Cirac, and P. Zoller, Physical Review A **97**, 023604 (2018).

[152] O. Gühne and N. Lütkenhaus, Phys. Rev. Lett. **96**, 170502 (2006).

[153] B. Jungnitsch, T. Moroder, and O. Gühne, Phys. Rev. Lett. **106**, 190502 (2011).

[154] T.-C. Lu and T. Grover, Phys. Rev. Research **2**, 043345 (2020).

[155] M. Bensimhoun, arXiv:1309.6664 .

[156] R. E. Curto and L. A. Fialkow, Houston J. Math. **17**, 603 (1991).

[157] C. D. Meyer, *Matrix Analysis and Applied Linear Algebra* (Society for Industrial and Applied Mathematics, 2000).

III

Symmetry-resolved entanglement in syntethic matter

This part is based on the following publications:

[1] *Symmetry-resolved dynamical purification in synthetic quantum matter*. V. Vitale, A. Elben, R. Kueng, A. Neven, J. Carrasco, B. Kraus, P. Zoller, P. Calabrese, B. Vermersch, M. Dalmonte, SciPost Physics 12 (3), 106 (2022).

[2] *Entanglement barrier and its symmetry resolution: theory and experiment*. A. Rath*, V. Vitale*, S. Murciano*, M. Votto, J. Dubail, R. Kueng, C. Branciard, P. Calabrese, B. Vermersch, arXiv 2209.04393 (2022)

6

Symmetry-resolved dynamical purification

6.1 Introduction

Symmetry and entanglement represent two cornerstones of our present understanding of many-body quantum systems. The former governs, e.g., the nature of phases of matter [1–3], while the latter characterizes different classes of quantum dynamics in and out-of-equilibrium [4–6]. Perhaps surprisingly, the intertwined role of these two pillars - falling under the umbrella of symmetry-resolved quantum information - has been relatively unexplored until comparatively recently [7–12]. Such connections are of immediate experimental interest in the context of quantum simulation and quantum computing. Aiming at the ultimate goal of engineering perfectly isolated quantum systems, experiments in synthetic quantum matter and quantum devices realize system dynamics where coupling to an external bath, whatever weak, is *ubiquitous* - two paradigmatic examples being quantum simulators [13, 14] and noisy intermediate-scale quantum (NISQ) devices [15]. In these settings, the microscopic dynamics is local, and is often captured by a master equation with global Abelian symmetries, related to observables such as magnetization or particle number. Against this background, it is an open question whether symmetry-resolved quantum information can reveal novel, generic classes of quantum dynamics that emerge as a genuine effect of the competition between unitary and incoherent dynamics that is epitomized by quantum simulators and NISQ devices. In fact, symmetry-resolved quantum information has never been studied in the context of open quantum systems.

Here, we develop a theory and an experimental probe protocol for symmetry-resolved quantum information dynamics in synthetic quantum matter and quantum devices. We are interested in the prototypical scenario depicted in Fig. 6.1a-b): an initial product state of a lattice model is subjected to the evolution of a $U(1)$ invariant dynamics, where coherent couplings (J) are stronger

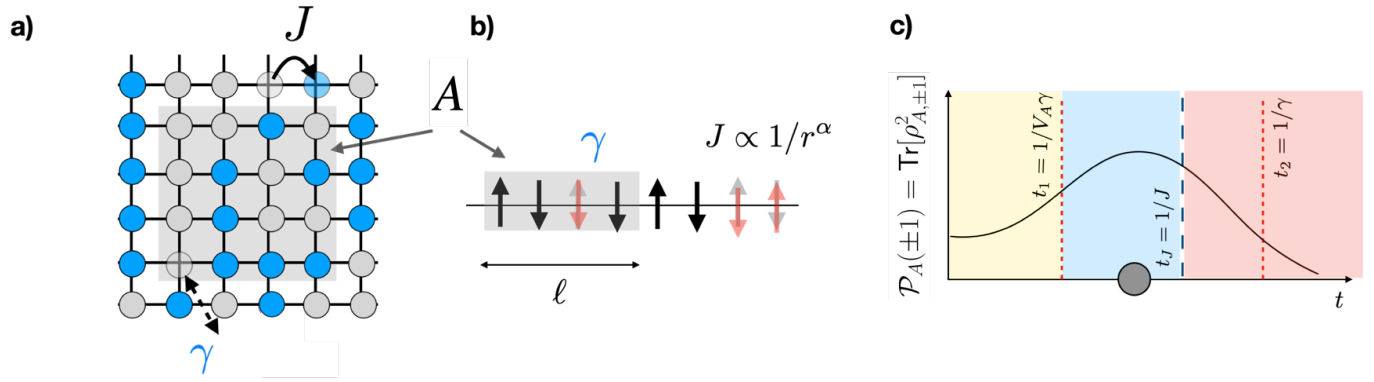

Figure 6.1: Evolution of symmetry-resolved entropies in NISQ devices. Panel *a,b)*: sketch of the models discussed in the main text. *a)*: free fermions on a square lattice, with tunneling matrix element J and one-body loss rate γ. *b)*: spin-1/2 chains with long-range XY exchange interactions, and single site spin relaxation rate γ. The grey areas represent the geometries of the A bipartition of linear length ℓ considered below. Panel *c)*: time evolution of the symmetry-resolved purity in the sector $q = \pm 1$, $\mathcal{P}_A(\pm 1) = \mathrm{tr}[\rho^2_{A,\pm 1}]$, in NISQ devices undergoing three distinct regimes (indicated by different colors, see text for their relations to microscopic timescales). The purity initially increases as a function of time, signalling dynamical purification (gray dot).

than incoherent ones (γ). Such scenarios are ubiquitous in current experiment settings, and encompass both interacting and free theories. They are realized in analogue quantum simulators as diverse as trapped ions [16], cold atoms in optical lattices [17], arrays of Rydberg atoms [18], and circuit quantum-electrodynamics settings [19]. Similarly, the interplay between coherent $U(1)$ dynamics and dissipation is of direct relevance to certain nascent quantum computers – those that implement two-qubit SWAP or phase gates with a conserved number of qubit excitations. Concrete examples include architectures based on superconducting qubits [20] and trapped ions [21].

Under these rather ubiquitous conditions, we show that a specific set of symmetry-resolved reduced density matrices undergo *dynamical purification* as a function of time. This phenomenon is strikingly different from purification to an uncorrelated steady state, because it does not come at the expense of quantum information. Using symmetry-resolved negativities, it can be addressed that entanglement remains finite and sizeable over the entire purification dynamics, both in its generic and symmetry-resolved formulation [1]. Furthermore, the scenario we are interested in is fundamentally different from (dissipative) state preparation protocols [23–25] (see below).

The dynamical purification we discuss is at odds with conventional expectations based on information dynamics in many-body systems: starting from low entropy states, Hamiltonian evolution is largely believed to lead to entropy increase, and similar considerations often apply to non-engineered dissipative evolution. What we show is that, for symmetric systems, there exist symmetry sectors [2] that evade this scenario. The reason behind this generic - and, we believe, surprising - exception is rooted into the so-far-unexplored combination of the competition between

[1] We note here that entanglement as witnessed by the negativity requires a different symmetry-resolution with respect to the reduced density matrix [22]. This is due to the presence of partial transposition.

[2] In fact, for continuous symmetries, a large majority of the symmetry sectors will display dynamical purification, albeit at different timescales.

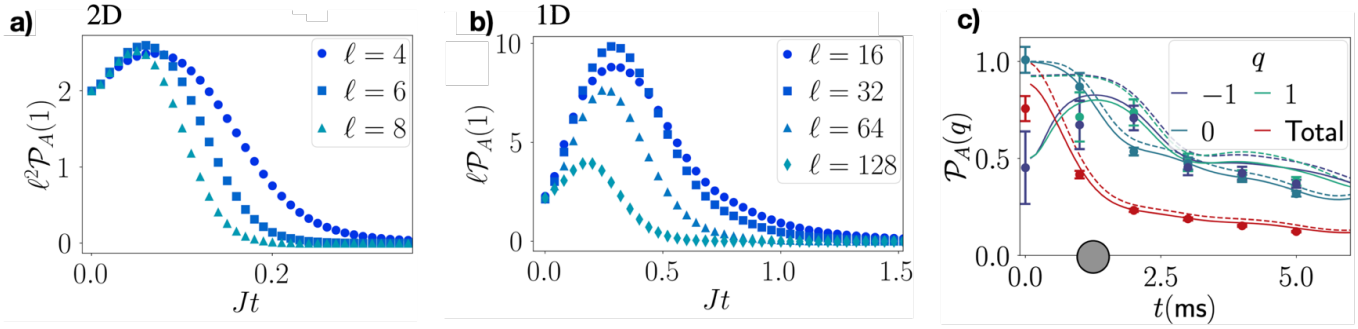

Figure 6.2: Evolution of symmetry-resolved entropies in NISQ devices. Panel *a,b)*: time evolution of the symmetry-resolved purity normalized by the partition volume, correspondent to a quantum quench from a charge-density-wave state, with the dynamics described in Fig.6.1a-b), respectively. At short times, decoherences induces a universal scaling behavior. Panel *c)*: symmetry-resolved purity for a long-range XY spin chain of $L = 10$ sites, with $\ell = 4$. The lines represent theoretical simulations, with (solid) and without (dashed) decoherence. Dynamical purification is only present in the first case. Circles represent experimentally reconstructed data from for the symmetry-resolved purity in the trapped ion experiment of Ref. [29]. Dynamical purification is experimentally observed for $q = -1$, and evident for $q = 1$ in agreement with both theory and numerics.

coherent and incoherent dynamics, and the presence of a global conserved charge in a many-body system.

In the exemplifying scenario we anticipated above, we let an initial product state evolve and observe that no purification takes place in the presence of only one of the two contributions (i.e. $J = 0$ or $\gamma = 0$). We note that symmetry plays a crucial role for the effect of such competition to arise, as the latter occurs in reduced density matrices restricted to specific symmetry sectors and is inaccessible in the absence of symmetry resolution. The fact that we need a global charge to be conserved and, most emphatically, that we predict unusual scaling laws for entanglement propagation (see below) allow us to designate dynamical purification as a genuine many-body effect. Thus, dynamical purification is fundamentally distinct from single-body phenomena known in the realm of quantum optics [26–28], such as collapses and revivals, where still purity can increase as a function of time for several reasons. From a more practical viewpoint, dynamical purification can be seen as a direct – and universal – signature of a dominant coherent dynamics in both quantum simulators and NISQ devices, thus providing a simple proxy to evaluate their functioning. Importantly, such phenomenon appears for a broad class of interacting theories, including Hubbard-like, long-range and even confining interactions.

The competition between coherent and incoherent processes reflects into the existence of two distinct dynamical regimes in terms of symmetry-resolved entropy scaling. At short times dissipation is the dominant effect and the symmetry-resolved entropy displays a *log-volume* behavior as function of the volume of the partition where it is computed. At intermediate time, it exhibits a *log-area* one, since coherent dynamics partly overcomes dissipation and enhances purity in given quantum number sectors. The corresponding change of dynamical behavior has dramatic consequences on the experimentally relevant symmetry-resolved purity: the latter quantity scales with

inverse volume and inverse area (Fig. 6.2a-b), respectively. Hence it provides an ideal proxy to diagnose scaling regimes during dynamical purification. For longer time scales, thermodynamics comes back into the game and all symmetry-resolved entropies show the standard extensive behavior in subsystem size [12].

The interplay between the two regimes can be illustrated in context of a simplified Markovian master equation for the symmetry-resolved reduced density matrix: within that framework, the presence of the coherent dynamics interferes with the action of dissipation and thus leads to a transient regime where entropy is soaked out of the symmetry-resolved reduced density matrix itself. We corroborate our theoretical framework with numerical simulations on a variety of experimentally relevant scenarios. In particular, we showcase the generality of dynamical purification by studying both one- and two-dimensional systems (some of them depicted in Fig. 6.1a-b) with partitions of different topologies, including both fermionic and bosonic degrees of freedom, and using different types of (weakly-entangled) initial states.

In order to connect our results to experiments, we develop a protocol to access symmetry resolved reduced density matrices building on the random measurement toolbox [30–36]. We show how experimentally demonstrated tools allow for accessing symmetry-resolved moments of symmetry-resolved reduced density matrices and symmetry-resolved Rényi entropies by means of post-selecting data. This procedure is very efficient and allows to reach system sizes that are considerably beyond what can be achieved via full-state tomography, when applicable (See Ref. [37] for a recent demonstration). We apply our protocol to the trapped ion experiment reported in Ref. [29], reconstructing both symmetry-resolved entropies and momenta of the symmetry-resolved reduced density matrix. The experiment reveals a sharp dynamical purification (Fig. 6.2c) which confirms our theoretical findings. This observation demonstrates the general applicability of our theoretical framework, and concretely illustrates the potential of utilizing symmetry as an enhanced probing tool in state-of-the-art settings.

This chapter is organized as follows. In Sec. 6.2, we specify the time evolution we are interested in, and develop a theory for the time evolution of both entropies and negativities in NISQ devices. We illustrate how entropies show distinct scaling behavior at short (log-volume) and intermediate (log-area) times, so that symmetry-resolved purities actually increase as a function of time (dynamical purification). We then argue that, along this purification, entanglement is typically preserved, so that purification does not take place at the expenses of quantum correlations. In Sec. 6.5, we present numerical results for both spin chains and fermionic systems supporting our theoretical findings. In Sec. 6.6, we discuss the protocol for the experimental measurement of symmetry-resolved entropies, and present a first application in the context of the trapped ion experiment, that supports the observation of dynamical purification. Finally, we draw our conclusions.

6.2 Time-evolution of symmetry-resolved entropies and negativities

In this section, we present a theoretical description of symmetry-resolved quantum information in NISQ devices. We are specifically interested in the short- to intermediate timescales, that is, before dissipation takes over the system dynamics overwhelming coherent effects.

We shall first discuss the generic setting and subsequently focus on a specific example that presents the generic features we are interested in: the existence of distinct regimes of entropy scaling, dynamical purification, and its interplay with entanglement. While, for the sake of clarity, most of the technical discussion will be based on illustrative examples, we point out that our conclusions are only relying on very generic conditions, that we now specify in the next section, 6.3. In the following, we will consider, for the sake of simplicity, $\hbar = 1$ and lattice constant $a = 1$.

6.3 Short-time dynamics: emergent purification

The system dynamics we are interested in features the following characteristics:

- a D-dimensional system, and a 'convex' partition A herein with smooth boundaries[3], volume $\mathcal{V}_A$ and area $\partial\mathcal{V}_A$;
- an initial state $|\psi_0\rangle$ which is a product state in real space;
- the full system dynamics shall be described by a Gorini-Kossakowski-Sudarshan-Lindblad (GKSL) master equation. In particular, we will be interested in Markovian time-evolution;
- the system Hamiltonian shall have a global symmetry G. For the sake of simplicity, we will consider $U(1)$ below [4]; most results are immediately extended to $\mathbb{Z}_N$ symmetries, and might also be applicable to the symmetry resolution of continuous non-Abelian groups when sectors are labelled by Abelian subgroups. We assume local (i.e., nearest-neighbor, one- and two-body) couplings, that are homogeneous in space. We define as J the energy scale associated to these terms. Below, we will discuss how sufficiently long-range interactions can also be included;
- dissipation shall instead be described by local (single-site) jump operators. For the sake of simplicity, it is assumed that all sites are affected by the same dissipative processes. Dissipation shall violate the symmetry G. We define as γ the energy scale associated to these terms,

[3] This assumption is only needed to a have simple count of the coherent processes. Essentially, we do not want to have sites of the complement that are accessible from two sites of the partition within first order perturbation theory.

[4] The treatment can be extended to local symmetries, and thus gauge theories. The latter case is more complicated due to the definition of reduced density matrices in Hilbert spaces without tensor-product structure. We consider a 1D case in the Sec. 6.5, that is closer in spirit to the case of global symmetries since Gauss law can be integrated exactly in that case.

that is, the bare inverse decay rate. Other sources of dissipation can in principle be introduced: as it will be clear below, we expect that their effects are not particularly interesting for the sake of our treatment.

Such assumptions are ubiquitous in the context of synthetic quantum systems, such as cold atoms in optical lattices or tweezers, trapped ions, and arrays of superconducting qubits. Engineering initial states in product state form (up to initialization errors) is of widespread practice, as this can be typically carried out by manipulating quantum states locally. The system dynamics is often local and associated to continuous symmetries, such as particle number or magnetization conservation. Dissipation is generically violating conservation laws associated to the latter quantities: examples include particle loss in cold atom Hubbard models, and fully depolarizing noise and spin relaxation in trapped ions and superconducting circuit architectures.

Most of the present experimental settings are able to access parameter regimes where dissipation is weaker than the coherent dynamics, with the ratio γ/J ranging from 10^{-3} to 10^{-1} [14, 17]. We will focus explicitly on this parameter regime, and consider dissipation as a perturbation on the top of the coherent dynamics.

Under these assumptions, one can identify three timescales: two intrinsic, and one typical of the subsystem one is interested in. The first one $t_J = 1/J$ is associated to coherent local dynamics. The second one $t_2 = 1/\gamma$ is instead related to a timescale after which (on average) all sites within the partition have undergone a quantum jump. The last one, typical of the subsystem A, $t_1 = 1/(\mathcal{V}_A\gamma)$ is related to the timescale required to observe a single quantum jump within A.

Let us mention here, that in contrast to the notion of dissipative state preparation [23–25], we study here a given evolution of a physical system. That is, we are not engineering the coupling to the bath to drive the system into a desired state, but rather, discuss the dynamics corresponding to naturally present quantum noise. In addition, whereas dissipative state preparation can be utilized to obtain as a unique stationary state a highly entangled many-body state, or states whose subsystems can be very pure, the situation we consider here is not related to long-time dynamics. We will indeed show that dynamical purification occurs at intermediate times.

For times $t \gg t_2$, ρ_A will be completely mixed, also in its symmetry-resolved sectors because the dissipative contribution is overwhelming. Similarly, for regimes where $\gamma \gg J$, the system dynamics is dominated by incoherent processes. A promising regime to observe competition between coherent and incoherent dynamics is thus $\mathcal{V}_A\gamma, J > \gamma$, and is the one we will consider below. We remark that this is a rather generic situation for quantum simulators of many-body systems, where one tries to realize dynamics that are as coherent as possible ($J > \gamma$) for large number of degrees of freedom ($\mathcal{V}_A \gg 1$). This second condition is not needed in general: however, it considerably simplifies the theoretical treatment, as it allows to treat timescales in a way that is easier to interpret. We will thus assume that below, and comment on that at the end of the section. In Sec. 6.5, we will discuss in more details in which experimental platforms such conditions are met.

We emphasize there that the presence of three dynamical regimes (that, as we will show below,

are captured by different entropy scaling) stems from purely geometrical considerations: while Hamiltonian dynamics is acting solely at the boundary between the partitions[5], incoherent processes are instead present over the entire volume of the partition one is interested in. As such, the short-time evolution of symmetry-resolved density matrices will be dictated by this competition, and is expected to be largely insensitive to other characteristics, including the partition geometry and topology, and (to a weaker extent) the initial state. The theoretical apparatus discussed in the next section can be adapted to incorporate such generic features. We nevertheless opted to focus on a simple, yet paradigmatic example, and defer the demonstration of generality of symmetry-resolved dynamical purification to the numerical experiments discussed in Sec. 6.5.

6.3.1 Explicit example: hard-core Bose-Hubbard model in 2D

For the sake of clarity and to make the connections with the numerical experiments below more evident, we start by focusing on a specific instance, and return to the general case at the end of the section. We consider a model of hard-core bosons hopping on an infinite 2D square lattice, described by the Hamiltonian

$$H = \frac{J}{2} \sum_{<i,j>} (b_i^\dagger b_j + \text{h.c.}). \tag{6.1}$$

Here, b_j ($b_j^\dagger$) is the bosonic annihilation (creation) operator at site j such that $n_j = b_j^\dagger b_j$ gives the number operator for that site. The Hamiltonian dynamics conserves the total number of bosons, and is thus $U(1)$ invariant. The system time-evolution is described by a master equation:

$$\partial_t \rho = -i[H, \rho] + \sum_j \gamma \left[b_j \rho b_j^\dagger + b_j^\dagger \rho b_j - \frac{1}{2}\{b_j b_j^\dagger + n_j, \rho\} \right] \tag{6.2}$$

where the second term describes single particle loss and gain processes with decay rate γ. The full dynamics is schematically depicted in Fig. 6.3a. While we will keep generality in the theory part with respect to the possible dissipation mechanisms, in the numerical examples below, we will only consider loss terms, as those are more readily accessible experimentally.

We investigate the dynamics starting from a charge-density wave (CDW), with alternating empty (grey) and filled (blue) sites (see Fig.6.3b). Within this state, we consider the reduced density matrix ρ_A corresponding to a rectangular partition A of size $L_x \times L_y$. Let $Q = \sum_{j\in A} n_j - \frac{1}{2} L_x L_y$ the number of bosons in the partition A above half-filling. Note that, while the full time evolution breaks $U(1)$ invariance, the reduced density matrix ρ_A preserves its block-diagonal form: this is more conveniently seen when interpreting Eq. (6.2) as a collection of quantum trajectories, each corresponding to the solution of a stochastic Schrödinger equation. Within each trajectory, the total number of particles at each time t is well defined: a single quantum jump only changes that value by an integer value. Following the previous section, we denote such symmetry-resolved

[5] In the case of sufficiently short ranged power-law interactions, such actions is extended to the few sites close to the boundary.

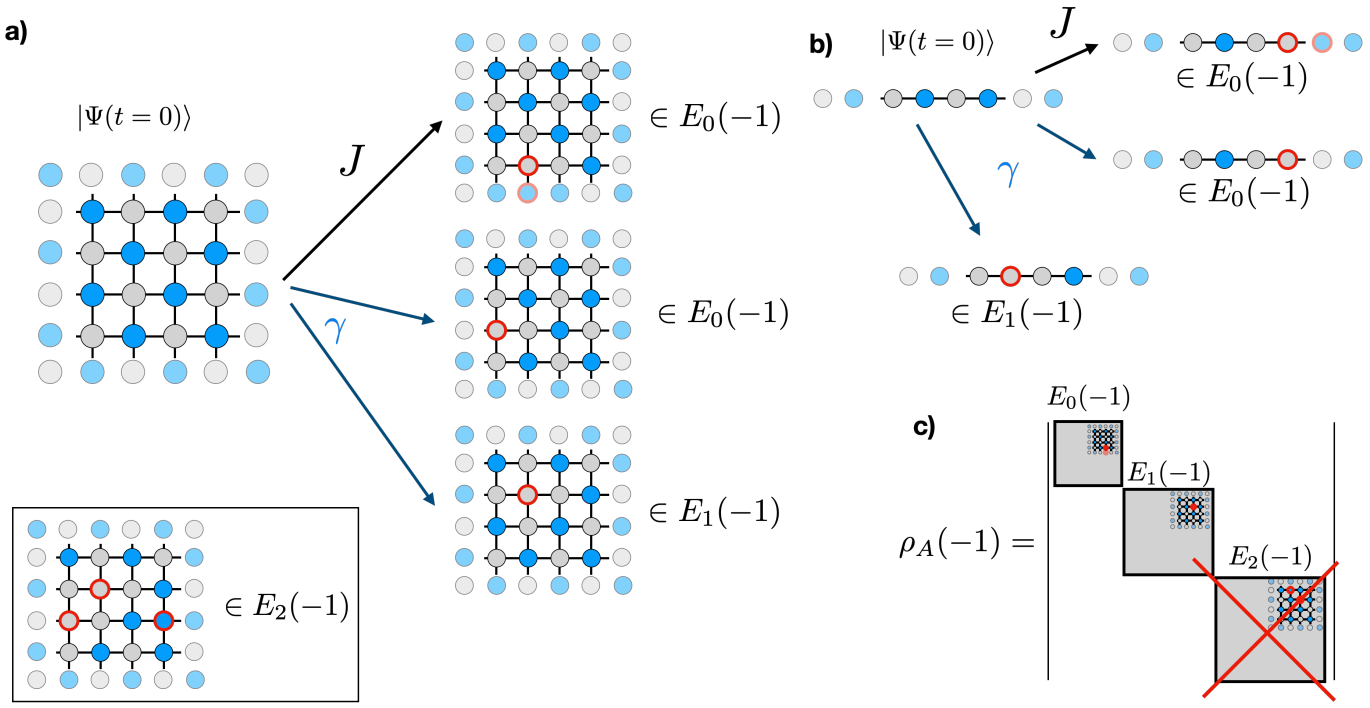

Figure 6.3: Schematics of the short-time dynamics in lattice models considered here; we show here the sector with $q = -1$. Panel *a*: the system is defined on a square lattice. The initial state is a charge-density wave $|\Psi\rangle$: grey and blue circles represent empty and full sites, respectively. At short time, the evolution involves states belonging to the E_0 and E_1 subspaces only (see examples, where sites circled in red are the ones changed with respect to $|\Psi\rangle$). The influence of the rest of the Hilbert space E_2 on the system dynamics is neglected, as accessing these states will require at least 3 proceeses starting from $|\Psi\rangle$. Panel *b)*: same as in panel a, but for the 1D case. Note that, in the following sections, several partition topologies will be discussed. Panel *c)*: structure of the time evolved reduced-density matrix. At short times, it is further block-diagonal in both E_0 and E_1, where the E_2 sector is traced away.

reduced density matrices as $\rho_A(q)$.

We are interested in short time evolution, where dissipation and coherent dynamics strongly compete. Specifically, we focus on timescales accessible within perturbation theory, that is,

$$J^2t^2, t\gamma \ll 1.$$

Therefore, we can solve Eq. (6.2) in second order in t to obtain the time-evolved density matrix $\rho(t)$ as a function of the initial state $\rho(0)$ [38]. We focus on the $q = -1$ sector of the reduced density matrix, that is, the one where the number of bosons in the partition is decreased by 1 with respect to half-filling. At short times, this is the most populated sector that does contribute to the initial state. We will comment on the other sectors below. Within this framework, we assume that only the diagonal elements of the reduced density matrix are affected by the time evolution. This assumption can be proven for initial states that are product states in real space.

We now divide $\rho_A(-1)$ into three blocks, schematically depicted in Fig. 6.3:

1. $E_0(-1)$: states that are connected to the CDW by a single hopping process: these states differ from the CDW by a single occupied site at the boundary. We denote the $(L_x + L_y)$ diagonal

eigenvalues of these states as $\lambda_k^{E_0}$;

2. $E_1(-1)$: states that are connected to the CDW by a single pump process in the bulk; these states differ from the CDW by a single empty site in the bulk. We denote the $(L_x-2)(L_y-2)/2$ diagonal eigenvalues of these states as $\lambda_k^{E_1}$;

3. $E_2(-1)$: states that are not connected to the CDW by a single tunneling or pump process. We denote the diagonal eigenvalues of these states as $\lambda_k^{E_2}$. For two-body interacting Hamiltonians, these states will be accessed only in third order perturbation theory.

At second order in perturbation theory (the lowest order relevant to the present case), one has the following scaling of the eigenvalues of $\rho_A(-1)$:

$$\lambda_k^{E_0} = (J^2t^2+\gamma t)/A(t),\ \lambda_k^{E_1} = \gamma t/A(t) \tag{6.3}$$

with $\lambda_k^{E_2}=0$, and

$$A(t) = \gamma t(L_xL_y-4)/2 + J^2t^2(L_x+L_y) \tag{6.4}$$

We can now compute the time-evolution of the symmetry-resolved entanglement entropies. At short times $t < t_1$, only dissipation is relevant. In particular, the rank of the reduced density matrix will be (L_xL_y), and the corresponding Renyi-2 entropy results:

$$S_A^{(2)}(q=-1) \propto \log[L_xL_y] \qquad \text{for } t \ll t_1,\ L_x, L_y \gg 1 \tag{6.5}$$

and is time-independent. The corresponding purity is:

$$\mathcal{P}_A(-1) \propto 1/[L_xL_y]. \tag{6.6}$$

It is worth noting that such 'log-volume' regime is valid at arbitrarily small times, the simple reason being that the initial state has no component in the $q=-1$ subspace.

At intermediate times $t_1 < t < t_J$, tunneling affects the system dynamics. While unitary time evolution generically leads to further information propagation and, correspondingly, entropy production, here, the opposite takes place: the symmetry-resolved density matrix *purifies* as a function of time, i.e., the purity increases and the entropy decreases. The reason for this phenomenon stems from the natural competition between volumetric and perimetral contributions to the system dynamics: while dissipation has an effect that scales with the volume of the partition, and thus populates a number of eigenvalues that are proportional to the volume itself, short-time coherent dynamics is related to boundary effects, and thus favors a much smaller number of states within the Hilbert space of the partition.

In order to elucidate this effect, we observe that our reduced density matrix is already normal-

ized, and compute

$$\mathcal{P}_A(-1) = \frac{t^2}{A(t)^2}[(L_x + L_y)(J^2 t + \gamma)^2 + (L_x - 2)(L_y - 2)\gamma^2]$$

that, in the large volume limit becomes

$$\mathcal{P}_A(-1) \;\simeq\; 1/(L_x + L_y) \quad \text{for} \quad t_J > t > t_1.$$

The corresponding Renyi-2 entropy follows a 'log-area' scaling:

$$S_A^{(2)}(q = -1) \propto \log[L_x + L_y] \quad \text{for} \quad t_J > t > t_1.$$

This implies that the transition between the two regimes is characterized by an emergent purification, that transits the system from a purity that is inversely proportional to the volume of the partition, to one that is inversely proportional to its surface. Note that the explicit time evolution can be computed from the previous equation, and in principle, the position of the 'maximum' of the purification can be extracted. While the corresponding formulas reveal no more physical insight, they signal the fact that the purification time decreases as the partition size increases. Due to the condition $t_J < t_2$, it is not possible to analytically compute the $\mathcal{V}_A \to \infty$ limit; we nevertheless expect dynamical purification to systematically decrease with the partition size, as a consequence of the area versus volume competition.

The calculation above can be straightforwardly generalized to any dimension, modulo the conditions mentioned at the beginning of the section, under the assumption that dynamics is acting non-trivially at the boundary (e.g., a state with a layer of empty sites at the boundary will not experience any meaningful coherent evolution at short times in the $q = -1$ sector). The corresponding scaling behavior decomposes into three regimes:

$$\mathcal{P}_A(-1) \propto \begin{cases} 1/\mathcal{V}_A & t_1 \gg t \geq 0 \text{ (short time)}, \\ 1/(\partial \mathcal{V}_A) & t_J > t > t_1 \text{ (int. time)}, \\ 1/2^{\mathcal{V}_A} & t \gg t_J \text{ (long time)}. \end{cases} \tag{6.7}$$

This equation succinctly describes the dynamical scaling regimes depicted in Fig. 6.1. Starting from an unsurprising short time behavior (top case), the system purifies at intermediate time scales (center case) before eventually getting fully mixed (bottom case) due to both coherent and incoherent system dynamics.

6.3.2 General remarks: nature of interactions, initial state, and dissipation

In the explicit example before, we have focused on the most populated sector of the reduced density matrix not present in the initial state, we expect dynamical purification to occur also

in other sectors - with, however, a weaker effect due to higher order perturbative processes. The presence of long-range interactions that decay fast enough (at most as power law) shall not change this picture at the qualitative level: however, it will lead to a renormalization of the timescale t_J. Importantly, long-range interactions will not modify the structure of the Hilbert subspaces discussed above.

While we have focused on purities, additional information can in principle be obtained from the population of the different sectors (denoted with $A(t)$ above) as well. One example is equilibration at long-times: this is beyond the perturbative treatment we have developed, and will be discussed in the next sections in both simulations and experiments.

The treatment above is specific to an initial state: however, the competition between volumetric and perimetral contributions is in fact generic to a much broader set of experimentally relevant configurations. For the case of pure states, dynamical purification shall occur as long as the initial state is separable or weakly entangled, as we show in one of the fermionic examples below. For highly entangled initial states, the theory above is not immediately applicable. Below, we will discuss a 1D numerical example, where the initial state has $\log(\ell)$ entanglement: in that case, we observe no purification. It is also important to stress that, while we have assumed $\gamma\mathcal{V}_A > J$, this is technically not needed at all: indeed, since dissipation acts already at first order in perturbation theory, there exists always a time scale for which $\gamma\mathcal{V}_A > J^2 t$. In fact, the size of the partition is irrelevant, as long as it can host significant dynamics within a given symmetry sector.

Most importantly, dynamical purification is present also for initial states that are globally mixed. In those cases, this is simply due to the fact that the coherent dynamics selects a subset of states in $\rho_A(-1)$ that are populated due to coupling to $\bar{A}$. The extent of the dynamical purification depends on the details of the action of the Hamiltonian on the initial state: we will investigate a specific scenario below while discussing trapped ion experiments.

Another aspect that is worth discussing is, which type of noise leads to dynamical purification. The noise we have considered here has two characteristics: (i) it is described by a Markovian master equation, and (2) it is quantum noise, as testified by the fact that it is described by non-hermitian jump operators. While these conditions are typically very well satisfied when describing the dynamics of cold atoms in optical lattices using a master equation, we find useful to provide a short discussion of these two elements in view of possible applications to other settings.

The first assumption above is delicate. Since we are interested in intermediate time dynamics, it is reasonable to expect that our findings will not be affected by a bath featuring short-lived memory effects, as long as the weak system-bath approximation (that we nevertheless consider, since $\gamma \ll J$) holds. However, more complicated bath structures including strong memory effects - such as a low-temperature Ohmic bath - cannot be immediately connected to the physical picture we present here.

The second assumption above is crucial: Hermitian jump operators (such as those, for instance, describing classical noise) would not lead to any dynamical purification. This can be easily seen by considering the action of dephasing on the various sectors of the symmetry-resolved

reduced density matrix: for the type of initial states we consider, the latter will not affect populations. This implies that entropy will be dominated by coherent dynamics, thus increasing with time. The relevance of the first assumption can potentially be exploited as a diagnostic in the context of quantum noise tomography; interestingly enough, such a probe would be very sensitive, as the effects we describe can be present for very small values of γ, and can be tuned by changing the volume of the partition in numerical simulations as well as in experiments.

Finally we find it useful to add two comments framing the physics we observe in the context of open quantum systems (especially since the primary physical platform we are interested in are nothing but many-body quantum optical systems, as exemplified by the experimental results below). First, we observe that the effective dynamics describing the evolution of ρ_A can be interpreted as the time evolution of a density matrix of a system coupled to a bath. This provides an additional viewpoint on the phenomenon we are interested in, that could be of help to translate it to other contexts (for instance, in case the two partitions are made of two different types of degrees of freedom, e.g., describing light-matter interactions). A detailed discussion of this fact is provided in the appendix, together with a proof of the fact that such effective dynamics is Markovian. Second, we point out that the phenomenology we describe here is fundamentally distinct from other instances of open system dynamics that may feature a decrease in entropy. One example here are revivals in the Jaynes-Cummings model [27] (and similar effects in the context of non-Markovian dynamics of single spins coupled to cavity modes): there, the phenomenon one observes is intrinsically few body, and has no relation whatsoever with (continuous) symmetries. This fundamental difference is clearly apparent into the fact that the universal regimes we have proposed have not been reported so far in those contexts.

6.4 Negativity over dynamical purification

While the system purifies at short time, due to its coupling to the environment, it cannot be established *a priori* whether this is associated to a loss of shared entanglement between the partition and its complement. For instance, dynamical purification (with or without symmetry resolution) can also occur at long times in systems under the presence of dissipation only: a typical example is relaxation to a vacuum state, that is driven by a single jump operator, and leads to a trivial state, with no left-over correlations between A and B, and within A. Below, we show explicitly how symmetry-resolved dynamical purification is drastically distinct from this mechanism: In particular we show how not only entanglement between A and B is generated as a function of time, but also that, in any given symmetry sectors (now labeled by quantum number differences), entanglement remains finite and sizeable (negativity of order 1) over the entire purification process. This is a key element that characterizes this symmetry-resolved phenomena, and we will show below how this is also captured within perturbation theory.

We study the entanglement dynamics for two connected partitions A and B of a spin (or hard-core boson) system, as governed by Eq. (6.2), in a regime where the partition A undergoes dy-

namical purification. For the sake of simplicity, we will deal explicitly with the 1D case analog to the setup described above (see Fig. 6.3b), and restrict the decoherence channels to particle loss, as this will allow us to keep our notations compact. Our findings are however general, as illustrated in the next section for various geometries and partition configurations.

In contrast to the situation of dynamical purification, the key features of short-time entanglement dynamics of the partial transpose reduced density matrix can already be captured by solving Eq. (6.2) in first-order perturbation theory, i.e. by studying the dynamics of $\rho(t)$ in first order in $t \ll 1/(\gamma N), 1/J$ ($\ll 1/\gamma$). We rewrite this as

$$\rho(t) = \rho(0) - i[H, \rho(0)]t + \gamma t \sum_j \left(b_j \rho(0) b_j^\dagger - \tfrac{1}{2} b_j^\dagger b_j \rho_0 - \tfrac{1}{2} \rho_0 b_j^\dagger b_j \right). \tag{6.8}$$

Consider for concreteness that the even sites $2m$, $m = 1, \ldots, N/2$ are occupied and, $N_A = N_B$ is even, the density matrix in first-order perturbation theory can be re-expressed as [6]

$$\rho(t) = \left(1 - \frac{N\gamma t}{2}\right) \rho(0) + Jt(-i b_{N_A+1}^\dagger b_{N_A} \rho(0) + h.c) + \gamma t \sum_{m=1}^{N/2} b_{2m} \rho(0) b_{2m}^\dagger + \ldots \tag{6.9}$$

which corresponds to a diagonal part parametrized by the decoherence rate γ, and a pair of off-diagonal elements associated with the hopping J. Note that there is no diagonal contribution due to the hopping, as this only appears in next-to-leading order as discussed above. Taking the partial transpose of Eq.(6.9) leads to

$$\rho^{T_A}(t) = \left(1 - \frac{N\gamma t}{2}\right) \rho(0) + Jt(-i b_{N_A+1}^\dagger \rho(0) b_{N_A}^\dagger + h.c) + \gamma t \sum_{m=1}^{N/2} b_{2m} \rho(0) b_{2m}^\dagger, \tag{6.10}$$

which has a 3-block structure associated with the quantum number $\tilde{q} = q_A - q_B$

$$\begin{aligned}
\rho^{T_A}(\tilde{q} = 0, t) &= \left(1 - \frac{N\gamma t}{2}\right) \rho(0) \\
\rho^{T_A}(\tilde{q} = -1, t) &= \gamma t \sum_{m=1}^{N_A/2} b_{2m} \rho(0) b_{2m}^\dagger + + Jt(-i b_{N_A+1}^\dagger \rho(0) b_{N_A}^\dagger + h.c) \\
\rho^{T_A}(\tilde{q} = 1, t) &= \gamma t \sum_{m=N_A/2+1}^{N} b_{2m} \rho(0) b_{2m}^\dagger.
\end{aligned} \tag{6.11}$$

The sector $\tilde{q} = 0$ corresponds to the initial state component, has a weight $\mathrm{tr}(\rho_{\tilde{q}=0}^{T_A}(t))$ of order 1, and features no entanglement. The sector $\tilde{q} = -1$, corresponding to the situation where the A partition loses one excitation with respect to partition B, has the richest structure, representing the interplay between particle loss from A and coherence dynamics (hopping from A to B). Finally,

[6] For the sake of clarity, we do not include intra-partition hopping terms: at lowest order, their only effect is to renormalize the dynamics in the $\tilde{q} = 0$, that we are not immediately interested here

the last sector $\tilde{q} = 1$ represent decoherence events occurring in the B partition. In each sector, we can calculate the spectrum

$$\tilde{\lambda}(\tilde{q}=0,t) = \left(1-\frac{N\gamma t}{2}\right) \tag{6.12}$$

$$\tilde{\lambda}^{(m=1,\ldots,\frac{N_A}{2}-1)}(\tilde{q}=-1,t) = \gamma t \tag{6.13}$$

$$\tilde{\lambda}^{(m=\frac{N_A}{2},\frac{N_A}{2}+1)}(\tilde{q}=-1,t) = (\gamma \pm \sqrt{\gamma^2+4J^2})\frac{t}{2} \approx (\frac{\gamma}{2} \pm J)t \tag{6.14}$$

$$\tilde{\lambda}^{(m=1,\ldots,\frac{N_B}{2})}(\tilde{q}=1,t) = \gamma t, \tag{6.15}$$

where, in the last part of the third line, we have neglected the term $\gamma^2 \ll J^2$.

The existence of a negative eigenvalue $\tilde{\lambda}^{(m=N_A/2)}(\tilde{q}=-1) = -Jt + \gamma t/2 \approx -Jt < 0$ demonstrates that the state is entangled, and remains so over dynamical purification. After normalization, we obtain the symmetry-resolved negativity

$$\mathcal{N}(\tilde{q}=-1) \approx \frac{2Jt}{N_A\gamma t} = \frac{2J}{N_A\gamma} \tag{6.16}$$

that features a characteristic $1/\gamma$ scaling (that is reminiscent of the fact that this is a perturbative effect). Interestingly, the short-time behavior of the negativity is constant: this is consistent with the fact that only one, large negative eigenvalue dominates its behavior. The inverse scaling with the partition size is due to the fact that we are normalizing symmetry-resolved density matrices, so boundary contributions to the entanglement generated by the mechanism described above are expected to be of order $1/N_A$.

6.5 Numerical results

6.5.1 Spin chains

In this section, we provide numerical evidence for symmetry-resolved purification in one-dimensional spin chains. Specifically, we consider quench dynamics in the XY-model with Hamiltonian

$$H_{\mathrm{XY}} = \sum_{i>j} J_{ij}(\sigma_i^+\sigma_j^- + \sigma_i^-\sigma_j^+) + \sum_i \delta_i\sigma_i^z \tag{6.17}$$

where $\sigma_j^{\pm} = (\sigma_j^x \pm i\sigma_j^y)/2$, subject to spin excitation loss with rate γ, modeled via the jump operators $\sqrt{\gamma}\sigma_i^-$ for $i = 1,\ldots,N$. The coherent hopping is here determined by the interaction matrix J_{ij}. We consider next-neighbour interactions, $J_{i,j} = J\delta_{i+1,j}$, and long-range interactions with power law coefficient α, $J_{i,j} = J/|i-j|^{\alpha}$, respectively. A disordered longitudinal field δ_i can be added which we sample independently for each lattice site from the uniform distribution on $[-\delta,\delta]$. We initialize the system with $N = 8$ sites, divided into subsystems $A = [1,2,3,4]$ and $B = [5,6,7,8]$,

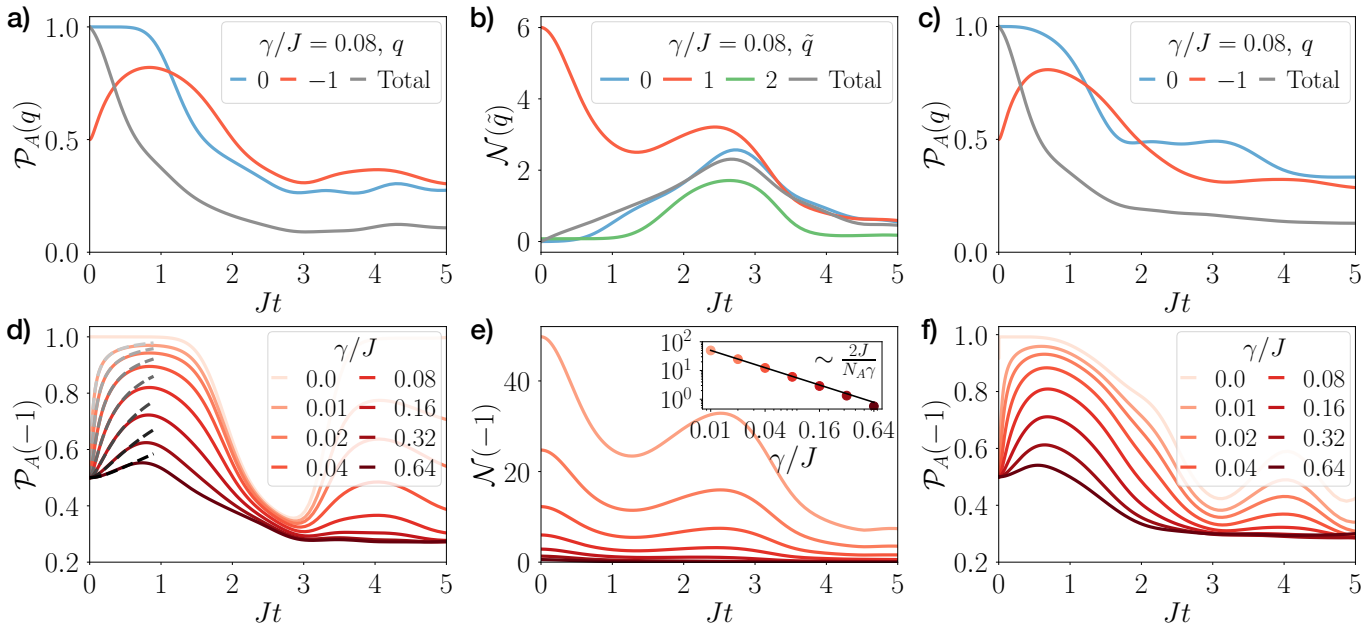

Figure 6.4: Dynamical purification and symmetry-resolved entanglement for one-dimensional XY spin models. We choose a system with $N = 8$, initialized in a Néel state $|{\downarrow\uparrow}\rangle^{\otimes N/2}$ and evolved with H_{XY} subject to particle loss with rate γ (see main text). We take $A = [1, 2, 3, 4]$ and $B = [5, 6, 7, 8]$. In panels (a,b,d,e), we consider short-range interactions $J_{ij} = J\delta_{i-1,j}$ and vanishing disorder $\delta/J = 0$. We present the symmetry-resolved purity $\mathcal{P}_A(q)$ [panels (a,d)] and the normalized symmetry-resolved negativity $\mathcal{N}(\tilde{q})$ [panels (b,e)] for various imbalance sectors $\tilde{q}$ (a,b) and decoherence rates γ (d,e). The inset in (e) shows the early time value $\mathcal{N}(-1)|_{t=0^+}$ as function of γ/J. In panels (c,f), we present the symmetry-resolved purity for various imbalance sectors (c) and decoherence rates (f) in a system with long-range interactions $J_{ij} \sim J/|i-j|^{1.2}$ and a fixed disordered longitudinal field, sampled uniformly from $[-\delta, \delta]$ with $\delta/J = 0.86$. Gray lines in (d,e) are results from perturbation theory, Eqs. (B.4) and (6.16), respectively.

in the Néel state $|\Psi_0\rangle = |{\downarrow\uparrow}\rangle^{\otimes N/2}$ with total magnetization $S_z = \sum_{i=1}^{N} \sigma_i^z = 0$. While the total magnetization is conserved by the Hamiltonian part of the dynamics H_{XY}, the incoherent spin excitation loss leads to a population of various sectors.

In Fig. 6.4 (a,d), we display the symmetry-resolved purity of the subsystem A with $N_A = 4$ sites for various sectors q in a system with short-range interactions $J_{ij} = J\delta_{i-1,j}$ and vanishing disorder $\delta/J = 0$. Clearly, the sector $q = -1$ exhibits dynamical purification at times $Jt \approx 1$ which is absent in the sector $q = 0$ and also for the purity $\mathrm{tr}[\rho_A^2]$ of the total density matrix ρ_A. Note that the second peak in panel (a) (at around $Jt = 4$) is a boundary effect due to the partition size. As predicted by perturbation theory [Eq. (6.7)], purification is pronounced most strongly for weak decoherence [see Fig. 6.4d)]. While the initial values $\mathcal{P}_A(1)|_{t=0^+} = 2/N_A$ is independent of γ, the peak of the purity is approaching the value of the purity for unitary dynamics. On the contrary, for $\gamma \gtrsim J$, the dynamics is dominated by decoherence, and purification is absent.

In Fig. 6.4 (b,e), we show the symmetry-resolved negativity $\mathcal{N}(\tilde{q})$. We observe that symmetry-resolved entanglement between A and B is dominated by the magnetization imbalance sector $\tilde{q} = -1$ sector. The magnitude of the negativity of sector $\tilde{q}$ is much larger than the total system negativity. In addition, as shown in the inset, the early time value at $Jt = 0^+$ is decreasing as $\sim 1/\gamma$ with increasing decoherence rate γ, as predicted by perturbation theory [Eq.(6.16)].

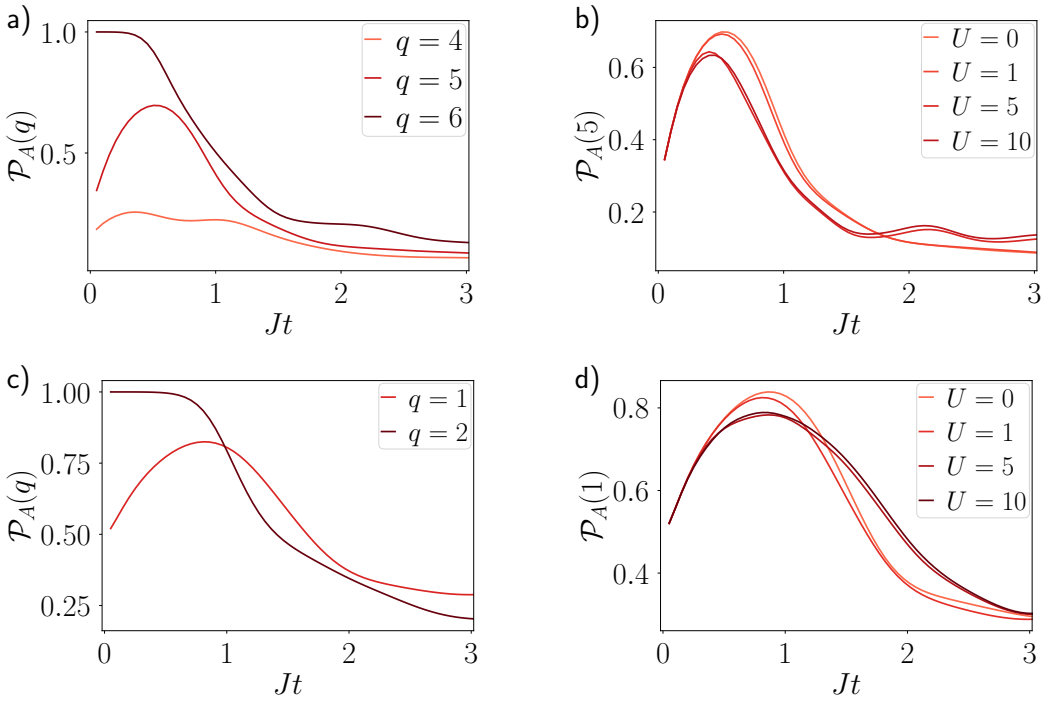

Figure 6.5: Symmetry-resolved purity for the Bose-Hubbard model in one dimension. We consider a system with $L = 8$ and we take $A = [1,2,3,4]$ and $B = [5,6,7,8]$. In panel a) and b) we start from the state $|\psi_0\rangle = |1,2\rangle^{\otimes L/2}$ and consider: a) $U = 0.5J$, $\gamma = 0.1J$; b) and $q = 5$, $\gamma = 0.1J$. In panel c) and d) we start from the state $|\psi_0\rangle = |0,1\rangle^{\otimes L/2}$ and consider: a) $U = 0.5J$, $\gamma = 0.1J$; b) and $q = 1$, $\gamma = 0.1J$.

Long-range, disordered spin chains. - To illustrate the phenomenon of dynamical purification in more generic interacting spin chains, we display in panels (c,f) the symmetry-resolved purity in a system with long-range hopping with powerlaw coefficient $\alpha = 1.2$ and in the presence of a fixed disordered longitudinal field with $\delta = 0.86J$. Our findings are qualitatively very similar to the case of the (non-interacting) model with short-range interaction: dynamical purification is clearly observed in the symmetry sector $q = -1$ with increasing magnitude for weaker decoherence.

Experimental setups. - The dynamics discussed in this section is relevant for a variety of setups. In the next section, we will discuss and demonstrate implementation with trapped ions in Paul traps. Another natural setting is Rydberg atoms in optical tweezers or optical lattices. Within those, the dipolar version of the XY Hamiltonian in Eq. (6.17) is naturally realized when considering direct dipole-dipole interactions within the Rydberg manifold (for a many-body demonstration, see Ref. [39]). Spin excitation losses occur naturally, and can be further enhanced via incoherently coupling the two Rydberg states. A very similar scenario (dipolar couplings) is also realized with superconducting qubits in 3D cavities, and with polar molecules or magnetic atoms in optical lattices.

6.5.2 Bose Hubbard model

In this section we discuss numerical simulations of the Bose-Hubbard model. This allows us to provide explicit evidence of dynamical purification in a full parameter regime connecting the strongly interacting case discussed above for the XY model, and Gaussian theories described later in the section.

The model Hamiltonian reads:

$$H_{BH} = J \sum_i \left(b_i^\dagger b_{i+1} + b_{i+1}^\dagger b_i \right) + U \sum_i n_i \left(n_i - 1 \right). \tag{6.18}$$

Here $b, b^\dagger$ are bosonic operators, $n_i = b_i^\dagger b_i$ is the number operator on site i. For computational convenience, we truncate the number of bosons at a maximum of two per site (this also emulates well experiments in the presence of strong three-body losses [40, 41]). The Hamiltonian preserves the total number of particles $N = \sum_i n_i$. The system dynamics is also subjected to particle loss modeled by γb_i, $i = 1, \ldots, L$. The loss parameter γ is fixed to $\gamma = 0.1J$ for all the simulations.

We consider a bipartite system of $L = 8$, where $A = [1, 2, 3, 4]$ and $B = [5, 6, 7, 8]$. According to the criteria discussed above, dynamical purification will take place for several choices of the initial state: we focus here on two cases: the state $|\psi_0\rangle = |1, 2\rangle^{\otimes L/2}$, where 2 means that the site is doubly occupied while 1 means that there is a single boson; and the state $|\psi_0\rangle = |0, 1\rangle^{\otimes L/2}$ where 0 denotes an empty site. We calculate, during the evolution of the system, the symmetry-resolved purity $\mathcal{P}_A(q)$, where q denotes the number of particles in subsystem A.

In Fig. 6.5 we plot the symmetry-resolved purity as a function of time, starting from the state $(1, 2, 1, 2..)$: in panel a) we consider sectors $q = 4, 5, 6$ with $U = 0.5J$, in panel b) we fix $q = 5$ and take into account different values of U. In agreement with our theory, we observe no purification in the sector $q = 6$ in panel a) since it is the only one occupied in the initial state. Sectors $q = 4, 5$ instead purify at intermediate times with a more pronounced purification visible in the nearest sector $q = 5$. Afterwards the curves approach the same value of purity as information equipartition shall occur at long times. In panel b) we observe the same phenomenology for several values of the interaction strength. Here the sector $q = 5$ experience purification but the value and the position of the peak changes as function of U.

In panels c) and d) of Fig. 6.5, we investigate the same scenario but starting from the state $(0, 1, 0, 1..)$, and consider in panel c) the symmetry-resolved purity for sectors $q = 1, 2$ with $U = 0.5J$, and in panel d) the same quantity for $q = 1$ and several values of U. We observe the same phenomenology of panel c) and d). Dynamical purification is, in fact, present for any initial state which is a product state. Here we observe that the sector $q = 1$ purifies and the effect is present also when the strength of the interaction increases, as witnessed in panel d).

The results of the Bose-Hubbard and XY models indicate, as predicted by our theory, that dynamical purification occurs over the entire interaction regime - from weak to infinite coupling. It is worth noticing that the maximum purity is weakly affected, while the time to reach the

maximum itself is sensitive to both initial filling fraction, and interactions. The first effect can be traced back to bosonic enhancement. The second is instead likely due to the effect of a more constrained dynamics for strong interactions (many states becoming non-resonant), that is likely affecting terms beyond second order in perturbation theory.

Experimental setups. - Bose-Hubbard models with single particle losses describe well the dynamics of cold atoms in optical lattices, where some of the probing techniques introduced here can be implemented [30, 32].

6.5.3 U(1) lattice gauge theory

An even stronger form of interacting system in 1D is provided by gauge theories with U(1) center. For those models, Coulomb interactions follow a genuine linear increase as a function of distance due to confinement. However, since charge creation is still a local process, one expects dynamical purification to still occur, albeit at a possibly slower rate when compare to models with local interactions. In order to illustrate this, we have investigated the short time dynamics of the lattice Schwinger model, a U(1) lattice gauge theory describing the coupling between fermions and U(1) gauge fields. The model Hamiltonian reads:

$$H = w\sum_i(\psi_i^\dagger U_{i,i+1}\psi_{i+1} + \text{h.c.}) + J\sum_i E_i^2 + m\sum_i(-1)^i\psi_i^\dagger\psi_i \tag{6.19}$$

where ψ are fermionic annihilation operators, U are U(1) parallel transporters, and E is corresponding electric field terms. The first term describes minimal coupling, the second the field interaction strength, and the third represents a mass term, that features a staggering typical of Kogut-Sussking (also known as staggered) fermions. For our simulations, we find it convenient to recast the Schwinger model as a spin Hamiltonian with long range interaction in the following way [42]:

$$\begin{aligned} H_S &= H_\pm + H_Z + H_E; \\ H_\pm &= w\sum_i\left(\sigma_i^+\sigma_{i+1}^- + \sigma_i^-\sigma_{i+1}^+\right); \\ H_Z &= \frac{m}{2}\sum_i(-1)^i\sigma_i^z - \frac{J}{2}\sum_{n=1}^{N-1}(n\text{mod}2)\sum_{l=1}^{N}\sigma_l^z; \\ H_E &= J\sum_{n=1}^{N-1}E_n^2. \end{aligned} \tag{6.20}$$

Here $\sigma_j^\pm = (\sigma_j^x \pm i\sigma_j^y)/2$. It can be shown that

$$H_E = J\sum_{n=1}^{N-1}\left[\epsilon_0 + \frac{1}{2}\sum_{l=1}^{n}\left(\sigma_l^z + (-1)^l\right)\right]^2. \tag{6.21}$$

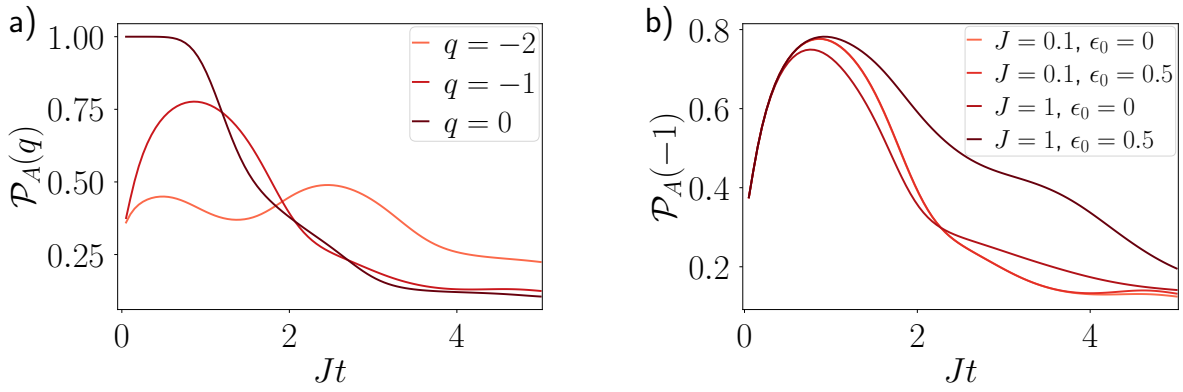

Figure 6.6: Symmetry-resolved purity for the Schwinger model in one dimension. We consider a system with $L = 8$ and we take $A = [1,2,3,4]$ and $B = [5,6,7,8]$. Panel a): $w = 1$,$\epsilon_0 = 0$, $m = 0$, $J = 0.1$, $\gamma = 0.05$. Panel b) $w = 1$, $m = 0$, $\gamma = 0.05$. The dynamics starts from state $|{\downarrow\uparrow}\rangle^{\otimes N/2}$.

It gives rise to a long range spin-spin interaction and local energy offsets, that represent Coulomb law between staggered fermions.

In Fig. 6.6 we plot the symmetry-resolved purity during the dynamics of spin system evolving under the Hamiltonian in Eq. (6.20), starting from the state $|\Psi_0\rangle = |{\downarrow\uparrow}\rangle^{\otimes N/2}$ with total magnetization $S_z = \sum_{i=1}^{N} \sigma_i^z = 0$. We observe that the coherent dynamics preserves the magnetization while the dissipation, modeled by $\sqrt{\gamma}\sigma_i^-$ ($\forall i = 1,\dots,L$), does not.

In panel a) the symmetry resolved purity is plotted for $w = 1$,$\epsilon_0 = 0$, $m = 0$, $J = 0.1$, $\gamma = 0.05$. In panel b) we fix $w = 1$, $m = 0$, $\gamma = 0.05$ and let J and ϵ_0 to vary. We see that even a long-range, strongly interacting system experience dynamical purification in both sectors $q = -2, -1$. Changing the values of the long range coupling J and of the background field ϵ_0 does not change qualitatively the picture. A richer structure seems to emerge in the $q = -2$ sector at long times, suggesting that, while dynamical purification occurs smoothly, entanglement equipartition does not.

Experimental setups. - The dynamics of the Schwinger model in the Wilson formulation has been realized in 4-site trapped ion experiments [43]. However, one would need larger system sizes to observe dynamical purification. Several proposals, based on a variety of platform, exist [44], either in the formulation including gauge fields, or on the integrated theory. Specific dissipation sources have not been discussed in detail so far: however, in most platforms, they are likely to be similar to the Bose-Hubbard case discussed above [44].

6.5.4 Fermionic systems in 1D and 2D

While all models discussed so far are intrinsically interacting, we now provide numerical evidences of the physics described in the previous sections in free fermionic systems [45, 46]. The latter allow us to consider larger system sizes and two-dimensional geometries. Most importantly, it allows us to check systematically specific features of our predictions, such as the dependence

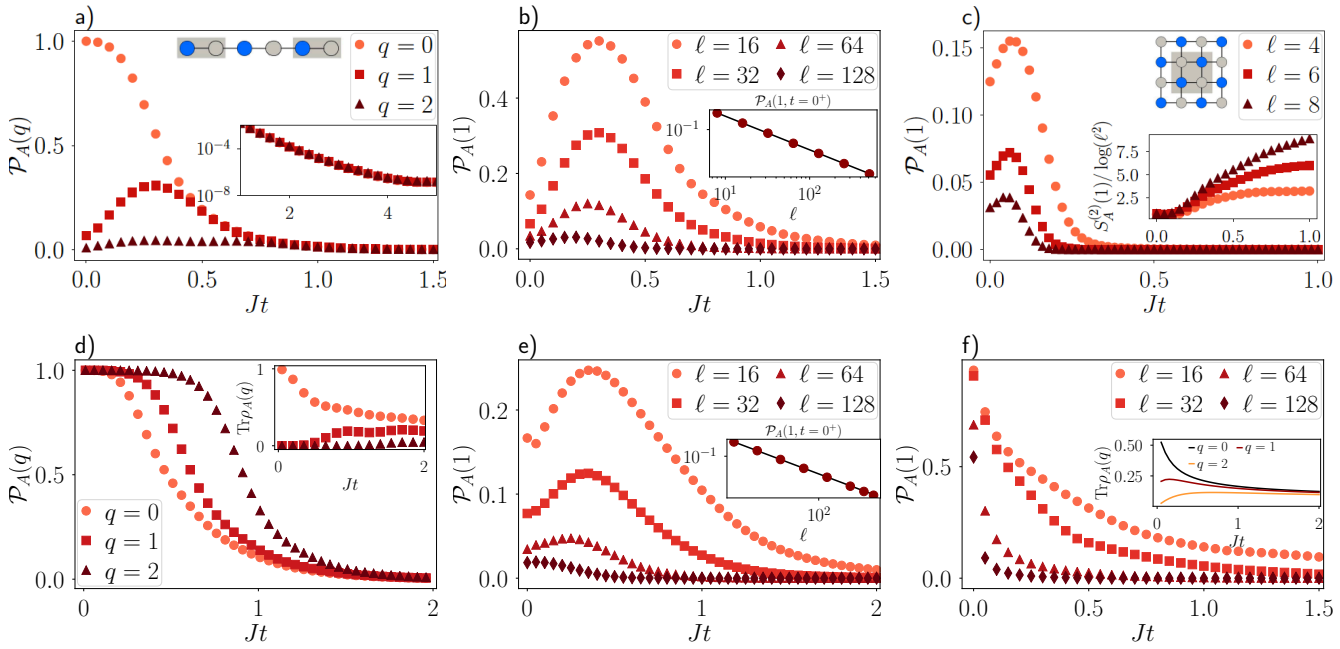

Figure 6.7: Results of the simulation of $\mathcal{P}_A(\ell/2+q)$ for a quadratic open fermionic system. We omit $\ell/2$ and use $q = q - \ell/2$ to label the symmetry sectors. Parameters: $J = 1$, $\mu = 0$. First line: symmetry-resolved Rényi entropy for a) 1D system with $L = 64$, $l = 32$, $\gamma = 0.05$; b) 1D system for $L = 2\ell$, $q = 1$, $\gamma = 0.05$; c) 2D system with $L = 4\ell$, $N = L^2$, $q = 1$, $\gamma = 0.2$. Second line: symmetry-resolved Rényi entropy for d) 1D system with $L = 64$, $l = 16$, $\gamma = 0$, purely coherent dynamics; e) 1D system for $L = 2\ell$, $q = 1$, $\gamma = 0.05$, starting from the Majumdar-Ghosh dimer state; f)1D system for $L = 2\ell$, $q = 1$, $\gamma = 0.05$, starting from the ground state of a nearest-neighbours tight binding model with $J = 1$.

on the partition size, dimensionality, and topology of the partition (e.g.: in 1D, we will consider explicitly disconnected partitions).

We start from a charge-density-wave (half-filling), and let it evolve according to a GKSL master equation master with jump operator $l_j = \gamma c_j$ and Hamiltonian:

$$H = -J \sum_{\langle i,j \rangle} c_i^\dagger c_j - 2\mu \sum_j \left(c_j^\dagger c_j - \frac{1}{2} \right) . \tag{6.22}$$

The first sum runs over nearest neighbours, $c_i^\dagger, c_i$ denote fermionic creation and annihilation operators, J is the hopping constant (that we set to unity below, $J = 1$) and μ is the chemical potential ($\mu = 0$ unless stated otherwise). In free fermionic theories, at each time t one can compute the charged-moments $Z_n(\alpha)$ (Eq. (7.11)) via the two-point fermionic correlation matrix $C_{ij} = \langle c_i^\dagger c_j \rangle$ and its evolution according to Ref. [47]. We consider both $1D$ chains and $2D$ square lattices and check numerically the analytical predictions in the previous sections. In 1D, the tight-binding model is mapped to the XY Hamiltonian (6.17) by a Jordan-Wigner transformation (but the jump operators are different): the GKSL master equation we will consider are similar to one of the examples discussed in Ref. [48].

In Fig. 6.7, we show some representative numerical results. In panels a)-b) we consider $\mathcal{P}_A(q)$, cf. Eq. (1.7), in 1D. The system is divided into three parts as $\mathcal{S} = A \cup B \cup A$ with $|A| = \ell/2$

and $\ell = L/2$, a representation of the system is in Fig 6.7a). The choice of the topology of the partition allows us to illustrate the generality of dynamical purification, that is indeed topology independent as long as $\ell \gg tJ$. In panel c) we compute the same quantity for a two-dimensional square lattice to highlight that the features of the dynamics are not dependent on the dimensionality or connectivity of the partition. Here we consider $\mathcal{S} = A \cup B$ where A is a square of linear dimension $\ell = L/4$ at the center of the system. In panels d)-e)-f) we focus on the behavior of the symmetry-resolved purity in the absence of dissipation, to emphasize that the bath plays a decisive role in the dynamical purification, and on quenches starting from different states, since we expect our results to hold when the initial state is separable (cf. 6.3). The initial state being at half-filling, $q = \ell/2$ is the only populated sector at $t = 0$. We will consider the quantity $\mathcal{P}_A(q)$ where, for instance, $q = 1$ refers to the sector $\ell/2 + 1$ (one particle more than half-filling). We omit $\ell/2$ to be concise. Let us now discuss the plots in details. In all the following simulations we always consider open boundary conditions (OBC).

In Fig. 6.7a), we show $\mathcal{P}_A(q)$ for $q = 0, 1, 2, 3$, $L = 128$. The sector $q = 0$ is the only one occupied at $t = 0$. It is pure at the start of the evolution and does not experience any purification. Oppositely, as soon as dynamics kicks in, the sector $q = 1$ becomes mixed. Its purity increases at intermediate times (*dynamical purification*) and approaches *equipartition* for longer times. This is highlighted in the inset showing the behavior of $\mathcal{P}_A(q)$ for $Jt \in [1, 5]$ in logarithmic scale. The purification for the other sectors is present, but less evident as it is connected to higher-order perturbative processes.

In Fig. 6.7b) we fix $q = 1$ and consider $\mathcal{P}_A(q)$ for different values of ℓ with $L = 2\ell$. In agreement with theory, the peak of the curves decreases, approaching zero. The point at $t = 0^+$ should approach zero as $\sim 1/\ell$, as well, like it has been anticipated in the previous sections. The inset shows a fit of $\mathcal{P}_A(q = 1, t = 0^+)$ as a function of ℓ, which demonstrates the log-volume regime already discussed.

The behavior of the symmetry-resolved purity for a two-dimensional systems is analogous. In Fig. 6.7c) we plot the purity, at fixed $q = 1$, for different values of L. The total number of sites of the lattice is $N = L^2$ and the subsystem A consists of $l^2 = N/16$ sites picked at the center of the square. Studying the position of the point at $t = 0^+$ one observes that it scales as $\sim 1/\ell^2$ as calculated in Eq. (6.6) and shown in Fig. 6.2a): this confirms a 2D log-volume scaling at short times, with the corresponding symmetry-resolved Rényi entropy displayed in the inset for the sake of completeness.

In Fig. 6.7d), we take into account the symmetry-resolved purity in the case of a purely coherent dynamics. This show remarkably how the purification process is strictly related to the presence of a bath for this class of models. We consider $L = 64$ and $\ell = 32$. While $q \neq 0$ sectors are mixed at time $t = 0^+$ in presence of bath, this is not the case for $\gamma = 0$. In the inset one can see the population of each given sector as a function of time. As the coherent dynamics starts playing its role, the population increases and the purity decreases correspondingly. The $q \neq 0$ sectors are involved in the evolution but they do not experience any purification, instead their purity de-

creases monotonously to a unique value independent of q, witnessing information equipartition. All these results are compatible with the exact ones reported in Ref. [12].

Finally, in Fig. 6.7e-f), we depict the symmetry-resolved purity in the sector $q = 1$, in the case of a global quench starting from two different states. Firstly, in e), we consider a global quench from the Majumdar–Ghosh dimer product state and an evolution under the Hamiltonian in Eq. (6.22); secondly, in f), we take as starting point the ground state of Eq. (6.22) and evolve the system according to a long range hopping Hamiltonian in the form:

$$H = -\sum_{ij} \frac{J}{|i-j|^{\alpha}} c_i^{\dagger} c_j, \tag{6.23}$$

where $\alpha = 2$.

The purpose of panels e) and f) is to show that the dynamical purification is present only in the case the initial state is separable, as it happens for Fig. 6.7b)-e). In the inset of Fig. 6.7e) we show a fit of $\mathcal{P}_A(q = 1, t = 0^+)$ as a function of ℓ, which exhibits a $1/\ell$ behavior, as predicted by perturbation theory. Oppositely, if the initial state is entangled, one cannot see any emergent purification during the dynamics (Fig. 6.7f)). This is due to the fact that the symmetry-resolved reduced density matrix is already mixed in all E_k sectors, and thus, local coherent dynamics is insufficient to purify the state, as the number of non-zero eigenvalues in each sector is exponentially large in the partition size. In the inset of the figure the populations of sectors $q = 0, 1, 2$ for $L = 256$ are shown. Evidently, all the sectors are occupied already at $t = 0$.

Experimental setups. - The $U(1)$ dynamics discussed in this section is of direct relevance for various experimental settings. The first ones are fermionic or (hard-core) bosonic atoms trapped into optical lattices. There, one of the main sources of dissipation (in addition to spontaneous emission, that can be made small with the use of blue detuned lattices) is single particle loss. While in principle loss rates due to inelastic background scattering are small when compared to the typical lattice dynamics, localized losses can be engineered in a variety of ways, including weak-laser coupling to untrapped levels or via electron beams.

The second setting that is relevant to this section are arrays of superconducting qubits. In the strong coupling limit, the dynamics of such systems can be well approximated by an XY model. Qubit relaxation will then play the same role as single particle loss.

6.6 Experimental protocol for measuring symmetry-resolved purities

Our protocol to extract symmetry-resolved purities is based on randomized measurements. These methods have been introduced and experimentally demonstrated to measure entanglement entropies [29, 31, 32, 34], and other nonlinear functions of the density matrix, such as state fideli-

ties [49], out-of-time ordered correlators [50, 51], topological invariants [52, 53], and entanglement negativity [36, 54]. In the quantum information context, the moments of statistical correlations between randomized measurements can also be used to define powerful entanglement witnesses without reference frames [36, 55–59].

While standard projective measurements performed in a fixed basis can only give access to expectation values of a particular observable, randomized measurements consist instead in measuring our quantum state in different random bases, giving access to complicated non-linear functionals of the density matrix, here symmetry-resolved purities.

As in Refs. [34, 36], our approach is based on the idea of combining two results: randomized measurement tomography [30, 60], and 'shadow' tomography [34, 61]. Let us consider here a spin system and show how to measure the symmetry-resolved purity of a reduced state ρ_A made of N_A spins.

Randomized measurements are realized by applying random local unitaries $\rho_A \to u\rho_A u^\dagger$, $u = u_1 \otimes \cdots \otimes u_{N_A}$, where each u_i is a spin rotation that is taken, independently, from a unitary 3-design [62, 63]. After the application of random unitary, a projective measurement is realized in a fixed basis. This procedure is repeated with M different random unitaries, in order to obtain a list of M measured bitstrings $\mathbf{k}^{(r)}$, $r = 1, \ldots, M$.

Randomized measurementsare tomographically complete in expectation and can be used to provide an estimator of the density matrix [30, 34, 35, 60, 64], a classical shadow [34],

$$\hat{\rho}_A^{(r)} = \bigotimes_{i\in A} \left[3(u_i^{(r)})^\dagger \left| k_i^{(r)} \right\rangle \left\langle k_i^{(r)} \right| u_i^{(r)} - \mathbb{I}_2 \right], \tag{6.24}$$

with the expectation value over randomized measurements $\mathbb{E}[\hat{\rho}_A^{(r)}] = \rho_A$. It is not our aim to reconstruct the density matrix based on Eq. (6.24) i.e., to perform tomography, as it will be too costly in terms of measurements (and classical post-processing). However, we can make use of this expression Eq. (6.24), in order to relate directly *polynomial functionals* of ρ to the measured data $\mathbf{k}^{(r)}$ [34]. For the symmetry-resolved purity, simply consider two independent randomized measurements $r \neq r'$, and define the symmetrized estimator

$$\mathcal{P}_A(q)^{(r,r')} = \tfrac{1}{2}\mathrm{tr}[(\hat{\rho}_A^{(r)}\Pi_q)(\hat{\rho}_A^{(r')}\Pi_q)] + \tfrac{1}{2}\mathrm{tr}[(\hat{\rho}_A^{(r')}\Pi_q)(\hat{\rho}_A^{(r)}\Pi_q)]. \tag{6.25}$$

Using Eq. (6.24), this can be seen as a simple bi-linear function of the measurement data. Averaging over many pairs (r, r'), boosts convergence to the estimator's expectation value

$$\mathbb{E}[\mathcal{P}_A(q)^{(r,r')}] = \tfrac{1}{2}\mathrm{tr}[(\mathbb{E}[\hat{\rho}_A^{(r)}]\Pi_q)(\mathbb{E}[\hat{\rho}_A^{(r')}]\Pi_q)] + \tfrac{1}{2}\mathrm{tr}[(\mathbb{E}[\hat{\rho}_A^{(r')}]\Pi_q)(\mathbb{E}[\hat{\rho}_A^{(r)}]\Pi_q)] = \mathcal{P}_A(q). \tag{6.26}$$

Here, we have used that $\hat{\rho}_A^{(r)}$ and $\hat{\rho}_A^{(r')}$ are independent realizations of Eq. (6.24). This means that $\mathcal{P}_A(q)^{(r,r')}$ is an unbiased estimator of the symmetry-resolved purity. This procedure can be straightforwardly extended to higher moments with triplets of randomized measurements

$r \neq r' \neq r''$, etc. Appropriate implementation of partial transposes moreover allows for extracting symmetry-resolved Rényi entropies (1.8). This is the content of Ref. [65], where we also provide a thorough statistical analysis for estimating symmetry-resolved quantities based on randomized measurements. The upshot is that estimator (6.25) can be equipped with rigorous confidence bounds. Already $2^{N_A}\mathcal{P}_A(q)/\epsilon^2$ measurement repetitions suffice to estimate a given symmetry-resolved purity $\mathcal{P}_A(q)$ up to accuracy ϵ. This favorable scaling is a key advantage over full quantum state tomography In particular, the scaling depends only on the symmetry resolved purity $\mathcal{P}_A(q)$ and not on (the inverse) of the population $\mathrm{tr}\rho_A\Pi_q$. This can make a large difference, especially when the population is tiny. Our analysis of experimental data, c.f. next section, support this favorable picture.

Therefore, we believe that symmetry-resolved purities can be measured in various NISQ platforms up to moderate partition sizes $N_A = 10 \sim 20$, which are sufficient large to observe many-body effects, such as dynamical purification. The second advantage of randomized measurements with respect to tomographic-type estimations is the post-processing step. Here, the estimation of $\mathcal{P}_A(q)^{(r,r')}$ from the data simply consists in multiplying estimators $\hat{\rho}_A^{(r)}$ with an efficient tensor-product representation (Eq. (6.24)) with a projection operator with sparse-matrix structure (which can be for instance efficiently written as a Matrix-Product-Operator [66]).

Note finally that here randomized unitaries do not have a symmetric structure, and therefore each estimation of the density matrix does not have a block-diagonal structure. Alternatively, one can envision to perform symmetry-resolved random unitaries incorporating symmetries [30, 32, 33]. While these random unitaries appear as more challenging to realize experimentally compared to local spin rotations, one should expect a reduction of statistical errors in this situation [60].

6.7 Experimental observation of dynamical purification in trapped ion chains

In this section, we demonstrate symmetry-resolved purification experimentally in a trapped ion quantum simulator, using data taken in the context of Ref. [29]. Here, quench dynamics with a long-range XY-model introduced in Eq. (6.17), with $\delta_i = B$, $J_{ij} \approx J/|i-j|^\alpha$ the coupling matrix with an approximate power-law decay $\alpha \approx 1.24$, and $J = 420s^{-1}$. The effective magnetic field is taken to be large $B \approx 2\pi \cdot 1.5\mathrm{kHz} \approx 22J$: this way, that the unitary dynamics conserve the total magnetization $S_z = \sum_i \sigma_i^z$, since terms that would break it (such as $\sigma_i^+\sigma_j^+ + \mathrm{h.c.}$) are energetically suppressed [29].

In addition, decoherence is present in the experiment, during initial state preparation, time evolution and the randomized measurement. As detailed in Ref. [29], we can model these decoherence effects as follows.

The time evolution is subject to local spin-flips, and spin excitation loss (spontaneous decay). We describe the corresponding dynamics with a master equation with jump operators

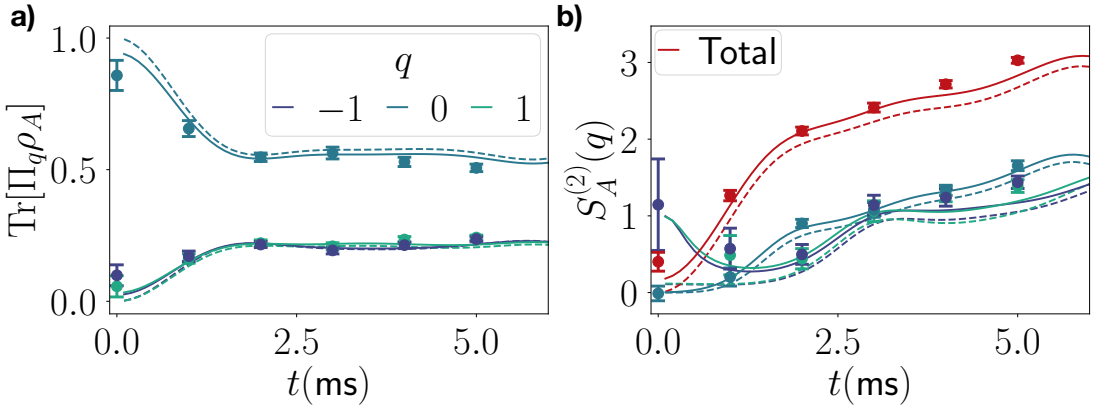

Figure 6.8: Experimental demonstration of symmetry-resolved purification in a trapped ion quantum simulator, using data obtained in the context of Ref. [29]. We consider a system of $N = 10$ spins, with subsystems $A = [4,5,6,7]$ and $B = [1,2,3,8,9,10]$. In panels a) and b), the symmetry-resolved populations and Rényi entropies of various magnetization sectors $q = 0, \pm 1$ of the reduced density matrix ρ_A are shown as function of time (see Fig. 6.2 for symmetry-resolved purities). Error bars have been calculated with Jackknife resampling. In panel b), data for the magnetization sector $q = 1$ at $Jt = 0$ has been omitted due to large errorbars, resulting from small populations. Lines are numerical simulations of unitary dynamics (dashed) and including decoherence (solid) as decribed in the text.

$C_i = \sqrt{\gamma_F}\sigma_i^x$ for $i = 1, \ldots, N$ and $C_{i+N} = \sqrt{\gamma_D}\sigma_i^-$ for $i = 1, \ldots, N$, capturing the spin flip and excitation loss, respectively. Here, the rates are $\gamma_F \approx \gamma_D \approx 0.7/s$.

In the experiments, the initial state is not pure, but rather it is a mixed product state

$$\rho_0 = \bigotimes_i \left(p_i \left|\uparrow\right\rangle \left\langle\uparrow\right| + (1 - p_i) \left|\downarrow\right\rangle \left\langle\downarrow\right| \right) \tag{6.27}$$

with $p_i \approx 0.004$ for i even and $p_i \approx 0.995$ for i odd. Finally, during the application of the local random unitary, local depolarizing noise is acting which is modeled as

$$\rho(t_{\text{final}}) \to (1 - p_{DP}N)\rho(t_{\text{final}}) + p_{DP} \sum_i \mathrm{tr}_i[\rho(t_{\text{final}})] \otimes \frac{\mathbf{1}_i}{2}$$

with $p_{DP} \approx 0.02$.

In Fig. 6.8, we present experimental results, obtained with the estimators defined in Eq. (6.25), and numerical simulations, for unitary dynamics and including the decoherence model described above. In panel a), the populations $\mathrm{tr}\Pi_q\rho_A$ of the magnetization sectors q of the reduced density matrix ρ_A are shown, with A consisting of spins $A = [4,5,6,7]$, and $\mathcal{V}_A = 4$. Initially, the $(q = 0)$-sector is predominantly populated, with small fractions in other sectors, due to the finite initial state preparation fidelity. With time, the population in other sectors, in particular $q = \pm 1$, increases.

The symmetry-resolved second Rényi entropy $S_A^{(2)}(q)$ is shown in panel b) for various magnetization sectors (see Fig. 6.2 for the corresponding symmetry-resolved purity). The experimental data clearly shows dynamical purification (decrease of the Rényi entropy) in the $q = -1$ sector. Data in the $q = +1$ sector are also suggestive of dynamical purification, even if a strong statement

cannot be made here due to comparatively larger error bars. In particular, this demonstrates that dynamical purification can be observed in one-dimensional systems with algebraically decaying long-range interactions (see also Sec. 6.3). At long times, the symmetry-resolved Rényi entropies approach similar values for all displayed sectors, consistent with expected equipartition of the symmetry sectors [10]. Finally, we note that, in the experiment, there is clear separation of scales $t_J \ll t_2$, while t_1 and t_J are not separated. As discussed in the theory section, this shows compellingly how the second condition is not required to observe dynamical purification, since at short times, decoherence dominates regardless of the volume of the partition considered.

6.8 Conclusions

Symmetry is an ubiquitous element characterising synthetic quantum matter - from quantum simulators, to noisy-intermediate scale quantum devices. We have developed a theoretical framework for the description of symmetry-resolved information spreading in such open quantum systems, focusing on the epitome case of $U(1)$ symmetries common to several experimental platforms - from cold gases in optical lattices, to trapped ions and superconducting circuits. We have shown how, for various settings encompassing a wide spectrum of interacting and non-interacting theories, specific quantum number sectors undergo dynamical purification under ubiquitous conditions of weak noise and separable initial states, without experiencing quantum information loss. Such phenomenology is general, occurs in any dimension, is not sensitive to the partition topology, and features specific scaling scenarios for the entropy as a function of partition size. Most importantly, the dynamical purification considered here occurs in symmetric systems and stems from the competition between coherent and incoherent dynamics that is a leitmotif of current NISQ devices.

We have introduced and experimentally demonstrated a protocol to measure symmetry-resolved quantum information quantities based on a combination of randomized measurement probing and shadow tomography. Our approach is scalable to partition sizes that are well beyond what is accessible to full state tomography, and is applicable to a broad spectrum of experimental settings with single site control and high repetition rate. Both scalability and applicability are of key importance in order to probe genuinely many-body features of entanglement dynamics in state-of-the-art experiments. Two key features of our protocol are the fact that symmetry can be enforced *a posteriori* on a given data set, without necessarily relying on the implementation of symmetry-preserving random unitaries, and that errors are provably under control even in cases where populations in given subsectors are small (that is a challenge specific to symmetry-resolved density matrices). Based on our protocol, we have shown how the experiments performed in Ref. [29] have already realized dynamical purification in a trapped ion chain described by a long-range XY model. This observation, in full agreement with our theory predictions, testifies for the generality of symmetry-resolved dynamical purification under experimentally realistic conditions. While our protocol is generically applicable to lattice models, it would be interesting to

extend it to continuous systems, where the role of symmetry-resolved information is relatively unexplored outside of conformal field theories [67, 68].

The capability of addressing the combined role of symmetry and quantum correlations in NISQ devices opens a novel interface between theory and experiments, where many-body effects intertwine with information theoretic applications. The first instance of that is what role symmetry plays in quantum information protocols, in particular, error correction. Our tools may be of particular importance here, as several error correcting codes can be cast as gauge theories, one example being the toric code [69]. In this context, the role of specific symmetry sectors is associated to the presence of excitations. It may thus be useful to employ the experimental tools we have used here to access how specific perturbations compromise the reliability of a quantum memory. Going beyond that, understanding whether dynamical purification occurs in the presence of local symmetries is an open question, that could be in principle addressed within the same methods presented here.

The second possible applications of our methods concerns the capability of utilizing dynamical purification as a proxy of the system dynamics, in particular, to determine its dissipative dynamics. One first element is that dynamical purification is expected for a quantum noise, that is local: it is thus informative about the nature of the dissipation. The fact that the dissipation rates intertwines with the partition size could also help to quantify the relative strength of incoherent versus coherent processes, at least in cases where specific initial states could be realized with high fidelity. Remarkably, despite being a short-to-intermediate time phenomenon, thanks to the area-to-volume ratio being tunable, dynamical purification is also informative about very weak dissipation: this is particularly important for diagnostics, as one would expect that the latter requires long-time evolution to be characterized.

On more general grounds, symmetry-resolved dynamical purification reveals how certain many-body phenomena can only be properly characterized utilizing symmetry to emphasize or even magnify relevant information. In particular, symmetry-resolution allows to properly diagnose physical phenomena that would not be accessible otherwise, by amplifying the role of sectors in the reduced density matrix whose information content could be otherwise overwhelmed by other less informative - but highly-weighted - sectors. In this context, the many-body theory we develop seems to suggest that symmetry can be used to develop improved entanglement detection that could outperform their respective 'symmetry-blind' counterparts [65].

7

Operator entanglement dynamics and its symmetry resolution

The operator entanglement (OE) is a key quantifier of the complexity of a reduced density matrix, and in out-of-equilibrium situations, e.g. after a quantum quench from a product state, it is expected to exhibit an *entanglement barrier*. The OE of a reduced density matrix initially grows linearly as entanglement builds up between the local degrees of freedom, it then reaches a maximum, and it ultimately decays to a small finite value as the reduced matrix converges to a simple stationary state through standard thermalization mechanisms. Here, by performing a new data analysis of the published experimental results of Ref. [29], we obtain the first experimental measurement of the OE of a subsystem reduced density matrix in a quantum many-body system. We employ the randomized measurements toolbox and we introduce and develop a new efficient method to post-process experimental data in order to extract higher-order density matrix functionals and access the OE. The OE thus obtained displays the expected *barrier* as long as the experimental system is large enough. For smaller systems it is absent. As $U(1)$ symmetry plays a key role in our analysis, we introduce the notion of symmetry resolved operator entanglement (SROE), in addition to the total OE. To gain further insights into the SROE, we provide a thorough theoretical analysis of this new quantity in chains of non-interacting fermions, which, in spite of their simplicity, capture most of the main features of OE and SROE. In particular, we uncover three main physical effects: the presence of a barrier in any charge sector, a time delay for the onset of the growth of SROE, and an effective equipartition between charge sectors.

7.1 Introduction

The investigation of the non-equilibrium dynamics of isolated many-body quantum systems is a major challenge of modern physics. Owing to the highly tunable modern experimental settings for analog simulations [16, 70–72], it has been possible to engineer Hamiltonian dynamics of isolated quantum systems, ranging from integrable to chaotic systems, and measure non-trivial physical properties, as the entanglement growth following a quantum quench [73–76] or out-of-time ordered correlators [77–79]. Unfortunately, the absence of numerical algorithms to effectively simulate these systems on a classical computer for large times is the main obstacle toward the complete understanding of quantum relaxation and thermalization. In this respect, the most effective and versatile algorithms are surely those based on matrix product state (MPS) and tensor networks methods [80–84]. However, the linear growth of the entanglement entropy [85, 86] requires an exponential complexity (bond dimensions) of the MPS approximating the physical state, severely limiting the largest simulable times [87]. Typically, these systems relax to statistical ensembles with little or no entanglement. How is it compatible with the growth of complexity of the MPS approximation? The solution of such a conundrum is simple: the relaxation being local [88–90], one has to focus solely on the reduced density matrix ρ of a subsystem S, not on the entire pure state containing physically irrelevant correlations. Indeed, rather than an MPS, the subsystem density matrix is approximated by a matrix product operator (MPO) with small bond dimension D [91–97]. What is the quantity that correctly assesses the validity of this approximation?

To this end, as anticipated in Sec. 1.7, it useful to note that every bipartite density matrix ρ_{AB} can be decomposed as follows:

$$\frac{\rho_{AB}}{\sqrt{\mathrm{Tr}(\rho_{AB}^2)}} = \sum_i \lambda_i O_{A,i} \otimes O_{B,i}. \tag{7.1}$$

This is called an *operator Schmidt decomposition* and it has the property that all expansion coefficients λ_i are positive and the associated operators $O_{A,i}, O_{B,i}$ are Hermitian and orthonormal with respect to the Hilbert-Schmidt inner product $(\mathrm{tr}(O_{A,i}^\dagger O_{A,j}) = \mathrm{tr}(O_{B,i}^\dagger O_{B,j}) = \delta_{i,j}$. Normalization on the lhs of Eq. (7.1) moreover ensures that the expansion coefficients obey $\sum_i \lambda_i^2 = 1$, i.e. the set $\{\lambda_i^2\}$ forms a probability distribution of (squared) Schmidt values. The smallest summation range for which Eq. (7.1) is possible is called the operator Schmidt rank of ρ_{AB} [98].

In an MPO algorithm, the density matrix ρ_{AB} is 'compressed' by truncating the full sum to only the D largest contributions. This thresholding approximation is accurate provided that the distribution $\{\lambda_i^2\}$ of squared Schmidt values in Eq. (7.1) has small Shannon entropy, i.e. $\mathrm{OE}(\rho_{AB}) = -\sum_i \lambda_i^2 \log(\lambda_i^2) \ll 1$. This quantity is called the *operator entanglement* [91, 92, 99, 100] of the bipartite density matrix ρ_{AB}.

The main physical feature of the operator entanglement of a density matrix is the presence

of an *entanglement barrier* [94, 101, 102]: after a quantum quench from a low-entangled state, the OE of a subsystem density matrix initially grows linearly and then decays at longer times, thus displaying a barrier-shaped curve. The initial linear growth is a consequence of the generic linear growth of the (state) entanglement entropy after a quench [85, 86], while the decay at later times reflects the convergence of the reduced density matrix towards a simple stationary state [94], through the mechanism of thermalization [88, 89, 103–108] (or relaxation to a Generalized Gibbs ensemble [109–112]). The emergence of the entanglement barrier for the OE of a reduced density matrix in ergodic dynamics can be linked straightforwardly to the distribution of squared Schmidt values $\{\lambda_i^2\}$ in Eq. (7.1). At early times the evolution starts from a pure product state, when only a single Schmidt value is different from zero. The building up of entanglement is reflected in the increasing number of nonzero Schmidt coefficients λ_i. Eventually, for long times the system locally approaches a Generalized Gibbs or Gibbs ensemble, which obeys the operator area law [94], i.e. it is constant in the subsystem size, and again only few Schmidt values give a sizeable contribution to the OE. For example, in the infinite temperature limit, since the density matrix is proportional to the identity, $\rho \propto \mathbf{1} = (\mathbf{1}_A \otimes \mathbf{1}_B)$, only a single Schmidt value is different from zero and the OE vanishes.

Inspired by the relevance of the *entanglement barrier*, our goal is to observe it in an experimental quantum many-body system, using the randomized measurement data of the trapped ion experiment of Ref. [75]. The randomized measurement toolbox [113] has enabled measuring state-agnostically properties of the underlying quantum state such as purity and Rényi entanglement entropies [75, 76, 113–115], negativities [54, 65, 116], state fidelities [117, 118] with a lower measurement cost compared to quantum state tomography [64, 119–122]. One particular fruitful development is the formalism of classical shadows [114, 123] that provides estimation of nonlinear functionals of the density matrix, such as the OE [124]. However, measuring OE using the current randomized measurement toolbox requires a prohibitively expensive postprocessing method. To overcome this limitation and observe OE for a reasonable system size, we introduce in this work the *batch shadows estimator*. This new estimator, which should be of independent interest for the randomized measurement toolbox, provides a fast postprocessing technique for estimating polynomial functions of the density matrix. Importantly, this method offers, up to factors of order one in the experimentally relevant scenario, the same performance guarantees as classical shadows in terms of required number of measurements to overcome statistical errors. This enables us to experimentally access the OE and, in turn, witness the entanglement barrier.

As a second important result, the experimental setup of Ref. [75] provides us with an opportunity to study how the OE content is structured due to the presence of symmetries, which is here a $U(1)$ symmetry associated with the number of spin excitations. In the case of pure state entanglement, the fruitful notion of symmetry-resolved entropies [125–127] has been introduced recently, computed theoretically [68, 128–136] and experimentally observed [65, 116, 137]. Here, we generalize this to the case of operator entanglement. Based on suitable supercharge opera-

tors[1], we introduce a notion of *symmetry resolved operator entanglement (SROE)*, for which we also provide tractable estimation protocols. We note, however, that a slightly different definition of SROE, with respect to the one in this thesis, was already introduced in Ref. [97].

Using the SROE, we can theoretically study and experimentally observe a symmetry-resolved entanglement barrier. This is relevant for understanding thermalization in $U(1)$ symmetric non-equilibrium quantum systems, but also for numerical simulations, as symmetries can be incorporated in MPO algorithms.

The chapter is organised as follows. In Sec. 7.2 we provide a bird's eye view of the results in this chapter. In Sec. 1.7 we introduce formally the operator entanglement (OE) and its symmetry resolution. In Sec. 7.3 we demonstrate and describe the details of the randomized measurement protocol used to measure OE and SROE of the experiment performed in Ref. [75]. In Sec. 7.4, using a combination of conformal field theory (CFT) and of exact analytical and numerical calculations in critical free fermion chains, we study the SROE of the reduced density matrix of a subsystem after a quantum quench.

7.2 Summary of the main results

Here we provide a short summary of the results in this chapter. The main points are also illustrated in Fig. 7.1. With the new analysis method we were able to measure the OE and SROE of a subsystem's density matrix in a many-body quantum system from the published experimental data of *Brydges et al.* [75] presenting a $U(1)$ conserved charge. We employ the *randomized measurements* toolbox [113] and introduce a new efficient method to post-process experimental data in order to extract arbitrary higher-order density matrix functionals of the form $\mathrm{Tr}\big(O^{(n)}\rho^{\otimes n}\big)$ expressed in terms of an n-copy operator $O^{(n)}$. A schematic of this procedure is shown in Fig. 7.1a) whose details are elaborated in Sec. 7.3 and in App.B of Ref. [138]. This tool is employed to extract the experimental results presented in Fig. 7.1b)-c). Here we show the measured OE and SROE, as in Eq. (1.43), which are supported by tensor network simulations modelling the full experiment, i.e. the open dynamics of a long-range XY model starting from the Néel state, with conserved magnetization along the z-axis. Our main observations of Sec. 7.3 are summarized here:

1. We witness experimentally the entanglement barrier of the OE and of the SROE, in the charge sector $q = 0$, (Fig. 7.1b), for a bipartite subsystem $A \cup B$ comprised of four out of $N = 20$ ions. These barriers present bump structures due to finite size effects. When N is too small these finite size effects suppress the emergence of the entanglement barrier, as we show in Fig. 7.1c) for a subsystem of four out of $N = 10$ ions.

2. We observe a qualitative agreement of SROE with the numerical results for charge sectors $q = \pm 1$ at early times. The sizeable deviation between theory and experiment for $N = 20$

[1]Throughout all the chapter we refer to the operators in the space of operators as superoperators and to the corresponding charges as supercharges.

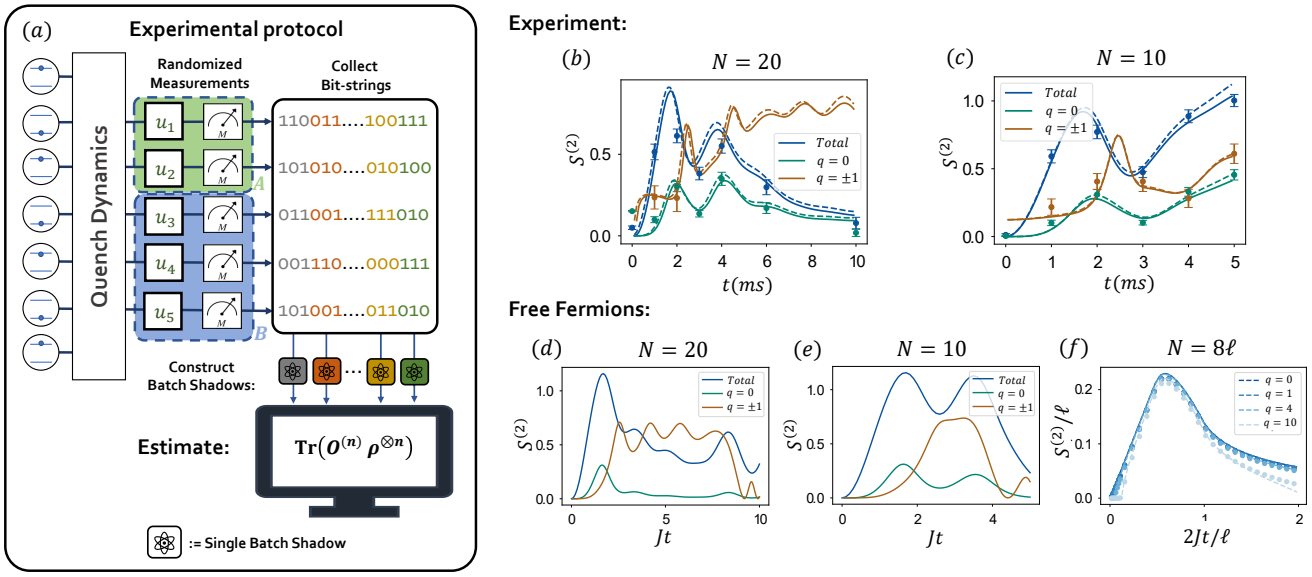

Figure 7.1: Overview of the results: a) Schematic of the method to post-process the experimental data. After the quench dynamics, randomized measurements are performed. The collected bit-strings are used to estimate OE and the SROE with a method we dub *batch shadows estimator*. b)-c) Experimental results for the Rényi 2-OE (Eq. (1.43)) and its symmetry resolution (Eq. (1.50)) of a reduced density matrix of partition of 4 ions out of 20 (panel (b)) and 10 ions (panel (c)) from the data of [75] after the global quantum quench. The points correspond to the experimental data, the curves are numerical results obtained via tensor network algorithms with (solid) or without (dashed) dissipation considered. The entanglement barrier is visible for the total operator entanglement and the symmetry sector $q = 0$ with $N = 20$. d)-f) Symmetry resolution of the OE of the reduced density matrix after a global quantum quench in a free fermion chain under unitary evolution. d) (and e)) Symmetry resolution of the OE of the reduced density matrix after a global quantum quench, for 4 sites out of a 20 (out of 10) sites chain. Comparing with the experimental results in b) and c) respectively, we can spot several qualitative features of OE although the model is short ranged and there is no dissipation. f) Numerical data (symbols) with subsystem length $\ell_A = 120$ compared with analytical prediction of Ref.[138] (continuous lines). This plot shows the three main features of the SROE in the thermodynamic limit, i.e. the barrier in each sector q, the delay time and the equipartition for small q.

(Fig. 7.1b) are caused by the small populations in the corresponding charge sectors and by the low measurement statistics performed in the experiment.

To gain insights into SROE and into its own entanglement barrier, we also provide an analysis in chains of non-interacting fermions, which despite their simplicity capture the main physical features of the OE and SROE. This is already visible for small system sizes N, by comparing Fig. 7.1b) and 7.1c) with 7.1d) and 7.1e), respectively. Moreover, for these free models it is possible to obtain a general formula using CFT results [138], which governs the evolution of the SROE. This formula allows us to uncover three main physical effects, which we expect to appear more generically in chains of qubits, beyond the simple non-interacting fermion ones. These effects are:

1. the appearance of a barrier for SROE in *any* charge sector, which resembles the behavior of the total OE;

2. a delay time for the onset of the SROE that grows linearly with the charge sector of the

subsystem;

3. the effective equipartition in the scaling limit of large time and subsystem size for small charges, where by equipartition we mean that the SROE is equally distributed among the different symmetry sectors.

These effects are visible in Fig. 7.1f). There we plot OE and SROE of the reduced density matrix, for a bipartition $A \cup B$, where A and B are of lengths ℓ_A and ℓ_B respectively (here $\ell \equiv \ell_A + \ell_B = 256$). The numerical results are obtained for a quench in the tight-binding model from the Néel state (the calculation is performed in a finite periodic chain of total size $N = 8 \times (\ell_A + \ell_B)$). The solid lines correspond to the theoretical prediction in Ref. [138].

7.3 Operator entanglement in the quench dynamics of trapped ions

Let us come to the development of tractable methods to extract Rényi $\alpha-$OE in an experiment, and the corresponding experimental observations of the entanglement barriers with Rényi 2−OE and its symmetry resolution.

In Sec. 7.3.1 we detail the experimental protocol of classical shadows and, in Sec. 7.3.2, the associated efficient method for the post-processing of the measurement data, dubbed as *the batch shadows estimator*. In Sec. 7.3.3 we discuss the experimental results and some of its features.

7.3.1 Rényi OE from randomized measurements

In the previous sections, we have expressed OE as a function of the Schmidt spectrum $\{\lambda_i\}$. In order to express estimators of these quantities based on experimental data, one needs to rewrite them into a functional of the density matrix ρ_{AB}. In particular, the Rényi 2−OE is a fourth order function of ρ_{AB} that explicitly writes as [124]:

$$S^{(2)} = -\log \frac{\mathrm{Tr}\left(\mathcal{S}\,\rho_{AB}^{\otimes 4}\right)}{\mathrm{Tr}(\rho_{AB}^2)^2} = \tilde{S}^{(2)}(\rho_{AB}) - 2R^{(2)}(\rho_{AB}), \tag{7.2}$$

where $\mathcal{S} = \mathbb{S}_{1,4}^{(A)} \otimes \mathbb{S}_{2,3}^{(A)} \otimes \mathbb{S}_{1,2}^{(B)} \otimes \mathbb{S}_{3,4}^{(B)}$ is defined in terms of the swap operators $\mathbb{S}_{k,l}(|i_k\rangle \otimes |i_l\rangle) = |i_l\rangle \otimes |i_k\rangle$. We also have defined the unnormalized Rényi 2-OE $\tilde{S}^{(2)}(\rho_{AB}) = -\log\left(\mathrm{Tr}(\mathcal{S}\rho_{AB}^{\otimes 4})\right)$. Similar expressions for the SROE in App. C.1.2. Such functions of the density matrix for a N-qubit system can be accessed in qubit experiments via randomized measurements [113, 114, 124], as shown in Fig. 7.1a). We start with the preparation of our N-qubit state in the experiment. We apply local random unitaries u_i ($i = 1, \ldots, N$), sampled from the circular unitary ensemble (CUE) or a unitary 2−design, on the N-qubit state. We store the measurement outcome recorded on a fixed basis $s = s_1, \ldots, s_N$. We repeat this procedure for a set of N_u distinct unitaries $u^{(r)}$ and

collect N_M bit-strings for each applied unitary $s^{(r,m)} = s_1^{(r,m)}, \ldots, s_N^{(r,m)}$ with $r = 1, \ldots, N_u$ and $m = 1, \ldots, N_M$. This recorded data can then be used to construct an operator $\hat{\rho}^{(r,m)}$ as

$$\hat{\rho}^{(r,m)} = \bigotimes_{i=1}^{N} \left[3(u_i^{(r)})^\dagger \left| s_i^{(r,m)} \right\rangle \left\langle s_i^{(r,m)} \right| (u_i^{(r)}) - \mathbb{I}_2 \right]. \tag{7.3}$$

This operator is called a *classical shadow* [114] and is an unbiased estimator of the underlying quantum state, i.e. $\mathbb{E}(\hat{\rho}^{(r,m)}) = \rho$, with the expectation value taken over the applied unitaries and measurement outcomes (see also App.B of Ref.[138]).

In order to measure functions $X_n = \mathrm{Tr}(O^{(n)}\rho^{\otimes n})$ that are expectation values of a n-copy observable $O^{(n)}$ (here, in particular, we are interested in $O^{(4)} = \mathcal{S}$ on four copies), one can define an U-statistics estimator $\hat{X}_n$ given by

$$\hat{X}_n = \frac{1}{n!}\binom{N_u}{n}^{-1} \sum_{r_1 \neq \ldots \neq r_n} \mathrm{Tr}\left[O^{(n)} \bigotimes_{i=1}^{n} \hat{\rho}^{(r_i)} \right] \tag{7.4}$$

where we have the classical shadow $\hat{\rho}^{(r)} = \mathbb{E}_{N_M}[\hat{\rho}^{(r,m)}]$ constructed by averaging over all measured bit-strings for an applied unitary $u^{(r)}$. The estimator $\hat{X}_n$ is unbiased, i.e $\mathbb{E}[\hat{X}_n] = X_n$.

This estimator has been used to access properties involving functions up to $n \leq 3$ [52, 65, 116]. However, such a procedure is computationally resource heavy as it requires summing over all possible combinations of n shadows $\hat{\rho}^{(r_1)}, \ldots, \hat{\rho}^{(r_n)}$ for $r_i \in [1, \ldots, N_u]$, whose runtime scales with the number of terms involved in the above sum: $\mathcal{O}(N_u^n)$, a number that grows exponentially with the polynomial degree n. This scaling prevents us from extracting the Rényi 2−OE from experimental data of [75] (as $n > 3$). Thus we are in dire need of an alternate method with a (substantially) reduced runtime.

7.3.2 Fast estimation of high order functionals using randomized measurements data via batch shadows

In order to improve the post-processing run time of classical shadows, we propose to form $b = 1, \ldots, n' \geq n$ 'batch shadows', where each of them is an average of N_u/n' shadows:

$$\tilde{\rho}^{(b)} = (n'/N_u) \sum_{r=(b-1)N_u/n'+1}^{bN_u/n'} \tilde{\rho}^{(r)}. \tag{7.5}$$

This allows us to define an alternate unbiased estimator as in Eq. (7.4):

$$\tilde{X}_n^{(n')} = \frac{1}{n!}\binom{n'}{n}^{-1} \sum_{b_1 \neq \ldots \neq b_n} \mathrm{Tr}\left[O^{(n)} \bigotimes_{i=1}^{n} \tilde{\rho}^{(b_i)} \right] \tag{7.6}$$

The first step to evaluate the above estimator needs the construction of n' batch shadows. This is achieved by summing up all classical shadows that belong to a respective batch – a subroutine that requires $O(N_u)$ arithmetic operations (provided that the sample complexity N_u exceeds the total number of degrees of freedom in the reduced density matrix). These individual summation steps can be obviously paralellized on n' cores. Note also that, in contrast to the bare classical shadows $\rho^{(r,m)}$, the batch shadows $\tilde{\rho}^{(b)}$ are stored in memory as dense $2^{N_{AB}} \times 2^{N_{AB}}$ matrices: $\mathbb{E}[\tilde{\rho}^{(b)}] = \rho$ for all batches $b = 1, \ldots, n'$. This limits our fast estimation methods to systems sizes of up to $N_{AB} \approx 15$ qubits.

The second step requires the evaluation of $\tilde{X}_n^{(n')}$ from the constructed batch shadows that scales as $\mathcal{O}(n'^n)$. Thus by choosing $n' = n$ and assuming that $N_u \gg n'^n$, we obtain the fastest estimator with an evaluation time $\mathcal{O}(N_u)$. This is a drastic runtime improvement compared to the original U-statistics estimator in Eq. (7.4): $\mathcal{O}(N_u)$ steps (new) vs. $\mathcal{O}(N_u^n)$ steps (old). As we increase n', one starts to incorporate more terms with distinct combinations of n different shadows that were not previously considered. This results in a convergence towards the U-stat estimator, i.e $\tilde{X}_n^{(N_u)} = \hat{X}_n$, as well as in an increasing of the post-processing run-time. In order to gauge the performance of the estimator $\hat{X}_n^{(n')}$, we study its the statistical error behavior.

Statistical errors — The statistical errors in randomized measurements arise due to applying a finite number of random unitaries N_u and performing finite number of readout measurements N_M. The statistical errors of any estimator $\hat{X}$ is governed by its variance $\mathrm{Var}[\hat{X}]$. One can provide rigorous performance guarantees to estimate X_n with an accuracy ϵ from our protocol by studying variance bound provided by the Chebyshev's inequality:

$$\Pr[|\hat{X}_n^{(n')} - X_n| \geq \epsilon] \leq \mathrm{Var}[\hat{X}_n^{(n')}]/\epsilon^2. \tag{7.7}$$

In App. C.1.1, we provide a general framework that can be applied to calculate variance bounds on the batch shadow estimator for arbitrary multi-copy operators. We can provide then rigorous performance guarantees for our estimation formulas, which we can also compare with the results for classical shadows presented in Ref. [139].

From this study, in the limit of $N_M = 1$, we notice that $\mathrm{Var}[\hat{X}_n^{(n')}]$ and $\mathrm{Var}[\hat{X}_n]$ have the same scaling behavior in the high accuracy regime of $\epsilon \to 0$: that is, they are first order in $1/N_u$ and scale $\propto n^2/N_u$. Moreover, for $n' = n$, at second order in $1/N_u$, $\mathrm{Var}[\tilde{X}_n^{(n)}]$ is larger than $\mathrm{Var}[\hat{X}_n]$ by a factor of $n/(n-1)$. This shows that the required number of measurements to achieve a given accuracy ϵ is essentially the same for the fast batch shadow estimator Eq. (7.6) and the standard shadow estimator Eq. (7.4).

Of course, we can apply our general variance bound formalism to the quantities of interest for this work: $O^{(2)} = S_{12}^{(AB)}$ and $O^{(4)} = \mathcal{S}$ that give access to $R^{(2)}(\rho_{AB})$ and $\tilde{S}^{(2)}(\rho_{AB})$, respectively. In the case of Clifford shadows (i.e. each random unitary is chosen uniformly from the single-qubit Clifford group) and $n' = n$, we find that in order to estimate them with a confidence interval of δ, that is $\Pr[|\tilde{X}_n^{(n)} - X_n| \geq \epsilon] \leq \delta$, we require a number of measurements that scale

as $N_u \propto 3^N/\epsilon^2$. See Ref.[138] for details. Hence, in the worst case scenario, our measurement bound of the batch-shadow estimator of $\tilde{X}_n^{(n)}$ scales as 3^N irrespective of the order $n = 2, 4$. For evaluating $\tilde{S}^{(2)}(\rho_{AB})$, in particular, this measurement bound is an exponential improvement over the previously obtained bounds in [124]. We conjecture that this desirable scaling persists when we increase α to evaluate higher-order Rényi $\alpha-$OE.

7.3.3 Experimental results using batch shadows

The batch shadow formalism allows us to extract experimentally the Rényi $2-$OE along with its symmetry resolution. We perform our set of observations on two sets of experiments, where a global quench with a long-range XY model was realized on a string of 10 and 20 ions respectively [75]. The global quench was followed by the implementation of randomized measurement protocol involving a total of $N_u = 500$ Haar random unitaries. For each of the applied unitaries $N_M = 150$ bit-string measurements were made. Details on the modelling of quench dynamics with tensor network algorithms and the protocol have been discussed in App. C.1.1.

We consider two bipartite reduced density matrices ρ_{AB} defined on the subsystems $A = [2, 3]$ and $B = [4, 5]$ and $A = [8, 9]$ and $B = [10, 11]$ for a total chain of 10 ion and 20 ion respectively, where we have labelled the ions along the chain from 1 to N. Fig. 7.1(b-c) and Fig. 7.2 show all our experimental results with corresponding numerical simulations with, and without decoherence of the experiment. Panels a) and b) in Fig. 7.2, highlight the extracted Rényi 2-OE with the simplest batch shadow estimator.

We first observe the entanglement barrier for the considered partition of the 20 ion system in Fig. 7.1b) and Fig. 7.2a). We observe a barrier composed of a growth phase from $t = 0$ to $t \approx 3$ ms, and a decay phase from $t \approx 3$ ms to the last data point at $t = 10$ ms. The peak at $t \approx 3$ ms actually looks more like a double-peak with maxima at $t \approx 1.8$ ms and $t \approx 3.8$ ms, but we interpret this as oscillations on top of the main barrier caused by the small size of subsystems A and B. This interpretation is supported by the fact that similar finite-size effects are found in our free fermion model, as shown in Fig. 7.2d (see also Sec. 7.4). The growth phase at early times signals the creation of correlations between the two subsystems A and B, while the decay phase reflects the fact that ρ_{AB} goes towards a thermal-like density matrix with small OE. Since the system is finite, we also expect revivals of the OE at longer times, however such revivals are not yet visible in the available time window. The barrier can also be understood as a competition between the terms $\tilde{S}^{(2)}(\rho_{AB})$ and $R^{(2)}(\rho_{AB})$ in the respective regimes as shown in Fig. 7.2c) [101]. In the growth phase, the unnormalised Rényi 2-OE $\tilde{S}^{(2)}(\rho_{AB})$ grows at a faster rate compared to the state entropy $2R^{(2)}(\rho_{AB})$. In the decay phase, this behavior is inverted. These general features are consistent with the theoretical predictions of different models shown in Refs. [94, 101, 140].

Comparing Fig. 7.2a) and b), we see, however, that in the smaller system of 10 ions no similar barrier is found. In particular, we do not observe the decay phase. We discuss this case in more detail below.

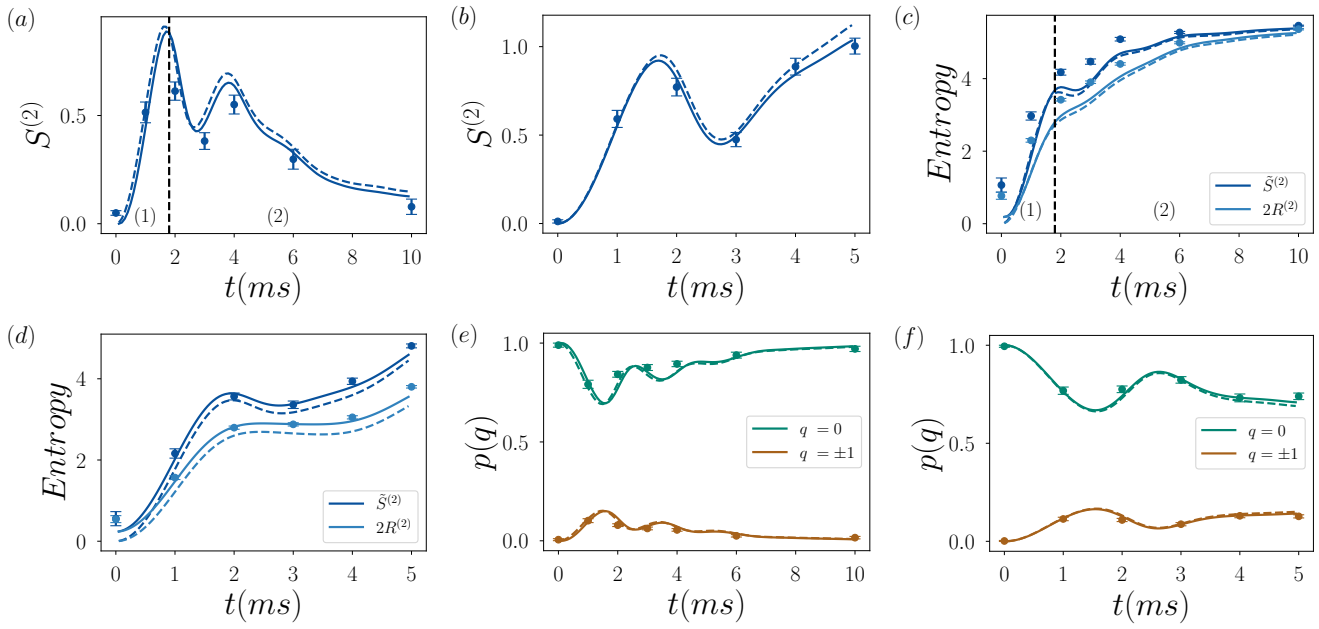

Figure 7.2: Further experimental observations: Panels (a-b) show the measured Rényi 2-OE and correspondingly, panels (c-d) the measured values of $\tilde{S}^{(2)}(\rho_{AB})$ and $R^{(2)}(\rho_{AB})$ relating to Rényi 2-OE as in Eq. (7.2) for a reduced density matrix of 4 ions from a total a system consisting of $N = 20$ and $N = 10$ ions. We observe the two phases of the entanglement barrier that is separated by a black dashed line for panels a) and c) given by: (1) the growth phase followed by (2) the decay phase. Panels (e-f) show the corresponding populations $p(q)$ for symmetry sectors $q = 0 \pm 1$, on a reduced density matrix of 4 ions taken from their respective total system of ($N = 20$ and $N = 10$). The points show experimental results with the error bars calculated with Jackknife resampling. Lines correspond to numerical simulations of the unitary dynamics (dashed) and including dissipation (solid).

Overall Fig. 7.2b) and d) show excellent agreement of the experimental data with the numerically modeled results for the 10 ion experiment. On the other hand, it is quite surprising to see that even though the individual estimations of $\tilde{S}^{(2)}(\rho_{AB})$ and $R^{(2)}(\rho_{AB})$ from the 20 ion experiment as shown in Fig. 7.2c) have systematic shifts of the experimentally measured values which is likely to an imperfect modeling of decoherence during the experiment and the measurement protocol, the corresponding measured Réyni 2-OE shows quite good agreement with the theoretical model as in Fig. 7.2a). This suggests a robustness feature of the Rényi 2-OE were errors in estimations of the two terms compensate each other. We also remark that the measured values of Rényi 2-OE are lower as shown in Fig .7.2(a-b) from the numerical simulations of the experiment.

The corresponding symmetry-resolutions for the considered bipartitions of $N = 20$ and $N = 10$ ions are shown Fig. 7.1b) and c). Their respective populations in a given symmetry sector q is given by $p(q) = \mathrm{Tr}(\Pi_q |\rho_{AB}\rangle \langle\rho_{AB}|)$ where Π_q is the projector into the eigenspace of the charge sector q [116]. This is highlighted in Fig. 7.2e) and f) respectively. At $t = 0$, we see that $q = 0$ sector is substantially populated, while the other sectors $q = \pm 1$ increase in population as a function of time. In particular, for the 20 ion system, as shown in Fig. 7.2e), we observe very low population for the section $q = \pm 1$ as it decays as a function of time. This and the finite measurement statistics available from the experiment prevents us to resolve the experimental

points for symmetry resolution sector of $q = \pm 1$ for later times. In general, we also observe from Fig. 7.1b) and c), that the sector $q = 0$, follows the features of the Rényi 2-OE. This translates, as shown in Fig. 7.1b), to an entanglement barrier for $q = 0$ sector for the 20 ions system. One can also note the absence of the barrier for $q = 0$ sector from the symmetry resolution of the 10 ion system.

Interestingly, our experimental results can also be interpreted based on the free fermions calculations detailed in Sec. 7.4, with which we can qualitatively reproduce the behavior of the OE and the SROE for systems of 10 and 20 qubits. The analogy between the experimental setup and our free fermion model originates in the fact that the breaking of integrability in the experiment is weak. Therefore the short-time dynamics is comparable to the one of an integrable system, where entanglement generation can be qualitatively understood in terms of entangled pairs of quasiparticles propagating freely through the system [86]. Deviations from integrable dynamics become relevant only on longer time scales, not accessible in the available data. As pointed out above, comparing Figs. 7.1b) and 7.1d) for 20 qubits and 20 fermionic sites respectively, we observe the same barrier shape for the OE, with oscillations due to the small subsystem size. The same barrier is found for the SROE for $q = 0$, while for $q = 1$, there is no apparent decay of the OE at long times.

We now come back to the absence of a barrier for 10 ions, Fig. 7.1c). Importantly, this absence is also noticeable in our free fermion simulations with 10 sites, see Fig. 7.1e). Instead of a single barrier, the free fermion OE displays a double-peaked shape. The second peak can be understood from a quasi-particle picture as a consequence of the subsystem A being particularly close to the boundary, as we explain now.

Recall that $A = [2, 3]$ and $B = [4, 5]$ for the chain of 10 ions, with ions labelled from 1 to 10. Importantly, part C then consists of two asymmetric pieces, $C = \{1\} \cup [6, 10]$, with a very short interval on the left and a longer one on the right. The first growth phase of the OE is interpreted as originating from pairs of quasi-particles, initially located at the same position, that travel through the system in opposite directions and generate entanglement when one member of the pair is in A and the other is in B. This interpretation of entanglement growth is usually given for the standard entanglement entropy [85], but it carries over to the OE. After the OE reaches its first maximum, it decreases because some quasiparticles, that formerly belonged to pairs shared between A and B, arrive in C and therefore stop contributing to the OE of ρ_{AB}. If the subsystems A and B were far away from the boundaries, then the OE would ultimately go to zero as the number of pairs shared between A and B would eventually vanish. This does not happen here because the particles that escape from A to C (i.e. go from site 2 to site 1 in the chain) are soon reflected against the left boundary of the system. Consequently, they come back and are re-injected into A. As a result, the OE grows again, which explains the second peak in Fig. 7.1.e). The decay of that second peak occurs because, after the reflection, both members of a pair travel to the right, so they ultimately escape to the right half-system $[6, 10]$. The decay of the second peak is not visible in the experiment, Fig. 7.1.c). We believe that the decay occurs later, on time scales not accessible

with the experimental data.

It should be possible to adapt the quasi-particle picture to describe both the experimental data and our free fermion results more quantitatively, following for what is done for the time evolution of the entanglement entropy in nearly integrable dynamics, see e.g. Ref. [141] which implements previous ideas for local observable [142]. This is however far beyond the scope of our work.

7.4 Symmetry-resolved operator entanglement in free fermionic chains

So far we have presented results for finite-size systems, in direct connection with the experimental setup. We have shown in Fig. 7.1 that most of their qualitative features can be also observed in free-fermion chains under unitary evolution, despite the model is short ranged and there is no dissipation. This connection led us to wonder whether one could extract the main physical traits of the OE and SROE of the reduced density matrix by studying the unitary time evolution of free fermions in the thermodynamic limit. Therefore, in this section, we show that in this regime the problem can be tackled analytically, unveiling some interesting properties of the SROE, such as the time delay of the charge sectors or the equipartition.

To achieve our goal, the calculation of the SROE by the definition (1.50) is a difficult task, especially for an analytic derivation. Therefore, we can apply a trick similar to what has been done for the standard entanglement resolution, i.e. connecting it with the computation of the charged moments of the reduced density matrix. Using the vectorized version of the operator ρ_{AB}, the object we want to compute is

$$\mathcal{Z}_\alpha(q) = \frac{1}{(\mathrm{Tr}[\rho_{AB}^2])^\alpha} \mathrm{Tr}[\Pi_q \left(\mathrm{Tr}_B(|\rho_{AB}\rangle \langle\rho_{AB}|)\right)^\alpha], \tag{7.8}$$

where q are the (integer) eigenvalues of $\mathcal{Q}_A$ and Π_q is the projection operator. To do so, we use the Fourier representation of Π_q

$$\Pi_q = \int_{-\pi}^{\pi} \frac{d\theta}{2\pi} e^{-iq\theta} e^{i\theta\mathcal{Q}_A}, \quad \sum_q \Pi_q = 1. \tag{7.9}$$

By plugging Eq. (7.9) into (7.8), we get

$$\mathcal{Z}_\alpha(q) = \int_{-\pi}^{\pi} \frac{d\theta}{2\pi} e^{-iq\theta} Z_\alpha(\theta), \tag{7.10}$$

where we have finally introduced the charged moments

$$Z_\alpha(\theta) = \frac{1}{(\mathrm{Tr}[\rho_{AB}^2])^\alpha} \mathrm{Tr}[\left(\mathrm{Tr}_B(|\rho_{AB}\rangle \langle\rho_{AB}|)\right)^\alpha e^{i\theta\mathcal{Q}_A}], \tag{7.11}$$

which will be the main objects we compute in the following part of this section. From Eq. (7.8), the SROE read

$$S_q^{(\alpha)}(\rho_{AB}) = \frac{1}{1-\alpha}\log\frac{\mathcal{Z}_\alpha(q)}{\mathcal{Z}_1^\alpha(q)}. \tag{7.12}$$

7.4.1 Free-fermion techniques for the OE

For the eigenstates of quadratic lattice Hamiltonians, it is possible to compute the entanglement entropies in terms of the eigenvalues of the correlation matrix of the subsystem [143, 144]. This trick can be applied also for the computation of the OE and, more generally, of the charged moments (7.11).

Let us take a free-fermionic chain of length N with $U(1)$ symmetry, described by the Hamiltonian

$$H = -\frac{1}{2}\sum_{i=1}^{N}(c_{i+1}^\dagger c_i + \text{h.c.}) \tag{7.13}$$

where $c_i^\dagger$ (c_i) is the creation (annihilation) operator such that the anticommutator $\{c_i, c_j^\dagger\} = \delta_{ij}$ and $c_{N+1} = c_1, c_{N+1}^\dagger = c_1^\dagger$, i.e. we impose periodic boundary conditions. The reduced density matrix for a subsystem $A\cup B$, ρ_{AB}, where $A\cup B = [1,\ell_A]\cup[\ell_A+1,\ell_A+\ell_B]$ consists of two adjacent intervals, can be put in a diagonal form as

$$\rho_{AB} = \bigotimes_{k=1}^{\ell_A+\ell_B}\frac{e^{-\lambda_k d_k^\dagger d_k}}{1+e^{-\lambda_k}}, \tag{7.14}$$

where $e^{-\lambda_k} = \frac{n_k}{1-n_k}$, with n_k the occupation number at a given wave vector k and d_k's are also fermionic operators satisfying $\{d_k, d_{k'}^\dagger\} = \delta_{kk'}$. It is more convenient to write Eq. (7.14) as

$$\rho_{AB} = \bigotimes_{k=1}^{\ell_A+\ell_B}\frac{|0\rangle_k\langle 0|_k + e^{-\lambda_k}|1\rangle_k\langle 1|_k}{1+e^{-\lambda_k}} = \bigotimes_{k=1}^{\ell_A+\ell_B}[(1-n_k)|0\rangle_k\langle 0|_k + n_k|1\rangle_k\langle 1|_k], \tag{7.15}$$

so that by applying the vectorization trick in Eq. (1.45) for ρ_{AB}, we get

$$\frac{|\rho_{AB}\rangle}{\sqrt{\text{Tr}[\rho_{AB}^2]}} = \bigotimes_{k=1}^{\ell_A+\ell_B}\frac{1}{\sqrt{Z_k}}[(1-n_k)|0\rangle_k|0\rangle_{\tilde{k}} + n_k|1\rangle_k|1\rangle_{\tilde{k}}] = \bigotimes_{k=1}^{\ell_A+\ell_B}\frac{1}{\sqrt{Z_k}}[1-n_k+n_k d_k^\dagger \tilde{d}_k^\dagger]|0\rangle, \tag{7.16}$$

where $Z_k = n_k^2 + (1-n_k)^2$ and the $\tilde{d}_k^\dagger$'s are new creation operators that anti-commute with all the d_k's, and $|0\rangle$ is the state annihilated by all the d_k's and $\tilde{d}_k$'s. The $2(\ell_A+\ell_B)\times 2(\ell_A+\ell_B)$ correlation matrix of the state $|\rho_{AB}\rangle$ reads

$$\langle\rho_{AB}|\begin{pmatrix} d_k^\dagger \\ \tilde{d}_k\end{pmatrix}\begin{pmatrix} d_{k'} & \tilde{d}_{k'}^\dagger\end{pmatrix}|\rho_{AB}\rangle = \frac{\delta_{kk'}}{Z_k}\begin{pmatrix} n_k^2 & n_k(1-n_k) \\ n_k(1-n_k) & (1-n_k)^2\end{pmatrix}. \tag{7.17}$$

In the basis of $d_k, \tilde{d}_k$'s, the supercharge operator takes the form

$$\mathcal{Q} = \sum_k d_k^\dagger d_k - \sum_k \tilde{d}_k^\dagger \tilde{d}_k. \tag{7.18}$$

We can collect the operators into the vector $\mathbf{f} = (d_1, \dots d_{\ell_A+\ell_B}, \tilde{d}_1^\dagger \dots \tilde{d}_{\ell_A+\ell_B}^\dagger)^t$ such that $\mathcal{Q}$ reads $\mathcal{Q} = \mathbf{f}^\dagger \mathbf{f} - (\ell_A + \ell_B)$, where $\ell_A + \ell_B$ is an additive constant.

At this point, to evaluate the charged moments in Eq. (7.11), we need to focus on the subsystem A, i.e. we can restrict the supercharge operator to $\mathcal{Q}_A$ and the correlation matrix to the subspace corresponding to the subsystem A. Going back to the spatial basis and diagonalising this matrix, we get $2\ell_A$ real eigenvalues ξ_i between 0 and 1. Therefore, one can compute the charged moments of the reduced density matrix built from $|\rho_{AB}\rangle$ in terms of the eigenvalues ξ_i as

$$Z_\alpha(\theta) = e^{-i\alpha(\ell_A+\ell_B)} \prod_{a=1}^{2\ell_A} (\xi_a^\alpha e^{i\theta} + (1-\xi_a)^\alpha). \tag{7.19}$$

Using the results in Eq. (7.12), we can compute exactly the SROE for the reduced density matrix of a free fermionic chain. We mention that this trick also allows the computation of the total OE as

$$S^{(\alpha)}(\rho_{AB}) = \frac{1}{1-\alpha} \sum_{a=1}^{2\ell_A} (\log[\xi_a^\alpha + (1-\xi_a)^\alpha)]. \tag{7.20}$$

Using this approach we compared the analytical result in Ref.[138] and the numerical results in the tight-binding model chain is displayed in Fig. 7.1f).

The agreement is good and we can also observe that there are some charge sectors with zero entanglement for $t < t_D$. However, for $t > (\ell_A + \ell_B)/2$ the discrepancy between the numerics and the analytical prediction is larger. One explanation could be that at finite ℓ_A and t the data exhibit some small corrections, and our prediction is recovered only in the scaling limit $t, \ell_A, \ell_B \to \infty$ with their ratio fixed.
For small $|q|$ we find that [138]

$$S_q^{(\alpha)}(\rho_{AB}) = \mathcal{J}(t) \left(2\log 2 - \frac{q^2}{\mathcal{J}(t)^2} \right). \tag{7.21}$$

This result states that for small $|q|$ there is an effective equipartition of the OE with violations of order $q^2/(\ell_A + \ell_B)$.
We observe that the SROE is small both at short and at large times, so it can be captured by an MPO with small bond dimension. However, it blows up linearly in the transient regime $t \leq (\ell_A + \ell_B)/(2)$, preventing efficient simulation using the MPO representation, whose bond dimension would blow up exponentially in that time window. This also happens for the total OE [94]. At short times, the reduced density matrix is still very close to the one of the pure state, and one does not gain much by approximating ρ_{AB} instead of the corresponding state; this trick becomes

efficient only at later times.
We conclude by commenting Figs. 7.1d) and 7.1e). We show that the dynamics of the SROE in the different charge sectors is affected by the finite size of the system. In particular, for $N = 20$ one can observe the entanglement barrier only in the sector $q = 0$, while for $q = 1$ the absence of the decay is consistent with the experimental results of Fig. 7.1b). Moreover, for this system size the total OE presents a single peak, while for $N = 10$, we notice the presence of two peaks in the total OE, which can be justified by the quasiparticle picture explained at the end of Sec. 7.3.3.

7.5 Conclusions

This chapter is devoted to a thorough analysis of the OE of the reduced density matrix after a global quantum quench and its symmetry resolution. These quantities linearly increase in time, before they decrease and saturate to a finite value. The presence of this barrier is strongly affected by the finite size of the system, as we demonstrated experimentally here. This feature is also visible for free fermionic systems evolving under unitary evolution.

The experimental results, also supported by tensor network simulations, have been obtained by a novel post-processing method of randomized measurements data, dubbed *batch shadows estimator*, that has practical applications to probe non-linear properties of quantum many-body systems. This method provides a faster and more efficient data-treatment technique with respect to the known ones [113] and enable us to effectively measure the OE.

We observe the presence of the entanglement barrier of the reduced density matrix of a partition of 4 ions out of $N = 10, 20$ both for the total OE and for the charge sector $q = 0$ and $N = 20$. However, the finite size effects prevent the appearance of such a barrier in the charge sectors $q = \pm 1$ and for $q = 0, N = 10$. When $N = 20$, in the charge sectors $q = \pm 1$, the available statistics only allows us to explore the early time behavior of the SROE.

For small system sizes N, the phenomenology mentioned above can be also observed in free fermionic systems without dissipation. Therefore, guided by conformal field theory and free-fermion techniques, we show that the semiclassical picture of moving quasiparticles [85, 86] can be adapted in this context, leading to a general conjecture for the charged OEs whose Fourier transform gives the desired SROE. Beyond the barrier, we observe a delay time proportional to the charge sector and an effective equipartition for small q.

Because of this phenomenology, we expect our main physical findings to show up for rather generic quench protocols. However, it would be very interesting to engineer situations in which some of them are absent, e.g. with the entanglement barrier appearing only in given charge sectors, breaking equipartition.

We mention that the time evolution of the total OE is closely related to other entanglement measures such as the reflected entropy [145, 146] (which is the OE of $\sqrt{\rho_{AB}}$), negativity [147–150], and temporal entanglement [151–153]: in these latter cases, the connection is only merely technical, but the fact that they can be computed in a similar way leads to analogous results, like

the entanglement barrier of the logarithmic negativity after a quench [154]. Our works naturally paves the way for their symmetry resolution and to understand whether their connection could be understood sector by sector.

To conclude, we remark that the also OEs of operators different from the RDM are known to capture important universal properties of the dynamics [91–94, 97, 101, 140, 155–157]. For instance, the OE of the evolution operator $U(t) = e^{-iHt}$ grows linearly in ergodic phases [94, 155], but only logarithmically in localized phases [93, 94]. Another example is the OE of a local operator O evolving in Heisenberg-picture, $O(t) = e^{iHt}Oe^{-iHt}$, which grows linearly in systems with chaotic dynamics [155] but only logarithmically for integrable dynamics [140, 156, 157]. It is then natural to wonder what happens to their SR version. Such analysis is presented in Ref.[138], where we show preliminary steps towards the general understanding of the symmetry resolution of OE, which certainly deserves further investigation.

B

Additional information on symmetry-resolved dynamics

B.1 Effective Markovian dynamics

We now provide a simple interpretation of the effective description derived in Sec 6.2. Our main interest here is to determine whether dynamical purification is an effect that relies on a specific correlation present in an effective bath (derived by applying the symmetry-resolved projectors to the density matrix), or whether it is unrelated to that, and thus captured entirely by an emergent Markovian dynamics describing $\rho_{A,q}$.

Indeed, even though the evolution of the global density matrix ρ is governed by the Markovian master equation of Eq. (6.2), the symmetry-resolved reduced density matrix $\rho_{A,q}$ could have a non-Markovian time evolution. The dissipation rates derived in Eq. (6.3) can be interpreted as an effective master equation acting directly on the symmetry-resolved reduced density matrix, with time dependent rates. We consider two arbitrary density-matrices product states, whose symmetry-resolved reduced density matrix can be written in diagonal form ρ_I, ρ_{II}, with matrix elements $a_{jj;I}$ and $a_{jj;II}$, respectively. What we are interested in is whether the two states can become dynamically more distinguishable as a function of time: if this is possible even for a finite time window, the time evolution is non-Markovian [158]. In order to address this point, we define the distance between these states as:

$$D_{I,II} = \mathrm{tr}\sqrt{\rho_I \rho_{II}}. \tag{B.1}$$

After a few lines of algebra, and defining as N, M the total rank of the density matrix and the

number of the states belonging to E_0, respectively, one obtains:

$$\begin{aligned}
\frac{\partial D}{\partial t} &= -\frac{1}{2(1+N\gamma t+MJ^2t^2)^2}\times \\
&\times \left[\sum_{j\in E_0}\frac{\gamma(a_{jj;I}+a_{jj;II}+2\gamma t)}{\sqrt{(a_{jj;I}+\gamma t)(a_{jj;II}+\gamma t)}}+\right. \\
&+ \left.\sum_{j\in E_1}\frac{(\gamma+2J^2t)(a_{jj;I}+a_{jj;II}+2\gamma t+2J^2t^2)}{\sqrt{(a_{jj;I}+\gamma t+J^2t^2)(a_{jj;II}+\gamma t+J^2t^2)}}\right]+ \\
&- \frac{2(N\gamma+2MJ^2t)}{(1+N\gamma t+MJ^2t^2)^3}\times \\
&\times \left[\sum_{j\in E_0}\sqrt{(a_{jj;I}+\gamma t)(a_{jj;II}+\gamma t)}+\right. \\
&+ \left.\sum_{j\in E_1}\sqrt{(a_{jj;I}+\gamma t+J^2t^2)(a_{jj;II}+\gamma t+J^2t^2)}\right]
\end{aligned}$$

so that, under the condition above, one has $\partial D/\partial t < 0$, as this is just the sum of two negative terms. This implies that arbitrary states of the type discussed above become less distinguishable as a function of time, a signature of effective Markovian dynamics.

The very same conclusion can be obtained on more general grounds by noticing that the rate equations above all have positive rates, thus satisfying P-divisibility criteria. At the physical level, this is a consequence of the fact that the relaxation time of the environment (in this case, the part of the system we are tracing upon in a symmetry-resolved fashion [1]) is much longer than the timescales we are interested in. For longer times (not accessible to the regime we can tackle with our theory, but definitely numerically accessible), we expect that such effective Markovian description would ultimately break down due to the bath dynamics timescales being comparable to the one characterizing the partition.

B.2 Purification in one-dimensional systems

The system we consider here is a one-dimensional version of the system considered in Sec. 6.3, that we divide into two connected partitions $A \cup B$ with N_A and N_B sites, respectively. We assume that the system is initialized in a charge-density wave $|\psi_0\rangle = |\downarrow,\uparrow,\ldots,\uparrow\rangle$ (a Néel state), and for simplicity, take N_A and N_B to be even. We consider dynamics governed by Eq. (6.8) and focus on timescales accessible within perturbation theory, that is, $J^2t^2, t\gamma \ll 1$. We are interested in the sector $q = -1$. Adapting the 2D calculations presented in the main text, we find that $\rho_A(q=-1)$

[1] We emphasize that we are dealing with a specific symmetry-resolved sector, as other sectors may feature information backflow - a proxy of non-Markovianity - at earlier times.

is divided into two blocks (in perturbation theory):

1. $E_0(-1)$: the state that is connected to the CDW by a single hopping process, or a loss event, at the boundary with rate $\lambda_0^{E_0}$
2. $E_1(-1)$: the $(N_A/2-1)$ states that are connected to the CDW by a single loss in the rest of the system with eigenvalue $\lambda_k^{E_1}$;

At the lowest order in perturbation theory, one has the following scaling of the eigenvalues of $\rho_A(-1)$:

$$\lambda_0^{E_0} = (J^2t^2+\gamma t)/A(t),\ \lambda_k^{E_1} = \gamma t/A(t)\ , \tag{B.2}$$

with normalization

$$A(t) = \gamma t(N_A/2) + J^2t^2. \tag{B.3}$$

This gives

$$\mathcal{P}_A(-1) \ = \ \frac{(N_A/2-1)\gamma^2t^2 + (J^2t^2+\gamma t)^2}{[(N_A/2)\gamma t + J^2t^2]^2}\ . \tag{B.4}$$

B.3 Sectors populations

In the quench dynamics we investigate, the population in each different subsector plays an important, practical role: it quantifies how relevant is the sector where dynamical purification occurs. Within the Bose-Hubbard model example, considering the approximation that the (-1) and (0) sectors are the only ones populated at short times, one expects that the population of the latter increases as a function of time in a manner that is linear at very short times, and quadratic in the regime of purification (a scaling similar to the prefactor $A(t)$).

In Fig. B.1, B.2, B.3, we show some sample results that illustrate this fact (that is also found in the experimental data). It is interesting to note that, for most cases, the population in the (-1) sectors is comparable to the one in the (0) around the purification timescale, irrespectively of system size and interaction regime. This feature signals that observing such effect beyond the spin models discussed in the text should involve only very modest post-selection.

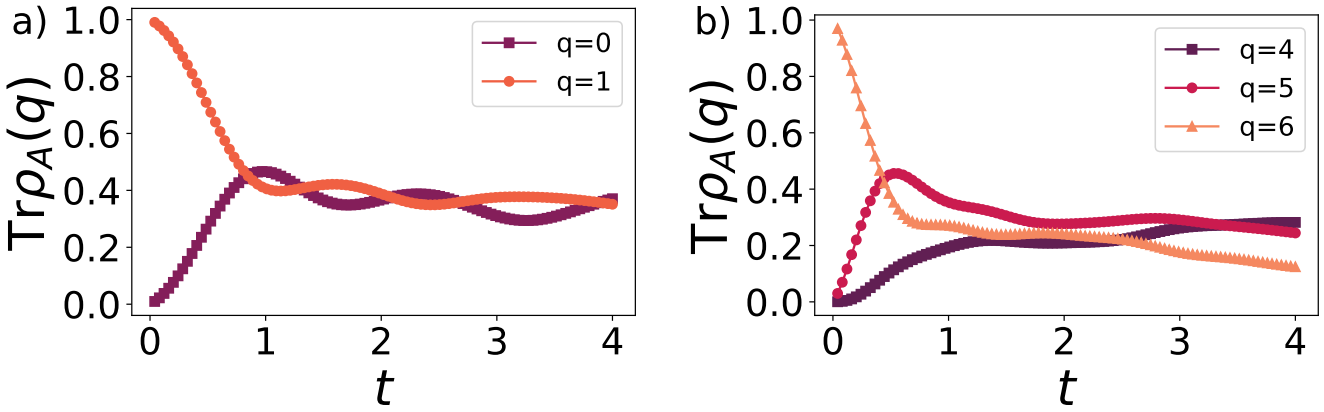

Figure B.1: Population of the symmetry sectors during the evolution of the systems described in Fig.s6.5. We consider a system with $L = 8$ and we take $A = [1,2,3,4]$ and $B = [5,6,7,8]$ Here we fix $U = 0.5J$, $\gamma = 0.1J$ and start from a) $|\psi_0\rangle = |0,1\rangle^{\otimes L/2}$, b) $|\psi_0\rangle = |1,2\rangle^{\otimes L/2}$.

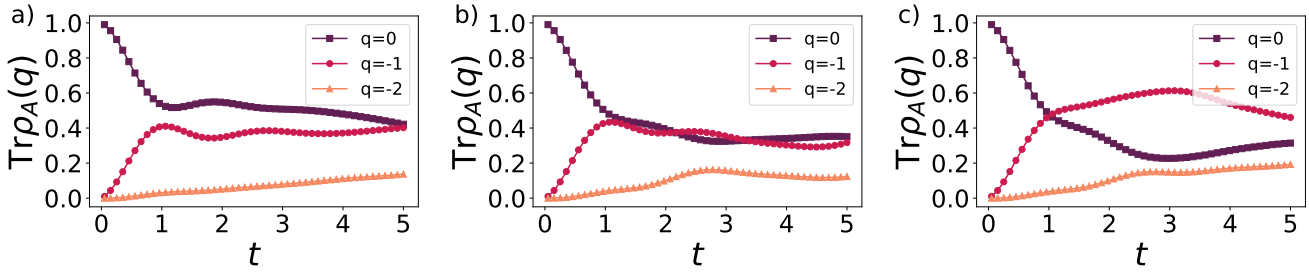

Figure B.2: Population of the symmetry sectors during the evolution of the system described in Fig.6.6, starting from state $|\downarrow\uparrow\rangle^{\otimes N/2}$. We consider a system with $L = 12$ and we take $A = [1,2,3,4,5,6]$ and $B = [7,8,9,10,11,12]$. Panel a) $w = 1$, $m = 0$, $J = 1$, $\epsilon_0 = 0$; b) $w = 1$, $m = 0$, $J = 0.1$, $\epsilon_0 = 0$; c)$w = 1$ $m = 0$, $J = 1$, $\epsilon_0 = 0.5$.

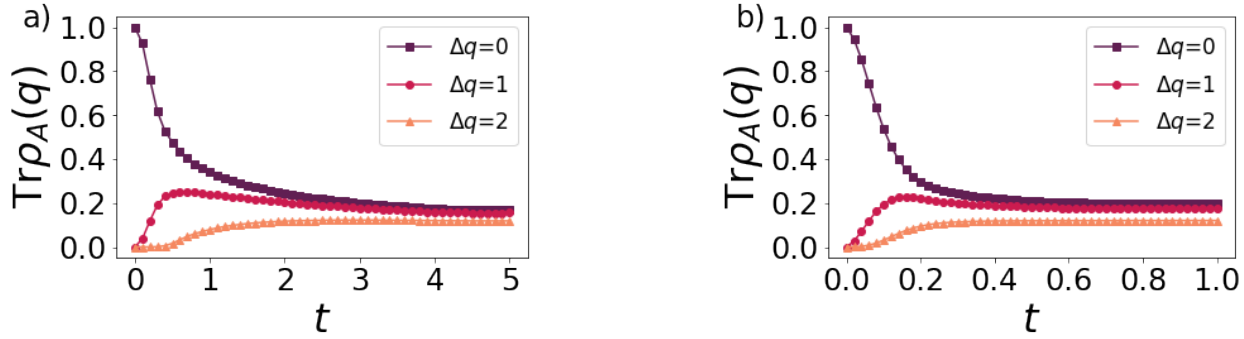

Figure B.3: Population of the symmetry sectors during the evolution of the systems described in Fig.s 6.7a)-c). We use $\Delta q = q - \ell/2$ to label the symmetry sectors. We fix $J = 1$, $\mu = 0$. In panel a) $1D$ chain with $L = 64$, $\ell = 32$, $\gamma = 0.05$; b) $2D$ square lattice, $L = 16$, $\ell = 4$, $\gamma = 0.2$.

C

Additional information on symmetry-resolved operator entanglement

C.1 More details on the experiment and classical shadows

C.1.1 Experimental platform and the theoretical modelling

This platform is realized with trapped $^{40}Ca^{+}$ atoms, each one encoding a single qubit. Coupling all ions off-resonantly with a laser beam subjects the ions to realize long-range Ising model in presence of a transverse field, whose effective Hamiltonian writes:

$$H = \hbar \sum_{i<j} J_{ij} \sigma_i^x \sigma_j^x + \hbar B \sum_i \sigma_i, \tag{C.1}$$

with $i, j = 1, \ldots, N$ and N is the total system size. To model the experiment using numerical simulations, we approximate the interaction matrix J_{ij} as a power-law $J_{ij} = J_0/|i-j|^{\alpha}$, where the values of J_0 and α depend on the specifics of each experimental realization and will be discussed later. The effective magnetic field B is considered much larger than the interaction term ($B \simeq 22 J_0$) such that terms that would break the conservation of the total magnetization, i.e. $\sigma_i^+ \sigma_j^+ + h.c.$ are energetically suppressed. The effects of decoherence on the system are taken into account considering the time evolution subject to local spin-flips and spin excitation loss. The full system dynamics is described according to a Gorini-Kossakowski-Sudarshan-Lindblad (GKSL) master equation whose $2N$ local jump operators are written as $C_i = \sqrt{\gamma_x}\sigma_i^x$ (spin flip), $C_{i+L} = \sqrt{\gamma_-}\sigma_i^-$ (excitation loss), $i = 1, \ldots, L$, with rates γ_x, γ_m. Furthermore, the experimentally prepared state is not pure. As such, it can be written as the following mixed product state

$\rho_0 = \bigotimes_i (p_i |\uparrow\rangle \langle\uparrow| + (1-p_i) |\downarrow\rangle \langle\downarrow|)$ with $p_i \approx 0.004$ for i even and $p_i \approx 0.995$ for i odd.
In the experiment, local depolarizing noise is acting during the application of the local random unitary. We model it as

$$\rho(\bar{t}) \to (1 - p_{DP}N)\rho(\bar{t}) + p_{DP} \sum_i \mathrm{Tr}_i[\rho(\bar{t})] \otimes \frac{\mathbb{I}_i}{2} \tag{C.2}$$

with $p_{DP} \approx 0.02$ and $\bar{t}$ denoting the time at which the measurement is performed.

C.1.2 Batch shadows for Rényi 2-OE and its symmetry resolution

We used the batch shadow estimator to access the Rényi 2-OE and its symmetry resolution from experimental data. The estimator of Rényi 2-OE constructed using n' batches explicitly writes following Eq: (7.2) as

$$S^{(2)} = -\log \frac{\tilde{X}_4^{(n')}}{\left(\tilde{X}_2^{(n')}\right)^2} = -\log \frac{\frac{1}{4!}\binom{n'}{4}^{-1} \sum_{b_1 \neq \ldots \neq b_4} \mathrm{Tr}\left[\mathcal{S} \bigotimes_{i=1}^4 \tilde{\rho}^{(b_i)}\right]}{\left(\frac{1}{2!}\binom{n'}{2}^{-1} \sum_{b_1 \neq b_2} \mathrm{Tr}\left[\mathbb{S} \bigotimes_{i=1}^2 \tilde{\rho}^{(b_i)}\right]\right)^2} \tag{C.3}$$

To estimate the Rényi 2-OE from the data as shown in the main text, we used the simple estimator with $n' = 4$. Alternately, the symmetry resolution for the Rényi 2-OE can be expressed as

$$S_q^{(2)} = -\log \frac{\mathrm{Tr}\left(\Pi_q \left[\mathrm{Tr}_B(|\rho_{AB}\rangle \langle\rho_{AB}|)\right]^2 \Pi_q\right)}{p(q)\mathrm{Tr}(\rho_{AB}^2)^2} \tag{C.4}$$

where Π_q is the projector into the eigenspace of the symmetry sector q and $p(q) = \mathrm{Tr}(\Pi_q |\rho_{AB}\rangle \langle\rho_{AB}|)$ are the probabilities of being in the charge sector q defined as a second order function of the density matrix ρ_{AB}. As $\mathbb{E}[\tilde{\rho}^{(b_i)}] = \rho_{AB}$ for all batch shadows, we can obtain a batch estimator of the SR Rényi 2-OE by replacing each vectorized density matrix by a distinct batch shadow. This explicitly writes:

$$S_q^{(2)} = -\log \frac{\frac{1}{4!}\binom{n'}{4}^{-1} \sum_{b_1 \neq \ldots \neq b_4} \mathrm{Tr}\left(\Pi_q \mathrm{Tr}_B\left(\left|\tilde{\rho}^{(b_1)}\right\rangle \left\langle\tilde{\rho}^{(b_2)}\right| \tilde{\rho}^{(b_3)}\right\rangle \left\langle\tilde{\rho}^{(b_4)}\right|\right)\right)}{\frac{1}{2!}\binom{n'}{2}^{-1} \sum_{b_1 \neq b_2} \mathrm{Tr}(\Pi_q \left|\tilde{\rho}^{(b_1)}\right\rangle \left\langle\tilde{\rho}^{(b_2)}\right|) \times (\tilde{X}_2^{(n')})^2} \tag{C.5}$$

The SR Rényi 2-OE were extracted from the experimental data by taking $n' = 16$.

Bibliography

[1] I. Montvay and G. Muenster, *Quantum Fields on a lattice* (Cambridge Univ. Press, Cambridge, 1994).

[2] B. Zeng, X. Chen, D.-L. Zhou, and X.-G. Wen, *Quantum Information Meets Quantum Matter* (Springer New York, 2019).

[3] S. Sachdev, *Quantum Phase Transitions* (Cambridge University Press, 2000).

[4] L. Amico, R. Fazio, A. Osterloh, and V. Vedral, Rev. Mod. Phys. **80**, 517 (2008).

[5] P. Calabrese, J. Cardy, and B. Doyon, Journal of Physics A: Mathematical and Theoretical **42**, 500301 (2009).

[6] N. Laflorencie, Physics Reports **646**, 1 (2016).

[7] P. Buividovich and M. Polikarpov, Physics Letters B **670**, 141 (2008).

[8] H. Casini, M. Huerta, and J. A. Rosabal, Physical Review D **89**, 085012 (2014).

[9] N. Laflorencie and S. Rachel, Journal of Statistical Mechanics: Theory and Experiment **2014**, P11013 (2014).

[10] J. C. Xavier, F. C. Alcaraz, and G. Sierra, Physical Review B **98**, 041106 (2018).

[11] M. Goldstein and E. Sela, Physical Review Letters **120**, 200602 (2018).

[12] G. Parez, R. Bonsignori, and P. Calabrese, Phys. Rev. B **103**, L041104 (2021).

[13] J. I. Cirac and P. Zoller, Nature Physics **8**, 264 (2012).

[14] I. Buluta, S. Ashhab, and F. Nori, Reports on Progress in Physics **74**, 104401 (2011).

[15] J. Preskill, Quantum **2**, 79 (2018).

[16] R. Blatt and C. Roos, Nature Physics **8**, 277 (2012).

[17] I. Bloch, J. Dalibard, and S. Nascimbène, Nature Physics **8**, 267 (2012).

[18] A. Browaeys and T. Lahaye, Nature Physics **16**, 132 (2020).

[19] S. Schmidt and J. Koch, Annalen der Physik **525**, 395 (2013).

[20] J. M. Gambetta, J. M. Chow, and M. Steffen, npj Quantum Information **3**, 2 (2017).

[21] H. Häffner, C. Roos, and R. Blatt, Physics Reports **469**, 155 (2008).

[22] E. Cornfeld, M. Goldstein, and E. Sela, Physical Review A **98**, 032302 (2018).

[23] S. Diehl, A. Micheli, A. Kantian, B. Kraus, H. P. Büchler, and P. Zoller, Nature Physics **4**, 878 (2008).

[24] F. Verstraete, M. M. Wolf, and J. Ignacio Cirac, Nature Physics **5**, 633 (2009).

[25] B. Kraus, H. P. Büchler, S. Diehl, A. Kantian, A. Micheli, and P. Zoller, Physical Review A **78**, 042307 (2008).

[26] H. P. Breuer and F. Petruccione, *The theory of open quantum systems* (Oxford University Press, 2002).

[27] S. Haroche and J. M. Raimond, *Exploring the Quantum: Atoms, Cavities, and Photons*.

[28] C. Gardiner and P. Zoller, *The Quantum World of Ultra-Cold Atoms and Light Book I: Foundations of Quantum Optics* (IMPERIAL COLLEGE PRESS, 2014).

[29] T. Brydges, A. Elben, P. Jurcevic, B. Vermersch, C. Maier, B. P. Lanyon, P. Zoller, R. Blatt, and C. F. Roos, Science **364**, 260 (2019).

[30] M. Ohliger, V. Nesme, and J. Eisert, New Journal of Physics **15**, 015024 (2013).

[31] S. J. van Enk and C. W. J. Beenakker, Physical Review Letters **108**, 110503 (2012).

[32] A. Elben, B. Vermersch, M. Dalmonte, J. I. Cirac, and P. Zoller, Physical Review Letters **120**, 050406 (2018).

[33] B. Vermersch, A. Elben, M. Dalmonte, J. I. Cirac, and P. Zoller, Physical Review A **97**, 023604 (2018).

[34] H.-Y. Huang, R. Kueng, and J. Preskill, Nature Physics , 1050 (2020).

[35] M. Paini and A. Kalev, (2019), arXiv:1910.10543 .

[36] A. Elben, R. Kueng, H.-Y. R. Huang, R. van Bijnen, C. Kokail, M. Dalmonte, P. Calabrese, B. Kraus, J. Preskill, P. Zoller, and B. Vermersch, Physical Review Letters **125**, 200501 (2020).

[37] D. Azses, R. Haenel, Y. Naveh, R. Raussendorf, E. Sela, and E. G. Dalla Torre, Physical Review Letters **125**, 120502 (2020).

[38] A. Messiah, *Quantum Mechanics*, Quantum Mechanics No. vol. 2 (Elsevier Science, 1981).

[39] S. de Léséleuc, V. Lienhard, P. Scholl, D. Barredo, S. Weber, N. Lang, H. P. Büchler, T. Lahaye, and A. Browaeys, Science **365**, 775 (2019).

[40] N. Syassen, D. M. Bauer, M. Lettner, T. Volz, D. Dietze, J. J. García-Ripoll, J. I. Cirac, G. Rempe, and S. Dürr, Science **320**, 1329 (2008).

[41] A. J. Daley, J. M. Taylor, S. Diehl, M. Baranov, and P. Zoller, Phys. Rev. Lett. **102**, 040402 (2009).

[42] C. Muschik, M. Heyl, E. Martinez, T. Monz, P. Schindler, B. Vogell, M. Dalmonte, P. Hauke, R. Blatt, and P. Zoller, New Journal of Physics **19**, 103020 (2017).

[43] E. A. Martinez, C. A. Muschik, P. Schindler, D. Nigg, A. Erhard, M. Heyl, P. Hauke, M. Dalmonte, T. Monz, P. Zoller, and R. Blatt, Nature **534**, 516 (2016).

[44] M. C. Bañuls, R. Blatt, J. Catani, A. Celi, J. I. Cirac, M. Dalmonte, L. Fallani, K. Jansen, M. Lewenstein, S. Montangero, C. A. Muschik, B. Reznik, E. Rico, L. Tagliacozzo, K. Van Acoleyen, Verstraete, *et al.*, The European Physical Journal D **74**, 165 (2020).

[45] I. Peschel, Journal of Physics A: Mathematical and General **36**, L205 (2003).

[46] I. Peschel and V. Eisler, Journal of Physics A: Mathematical and Theoretical **42**, 504003 (2009).

[47] P. Kos and T. Prosen, Journal of Statistical Mechanics: Theory and Experiment **2017**, 123103 (2017).

[48] V. Alba and F. Carollo, Phys. Rev. B **103**, L020302 (2021).

[49] A. Elben, B. Vermersch, R. van Bijnen, C. Kokail, T. Brydges, C. Maier, M. K. Joshi, R. Blatt, C. F. Roos, and P. Zoller, Physical Review Letters **124**, 010504 (2020).

[50] B. Vermersch, A. Elben, L. M. Sieberer, N. Y. Yao, and P. Zoller, Physical Review X **9**, 021061 (2019).

[51] M. K. Joshi, A. Elben, B. Vermersch, T. Brydges, C. Maier, P. Zoller, R. Blatt, and C. Roos, Physical Review Letters **124**, 240505 (2020).

[52] A. Elben, J. Yu, G. Zhu, M. Hafezi, F. Pollmann, P. Zoller, and B. Vermersch, Science Advances **6**, eaaz3666 (2020).

[53] Z.-P. Cian, H. Dehghani, A. Elben, B. Vermersch, G. Zhu, M. Barkeshli, P. Zoller, and M. Hafezi, Phys. Rev. Lett. **126**, 050501 (2021).

[54] Y. Zhou, P. Zeng, and Z. Liu, Physical Review Letters **125**, 200502 (2020).

[55] M. C. Tran, B. Dakić, F. Arnault, W. Laskowski, and T. Paterek, Physical Review A **92**, 050301 (2015).

[56] M. C. Tran, B. Dakić, W. Laskowski, and T. Paterek, Physical Review A **94**, 042302 (2016).

[57] A. Ketterer, N. Wyderka, and O. Gühne, Physical Review Letters **122**, 120505 (2019).

[58] W.-H. Zhang, C. Zhang, Z. Chen, X.-X. Peng, X.-Y. Xu, P. Yin, S. Yu, X.-J. Ye, Y.-J. Han, J.-S. Xu, G. Chen, C.-F. Li, and G.-C. Guo, Physical Review Letters **125**, 030506 (2020).

[59] L. Knips, J. Dziewior, W. Kłobus, W. Laskowski, T. Paterek, P. J. Shadbolt, H. Weinfurter, and J. D. A. Meinecke, npj Quantum Information **6** (2020), 10.1038/s41534-020-0281-5.

[60] A. Elben, B. Vermersch, C. F. Roos, and P. Zoller, Physical Review A **99**, 052323 (2019).

[61] S. Aaronson, *Proceedings of the 50th Annual ACM SIGACT Symposium on Theory of Computing*, STOC 2018 (Association for Computing Machinery, New York, NY, USA, 2018) pp. 325–338.

[62] D. Gross, K. Audenaert, and J. Eisert, Journal of Mathematical Physics **48**, 052104 (2007).

[63] C. Dankert, R. Cleve, J. Emerson, and E. Livine, Physical Review A **80**, 012304 (2009).

[64] M. Guţă, J. Kahn, R. Kueng, and J. A. Tropp, J. Phys. A **53**, 204001 (2020).

[65] A. Neven, J. Carrasco, V. Vitale, C. Kokail, A. Elben, M. Dalmonte, P. Calabrese, P. Zoller, B. Vermersch, R. Kueng, and B. Kraus, npj Quantum Inf **7**, 152 (2021).

[66] U. Schollwöck, Annals of Physics **326**, 96 (2011).

[67] E. Cornfeld, E. Sela, and M. Goldstein, Phys. Rev. A **99**, 062309 (2019).

[68] S. Murciano, R. Bonsignori, , and P. Calabrese, SciPost Phys. **10**, 111 (2021).

[69] A. Kitaev, Annals of Physics **321**, 2 (2006).

[70] C. Monroe, W. C. Campbell, L.-M. Duan, Z.-X. Gong, A. V. Gorshkov, P. Hess, R. Islam, K. Kim, N. M. Linke, G. Pagano, *et al.*, Review Modern Physics **93**, 025001 (2021).

[71] A. Browaeys and T. Lahaye, Nature Physics **16**, 132 (2020).

[72] L. K. Joshi, A. Elben, A. Vikram, B. Vermersch, V. Galitski, and P. Zoller, Physical Review X **12**, 011018 (2022).

[73] A. M. Kaufman, M. E. Tai, A. Lukin, M. Rispoli, R. Schittko, P. M. Preiss, and M. Greiner, Science **353**, 794 (2016).

[74] J. Vovrosh and J. Knolle, Scien. Reports **11**, 1 (2021).

[75] T. Brydges, A. Elben, P. Jurcevic, B. Vermersch, C. Maier, B. P. Lanyon, P. Zoller, R. Blatt, and C. F. Roos, Science **364**, 260 (2019).

[76] K. J. Satzinger, Y.-J. Liu, A. Smith, C. Knapp, M. Newman, C. Jones, Z. Chen, C. Quintana, X. Mi, A. Dunsworth, C. Gidney, I. Aleiner, F. Arute, K. Arya, J. Atalaya, Babbush, *et al.*, Science **374**, 1237 (2021).

[77] J. Li, R. Fan, H. Wang, B. Ye, B. Zeng, H. Zhai, X. Peng, and J. Du, Physical Review X **7**, 031011 (2017).

[78] M. K. Joshi, A. Elben, B. Vermersch, T. Brydges, C. Maier, P. Zoller, R. Blatt, and C. F. Roos, Physical Review Letters **124**, 240505 (2020).

[79] X. Mi, P. Roushan, C. Quintana, S. Mandrà, J. Marshall, C. Neill, F. Arute, K. Arya, J. Atalaya, R. Babbush, J. C. Bardin, R. Barends, J. Basso, A. Bengtsson, S. Boixo, *et al.*, Science **374**, 1479 (2021), https://www.science.org/doi/pdf/10.1126/science.abg5029 .

[80] Nature Review Physics **1**, 538 (2019).

[81] G. Vidal, Physical Review Letters **93**, 040502 (2004).

[82] F. Verstraete, V. Murg, and J. Cirac, Adv. Physics **57**, 143 (2008).

[83] U. Schollwöck, Ann. Physics **326**, 96 (2011).

[84] S. Paeckel, T. Köhler, A. Swoboda, S. R. Manmana, U. Schollwöck, and C. Hubig, Ann. Physics **411**, 167998 (2019).

[85] P. Calabrese and J. Cardy, Journal of Statistical Mechanics , P04010 (2005).

[86] V. Alba and P. Calabrese, PNAS **114**, 7947 (2017).

[87] S. Norbert, W. Michael M., V. Frank, and C. J. Ignacio, Physical Review Letters **100**, 030504 (2008).

[88] T. Barthel and U. Schollwöck, Physical Review Letters **100** (2008).

[89] M. Cramer, C. M. Dawson, J. Eisert, and T. J. Osborne, Physical Review Letters **100**, 030602 (2008).

[90] P. Calabrese, F. H. L. Essler, and M. Fagotti, Physical Review Letters **106**, 227203 (2011).

[91] T. Prosen and I. Pižorn, Physical Review A **76**, 032316 (2007).

[92] I. Pižorn and T. Prosen, Physical Review B **79**, 184416 (2009).

[93] T. Zhou and D. J. Luitz, Physical Review B **95**, 094206 (2017).

[94] J. Dubail, J. Physics A **50**, 234001 (2017).

[95] K. Noh, L. Jiang, and B. Fefferman, Quantum **4**, 318 (2020).

[96] T. Rakovszky, C. von Keyserlingk, and F. Pollmann, Physical Review B **105**, 075131 (2022).

[97] D. Wellnitz, G. Preisser, V. Alba, J. Dubail, and J. Schachenmayer, arXiv:2201.05099 (2022).

[98] O. Gühne and G. Tóth, Physics Reports **474**, 1 (2009).

[99] P. Zanardi, C. Zalka, and L. Faoro, Physical Review A **62**, 030301 (2000).

[100] P. Zanardi, Physical Review A **63**, 040304 (2001).

[101] H. Wang and T. Zhou, Journal of High Energy Physics **2019** (2019).

[102] I. Reid and B. Bertini, Physical Review B **104**, 014301 (2021).

[103] M. Rigol, V. Dunjko, and M. Olshanii, Nature **452**, 854 (2008).

[104] T. Mori, T. N. Ikeda, E. Kaminishi, and M. Ueda, J. Physics B **51**, 112001 (2018).

[105] K. Mallayya, M. Rigol, and W. De Roeck, Physical Review X **9**, 021027 (2019).

[106] J. M. Deutsch, Physical Review A **43**, 2046 (1991).

[107] M. Srednicki, Physical Review E **50**, 888 (1994).

[108] L. D'Alessio, Y. Kafri, A. Polkovnikov, and M. Rigol, Adv. Physics **65**, 239 (2016).

[109] M. Rigol, V. Dunjko, V. Yurovsky, and M. Olshanii, Physical Review Letters **98**, 050405 (2007).

[110] M. Cramer and J. Eisert, New J. Physics **12**, 055020 (2010).

[111] L. Vidmar and M. Rigol, Journal of Statistical Mechanics , 064007 (2016).

[112] P. Calabrese, F. H. L. Essler, and G. Mussardo, Journal of Statistical Mechanics , 064001 (2016).

[113] A. Elben, S. T. Flammia, H.-Y. Huang, R. Kueng, J. Preskill, B. Vermersch, and P. Zoller, arXiv:2203.11374 (2022).

[114] H.-Y. Huang, R. Kueng, and J. Preskill, Nature Physics **16**, 1050 (2020).

[115] A. Rath, R. van Bijnen, A. Elben, P. Zoller, and B. Vermersch, arXiv:2102.13524 .

[116] V. Vitale, A. Elben, R. Kueng, A. Neven, J. Carrasco, B. Kraus, P. Zoller, P. Calabrese, B. Vermersch, and M. Dalmonte, SciPost Phys. **12**, 106 (2022).

[117] A. Elben, B. Vermersch, R. Van Bijnen, C. Kokail, T. Brydges, C. Maier, M. K. Joshi, R. Blatt, C. F. Roos, and P. Zoller, Physical Review Letters **124**, 10504 (2020).

[118] D. Zhu, Z.-P. Cian, C. Noel, A. Risinger, D. Biswas, L. Egan, Y. Zhu, A. M. Green, C. H. Alderete, N. H. Nguyen, Q. Wang, A. Maksymov, Y. Nam, M. Cetina, N. M. Linke, M. Hafezi, and C. Monroe, arXiv:2107.11387 (2021).

[119] D. Gross, Y.-K. Liu, S. T. Flammia, S. Becker, and J. Eisert, Phys. Rev. Lett. **105**, 150401 (2010).

[120] R. Kueng, H. Rauhut, and U. Terstiege, Appl. Comput. Harmon. Anal. **42**, 88 (2017).

[121] R. O'Donnell and J. Wright, in *STOC'16—Proceedings of the 48th Annual ACM SIGACT Symposium on Theory of Computing* (ACM, New York, 2016) pp. 899–912.

[122] J. Haah, A. W. Harrow, Z. Ji, X. Wu, and N. Yu, IEEE Trans. Inf. Theory **63**, 5628 (2017).

[123] M. Paini and A. Kalev, arXiv preprint arXiv:1910.10543 (2019).

[124] Z. Liu, Y. Tang, H. Dai, P. Liu, S. Chen, and X. Ma, arXiv:2203.08391 (2022).

[125] N. Laflorencie and S. Rachel, Journal of Statistical Mechanics **2014**, P11013 (2014).

[126] M. Goldstein and E. Sela, Physical Review Letters **120**, 200602 (2018).

[127] J. C. Xavier, F. C. Alcaraz, and G. Sierra, Physical Review B **98**, 041106 (2018).

[128] G. Parez, R. Bonsignori, and P. Calabrese, Physical Review B **103**, L041104 (2021).

[129] G. Parez, R. Bonsignori, and P. Calabrese, Journal of Statistical Mechanics **2021**, 093102 (2021).

[130] D. Azses, E. G. Dalla Torre, and E. Sela, Physical Review B **104**, L220301 (2021).

[131] X. Turkeshi, P. Ruggiero, V. Alba, and P. Calabrese, Physical Review B **102**, 014455 (2020).

[132] S. Murciano, G. Di Giulio, and P. Calabrese, Journal of High Energy Physics **2020**, 1 (2020).

[133] L. Capizzi and P. Calabrese, Journal of High Energy Physics **2021**, 1 (2021).

[134] S. Murciano, P. Ruggiero, and P. Calabrese, Journal of Statistical Mechanics **2020**, 083102 (2020).

[135] S. Murciano, G. D. Giulio, and P. Calabrese, SciPost Physics **8**, 46 (2020).

[136] S. Fraenkel and M. Goldstein, SciPost Physics **11**, 85 (2021).

[137] A. Lukin, M. Rispoli, R. Schittko, M. E. Tai, A. M. Kaufman, S. Choi, V. Khemani, J. Léonard, and M. Greiner, Science **364**, 256 (2019).

[138] A. Rath, V. Vitale, S. Murciano, M. Votto, J. Dubail, R. Kueng, C. Branciard, P. Calabrese, and B. Vermersch, arXiv:2209.04393 (2022).

[139] A. Rath, C. Branciard, A. Minguzzi, and B. Vermersch, Physical Review Letters **127**, 260501 (2021).

[140] B. Bertini, P. Kos, and T. Prosen, SciPost Physics **8**, 67 (2020).

[141] B. Bertini and P. Calabrese, Physical Review B **102**, 094303 (2020).

[142] B. Bertini, F. H. L. Essler, S. Groha, and N. J. Robinson, Physical Review Letters **115**, 180601 (2015).

[143] I. P. M. C. Chung, Physical Review B **64**, 064412 (2001).

[144] I. Peschel, J. Physics A **36**, 205 (2003).

[145] S. Dutta and T. Faulkner, Journal of High Energy Physics **3**, 178 (2021).

[146] P. Bueno and H. Casini, Journal of High Energy Physics **5**, 103 (2020).

[147] P. Calabrese, J. Cardy, and E. Tonni, Physical Review Letters **109**, 130502 (2012).

[148] P. Calabrese, J. Cardy, and E. Tonni, Journal of Statistical Mechanics: Theory and Experiment **2013**, P02008 (2013).

[149] V. Eisler and Z. Zimborás, New Journal of Physics **17**, 053048 (2015).

[150] H. Shapourian, K. Shiozaki, and S. Ryu, Physical Review B **95**, 165101 (2017).

[151] A. Lerose, M. Sonner, and D. A. Abanin, Physical Review X **11**, 021040 (2021).

[152] M. Sonner, A. Lerose, and D. A. Abanin, Ann. Physics **431**, 168552 (2021).

[153] G. Giudice, G. Giudici, M. Sonner, J. Thoenniss, A. Lerose, D. A. Abanin, and L. Piroli, Physical Review Letters **128**, 220401 (2022).

[154] V. Alba and P. Calabrese, EPL **126**, 60001 (2019).

[155] C. Jonay, D. A. Huse, and A. Nahum, arXiv:1803.00089 (2018).

[156] V. Alba, J. Dubail, and M. Medenjak, Physical Review Letters **122**, 250603 (2019).

[157] B. Bertini, P. Kos, and T. Prosen, SciPost Physics **8**, 068 (2020).

[158] H.-P. Breuer, E.-M. Laine, J. Piilo, and B. Vacchini, Reviews of Modern Physics **88**, 021002 (2016).

IV

Entanglement based topological invariants

This part is based on the following publications:

[1] *Entanglement topological invariants for one-dimensional topological superconductors*. P. Fromholz, G. Magnifico, V. Vitale, T. Mendes-Santos, M. Dalmonte, Physical Review B 101 (8), 085136 (2020)

[2] *Topological entanglement properties of disconnected partitions in the Su-Schrieffer-Heeger model*. T. Micallo, V. Vitale, M. Dalmonte, P. Fromholz, SciPost Phys. Core 3, 012 (2020)

8

Kitaev p-wave superconductor

8.1 Introduction

Recently, entanglement has emerged as a groundbreaking diagnostic to characterize and classify many-body quantum phenomena in- and out-of-equilibrium [1–4]. An archetypal example is the possibility of unambiguously detecting topological order in two-dimensional systems via the topological entanglement entropy (TEE) [5–7]. The latter spots the presence of 'long-range' entanglement which is not distillable via local operations; consequently, it defines a genuine entanglement order parameter, that distinguishes phases depending on their quasiparticle content [8]. This insight has been widely employed in the characterization of topologically ordered states in numerical simulations [9–11], and has stimulated the search for experimentally realistic entanglement probes [12–18].

While the definition of the TEE naturally emerges from gauge theories in two-dimensions, the existence of topological invariants based solely on entanglement properties in one-dimensional (1D) topological matter - e.g., in the form of an order parameter - is presently not clear. In 1D, bipartite entanglement of *connected* partitions does not display informative scaling corrections [2, 3]. Its finer structure - captured by the entanglement spectrum -, provides sharp *sine qua non* [19–21], but even the entanglement spectrum of single partitions is not able to distinguish the topological character of wave functions [1]. Indeed, at the field theory level and in 1D, connected bipartite entanglement is strongly influenced by ultra-violet contributions due to edges, and is thus not immediately linked to 'universal' information.

In this work, we show how entanglement and Rényi entropies of *disconnected partitions* provide a set of entanglement order parameters for one-dimensional topological superconductors

[1] Examples include the equivalence between the entanglement spectra of the ground state of finite Ising and Kitaev chains, and spin ladders [19].

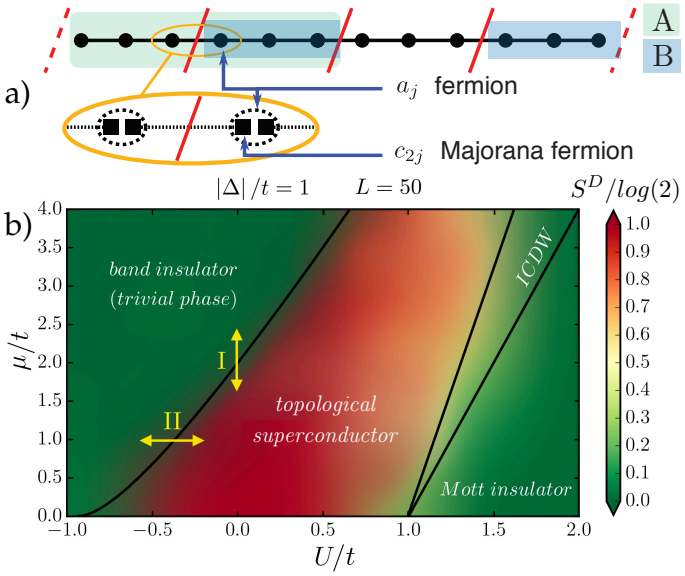

Figure 8.1: (Color online) Partitions associated with the entanglement topological order parameter and the phase diagram of the interacting Kitaev chain. Panel *a)*: schematics of the partitions A (shaded, green) and B (shaded, blue) considered here. Each site of the chain hosts a spin-less fermion degree of freedom a_j, that can be decomposed into two Majorana fermions c_{2j} and c_{2j+1}. The orange circle magnifies the cut across partitions: deep in the topological phase, neighboring Majorana fermions belonging to different physical sites are coupled (dashed line). The partition cut takes place exactly between the two coupled Majorana fermions. Panel *b)*: disconnected von Neumann entropy S^{D} as a function of $\mu/t, U/t$, at fixed $\Delta = 1$. Black lines are from Ref. [22]. The color plot is obtained via interpolation on a 5 x 7 grid. Clearer evidence of the quantization of S^{D} in a phase and the sharpness of the transition requires a lot of points, as we highlight on the lines I and II in Sec. 8.3.2.

(TSCs) [23, 24]. These order parameters satisfy the following properties: *(i)* they are quantized to 0 or $\log 2$ when the phase is topologically trivial or not-trivial respectively, and are thus able to detect the single entanglement bit - an ebit - that can be distilled from the ground state manifold; *(ii)* they display a scaling behavior when approaching quantum phase transitions, thus defining entanglement critical exponents that describe the build-up of non-local quantum correlations across such transitions; *(iii)* some of them are experimentally measurable in- and out-of-equilibrium utilizing recently introduced [14, 15] and demonstrated [25] techniques based on random measurement methods [26].

Following Ref. [27], we consider the F-function between two partitions A, B, which compensate for all edges and volume contributions in an open chain of length L. These properties are required to avoid non-universal effects: the significance of our diagnostics relies on an underlying gauge theory description below, which calls for quantities that are divergence-free in the continuum limit, whose details can be found in Ref. [28]. To diagnose the presence of non-local correlations in the system, we choose two partitions with *different connectivity*, as shown in Fig. 8.1 a). The resulting disconnected n-entropies S_n^{D} read:

$$S_n^{\mathrm{D}} = S_{A,n} + S_{B,n} - S_{A\cup B,n} - S_{A\cap B,n}, \tag{8.1}$$

where $S_{F,n}$ is the bipartite Rényi entropy of order n of the partition $F = A, B, A \cup B$ or $A \cap B$. We define L_α as the size of a given partition and L_D as the distance between the two different parts of B. Unless stated otherwise, we consider the representative case $L_A = L_B$, which provides a cleaner finite-size scaling analysis.

We denote the case $n = 1$ as S^{D}, that corresponds to the von Neumann entropy, and satisfies $S^{\mathrm{D}} > 0$ because of strong subadditivity. This entropy improves from Ref. [29] that uses two systems with different boundary conditions. It has been considered in Ref. [30], which pointed out a strong analogy between bosonic symmetry-protected topological phases (SPTPs) and error-correcting codes. Here, we focus instead on fermionic phases where topology stems from an underlying fundamental symmetry (parity) which cannot be broken by any Hamiltonian perturbation. This condition plays a crucial role in defining the gauge-theory picture describing the entanglement content of such states while the non-local correlations introduced by the fermionic algebra via the Jordan-Wigner string are responsible for such analogy.

At a qualitative level, the key in S^{D}_n is the disconnected partition B: all other terms are complementary, and only required to eliminate non-universal boundary and volume terms. In Fig. 8.1 b), we show the finite-size behavior of S^{D} across the phase diagram of interacting Kitaev chains: this plot illustrates graphically how, even at modest system and partition sizes, S^{D} clearly distinguish topological from trivial phases. We note that Ref. [31] computes a quantity coinciding with S^{D}_n for the non-interacting Kitaev chain, but it should deviate when a quantum spontaneous symmetry breaking phase is involved.

The present study is divided into the theoretical part Sec. 8.2 and the computational part Sec. 8.3. The first part introduces shortly the Kitaev model (Sec. 8.2.1). Then, it both derives and gives an intuitive picture of entanglement and the topological order parameter S^{D} in the deep topological or trivial regime (Sec. 8.2.2) and using lattice gauge theories (App. D.1). The computational part displays the efficiency of S^{D} as a topological detector (Sec. 8.3.1), reveals its universal behavior at the transition (Sec. 8.3.2), shows its response to quenches which is typical of a topological invariant (Sec. 8.3.3), and confirms its robustness to symmetry-preserving disorder (Sec. 8.3.4). We then discuss the existing experimental relevancy of the detector in Sec. 8.4, before concluding. The appendices mirror the main structure of the article and add miscellaneous details referred to in the text. In particular, appendix D.2 provides a longer introduction on the Kitaev wire for the unfamiliar reader while appendix D.4 attempts a proof of the equivalence between all S^{D}_n as topological detecting quantities.

8.2 Disconnected entropy of the interacting Kitaev wire

The Kitaev wire gives a prime example of a topological phase in 1D, with well-known behavior deep into either the topological or trivial phase. There, a topological signature is more easily extracted and identified from the entanglement of a ground state. An analytical treatment is possible and presented here.

8.2.1 The Model Hamiltonian.

We consider the interacting version of Kitaev p-wave superconductor, whose Hamiltonian reads:

$$H = \sum_{j=1}^{L-1} \left[-t(a_j^\dagger a_{j+1} + \text{h.c.}) + (\Delta a_j a_{j+1} + \text{h.c.}) + 4U \left(n_j - \frac{1}{2} \right) \left(n_{j+1} - \frac{1}{2} \right) \right] - \mu \sum_{j=1}^{L} n_j, \quad (8.2)$$

where $a_j^\dagger$ (a_j) are the creation (annihilation) operators of the spinless fermion on site j, $n_j = a_j^\dagger a_j$, t is the hopping amplitude, Δ is the superconducting amplitude, U is the nearest-neighbor interaction, and μ is the chemical potential. The phase diagram of the model is known [22, 32] and displays a TSC phase, in addition to topologically trivial phases, including a band insulator, a Mott insulator, and an incommensurate charge-density-wave (ICDW) phase. For any state in the Hilbert space, the bipartite properties of a simply connected partition are equivalent to the ones of the XYZ spin chain obtained from Eq. (8.2) after applying a Jordan-Wigner transformation. As such, they are uninformative about the topological origin of a given phase.

8.2.2 Disconnected entropies at exactly soluble points

Therefore, the goal is to find a combination of entropies able to both unambiguously capture the influence of non-locality in the ground state properties and identify the amount of information - in this case, a single ebit - that can be stored in the ground state manifold. The goal is reached for S^{D} which contains the simplest non-trivial disconnected partition, S_B while all other terms only compensate possible volume and edge effects.

For conformal phases, S_n^{D} is immediately given by conformal field theory [2, 33, 34], and vanishes in the thermodynamic limit. For gapped phases, one has to distinguish between topologically trivial and non-trivial phases. We analyze here the limiting cases.

(i) $t = \Delta = U = 0, \mu > 0$: the system is a band insulator, and the density matrix of arbitrary partitions has rank 1 both in fermionic and spin systems. This immediately gives $S_n^{\text{D}} = 0$. The same result holds in the Mott insulator phase. Thus, the thermodynamic limit of S_n^{D} cannot distinguish conformal phases and trivial phases. Only the finite size correction of S_n^{D} may distinguish them.

(ii) $t = \Delta = 1 \gg |\mu|, U = 0$: this regime is representative of the TSC phase. Its correspondent in the XYZ model is a ferromagnetic phase, which we analyze first as a representative of a symmetry-broken phase. There, the lowest energy states at any finite size are equal weight superpositions of the two ferromagnetic states, $|\Psi_{XYZ}\rangle = (|\uparrow\uparrow\uparrow ...\rangle \pm |\downarrow\downarrow\downarrow ...\rangle / \sqrt{2}$, separated by a gap $\delta \propto \mathrm{e}^{-L}$. For both states, any reduced density matrix of an arbitrary spatial partition is equivalent, and thus $S_n^{\text{D}} = 0$.

For the TSC, the situation is different. While $S_A, S_{A\cap B}, S_{A\cup B}$ are the same as in the spin model, S_B has a sharply different behavior. In this regime, the ground state is two-fold degenerate (again, up to a gap $\delta \propto \mathrm{e}^{-L}$): Each of the two states $|\Psi\rangle_\pm$ can be written as an equal weight superposition

of states with a given parity $|\psi\rangle_\pm$, i.e., $|\Psi\rangle_\pm = (1/2^{L-1}) \sum_\psi |\psi\rangle_\pm$. The proper fermionic trace evaluates the entanglement structure of arbitrary partitions so that we obtain $S_B = 2\log 2$. This returns a disconnected entropy $S^{\mathrm{D}} = \log 2$. A full derivation is given in appendix D.3.

The behavior of these cartoon wave functions sharply distinguishes the TSC phase with respect to all other phases. We need to go beyond these cartoons to understand if this behavior is a property of a phase, and if the value of S^{D} remains quantized in the whole TSC phase. Before presenting numerical results in support of these findings, we now illustrate how the quantization of S^{D} emerges naturally when utilizing a lattice gauge theory (LGT) description of the Kitaev chain.

8.3 S_n^{D} as a topological invariant order parameter

S^{D} is efficient as a topological order parameter even for modest system size. Indeed, we simulate the quantity and obtain a sharp phase diagram of the Kitaev wire. Sharp, because close to the phase transition, it displays universal behavior typical of an order parameter and allows definition of critical entanglement exponents. Its characteristics as a topological invariant are confirmed by its invariance after a quench as expected from Sec. D.1 and by its robustness to disorder.

8.3.1 Scaling of S^{D} and phase diagram

We therefore turn to the numerical investigation of Eq. (8.2). We used free fermion techniques [35] to investigate the non-interacting case $U = 0$, and density-matrix-renormalization group (DMRG) [36, 37] for $U \neq 0$. Since DMRG does not give immediate access to S_B, we performed separate simulations to obtain this quantity, by modifying the lattice connectivity. We kept at least 1200 states after truncation and performed at least 30 sweeps. Typical discarded weights at the end of the simulation were of order 10^{-8}.

The phase diagrams in Figs. 8.1 b) and 8.2 a) (with and without interactions) show how, even at very modest partition sizes, S^{D} is large and finite only in the TSC phase. Comparison between Figs. 8.2 a) and b) shows the equivalence between S^{D} and S_2^{D}. In Fig. 8.3 a), we show the finite-size-scaling behavior of S^{D} for representative points in the TSC ($\mu/t = 1.0, 1.5$) and topologically trivial ($\mu/t = 4$) phase. The asymptotic values are quantized within numerical accuracy of our fits to $\log 2$ and 0, respectively, in agreement with the theoretical discussion above. Fig. 8.3 b) shows how, in the TSC phase, quantization is approached exponentially fast in system size; the same holds true for S_n^{D}.

8.3.2 Universal behavior and entanglement critical exponents.

Since S^{D} captures universal properties of each phase, it is natural to wonder whether such quantities can display universal scaling behavior when crossing a quantum phase transition. Here, we focus on the transition between TSC and band insulator, which belongs to the Ising universality class.

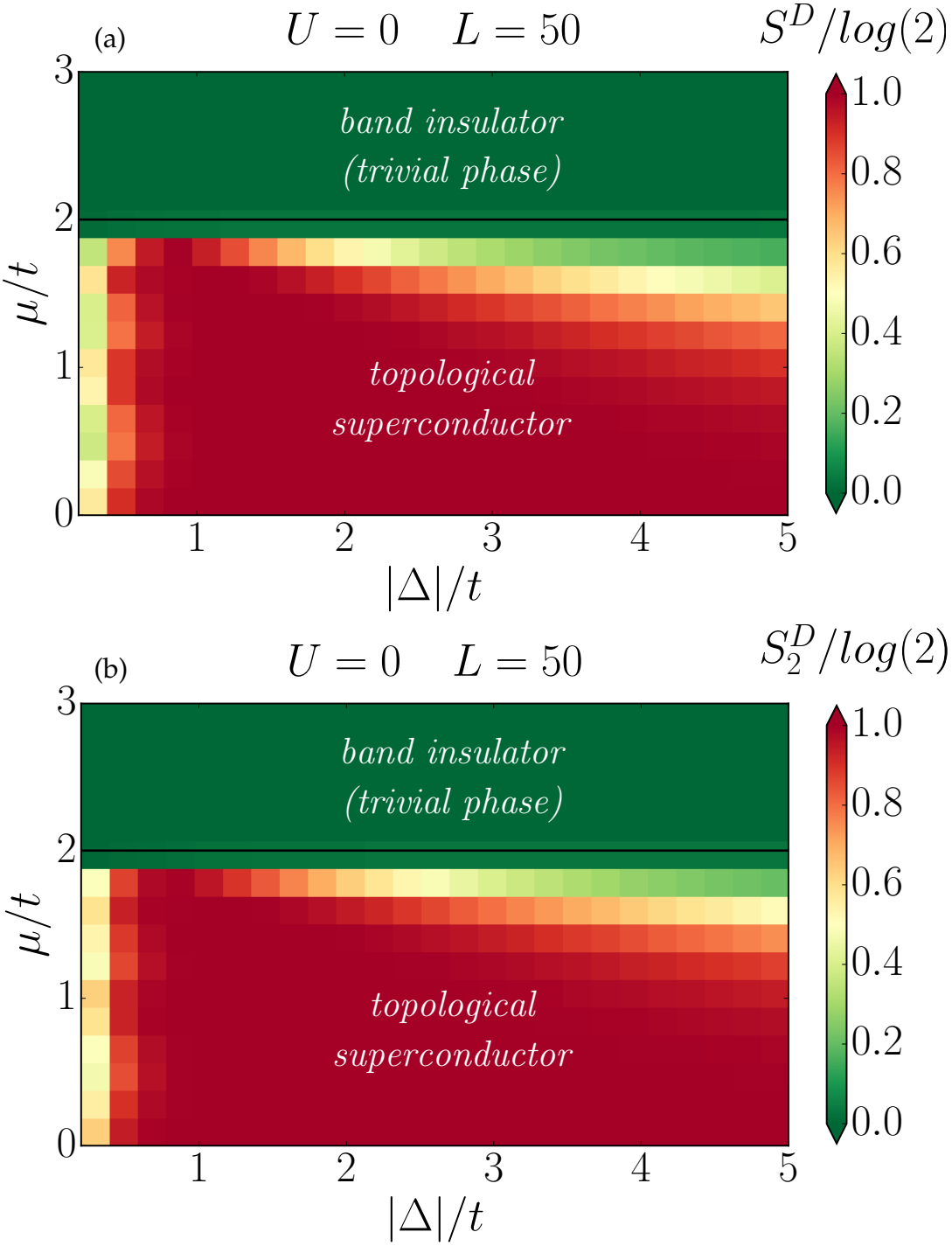

Figure 8.2: Color plot of the disconnected n-entropies, S_n^D, of the Kitaev wire without interaction, $U = 0$, for (a) $n = 1$ and (b) $n = 2$. The results are obtained with the free-fermion technique. The y-axis represents the chemical potential, μ/t, while the x-axis the superconducting amplitute, $|\Delta|/t$. A grid with 16×30 points is considered. The two theoretically expected phase transition lines occur for $|\Delta| = 0$ and $\mu/t = 2$, respectively. Using the definitions of Fig. 8.1 a), $L = 50$, $L_A = L_B = 12$ and $L_D = 32$. The diagrams coincide with the results obtained in Ref. [31].

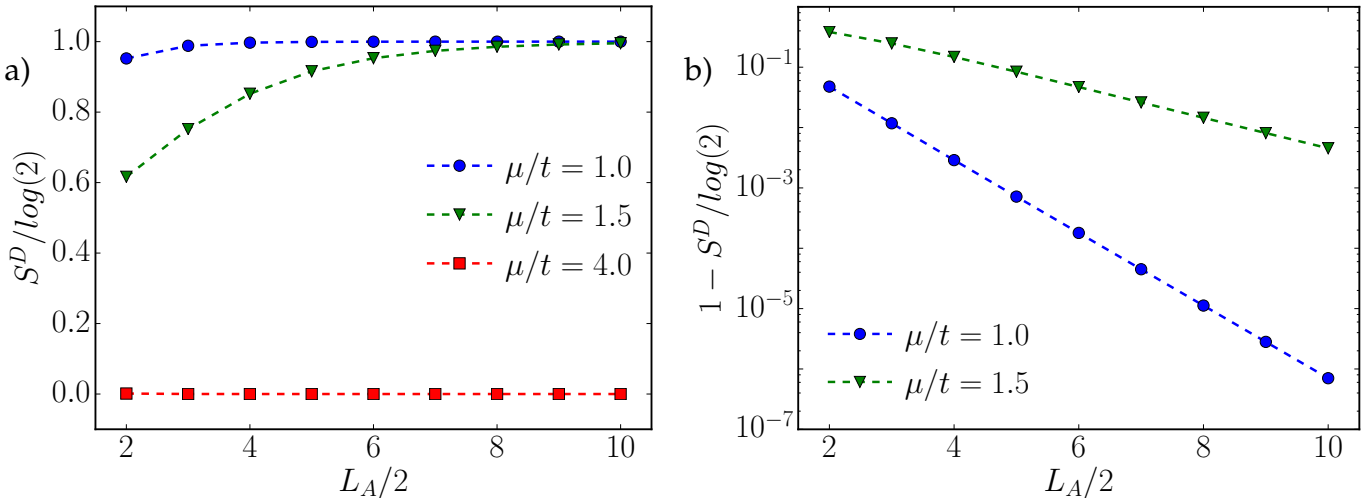

Figure 8.3: (Color online) Finite-size scaling properties of S^{D} in a) normal scale, b) log scale, for a chain with $L_A = L_B = (L_{A\cap B} + L_{A\cup B})/2$, and $U = 0, \Delta/t = 1$. In the topologically trivial phase, S^{D} quickly vanishes. In contrast, in the topological phase ($\mu = 1.0, 1.5$), S^{D} increases as a function of system size, and approaches its thermodynamic value exponentially fast when increasing L_A, as shown in b).

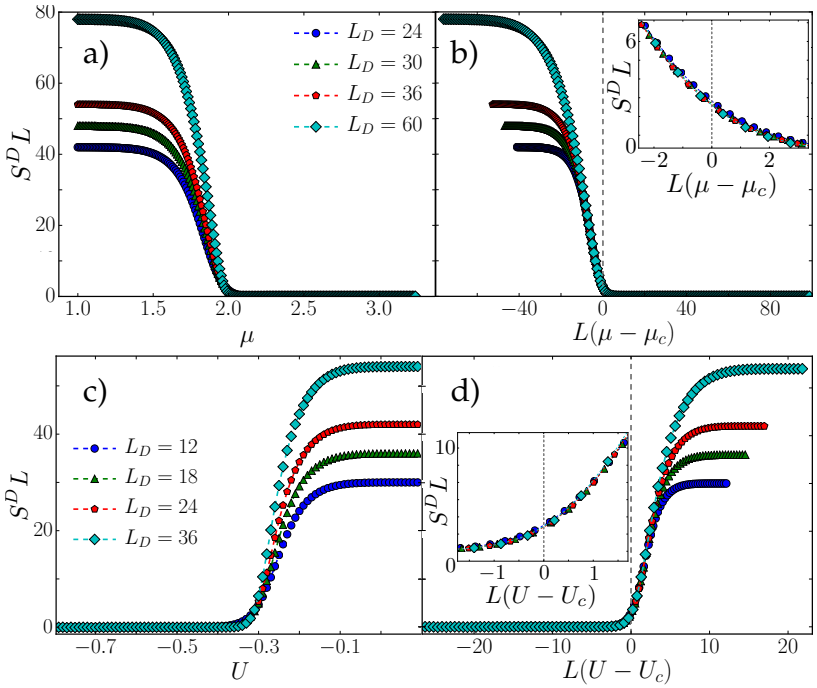

Figure 8.4: Finite size scaling of S^D (in units of $\log_2$) along the line (I) and (II) of Fig. 8.1 as a function of L_D and μ or U using DMRG. In all plots, $L_A = L_B = 12$. (a) $S^D L$ as a function of μ for different sizes: the critical value μ_c is the intersection of all curves; we obtain $\mu_c = 1.978$. (b) Scaling of $\lambda(x)$ for different system sizes: curve collapse. The collapse is best realized for $a = b = 1$, values that also minimize the square root of the residual sum of squares.(c) $S^D L$ as a function of U for different sizes: the critical value is here $U_c(12) = -0.314$. (d) The collapse is again best realized for $a = b = 1$. Simulations with more sites (especially using free fermion techniques) only confirm these results.

Similarly to conventional quantum critical behavior, we fit S^{D} using a phenomenological finite-size scaling ansatz:

$$S^D L^{\frac{a}{b}} = \lambda\left(L^{\frac{1}{b}}(\alpha - \alpha_c)\right), \tag{8.3}$$

where $\alpha = \mu$ or U is the varying parameter chosen, a and b (*a priori* different depending on the chosen parameter) take place of the usual critical exponent β and ν, and $\lambda(x)$ is a scaling function. We extract these parameters using curve intersections and collapse shown in Figs. 8.4 across the transition indicated in Fig. 8.1 with the yellow arrows (I) and (II). The results of the collapse scaling locates correctly the transition point (with errors 10^{-4}). Most surprisingly, we find that the entanglement critical exponents satisfy $a = b = 1$ irrespectively of where the transition line is crossed, a sharp signature of universal behavior. The quality of the collapse scaling in the interacting case is already good for modest system sizes, further corroborating such universal behavior.

8.3.3 Invariance of S_n^{D} under coherent dynamics.

In the thermodynamic limit, topological invariants cannot change under unitary evolution (as long as specific symmetries are not broken explicitly [38–40]). To check that S^D is a true topological invariant, we performed an extensive investigation based on quantum quenches within and across the topological phase.

A representative sample of our results is presented in Figs. 8.5. In panel *a)*, we plot the time evolution of S^D for a quench from an initial value of the superconducting amplitude $\Delta = 0.5$ to a final value $\Delta = 1.5$. Different lines correspond to different system sizes. For each size, one can sharply distinguish two regimes. At short times, S^D does not change with time and exhibits a plateau up to a time t_c that depends on L_A. After this timescale, quantization is lost, and the dynamics is dictated by non-universal dynamics. To understand whether quantization is a robust feature, we perform a finite-size scaling analysis in panel *d)*: our results show that t_c (defined as the time when $S^{\mathrm{D}} = 0.95$) grows approximately linearly with system size and will diverge at the thermodynamic limit. This behavior confirms the topological invariant nature of S^{D}. Panels *b)*, *e)*, and *c)*, *f)* confirms these results for the quench $\mu_0 = 1.0$ to $\mu = 3.0$ (from topological to trivial) and $\mu_0 = 3.0$ to $\mu = 1.0$ (from trivial to topological). For f), t_c is the time when $S^{\mathrm{D}} = 0.05$.

8.3.4 Robustness of S_n^{D} to disorder

In 1D, the effect of disorder is the most drastic: localization of the wave function occurs as soon as disorder exists, and not even diffusive transport is possible [41]. Topological insulators and superconductors escape the effect, in the sense that their extended edge states stay robust against symmetry-preserving disorder. The same disorder should also preserve S^{D} that relies on these edge states. Numerical simulations indeed confirm the robustness of S^{D} to disorder for the non-interacting Kitaev wire.

We introduce finite Anderson-like disorder using:

$$\mu_i = \mu + \delta_i, \quad \delta_i \in [-W/2; W/2]\,, \tag{8.4}$$

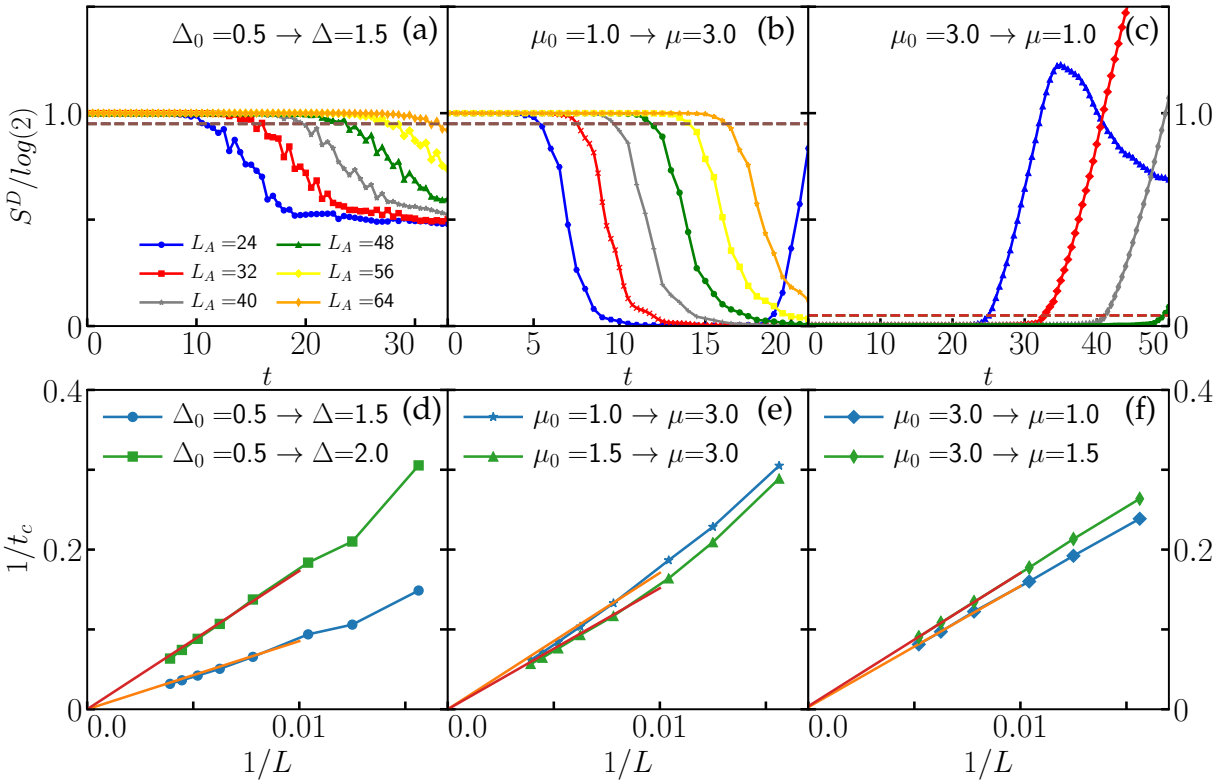

Figure 8.5: (Color online) Time evolution of S^{D} after a quantum quench from a) $\Delta_0 = 0.5$ to $\Delta = 1.5$, b) from $\mu_0 = 1.0$ to $\mu = 3.0$ and c) from $\mu_0 = 3.0$ to $\mu = 1.0$ with $U = 0, \mu = 0, L = 8L_A$. Finite-size scaling of t_c or t_c' for two values of d) Δ, e) μ_0 and f) μ of the quenched Hamiltonian. In all cases, the width of the plateau diverges linearly with system size, as expected for topological invariants. The threshold lines of S^{D} according to the definition of t_c are depicted as a dashed line.

where μ_i is the new position-dependent (i) chemical potential in the Hamiltonian Eq. (8.2) (with $U = 0$). δ_i is a random variable of uniform distribution, and W is the amplitude of the disorder. The new potential breaks the translation symmetry, but not the protecting symmetries of the topological phase that persists for a reasonable amplitude of the disorder. In Fig. 8.6, we draw the mean value of S^{D} over realizations of disorder for different W as we increase the system size L. S^{D} scales exponentially in system size towards the quantized value of $\log 2$ for the topological phase, 0 otherwise.

8.4 Experimental measurement and comparison to other diagnostics.

The probes S_n^{D} are experimentally-relevant because they are already informative for modest partition sizes, and because Rényi entropies can be measured. The proposals in Ref. [14] discuss how to perform measurements of Rényi-2 entropies in synthetic quantum systems: the complexity of the measurements is not sensitive to the connectivity of the partition itself, but only to its total size. Given that a large L_D allows the distillation of the correct information from the wave func-

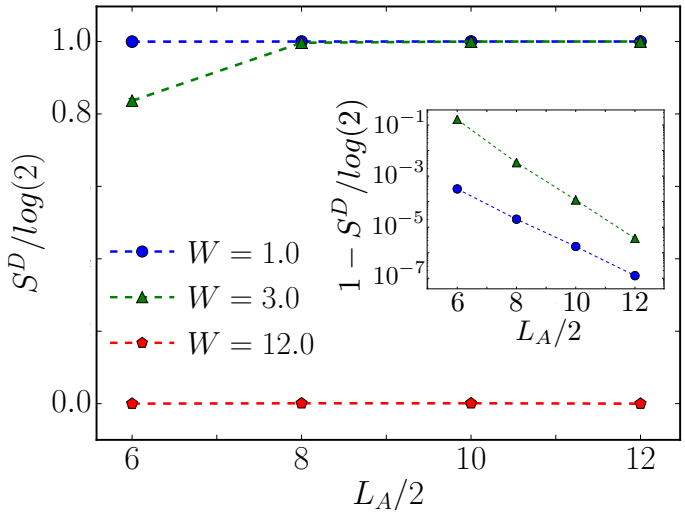

Figure 8.6: Scaling in system size of the mean value of SD for $t = \Delta = \mu = 1$, $U = 0$, $L_A = L_B = (L_{A\cap B} + L_{A\cup B})/2$ and for three amplitudes of disorder: $W = 1$ and 3 in the topological phase, and $W = 12$ for the trivial disordered phase (200 realizations of the disorder for each point). The inset provides a logarithmic scale for the axis of S^D: the scaling is exponential. The standard deviation is smaller than 10^{-6} for each point. The same study using Rényi-2 entanglement entropies leads to the same results quantitatively. The phase transition is expected at $W_c \sim 11$ for these parameters [42, 43].

tion, measuring S^D is as complex as measuring its largest partition A. We note that partitions of sizes up to 10 spins have already been probed in experiments [25].

Finally, we comment on the relation between S^D and other diagnostics. Topological invariants such as the many-body Chern number [4, 44] are unrelated to bipartite entanglement properties, as they do not depend solely on the spectrum of density matrices, but also on their eigenfunctions. For specific symmetries, specific topological invariants can be defined [45–50] (and potentially experimentally measured [51]) also utilizing the matrix-product-state (MPS) classification of SPTPs; these quantities are genuinely sensitive to the response of a state to specific (symmetric) operations, and not immediately connected to entanglement. From a theoretical viewpoint, all these diagnostics represent complementary tools, that give access to qualitatively different features characterizing topological matter. Examples now include: response of wave functions under changing boundary conditions (Chern number), properties with respect to protecting symmetry (MPS order parameters), and non-local entanglement content of wave functions (disconnected entropies).

8.5 Conclusions.

We have shown how the entanglement of disconnected partitions uniquely distinguishes topological superconducting phases in one-dimensional systems. This distinction is naturally interpreted within a lattice gauge theory framework, and leads to key footprints both at the ground state level, and in quantum quenches. Entanglement order parameters display universal scaling behavior when crossing phase transitions, characterized by entanglement critical exponents.

Our findings show that modest partition sizes - of the order of what has been already experimentally demonstrated - are sufficient to uniquely characterize topological superconductors via entanglement. It would be intriguing to investigate whether other forms of quantum correlations between disconnected partitions, such as discord [52] or quantum coherences [53], display similar characteristic features, and if entanglement topological invariants can be used to characterize the real-time dynamics of interesting topological matter [40].

9

SSH Model

9.1 Introduction

When a phase is topological, then its ground state(s) displays robust entanglement properties. The converse is more uncertain: to what extent are entanglement properties unique to topological states? This attempt at understanding topological phases through the lens of entanglement is recent [8]. It has been successful for (true) topological order that is now characterized by the topological entanglement entropy (TEE) [5–7]. This quantity works both in- [1–4] and out-of-equilibrium [54–56], and is included in the textbooks' definition of these phases [57, 58]. It provides a useful discriminating characterization of topology for numerical simulations [9–11] and it stimulated the search for corresponding experimental entanglement probes [12–18].

Topological insulators and superconductors or, more generally, symmetry-protected topological phases (SPTP) also display characteristic entanglement features. Amongst these features, the most used is the entanglement spectrum [19, 21, 59]. It serves as an entanglement-based *sine qua non* signature of an SPTP. This spectrum corresponds to all the eigenvalues of the bipartite reduced ground state's density matrix of the system. The degeneracy of the matrix' few largest eigenvalues is imposed by the dimension of the possible representations of the edge states [19, 59–61]. Because the same spectrum may come from a non-topological state, the diagnosis it provides is a necessary but not sufficient condition [1].

The disconnected entanglement entropy S^{D} is another entanglement signature for SPTPs of systems with open boundary conditions. S^{D} was suggested and tested through simulations for some examples of bosonic topological phases in Ref. [50]. Like the TEE, it extracts a topological-

[1] An example is the entanglement spectrum of the topological ground state of the Kitaev wire, which is identical to the spectrum of the corresponding ground state of the non-topological ferromagnetic spin 1/2 Ising chain after the Jordan-Wigner mapping.

exclusive contribution to the bipartite entanglement entropy. Unlike the TEE [7, 62], this contribution is not (yet) predicted by quantum field theory as it is related to short-range or edge-edge entanglement. Ref. [28] used the Kitaev wire [63] to prove that S^{D} is also valid for 1D topological superconducting phases, where it is captured within a lattice gauge theory framework. In the Kitaev wire, S^{D} is traced back to the entanglement necessarily present by construction between the only two fractional (Majorana) modes of the model, even when the modes are localized on each edge of the chain.

This paper aims at characterizing the properties of S^{D} for the case of one-dimensional topological insulators, focusing on a simple, yet paradigmatic example: the Su-Schrieffer-Heeger model [64, 65] (SSH). This model of spinless fermions displays a topologically trivial phase and an SPTP with two edge modes. Each of these states is usually represented as one dangling fermion unentangled with the bulk on either side of the chain. The bulk is short-range entangled [66]. However, the finite size of the chain ensures a systematic maximal entanglement between the two a priori independent edge states as predicted in bosonic topological phases [67, 68]. As we show below, S^{D} is sensitive to this long-range entanglement and takes the maximal possible value of $2\log 2$ in the SPTP [2]. In contrast, this value is 0 in the trivial phase. Therefore, our first claim is that S^{D} can be a good signature of topology for SPTP without fractional edge states like in the SSH model.

We also find that S^{D} provides additional quantitative topological exclusive information on the entanglement properties of the ground state. Indeed, S^{D} displays a system-size scaling behavior close to the critical phase transition, akin to the magnetization of an Ising chain. We obtain the resulting critical exponents using exact numerical methods. Within the topological phase, S^{D} remains quantized on average in the presence of disorder. Such a scaling behavior and critical exponents are different with respect to the Kitaev wire [28] (the only other occurrence of such an analysis for fermionic systems to our knowledge) and to bosonic cluster models realized as instances of random unitary circuits (e.g. Ref. [69]). This indicates that while scaling behavior is likely a generic feature of S^{D} at criticality, the corresponding critical entanglement exponents depend on the nature of the associated topological phase transition.

Finally, we apply unitary evolution to the system in the form of quantum quenches either within the two phases or across the phase transition. After the quench, we observe that S^{D} keeps its initial value in the limit of an infinite chain, a behavior characteristic of a topological invariant associated with particle-hole symmetry [70]. This set of observations mimics the phenomenology observed for the TEE in the context of true topological order and allows us to define S^{D} as a valid entanglement order parameter.

This work is structured as follows. We introduce the SSH model and the disconnected entanglement entropy in Sec. 9.2. In Sec. 9.3, we present the analytical computation of S^{D} in the topological phase, trace it back to the systematic maximal entanglement of the edge states, and

[2] This result is consistent with a previous study of the spinfull interacting SSH model in Ref. [29]. Another quantity is used then that also extracts the edge entanglement and coincides with S^{D} for this model.

explain its exponential finite-size scaling. In Sec. 9.4, we present our numerical results for the case of the ground state of a clean SSH chain. In Sec. 9.5, we investigate quantum quench protocols, that provide a clear characterization of S^{D} as a topological invariant. In Sec. 9.6, we showcase one application of S^{D}, by investigating the entanglement properties of disordered SSH chains, and showing how the disconnected entropy recovers the predicted phase diagram. We discuss the generality of our findings within the BDI and D classes of the tenfold-ways in Sec. 9.7, and conclude the study in Sec. 9.8.

9.2 Model Hamiltonian and disconnected entropies

We briefly introduce the SSH model and both its topological and trivial phases in Sec. 9.2.1. We introduce S^{D} in Sec. 9.2.2. In Sec. 9.2.3, we confront the strengths and the limits of S^{D} that become apparent for the SSH model with periodic boundary conditions. We establish the equivalence of using S^{D} with either the von Neumann and Rényi-2 entanglement entropies for the SSH model in Sec. 9.2.4.

9.2.1 The SSH model

The Su-Schrieffer-Heeger model [64, 65] describes a one-dimensional spinless fermionic chain with a staggered hopping between sites. The chain is composed of N unit cells. Each cell is divided into one site A connected to one site B. The number of sites in a chain is, hence, $L = 2N$. The Hamiltonian of the model with open boundary conditions is:

$$H_{\mathrm{SSH}} = -v \sum_{i=1}^{N} \left(c_{iA}^{\dagger} c_{iB} + h.c \right) - w \sum_{i=1}^{N-1} \left(c_{i+1A}^{\dagger} c_{iB} + h.c \right), \tag{9.1}$$

where $c_{iX}^{\dagger}$ (c_{iX}) is the creation (annihilation) operator of a spinless fermion on the unit cell i, site $X = A, B$. $v > 0$ ($w > 0$) is the intra-(inter-)cell hopping amplitude. The chain is represented in Fig. 9.1a).

At half-filling, the model displays two phases. When $v/w \gg 1$, A and B within a unit cell dimerize and the phase is topologically trivial. There is one particle per unit cell (box in Fig. 9.1a)). The vanishing entanglement between the unit cells increases until $v/w = 1$ where the phase transition occurs. When $v/w < 1$, the phase is topological. The single-particle spectrum displays two zero-mode edge states in the gap between two bands. When $v/w \ll 1$, the density profile of each edge state shows one localized fermion in the leftmost or rightmost site of the chain. The dynamics of this fermion is independent of symmetry-preserving perturbations of the bulk. Since Pauli's filling rule applies, at half-filling and zero temperature, all the lower band is occupied. The ground state is unique and its bulk is short-range entangled: one fermion forms a Bell pair on each strong link (darkest line in Fig. 9.1a)). When $v = 0$, the Bell pair on the link between cell i and

$i+1$ is strictly localized. The Bell pair can be expressed as:

$$\left(|0_{iB}1_{i+1A}\rangle + |1_{iB}0_{i+1A}\rangle\right)/\sqrt{2}. \tag{9.2}$$

For a finite chain with open boundary conditions, the ground state has one fermion populating each strong link, and one extra fermion in the superposition of Eq. (9.2) of the two edge states (see Sec. 9.3). This superposition entangles the two distant edges maximally. It is the only long-range entanglement in the system and contributes to the entanglement entropy. We will show that this is the contribution extracted by S^{D} (Sec. 9.2.2). The topological and the trivial phases are separated by a critical phase transition at $v/w = 1$.

The topological invariant of this model is the Zak phase [71], a quantity proportional to the Berry phase [72]. By definition, a topological invariant is constant and quantized over the whole phase and only changes across a phase transition. Here, the Zak phase distinguishes the two regimes of v/w while the way their ground states at half-filling breaks the initial symmetries can not. This situation is beyond the spontaneous symmetry breaking paradigm and signals that at least one of the two phases is topological. For open boundary conditions, the topological regime is the only one displaying edge states (and a non-zero Zak phase). For periodic boundary conditions, the values of the Zak phase for the two regimes can be exchanged with the *renaming*:

$$A \to B, \quad v \to w, \tag{9.3a}$$

$$B \to A, \quad w \to v, \tag{9.3b}$$

with unchanged values of the amplitudes. In this case, the Zak phase only ensures that the two phases are topologically distinct.

The topological edge states are protected by charge conservation (U(1) symmetry), the time-reversal T, the particle-hole C, and the chiral S (or rather, the sublattice) symmetry [3]. The phase is part of of the BDI-class of the Altland-Zimbauer ten-fold ways [74] leading to a $\mathbb{Z}$ classification. This classification indicates that there are an infinite countable number of distinct topological phases with unbroken T,C and S in 1D. The classification will be $\mathbb{Z}_8$ if symmetry-preserving interactions are allowed [75]. This latter classification means that there are only seven non-trivial topological phases left. While the translation symmetry is needed to compute some non-local topological order parameters such as the winding number in k space, the topological phase is not protected by this last symmetry.

In simulations, the Zak phase, the winding number, the presence of edge states, or the entanglement spectrum have all served as smoking guns for topology. In experiments, the winding number was measured [76, 77] for the SSH model and its generalization [78]. In these instances, the winding number is contained in the time evolution of the chiral mean displacement observable. This observable quantifies the relative shift between the two projections of the tracked state

[3] There are several definitions of these symmetries, leading to several self-consistent 10-fold ways. We use the definitions of Ref. [73].

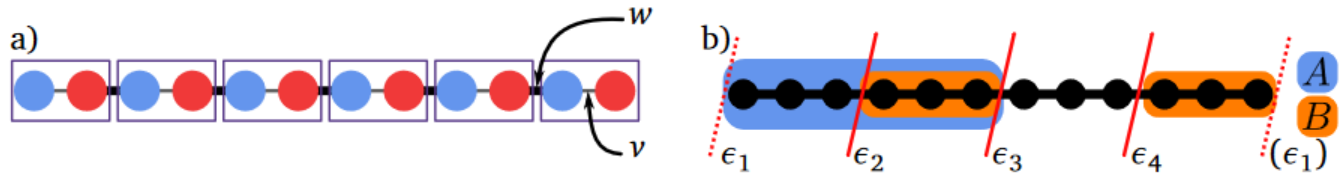

Figure 9.1: (Color online) The SSH chain and the partition used for S^{D}. a) The SSH chain is a spinless fermionic chain of sites A and B (blue and red on the figure) connected with staggered hoppings v and w. A pair of sites A and B forms a unit cell (a box on the figure). b) Partitions A (shaded, blue) and B (shaded, orange) associated with the entanglement topological order parameter S^{D}. For large systems, the exact locations of the cuts ϵ_i, $i = 1, 2, 3, 4$, of each partition do change the value of the bipartite entanglement entropy but do not change S^{D}.

onto the eigenstates of the chiral operator [77]. It follows a random walker [77] or the entire atomic population after a sudden quench [76, 78]. The observable is measured using chiral- and site-resolved imaging over several times. S^{D} completes this list of topological detectors. Amongst them, S^{D} is the only probe that is both unambiguous and entanglement-based [4]. Thus, S^{D} is the optimal tool to study the topological entanglement properties of the SSH model.

9.2.2 The disconnected entanglement entropy S^{D}

The *disconnected* entanglement entropy S^{D} has been introduced in Ref. [50] as a generalization of the topological entanglement entropy S_{topo} for all the topological phases (topological order and SPTP). S_{topo} is an exclusive marker for topological orders. Both S^{D} and S_{topo} aim to isolate a constant topological-exclusive contribution in the bipartite entanglement entropy. Thus, they are both built using the same linear combination of entropies but they differ in the partitioning of the system. In both cases, the combinations are chosen to cancel volume law (linear in system size) and area law (linear in the number of internal cuts) contributions in the bipartite entanglement entropy. For S_{topo}, the leftover constant contribution is topological-exclusive, as shown by topological quantum field theory arguments [7, 62]. A similar generic proof is missing for S^{D}. Instead, simulations, exact solutions, or a gauge theory analogy validate its success for some examples [28, 50, 80].

The original definition of S^{D} [50] uses the von Neumann entanglement entropy of a bipartition of the system. For a chain divided into two complementary subsets A and $\bar{A}$, the reduced density matrix of the subset A is

$$\rho_A = \mathrm{tr}_{\bar{A}}\rho.$$

$\mathrm{tr}_{\bar{A}}$ stands for the partial trace on the subset $\bar{A}$, and ρ is the full (pure) density matrix of the system, always taken as a ground state in this study. A may be a collection of disconnected sites of the

[4] Another entanglement-based topological detecting quantity that applies to the SSH model would be the boundary susceptibility [79].

chain. The von Neumann bipartite entanglement entropy follows:

$$S_A = -\mathrm{tr}_A \rho_A \log(\rho_A). \tag{9.4}$$

S^{D} uses the partitioning of the chain in Fig 9.1b), so that:

$$S^{\mathrm{D}} = S_A + S_B - S_{A\cup B} - S_{A\cap B}. \tag{9.5}$$

The lengths of A, B, and the disconnected subset $D = \overline{A \cup B}$ are respectively L_A, L_B, and L_D.

The formula is best understood when comparing what happens for the other possible gapped phases in 1D: disordered (paramagnetic) and ordered phases, the latter ones characterized by some of form of spontaneous symmetry breaking (SSB) of a discrete symmetry.

A trivial phase always has one single ground state independently of its boundary conditions and for both the thermodynamical limit (large number of particle) and finite (large) size. When this state is a product state, any choice of partition leads to a bipartite entanglement entropy of zero. An example of such a case is the ground state of a (quantum) spin-1/2 chain with only a magnetic field. The ground state can also be short-range entangled: if C_1 and C_2 are two simply connected partition of the chain separated by a large distance, then

$$\rho_{C_1C_2} \sim \rho_{C_1} \otimes \rho_{C_2}. \tag{9.6}$$

The trivial SSH phase is an example of this scenario. In that phase, the mutual information $I(C_1 : C_2)$ of two disjoint and distant partitions is zero, and so is S^{D} for open boundary conditions (the *conditional* mutual information in this context). Indeed, for large subsets in Fig. 9.1b), Eq. (9.6) applies, such that :

$$S^{\mathrm{D}} = S_A + \left(S_{A\cap B} + S_{B\backslash A}\right) - \left(S_A + S_{B\backslash A}\right) - S_{A\cap B} = 0 \tag{9.7}$$

for A and B the partitions in Fig. 9.1b), and where $B\backslash A$ means B without $A \cap B$. For periodic boundary conditions, both A and $B\backslash A$ are connected such that $S^{\mathrm{D}} = I(A : (B\backslash A))$. For these conditions, S^{D} may vary within a phase.

A SSB phase always has several 'ground states' independently of its boundary conditions. A basis of these states may be expressed as product states. For a finite-size systems, the degeneracy is lifted by corrections that are exponentially small in system size: the single ground state has a GHZ-type of quantum entanglement [50]. An example of a SSB phase is the Ising chain with a small transverse magnetic field. The true finite-size ground state is then the maximally entangled symmetric superposition between the state with all spin up and all spin down: the GHZ-state. Any bipartite entanglement entropy of this state has the same non-zero value such that all the entropies in Eq. (9.5) are equal and $S^{\mathrm{D}} = 0$ [5]. Like in the trivial case, additional short-range

[5] When $L_D = 0$, $A \cup B$ spans over the whole system. In this case, the combination Eq. (9.5) reduces to the *tripartite*

entanglement in the ground state does not change S^{D}.

For periodic boundary conditions, the ground state of an SPTP is unique. This state is short-range entangled after defining the proper unit-cell. Like the periodic trivial case, $S^{\mathrm{D}} = I(A : (B\backslash A))$ then. Unlike the trivial case, the SPTP imposes neighboring unit cells to be maximally entangled, saturating S^{D} (cf Sec. 9.2.3) so that it will not vary within the same phase. For open boundary conditions, an SPTP displays edge (zero)-modes. A basis of these modes can sometimes be written as separable states, like the SSB case [6]. Unlike the SSB case, the edge modes all have the same bulk, and the superposition of the same bulk does not increase the entanglement. For a SSH chain with two edges, the true ground state is a maximally entangled superposition of these edge states. This superposition generates an additional saturated contribution (i.e. of maximal possible value) to the entanglement entropy of a partition that includes one edge without the second (like A and B in Fig. 9.1b)). S^{D} then behaves like in Eq. (9.7), but with this extra edge contribution for S_A and S_B that is not compensated by $S_{A\cup B}$ and $S_{A\cap B}$.

Only this edge contribution sets S^{D} to a quantized, non zero value. Similarly to Ref. [29], the value of S^{D} in the thermodynamical limit is fixed by the number of edge states $\mathcal{D}$ (or, equivalently, by the dimension $2^{\mathcal{D}}$ of the Hilbert space they span):

$$\lim_{L\to\infty} S^{\mathrm{D}} = 2\log\mathcal{D}. \tag{9.8}$$

$\mathcal{D}$ is fixed by the bulk-edge correspondence outside of the accidental increase of global symmetry due to fine-tuning. Thus, $\mathcal{D}$ is almost a robust topological invariant, and so is S^{D}. The SSH topological phase fits in this scenario.

Thus, the SPTP case can be interpreted as a trivial gapped phase with saturated short-range entanglement in the bulk, with an extra entanglement between the edge states for a finite open system.

9.2.3 Periodic boundary conditions

Following the previous discussion, we will solely focus on open boundary conditions in the rest of the text. We take a brief detour in this section to discuss the physical interpretation of S^{D} for closed chains.

For periodic boundary conditions and at half-filling, S^{D} only extracts the saturated entanglement of the cut between the connected partitions A and $B\backslash A$ of the single bulk ground-state. The saturation comes from cutting the singlet between two neighboring projective representations on each side of the cut. This picture stems from the cohomology and supercohomology classification [81, 82]. It means that if G is the unbroken symmetry group of the chain, then cutting a chain

entanglement entropy [50], and is non-zero for both SSB and SPT phases.

[6] If we define separable in terms of sites, the edge states are separable for the topological SSH, but they are not separable for the topological Kitaev wire. In terms of Majorana fermions, both are separable. In terms of unit cells, neither are separable. Interactions typically prevents separability.

between two unit cells leaves an edge state on each side of the cut. One edge state transforms according to a projective representation of G, and the other transforms according to the conjugate representation of the former edge. When connected back, the two edge states form a singlet that is maximally entangled by construction. This topological pattern repeats all along the chain and explains the saturation of the bulk short-range entanglement.

The projective representations involved in this internal cut also transforms the edge states of the chain with open boundary conditions. S^{D} has thus the same saturated value for both boundary conditions in the topological phase. In contrast, S^{D} is systematically zero only for the trivial phase of a system with open boundaries. Therefore a sharp phase transition between the two phases only exists for open boundary conditions.

This structure is explicit in the SSH model: the two phases for $v/w < 1$ and $v/w > 1$ are a collection of coupled dimers between B and A or A and B (the order matters) respectively. These dimers become uncoupled when $v = 0$ and $w = 0$ respectively. The contribution to the entanglement entropy for any bipartition of the system then corresponds to the contribution of each cut: $\log 2$ for a cut in the middle of a dimer and 0 otherwise. Defining $\epsilon_j = 1$ when the cut $j = 1, 2, 3, 4$ (see Fig. 9.1b)) separates a dimer and $\epsilon_j = 0$ when the cut is between two of them, Eq. (9.5) becomes:

$$\begin{aligned} S^{\mathrm{D}}/\log 2 &= ((\epsilon_1 + \epsilon_3) + (\epsilon_1 + \epsilon_2 + \epsilon_3 + \epsilon_4) - (\epsilon_3 + \epsilon_4) - (\epsilon_2 + \epsilon_3)) \\ &= 2\epsilon_1. \end{aligned} \tag{9.9}$$

Eq. (9.9) is not one-site translation-invariant for the two phases. This lack of invariance stems from the ambiguity highlighted in Eq. (9.3) and is only lifted after defining the unit cell and always cutting between two of them. Note that ϵ_1 is exactly the quantity extracted by the "edge entanglement entropy" of Ref. [29] when there are no volume nor GHZ-like contributions in the bipartite entanglement entropy. ϵ_1 is also the contribution in the value of the bipartite entanglement entropy that is linked to the Zak phase in the small localization length and thermodynamical limit [83]. Consequently both ϵ_1 and the Zak phase change depending on the definition of the unit cell.

9.2.4 Disconnected Rényi-2 entropy

Similarly to the bipartite entanglement entropy, it is possible to define and use the disconnected entropy using the Rényi-α entanglement entropies [28]. These extensions are useful for two reasons. First, for small values of α, the Rényi-α entanglement entropies are experimentally measurable. Second, for $\alpha = 2$ (and, with increasing complexity, for larger integer values of α as well), they can be computed using Monte Carlo methods, providing a natural framework to extend our methods to interacting systems.

The Rényi-α entanglement entropy [84] of a bipartition A, $\bar{A}$ of the chain is defined as:

$$S_{A,\alpha} = \frac{1}{1-\alpha} \log \mathrm{tr}_A \left(\rho_A^\alpha\right), \tag{9.10}$$

where the case $\alpha \to 1$ is the von Neumann entanglement entropy. The subsequent versions of S^{D} are:

$$S_\alpha^{\mathrm{D}} = S_{A,\alpha} + S_{B,\alpha} - S_{A\cup B,\alpha} - S_{A\cap B,\alpha}, \tag{9.11}$$

for the partition of the chain in Fig. 9.1b). To motivate and then support the relation between S^{D} and S_α^{D}, we will make use of the following known properties:

1. For all $\alpha \in]0,+\infty[$, S_α has the property of minimum value [85] (i.e. $S_\alpha(\rho) = 0 \quad \Leftrightarrow \quad \rho$ is a pure state). Hence every individual bipartition in Eq. (9.5) and Eq. (9.11) are simultaneously zero or non-zero, i.e. $S_{X,\alpha} \neq 0 \quad \Leftrightarrow \quad S_X \neq 0$.

2. For all $\alpha > 1$, S_α has the property of monotonicity [86], i.e., for $1 < \alpha_1 \leq \alpha_2$, $S_{\alpha_1}(\rho) \geq S_{\alpha_2}(\rho)$. This property can be extended to the von Neumann case $\alpha = 1$. All bipartite von Neumann entanglement entropy of 1D gapped isolated systems are finite, and thus, by monotonicity, so will be their Rényi-$\alpha > 1$ counterpart. Thus, there are no divergent terms in Eq. (9.11) for the SSH model with $w \neq v$ [7].

3. Despite open boundary conditions and for large enough subsets, translation invariance imposes equality of finite entropies of simply connected subset, i.e. $S_{A,\alpha} = S_{A\setminus B,\alpha} = S_{B\setminus A,\alpha}$ and $S_{A\cap B,\alpha} = S_{D,\alpha}$ (the presence of exactly one edge matters). With additional homogeneous disorder, the equalities become $\langle S_{A,\alpha}\rangle = \langle S_{A\setminus B,\alpha}\rangle = \langle S_{B\setminus A,\alpha}\rangle$ and $\langle S_{A\cap B,\alpha}\rangle = \langle S_{D,\alpha}\rangle$. A corollary follows: if X and Y are simply connected large subsets that include the same number of edges, then $S_X = S_Y \quad \Longleftrightarrow \quad S_{X,\alpha} = S_{Y,\alpha}$. When the system is translation-invariant every two sites (or more) instead, like the SSH model, the value of a connected entropy changes depending on the position of its two cuts relatively to the unit cells. These changes are compensated in S^{D}, similarly to how internal cuts compensate each others in Eq. (9.9). This difficulty can be bypassed by considering only the unit cells instead of the sites, and only the cuts between unit cells.

4. For all $\alpha > 1$, S_α has the property of additivity. This property imposes $S_{B,\alpha} = S_{A\cap B,\alpha} + S_{B\setminus A,\alpha}$ for short-range entangled 1D systems.

The first point establishes the qualitative correspondence between the von Neumann and the Rényi-α bipartite entanglement entropies: one of the two entropies is zero if and only if the second is also zero. The von Neumann entanglement entropy never diverges for gapped phases.

[7] For $\alpha \in]0,1[$, we must assume that each term in Eq. (9.11) will also be finite for all bipartition of 1D gapped system. Then, the rest of the demonstration applies, and S_α^{D} can also be used for $\alpha \in]0,1[$. The Rényi-1/2 entanglement entropy is useful as it coincides with the logarithmic negativity for pure states.

As a consequence, the second point prevents the Rényi entropies to diverge as well. The third point ensures that the considerations of Sec. 9.2.2 for the archetypal trivial phase and SSB phase stay valid for S_α^{D}. The fourth point extends this validity for the short-range entangled variations around the archetypal cases and the SPTP. The value of S^{D} and S_α^{D} may differ by a finite factor γ_α: $S^{\mathrm{D}} = \gamma_\alpha S_\alpha^{\mathrm{D}}$.

The von Neumann entanglement entropy is important in quantum information as it counts the maximum amount of distillable entangled pair between a subset and its complementary. Instead, the Rényi-2 entropy can be measured experimentally [14, 15, 25, 87] for all systems in all dimensions, so that S_2^{D} is experimentally measurable for small subset sizes. The disconnected part can be large. The sizes of $L_A = 8$ or 12 are both accessible experimentally [25] and enough to reach the saturated value of S_2^{D} in the simulations Sec. 9.4 to 9.6. In practice, measuring S_2^{D} is done by measuring each bipartite entanglement entropy in Eq. (9.5) successively (using the same system if needed).

9.3 Analytical predictions on S^{D}: long-range entanglement between edges

In this section, we present an explicit calculation of S^{D} for the SSH model to justify the cartoon pictures of Sec. 9.2. In the topological phase, we show that the ground state always contains the maximally entangled superposition of the two localized edge states. This superposition ensures that $S^{\mathrm{D}} = 2\log 2$ up to exponential corrections in the size of the system. $S^{\mathrm{D}} = 0$ for the non-topological phase. This result is valid only when the chain has two edges, i.e. for a finite chain of arbitrary large length.

We first show that the two edge states in the one-body spectrum are in the symmetric and antisymmetric superposition when the chain is finite but of arbitrary large length. We obtain the exact expressions of the two states for weak link hopping $v = 0$ (see Fig. 9.1a)) and track their change when v increases [88]. This hopping v slightly spreads the localized edge states and lifts the degeneracy between the two such that the symmetric superposition of the two is lower in energy. We thus observe the exponential convergence of S^{D} in L to $2\log 2$. This result is quantitatively consistent with the simulations (see Fig. 9.2b)) away from the phase transition ($v = w = 1$) and for large system size. Ref. [89] provides an exact but more involved derivation of the spectrum and eigenstates of the SSH chain for all v and w.

Ref. [88] provides the detailed derivation followed in this section. We remind here the main steps and results. The SSH Hamiltonian with disorder is:

$$H_{\mathrm{SSH}}^{\mathrm{dis}} = -\sum_{i=1}^{N} v_i \left(c_{iA}^\dagger c_{iB} + h.c\right) - \sum_{i=1}^{N-1} w_i \left(c_{i+1A}^\dagger c_{iB} + h.c\right). \tag{9.12}$$

Since the Hamiltonian is non-interacting, a complete solution only requires the one-body spec-

trum and the corresponding eigenstates. At zero temperature, each state is filled in order of increasing energy until the target filling fraction is reached. Because of chiral symmetry, the spectrum is symmetric around $E = 0$, and when they exist, the edge states are the only states at that energy. It follows that the ground state of the topological phase corresponds to the full lower band filled (i.e. all bulk dimers filled with one particle each), and one edge state populated. To express the wave function of latter, we consider the most generic one-body wave function:

$$|\Psi\rangle = \sum_{i=1}^{N} \left(a_i c_{i,A}^\dagger + b_i c_{i,B}^\dagger \right) |0\rangle, \tag{9.13}$$

where $|0\rangle$ is the particle vacuum and a_i and b_i are complex weights. This state is a zero-mode of the Hamiltonian Eq. (9.12) for the infinite chain. For the finite chain (of arbitrarily large length), the approximation $H_{SSH}^{\text{dis}}|\Psi\rangle = 0$ imposes (for $v_i, w_i > 0$):

$$\begin{aligned} &\text{For } i = 2, ..., N, && a_i = a_1 \Pi_{j=1}^{i-1} \frac{-v_j}{w_j}, \\ &\text{For } i = 1, ..., N-1, && b_i = b_N \frac{-v_L}{w_i} \Pi_{j=i+1}^{N-1} \frac{-v_j}{w_j}, \\ & && b_1 = a_N = 0. = \end{aligned} \tag{9.14}$$

In the limit $N \to \infty$, first and second equations of Eq. (9.14) reveal two states, $|L\rangle$ and $|R\rangle$. The two states are exponentially localized on either the first site A or the last site B of the chain with (average) localization length:

$$\xi = \frac{N-1}{\log\left(\Pi_{i=1}^{N-1} |w_i|/|v_i| \right)}. \tag{9.15}$$

The third condition of Eq. (9.14) is instead incompatible with the existence of zero-energy modes and one must consider the (small) lift in the degeneracy between the two edge states. In this case, the best approximations of the two edge states are the two orthogonal real equal-weighted superpositions of $|L\rangle$ and $|R\rangle$. When the cuts in Fig. 9.1b) are far apart both from each other and the boundaries, this superposition ensures $S^{\text{D}} = 2 \log 2$ approached exponentially.

When one $v_i = 0$, the exponential tail of both localized edge state $|L\rangle$ and $|R\rangle$ is truncated at site i. When instead one $w_i = 0$, the exponential tails also stop and two new edge states appear between the cells i and $i+1$. Subsequent hybridization between the now four edge states lifts the degeneracy. The "edge" states around i are not robust against the small local perturbation of $w_i = 0$ in contrast to the real boundary edge states that require a non-local perturbation connecting the two ends. Hence, the system with one $w_i = 0$ still belongs to the regular topological phase of the SSH model. The value of S^{D} is lower, however.

When two zero v's or w's are too close to each other, the approximation breaks down. More generally, when the disorder is too strong, it induces a phase transition beyond which no zero modes may exist anymore.

9.4 S^{D} within a phase and scaling analysis at the phase transition

In this section and the next, we employ free fermion techniques to obtain S^{D} for generic parameters of the system. This method is equivalent to exact diagonalization and relies on the fact that the SSH model describes non-interacting fermions. We briefly review this technique in Sec. 9.4.1. In Sec. 9.4.2, we obtain S^{D} for a range of parameters around the phase transition where S^{D} displays a system-size scaling behavior.

9.4.1 Computing the entanglement spectra

The combination of analytical and numerical techniques reviewed in Ref. [35, 90] allows direct access to the spectrum and eigenvalues of any quadratic Hamiltonians. It computes efficiently the reduced density matrix' entanglement spectra that are necessary to deduce S^{D} in Eq. (9.5). The technique is faster than direct exact diagonalization as its complexity grows only algebraically in system size. The reader may also refer to Ref. [79] that also uses the same technique for the SSH model to study entanglement at the phase transition. The scaling analysis realized in Ref. [79] concerns the bipartite entanglement for increasing subset size for infinite or semi-infinite chains. In contrast, we use the technique in Sec. 9.4.2 to study S^{D} for increasing system size.

The correlation matrix is related to the reduced density matrix. The many-body reduced density matrix ρ_X of a subsystem X can be written as

$$\rho_X = Z_X^{-1} \mathrm{e}^{-\mathcal{H}_X}, \tag{9.16}$$

with $Z_X = \mathrm{tr}_X \left[\mathrm{e}^{-\mathcal{H}_X}\right]$ and where $\mathcal{H}_X$ is the *entanglement Hamiltonian* of ρ_X. $\mathcal{H}_X$ is a quadratic Hamiltonian as long as the system's Hamiltonian describes non-interacting fermions. The SSH Hamiltonian Eq. (9.1) preserves the number of particles, so the technique provides the eigenvalues of $\mathcal{H}_X$, i.e. the entanglement spectrum, using only the correlation matrix $(C_X)_{mn} = \langle c_m^\dagger c_n \rangle$ of the state of interest, where m, n are site indices belonging to X. Indeed, the entanglement Hamiltonian and the correlation matrix are related [91]:

$$\mathcal{H}_X = \log \frac{1 - C_X}{C_X}. \tag{9.17}$$

The one-body eigenstates of the initial Hamiltonian H, the $\{\Phi_k\}_k$, are obtained with exact diagonalization (restricted to one-body states). The many-body ground state correlation matrix C_X follows:

$$(C_X)_{mn} = \sum_{|k|<k_{\mathrm{F}}} \Phi_k^*(m) \Phi_k(n), \tag{9.18}$$

where k_{F} is Fermi's momentum. We then numerically diagonalize the matrix Eq. (9.18) (of the same length of X) using a computer. From the spectrum, we compute the entanglement entropies in S^{D} using Eqs. (9.17), (9.16) and (9.4).

The procedure is also useful to track a time-dependent state and its entanglement: Starting from the ground state of $H_0 = \sum_{ij} h^0_{ij} c^\dagger_i c_j$ for $t < 0$, the system evolves after a sudden quench at $t = 0$. The Hamiltonian becomes $H = \sum_{ij} h_{ij} c^\dagger_i c_j$ for $t > 0$. Along with the state $\rho(t)$, the correlation matrix acquires a time dependence:

$$\begin{aligned}(C_X)_{mn}(t) &= \mathrm{tr}\left[\rho(t) c^\dagger_m(0) c_n(0)\right] \\ &= \mathrm{tr}\left[\rho(0)\, c^\dagger_m(t) c_n(t)\right] \\ &= \sum_{kk',m'n'} \Phi^*_k(m)\Phi_{k'}(n)\mathrm{e}^{-\mathrm{i}E_{k'}t}\mathrm{e}^{\mathrm{i}E_k t}(C_X)_{m'n'}(0)\Phi^*_{k'}(n')\Phi_k(m'),\end{aligned} \tag{9.19}$$

where E_k and Φ_k are the eigenvalues and the eigenvectors of H, $c^\dagger_m(t)$ (resp. $c_m(t)$) is the Heisenberg representation of $c^\dagger_m$ (resp. c_m), $(C_X)_{mn}(0)$ follows Eq.(9.18) for the ground state of H_0, and the sum over the k and k' in Eq. (9.19) includes all the momenta. Eq. (9.19) is valid for any reduced subsystem X. From the spectrum of $C_X(t)$ for any $X = A, B, A \cup B$, and $A \cap B$, we obtain $S^{\mathrm{D}}(t)$.

9.4.2 Phase diagram and scaling analysis

Using this technique, we compute S^{D} and recover the expected phase diagram for the SSH model with open boundary condition in Fig. 9.2a). S^{D} fulfils its role as a "topological detector" as it is non-zero in the topological phase ($v/w < 1$) and zero in the topological-trivial phase ($v/w > 1$). S^{D}_2 (as in Eq. (9.11)) is found identical, up to minor quantitative changes close to the phase transition.

Both the correlation length and the localization length increase close to the transition. The resulting spreading of the internal dimers and the edge states prevents a clean extraction of the edge entanglement, damping the value of S^{D}. In the large size limit ($L_A, L_B, L_D \to \infty$), the well-quantized plateau of $S^{\mathrm{D}} = 2\log 2$ and $S^{\mathrm{D}} = 0$ extends over their whole respective phases according to the scaling of Fig. 9.2b).

We observe a system-size scaling behavior for S^{D} at the second-order phase transition as in Ref. [28]. We use the following Ansatz, typical of an order parameter:

$$S^{\mathrm{D}} L^{\frac{a}{b}} = \lambda\left(L^{\frac{1}{b}}(\alpha - \alpha_c)\right), \tag{9.20}$$

with fixed L_A and L_B so that $L(L_D)$ is the only scaling parameter left. $\alpha = v/w$ is the varying parameter and α_c is the critical value of this parameter at the phase transition. $\lambda(x)$ is the universal function at the phase transition, and a and b are entanglement critical exponents, similar to β and ν for the 1D Ising chain at the paramagnetic/ferromagnetic phase transition. $\lambda(x)$ behaves

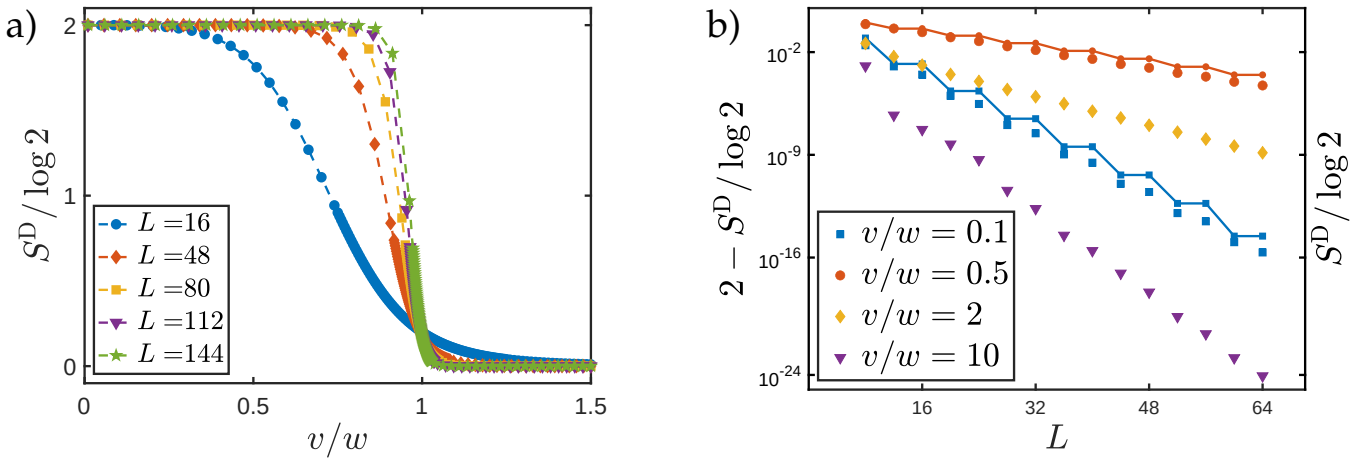

Figure 9.2: (Color online) a) S^D as a function of the ratio v/w and the total length L for $L = 2L_A = 2L_B = 4L_D$. The critical point is at $v/w = 1$. S^D is non-zero for the topological phase, and zero outside: S^D qualifies as a good topological detector. b) Scaling behavior of S^D towards its quantized convergence value. For the topological phase (left y-axis; $v/w = 0.1$ and 0.5 resp. squares and dots), S^D converges to $2\log 2$. For the non-topological phase (right y-axis; $v/w = 2$ and 10 resp. diamonds and triangles), S^D converges to zero. The increments on both the left and right y-axis are the same. The scaling behavior of S^D is exponential with the size of the chain $L = 2L_A = 2L_B = 4L_D$ for parameters in both phases. The results of the simulations (scattered points) agree with the analytic approximations of Sec. 9.3 (full lines). The saw-teeth variations of the latter are due to the alternating sign in Eq. (9.14).

asymptotically as:

$$\lambda(x) \to \infty \qquad \text{when } x \to -\infty, \tag{9.21a}$$

$$\lambda(x) \to 0 \qquad \text{when } x \to +\infty. \tag{9.21b}$$

The curve intersection and curve collapse of Figs. 9.3 give the value $\alpha_c = 0.958$, $a = 1.01$, and $b = 0.81$ for the best mean square fit. The exponents a and b are obtained as the optimal values from a discrete mesh of spacing 0.01. It is not straightforward to assign a rigorous interval of confidence to the values we have obtained. From the data shown in the inset of Fig. 9.3(a), one can observe a drift of order 1% in the crossing position between the curves representing the two smaller (blue and red line) and the two larger (yellow and violet) system sizes, respectively. It is thus reasonable to assume that the relative error on α_c is at the percent level.

The Ansatz Eq. (9.20) fails to describe the scaling behavior of S^D close to quantized plateau at $2\log(2)$ at $\alpha = \alpha_t(L)$. $\alpha_t(L)$ gives an estimate of the transition region. With L_A and L_B still fixed, we have, in general:

$$S^D L^{\frac{a}{b}} = \Theta\left(L, L^{\frac{1}{b}}(\alpha - \alpha_c)\right), \tag{9.22}$$

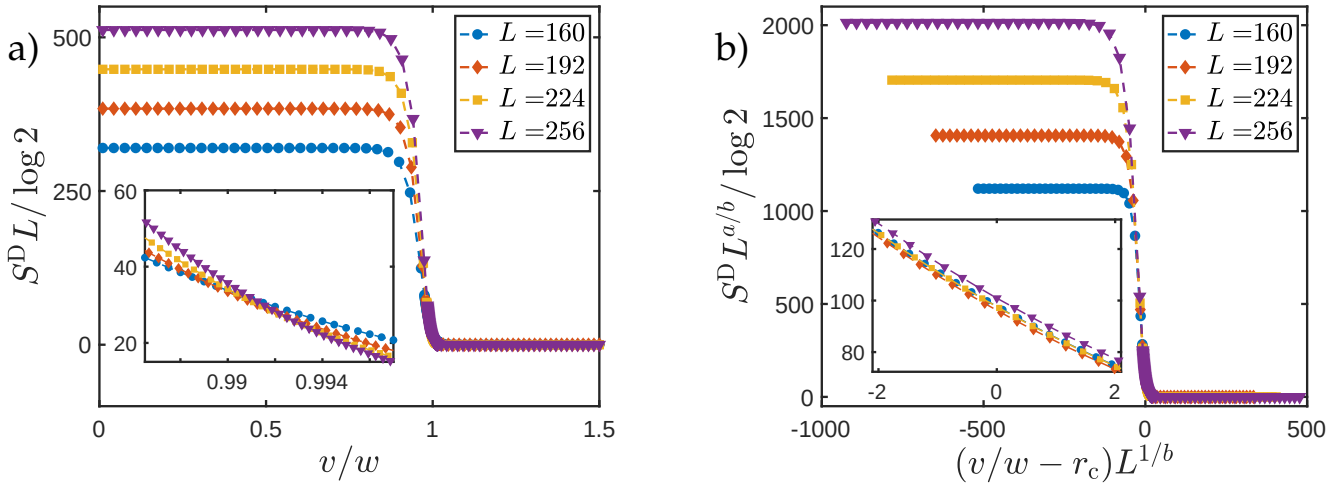

Figure 9.3: (Color online) a) Curve intersection of $S^{\mathrm{D}}L$ as a function of the ratio v/w for $L_A = L_B = 64$. It extracts the critical point at the crossing, $v/w = 0.958$ here (1 theoretically). b) Best curve collapse of the Ansatz Eq. (9.22) obtained for $a = 1.01$ and $b = 0.81$. The clear collapse in inset signals the universal behavior of λ at the transitions.

such that, according to Fig. 9.3 b):

$$\Theta\left(L, L^{\frac{1}{b}}(\alpha-\alpha_c)\right) = \begin{cases} L\log 2 & \text{when } L^{\frac{1}{b}}(\alpha-\alpha_c) < x^*(L), \\ \lambda\left(L^{\frac{1}{b}}(\alpha-\alpha_c)\right) & \text{when } L^{\frac{1}{b}}(\alpha-\alpha_c) > x^*(L), \\ \text{a non universal} & \\ \text{regularization} & \text{when } L^{\frac{1}{b}}(\alpha-\alpha_c) \sim x^*(L), \end{cases} \tag{9.23}$$

where $x^*(L) = L^{\frac{1}{b}}(\alpha_t(L) - \alpha_c) < 0$ marks the end of the plateau and the start of the universal regime. We find neither $x^*(L)$ nor $\alpha_t(L)$ to be universal, a result that is not unexpected as the plateau is due to a UV property of the phase.

9.5 Invariance of S^{D} after global quenches

In this section, we show that disconnected entanglement carries robust signatures of quantization after global quantum quenches, as expected for topological invariants associated with particle-hole symmetry (PHS) [70].

In Sec. 9.5.1, we elaborate on two arguments discussed in Ref. [70]. These arguments predict the conservation of topological edge states over time, and thus, according to Eq. (9.8), the conservation of S^{D}. This prediction is consistent with our simulations in Sec. 9.5.2. Quantum quenches are thus ideal test-bed to determine whether a given quantity is indeed a topological invariant associated with particle-hole symmetry.

9.5.1 Invariance of S^{D} during unitary evolution: the role of particle-hole symmetry

We provide here the two arguments explaining why topological invariants associated with PHS are invariant to symmetry-preserving quenches that are presented in Ref. [70]. In particular, we explicitely prove why the D classification applies to the Hamiltonian in the interaction picture, which is an important step in one of the two arguments. We then use one of the conclusion of Ref. [70]: the stability of the edge states after a quench, to prove the invariance of S^{D}. Thus, we argue that S^{D} behaves like a topological invariant that keeps track of the initial maximally entangled edge states.

Given a system, a quantized topological invariant associated with a symmetry is computed from the ground state. If this state locally evolves in time without breaking the symmetry, the topological invariant remains constant. To prove the statement for PHS, we denote as $\mathcal{H}^i$ and $\mathcal{H}^f$ the initial Hamiltonian (before quench) and the final Hamiltonian (after quench), respectively. If $|\psi(0)\rangle$ is a ground state of $\mathcal{H}^i$, then the state evolves after the quench as $|\psi(t)\rangle = U(t)|\psi(0)\rangle$, where the unitary evolution operator depends only on $\mathcal{H}^f$ and t. $\mathcal{H}^i$ is PHS if $CH^*C^\dagger = -H$, where C is the PHS operator and $\mathcal{H}^i = \sum_{ml} \psi_m^\dagger H_{ml} \psi_l$. In that case, $\rho(0) = |\psi(0)\rangle\langle\psi(0)|$ is also PHS, i.e. $C\rho^*C^\dagger = 1 - \rho$. If $\mathcal{H}^f$ is also PHS, so will $\rho(t)$. So if a topological invariant associated with PHS is initially fixed to a quantized value by $\rho(0)$, this value remains quantized along the PHS-preserving dynamics.

The second alternative argument consists in viewing the evolving state as the ground state of the quenched Hamiltonian in the interaction picture. Time becomes a parameter of this fictitious Hamiltonian on which we apply the topological insulator classification associated with the PHS symmetry. Specifically, $|\psi(t)\rangle$ is a ground state of the fictitious Hamiltonian $\mathcal{H}^{\mathrm{fic}}(t)$:

$$\mathcal{H}^{\mathrm{fic}}(t) = U(t)\mathcal{H}^i U(t)^\dagger.$$

$\mathcal{H}^{\mathrm{fic}}(t)$ is PHS if $\mathcal{H}^i$ and $\mathcal{H}^f$ are PHS. The spectrum is invariant in time, so there is no gap closing along the dynamics. Since $\mathcal{H}^i$ and $\mathcal{H}^f$ are finite-ranged, we show explicitly that $\mathcal{H}^{\mathrm{fic}}(t)$ is short-ranged. Indeed, using the Baker-Campbell-Hausdorff formula,

$$\mathcal{H}^{\mathrm{fic}}(t) = H^i + \sum_{n=1}^{\infty} \frac{(it)^n}{n!} C_n(H^f, H^i), \tag{9.24}$$

where $C_n(H^f, H^i) = [H^f, [H^f, ...[H^f, H^i]...]]$ where H^f appears n times and $[A, B]$ is the commutator between A and B. Assuming that both H^i and H^f only involve nearest neighbors hoping, we write $n = 2l$ when n is even, $n = 2l - 1$ when n is odd. Thus:

$$C_{2l}(H^f, H^i) = \sum_{k=0,l} \alpha_{i,k}(l) c_i^\dagger c_{i+2k+1} + H.c. \tag{9.25a}$$

$$C_{2l-1}(H^f, H^i) = \sum_{k=1,l} \tilde{\alpha}_{i,k}(l) c_i^\dagger c_{i+2k} + H.c. \tag{9.25b}$$

where $|\alpha_{i,k}| \leq \Lambda^{2l+1} 2^{2l} S_k^l$ and $|\tilde{\alpha}_{i,k}| \leq \Lambda^{2l} 2^{2l-1} S_k^l$ (for all i). Λ is the largest absolute value of all the hopping amplitude in H^i and H^f and S_k^l are obtained from the Catalan triangle [92] such that ($l \in \mathbb{N}^*$, $0 \leq k \leq l$):

$$S_k^l = \text{Binomial}(2l, l-k) - \text{Binomial}(2l, l-k-1) \quad \text{if } n \text{ is even}, \tag{9.26a}$$

$$S_k^l = \text{Binomial}(2l-1, l-k) - \text{Binomial}(2l-1, l-k-1) \quad \text{if } n \text{ is odd}, \tag{9.26b}$$

where by convention Binomial(n, -1)=0. Rewriting $\mathcal{H}^{\text{fic}}(t)$ as:

$$\mathcal{H}^{\text{fic}}(t) = \sum_{i,r} \beta_{i,r}(t) \left(c_i^\dagger c_{i+r} + H.c \right).$$

We thus have:

$$|\beta_{i,r}(t)| \leq \sum_{l=k}^{\infty} \Lambda^{2l+1} \frac{(2t)^{2l}}{(2l)!} S_k^l \quad \text{if } r = 2k-1 \text{ using Eq.(9.26a)}, \tag{9.27a}$$

$$|\beta_{i,r}(t)| \leq \sum_{l=k}^{\infty} \Lambda^{2l} \frac{(2t)^{2l-1}}{(2l-1)!} S_k^l \quad \text{if } r = 2k \text{ using Eq.(9.26b)}. \tag{9.27b}$$

Using *Mathematica*:

$$\sum_{l=k}^{\infty} \Lambda^{2l+1} \frac{(2t)^{2l}}{(2l)!} S_k^l = \frac{(2k+1) I_{2k+1}(4\Lambda t)}{2t} = o(1/k), \tag{9.28a}$$

$$\sum_{l=k}^{\infty} \Lambda^{2l} \frac{(2t)^{2l-1}}{(2l-1)!} S_k^l = \frac{2k I_{2k}(4\Lambda t)}{2t} = o(1/k), \tag{9.28b}$$

where $I_n(x)$ is the modified Bessel function of the first kind such that $I_0(0) = 1$. Thus, $\beta_{i,r}(t) = o(1/r)$ on all sites and for all times: although the range of $\mathcal{H}^{\text{fic}}(t)$ increases with time, the Hamiltonian is short range.

$\mathcal{H}^i$ and $\mathcal{H}^{\text{fic}}(t)$ are thus connected unitarily, continuously, locally and without closing the gap, as if by an adiabatic connection [38–40] (no extra hypothesis of adiabaticity was imposed in the reasoning). Therefore, unless the system experiences a dynamical phase transition, $\mathcal{H}^i$ and $\mathcal{H}^{\text{fic}}(t)$ are in the same topological phase relative to the PHS, and if one has robust edge states, so does the other. Consequently, the topological invariant associated with the PHS (like the Zak phase modulo 2π) is also invariant. The reasoning extends to interacting systems according to Ref. [70]. Note that, when the system is finite, and after a certain time $t \sim t_c$, $U(t)$ effectively becomes an infinite-ranged (non-local) transformation such that the topology associated with the state $|\psi(t)\rangle$ is not well-defined anymore. The topological invariant starts then to vary.

We stress that these considerations concern PHS (a unitary symmetry leaving time invariant)

only, and not the time-reversal (TRS) or chirality symmetry (CS), which are broken by time evolution in this reasoning. Hence, a topological invariant fixed by, e.g. TR, may vary in time even when both $\mathcal{H}^i$ and $\mathcal{H}^f$ are TRS. This means that, while there is an infinite amount of topological phases in the BDI class that can be distinguished using the Zak phase (in $\pi\mathbb{Z}$, fixed by TRS, PHS, and CS), only two are distinguished by the Zak phase modulo 2π (fixed by THS) as time evolves.

Thus, if S^{D} is a topological invariant, then S^{D} of a topological ground-state (at equilibrium) is conserved when the state is time-evolved by any local, unitary, and symmetry-preserving operator until a time t_c fixed by the finite size of the chain. We argue that the quenches we consider only induce such time-evolution. The conservation of the topological invariants of the system implies the conservation of the associated bulk-boundary correspondence. The conserved correspondence implies conserved edge states, and, thus, conserved S^{D}. Indeed, we observe this conservation of S^{D} in Sec. 9.5.2. We conclude that S^{D} is likely a topological invariant.

The reasoning also shows that S^{D} keeps track of the topology of the initial state while the topological invariant associated with PHS, the Zak phase (modulo 2π), does not. Indeed, the Zak phase in the topological phase of the SSH model is $2\pi = 0$ modulo 2π (while the Zak phase of e.g. the Kitaev model is π). Hence, the topological SSH phase and the trivial phase are not expected to be topologically different in the dynamical context. Yet, S^{D} distinguishes between states with and without long-range edge entanglement, an observable feature that we traced back to topology.

We conclude that S^{D} is likely a topological invariant. Furthermore, S^{D} keeps track of the topology of the initial state, whereas another topological invariant like the Zak phase modulo 2π does not.

9.5.2 Invariance of S^{D} after quenches: finite-size scaling analysis

We performed an extensive investigation of the evolution of S^{D} after a quantum quench within and across the topological phase. We used the procedure detailed in Sec. 9.4.1. Specifically, we first derive the one-body eigenvalues of the desired initial Hamiltonian H_0. Using these eigenvalues and Eq. (9.18), we obtain the full correlation matrix $C_X(0)$ of the initial ground state. Similarly, we derive both the one-body spectrum and the eigenvalues of the Hamiltonian post-quench H. Using $(C_X)_{mn}(0)$, the spectrum and eigenvalues of H, and Eq. (9.19), we obtain the time-dependent full correlation matrix $C_X(t)$ of the quenched state. From $C_X(t)$, we finally compute $S^{\mathrm{D}}(t)$ like in the static case. Fig. 9.4a) gives the representative example of the time evolution of $S^{\mathrm{D}}(t)$ after a quench from the topological phase to the trivial phase. Instead, Fig. 9.4c) corresponds to a quench from to trivial phase to the topological phase.

For both quenches and for quenches within the topological or within the trivial phase, we observe the same phenomenology: S^{D} sticks to its initial value until a certain timescale t_c that depends on the quench and the size of the system as in Ref. [28]. The corresponding phenomenon in the bipartite entanglement entropy is a constant offset during the time evolution [93]. We define the timescale t_c as the time when S^{D} varies of $2\log 2/100$ from its initial value (dotted line in inset

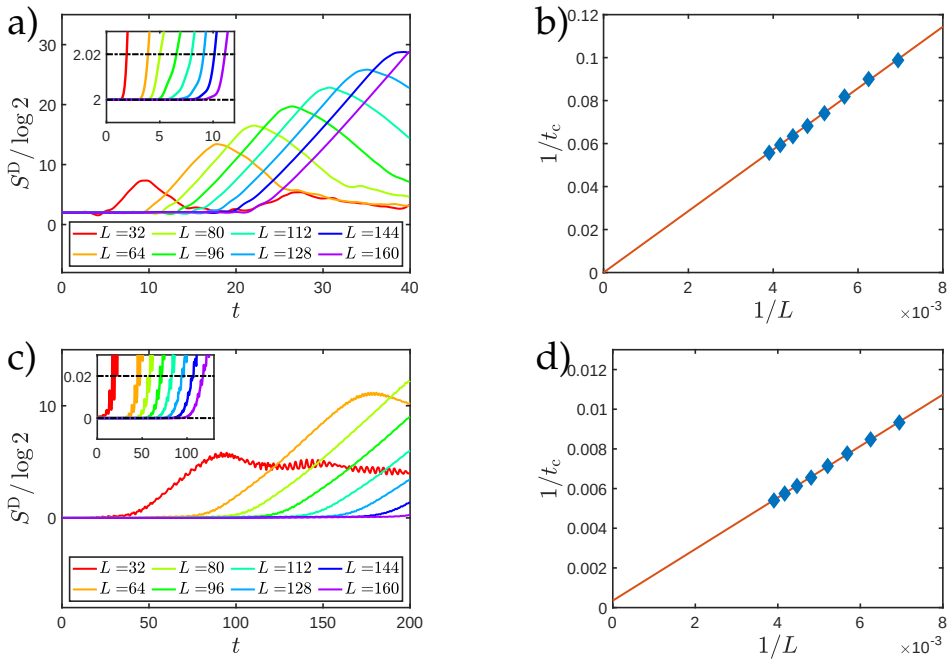

Figure 9.4: (Color online) a) and c) Time evolution of S^D after quenching the Hamiltonian from a) $v/w = 0.1$ (topological phase) to $v/w = 1.5$ (trivial phase) and c) $v/w = 1.5$ to $v/w = 0.1$ at $t = 0$ and for different total length L with $L_A = L_B = 2L_D = L/2$. S^D remains at its initial value until finite-size effects change it at $t \sim t_c$. Insets: zoom on the graph around $t \sim t_0$ and for $|S^D(t) - S^D(0)| \lesssim 2\log 2/100$. b) and d) Scaling behaviour of t_c after the sudden quench a) and c) respectively. The point corresponding to smallest L in both b) and d) is not included in the linear fit (orange line). In d), the fit includes the origin within two standard deviation. Thus, when $L \to \infty$, t_c diverges, demonstrating that S^D does not evolve after unitary evolution for large systems.

of Fig. 9.4a) and c)). We observe that $t_c \sim L/\eta$ when $L > 100$ in Fig. 9.4b) and d). η increases when the amplitude of the quench increases. When $L \to \infty$, $t_c \to \infty$ showing that S^D behaves like a topological invariant.

9.6 Robustness of S^D to disorder

For 1D non-interacting systems, Anderson localization kicks in as soon as disorder is introduced [94] (or reviewed in Ref. [95]). This localization is not antagonistic to topological phases. Both can coexist. The disorder can even favor the topological phase, as known for the case of quantum Hall effects in $D > 1$. In the SSH model, disorder can extend the topological phase past $v/w > 1$. This extended regime is called a topological Anderson insulator [96–98].

Using S^D we successfully reproduce the disorder-induced phase diagram of the SSH model, see Fig. 9.5. This phase diagram is known and was partially measured for uniform disorder [76] and is known for quasiperiodic potential [99]. The former work extrapolated the winding number from measurements. This topological invariant stays well quantized to 1 or 0 (mod 2) despite the disorder for both the topological and the trivial phase. We observe a similar behavior for S^D. The robustness to disorder of S^D follows the robustness of the edge states of SPTP [100].

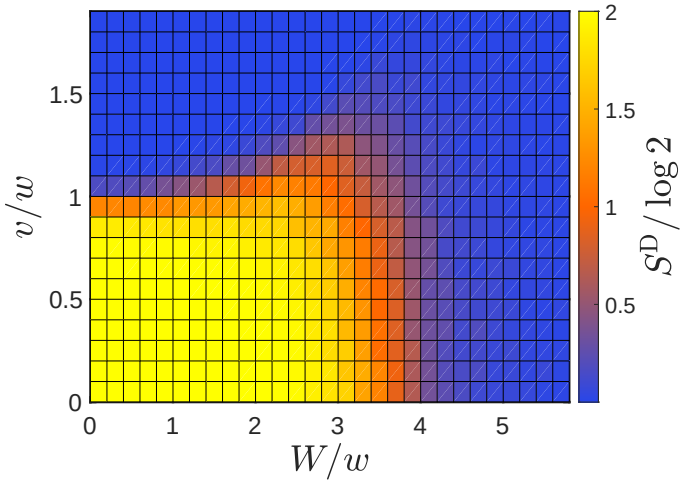

Figure 9.5: (Color online) Phase diagram of the SSH model obtained with S^{D} for the uniform disorder of Eq. (9.29) with $2W_1 = W_2 = W$. We set $L_A = L_B = 2L_D = 32$. S^{D} is averaged over 400 realizations for each point. The "bump" of the topological phase (in yellow) constitutes the topological Anderson insulator regime.

Specifically, we consider uniform, chirality-preserving disorder on the hoppings of Eq. (9.12):

$$w_i = w + W_1\delta_i, \tag{9.29a}$$

$$v_i = v + W_2\Delta_i, \tag{9.29b}$$

with $w = 1$ fixed, δ_i and Δ_i being random variables of uniform distribution in $[-0.5, 0.5]$. We then average S^{D} over the realizations. For weak disorder, Fig. 9.5 ($2W_1 = W_2 = W$) shows that the topological phase is stable when $S^{\mathrm{D}} = 2\log 2$. The phase is trivial at strong disorder, and $S^{\mathrm{D}} = 0$.

We also observe the topological Anderson insulator regime like in Ref. [76]. For $W_1 = W_2 = W$ (not shown), the phase transition line is monotonous with W. The locations of both transition lines we observe are compatible with the literature [76, 99]. Unlike the critical point $W_1 = W_2 = 0$ of Sec. 9.4.2, S^{D} is well-quantized at either 0 or $2\log 2$ around the phase transition line. Its distribution is however a bimodal hence the damped value of the average at the transition. It is unclear to us if such a distribution is a marker of first order phase transition.

9.7 Disconnected entropies in the BDI class

We now discuss the generality of our results in the context of the BDI class of the tenfold-way [74, 101, 102].

The SSH can be mapped locally to a stack of two coupled Kitaev wires [103]. In the formalism of Ref. [104], this stack is called a 2-chain whereas the non-interacting Kitaev chain is the 1-chain. Both the 1- and 2-chain can be understood with the same $\mathbb{Z}$ classification. The topological phases they display belong to different classes within the BDI classification as they have a different value for their topological invariant: the Zak phase. Specifically, the Zak phase is π in the 1-chain and

2π in the 2-chain.

The edge states of the two chains are also different. Both chains have one (e.g., left) edge mode protected by the time-reversal symmetry, while the other (right) mode is protected by both the parity and the time-reversal symmetry [103]. In the 1-chain, the left and right parity operators do not commute. It is impossible to write the left and right edge modes as linearly independent in the same local basis. Thus, the ground state naturally requires a non-local description due to these edge modes. This specific form of non-locality implies a non-zero value for S^{D}.

In the 2-chain, the left and right parity operators commute. The edge modes can be written independently from each other in a local basis (cf Sec. 9.3), and are local. For an infinite chain, the edge entanglement can thus be zero. As we showed in this paper, that is not the case, and the edge entanglement remains quantized and is maximal (given the Hilbert space dimension of the edge modes) for any finite chain.

We extend the conclusions shared between the 1-chain and the 2-chain to the whole BDI classification. Indeed, all topological phases of BDI either have non-local (fractional) edge states or local edge states, like in the 1- and the 2-chains respectively [103]. Only the association between the protecting symmetry (time-reversal or the composition parity and time-reversal) and the protected edge (left or right) varies. These variations should have no consequences to S^{D} that does not distinguish between left and right. We conclude that the validity of S^{D} extends to all BDI, as the phenomenology of edge modes is the same as the two models considered so far.

While this is not directly relevant for the model discussed here, the generality of our conclusion likely extends to the D classification. Even without time-reversal symmetry, the Kitaev wire displays a topological phase and a trivial phase. Both phases belong to the D classification which is a $\mathbb{Z}_2$ classification associated with the only particle-hole symmetry. The edge states of the topological Kitaev wire in the D class are the same as in the BDI class [8].

9.8 Conclusions

We have shown how entanglement entropies distinguish topological and non-topological insulating phases in the Su-Schrieffer-Heeger one-dimensional model with open boundary conditions. This entanglement is quantified by the disconnected entanglement entropy S^{D} computed for the ground state of the system. It is 0 in the trivial phase and $2\log 2$ for the topological phase in the large system limit. We related S^{D} to the number of zero-mode edge states, a topological invariant. Thus, S^{D} is quantized and enjoys robustness disorder. As the model is particle-hole symmetric, S^{D} is also invariant during local, unitary, and symmetry-preserving time evolution for large system size. S^{D} also displays a universal scaling behavior when crossing the phase transition, akin to an order parameter. Numerical simulations show that modest and experimentally accessible partition sizes are sufficient for S^{D} to reach its quantized regime. Finally, combining the present

[8] although they are not protected by the same set of symmetries.

findings with older results on fermionic S^{D} in the Kitaev chain, we argued that our conclusions extend to the full BDI class of the topological insulators and superconductors classification.

To complete the comparison of S^{D} to a topological invariant, it would be interesting to investigate the evolution of S^{D} when the protecting symmetry is explicitly broken and the maximal entanglement of the edge state is no more set topologically, such as in the Rice-Mele model [105]. It would also be interesting to use entanglement topological invariants to characterize the real-time dynamics of other instances of topological insulators in the presence of a bath [40].

D

Additional information on the Kitaev model

D.1 Gauge theory characterization of entanglement properties.

The starting point is the exact relation [106] between Eq. (8.2) and a $\mathbb{Z}_2$ LGT, that we schematically review. The $\mathbb{Z}_2$ LGT describes the coupling between the $\mathbb{Z}_2$ gauge fields residing on bonds (represented here by Pauli matrices, $\sigma^{\alpha}_{j,j+1}$), and the hard-core Higgs fields φ_j, with $n_j = \varphi_j^{\dagger}\varphi_j$, defined on the vertices. The gauge-invariant Hilbert space is defined as the set of states where the local parity $P_j = (1-2n_j)\sigma^z_{j-1,j}\sigma^z_{j,j+1}$ is fixed to 1 (see Fig. D.1). Under open boundary conditions (OBC), we fix to $\sigma^z_{0,1} = 1$ the value of the first gauge field without loss of generality. The value of the last gauge field $\sigma^z_{L,L+1} = P$ gives the total parity of the system due to gauge invariance.

The ground state wave functions $|\Psi\rangle_{\pm}$ can be described in terms of either fermionic or gauge fields, since, in 1D, those are mutually fixed by Gauss law. In terms of LGT, the ground states are equal-weight superpositions of all possible string states of arbitrary length, and compatible with the boundary conditions: a sample of those are depicted in Fig. D.1 for the case $P = 1$. This picture describes a 1D gauge theory in a phase with strongly fluctuating gauge fields, and is strongly reminiscent of the loop description of 2D quenched $\mathbb{Z}_2$ LGT [8, 50, 107].

Evaluating entanglement entropies in this phase is straightforward by exploiting gauge invariance:

i) The entropy of each connected partition is $\log 2$. Indeed, let us define σ^z_L, σ^z_R as the two boundary spins of the partition. Their product is equal to the parity of the partition: the density matrix of the partition is block-diagonal in this conserved quantum number. If the correlation length is much smaller than the partition length, both positive and negative parities are equally probable and all states count with equal weight. The corresponding von Neumann entropy is thus $\log 2$.

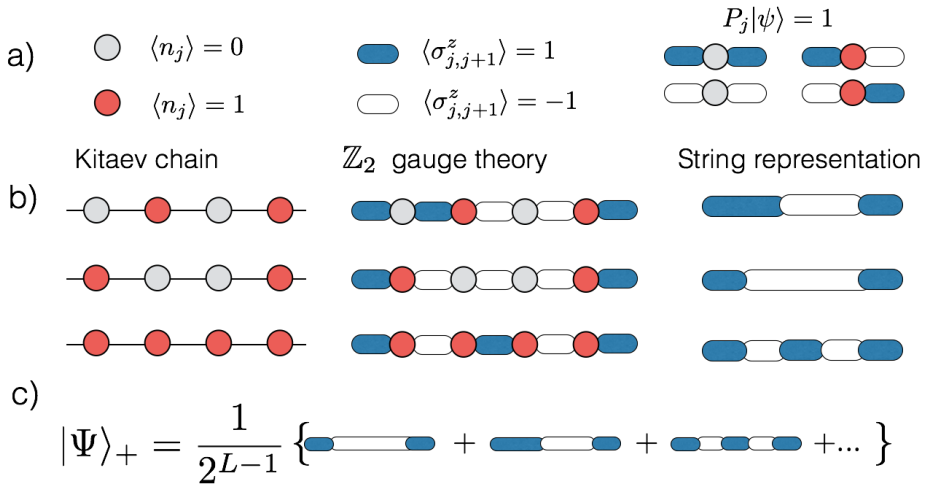

Figure D.1: (Color online) Schematics of the correspondence between the Kitaev chain and $\mathbb{Z}_2$ lattice gauge theories. *a)*: Hilbert space structure and gauge-invariant building blocks. *b)*: three examples of the mapping between states in the fermionic (left), gauge theory (center), and string representation (right). *c)*: string representation of $|\Psi\rangle_+$.

ii) the entropy of disconnected partitions is $(N_c - 1)\log 2$, where N_c is the number of partitions such that $N_c = 2$ corresponds to the standard bipartition of the chain into two halves. Indeed, let us define as $\sigma^z_{L,h}, \sigma^z_{R,h}$ the gauge fields at the boundaries of the partition h. As long as the length of each partition is larger than the correlation length, each patch is an equal-weight superposition of all possible states, under the condition that $P_h = +1$ or -1 for partitions with or without an out-coming flux respectively. For a fixed total parity, there are 2^{N_c-1} finite, equal values of the corresponding density matrix, which returns an entropy equal to $(N_c - 1)\log 2$.

We emphasize that the gauge theory description enables a simple calculation of the entropies (by replacing fermionic statistics with a $\mathbb{Z}_2$ gauge field), and, at the same time provides a simple, compelling physical picture, that might be extended to more exotic types of order.

D.2 The Kitaev model without interaction

In this section, we briefly present the Kitaev model and detail the derivation of all the analytical results mentioned in the main text. More specifically, we focus on the regime described in Kitaev's original paper [23] whose algebra is simpler while containing important features on the entanglement properties of the whole model when it displays a topological phase. We give here a brief reminder of the Kitaev wire of Kitaev's seminal paper Ref. [23] for the unfamiliar reader. The Kitaev wire is a chain of L spinless fermions with open boundary conditions described by the

Hamiltonian:

$$H = \sum_{j=1}^{L-1} \Big(-t \left(a_j^\dagger a_{j+1} + a_{j+1}^\dagger a_j \right) \\ -\mu \left(a_j^\dagger a_j - \frac{1}{2} \right) + \Delta a_j a_{j+1} + \Delta^* a_{j+1}^\dagger a_j^\dagger \Big), \tag{D.1}$$

where t is the hopping amplitude, μ is the chemical potential, and $\Delta = |\Delta| e^{i\theta}$ the induced superconducting gap. It is convenient to absorb the complex phase of the latter in a (completely local) redefinition of the local creation and annihilations operators $a_j^\dagger$ and a_j such that:

$$(a_j^\dagger, a_j) \to (e^{-i\theta/2} a_j^\dagger, e^{i\theta/2} a_j), \tag{D.2}$$

and consider Eq. (D.1) with Δ real only. It is then useful to introduce the Majorana fermions operators c_j (for $j = 1, ..., L$):

$$c_{2j-1} = a_j + a_j^\dagger, \quad c_{2j} = \frac{a_j - a_j^\dagger}{i}, \tag{D.3}$$

such that:

$$\{c_m, c_l\} = 2\delta_{m,l}, \quad c_m^\dagger = c_m, \tag{D.4}$$

where $\delta_{m,l}$ is the Kronecker delta. The Hamiltonian Eq. (D.1) then becomes:

$$H = \frac{i}{2} \sum_{j=1}^{L-1} \left(-\mu c_{2j-1} c_{2j} + (t + |\Delta|) c_{2j} c_{2j+1} \right. \\ \left. + (-t + |\Delta|) c_{2j-1} c_{2j+2} \right). \tag{D.5}$$

In the special regime of parameters when $|\Delta| = t > 0$ and $\mu = 0$ (which we call the stereotypical regime), the Hamiltonian Eq. (D.5) becomes:

$$H = it \sum_{j=1}^{L-1} c_{2j} c_{2j+1}, \tag{D.6}$$

where it is important to note that the Majorana operators appearing in each term of the sum are not from the same sites. One can define new local fermionic creation and annihilation operators on the link such that (for $j = 1, ..., L-1$ only):

$$\tilde{a}_j = \frac{c_{2j} + i c_{2j+1}}{2}, \quad \tilde{a}_j^\dagger = \frac{c_{2j} - i c_{2j+1}}{2}, \tag{D.7}$$

that only mixes two neighbouring sites. The Hamiltonian Eq. (D.6) becomes diagonal:

$$H = 2t \sum_{j=1}^{L-1} \left(\tilde{a}_j^\dagger \tilde{a}_j - \frac{1}{2} \right), \tag{D.8}$$

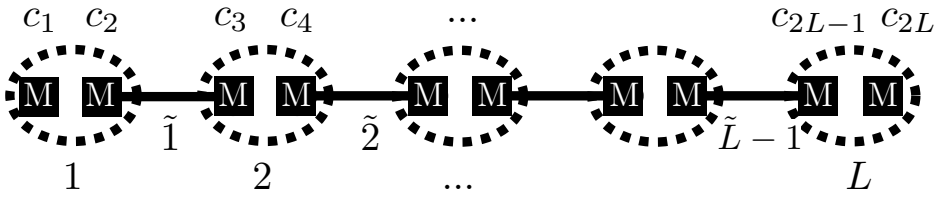

Figure D.2: The Kitaev chain with L sites and open boundary conditions. Each site i (denoted by a dashed circle) can be occupied by one spinless fermion, and can be decomposed into two Majorana fermions (denoted by black dots) in $2i-1$ and $2i$. Associating the Majoranas $2i$ and $2i+1$ allows the construction of a new quasi local fermionic basis denoted with tildes. The ground states in the topological stereotypical regime will see its neighbouring Majorana fermions pairing up, so that, in the tilded basis, each site is unoccupied. Only the two Majorana on the edges do not need to pair up.

and has two degenerate ground states, each pairing a Majorana fermion of one edge with a Majorana fermion of the other (cf Fig. D.2). Defining the non-local operators:

$$b = \frac{c_{2L} + ic_1}{2}, \quad b^\dagger = \frac{c_{2L} - ic_1}{2}, \tag{D.9}$$

the two ground states $|0\rangle$ and $|1\rangle$ satisfy:

$$\begin{aligned} \forall j \in [\![1, L-1]\!], \ \tilde{a}_j|0\rangle &= 0, \\ \forall j \in [\![1, L-1]\!], \ \tilde{a}_j|1\rangle &= 0, \\ b|0\rangle = 0, & \\ b^\dagger|0\rangle &= |1\rangle. \end{aligned} \tag{D.10}$$

In the case of periodic boundary conditions, $|0\rangle$ becomes the only ground state.

D.3 The entanglement properties of the topological phase in the stereotypical regime

To understand the entanglement properties of this topological phase and analytically compute the disconnected entanglement entropy S^{D}, it is useful to compute any reduced density matrices for the ground states $|0\rangle$ and $|1\rangle$ obtained in the stereotypical regime when $|\Delta| = t > 0$ and $\mu = 0$. To do so, it is useful to rewrite these states in the “second quantization" formalism, but in the new tilted basis where:

$$\begin{aligned} \forall j \in [\![1, L-1]\!], \ \tilde{n}_j &= \tilde{a}_j^\dagger \tilde{a}_j, \\ n_b &= b^\dagger b, \end{aligned} \tag{D.11}$$

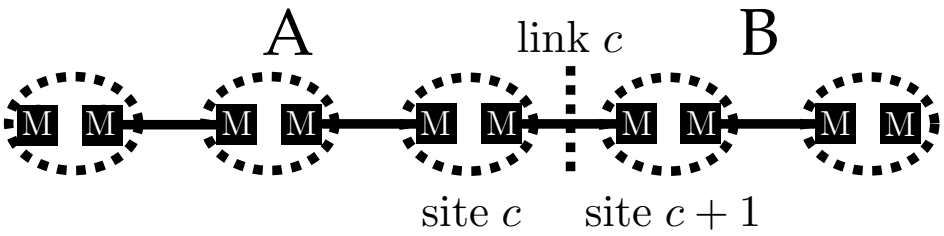

Figure D.3: A physical cut can only be done between sites, here, on the link c, partitioning the chain into two subsets: A and B.

where the index b stands for boundary. In that case, the two ground states can be rewritten as:

$$|0\rangle = |\tilde{n}_1 = 0, \tilde{n}_2 = 0, \ldots, \tilde{n}_{j-1} = 0, n_b = 0\rangle, \tag{D.12a}$$
$$|1\rangle = |\tilde{n}_1 = 0, \tilde{n}_2 = 0, \ldots, \tilde{n}_{j-1} = 0, n_b = 1\rangle, \tag{D.12b}$$

which is a quasi local basis in the sense that each $\tilde{n}_j$ can be expressed in terms of operators acting only on sites j and $j+1$. For a connected bipartition of the system, as illustrated in Fig. D.3, the ground states [Eqs. (D.12)] cannot be written as a product state, due to both the presence of edge states and the way Majorana fermions are linked in the bulk of the system (for instance, see link $c \in [\![1, L-1]\!]$ of Fig. D.3).

To properly do the partial trace and obtain the reduced density matrix ρ_A, it is better to express the ground states in terms of a local basis for both A and B. This becomes possible when rewriting the two parts of the open Kitaev wire as two open Kitaev wires connected into a singlet on the link c. Calling L_A the size of A, and L_B the size of B, such that $L_A + L_B = L$, we define a new fermionic basis, local in A and B:

$$a_A = \frac{1}{2}\left(c_{2L_A} + ic_1\right), \tag{D.13a}$$
$$a_A^\dagger = \frac{1}{2}\left(c_{2L_A} - ic_1\right), \tag{D.13b}$$
$$a_B = \frac{1}{2}\left(c_{2L_A+2L_B} + ic_{2L_A+1}\right), \tag{D.13c}$$
$$a_B^\dagger = \frac{1}{2}\left(c_{2L_A+2L_B} - ic_{2L_A+1}\right), \tag{D.13d}$$
$$\tilde{a}_c = \frac{1}{2}\left(c_{2L_A} + ic_{2L_A+1}\right), \tag{D.13e}$$
$$\tilde{a}_c^\dagger = \frac{1}{2}\left(c_{2L_A} - ic_{2L_A+1}\right), \tag{D.13f}$$
$$b = \frac{1}{2}\left(c_{2L} + ic_1\right), \tag{D.13g}$$
$$b^\dagger = \frac{1}{2}\left(c_{2L} - ic_1\right), \tag{D.13h}$$

so that a_A and a_B (and hermitian conjugate) act as boundary operators for the subchains A and B respectively. Hence, in second quantization, and after dropping the redundant mentions of the

$\tilde{n}_j$, $j \in [\![1, L-1]\!] \setminus \{c = L_A\}$, the two ground states of the full chain are $|n_b = 0, \tilde{n}_c = 0\rangle$ and $|n_b = 1, \tilde{n}_c = 0\rangle$. The local basis of A and B is $\{|n_A, n_B\rangle\}$ where $n_A = a_A^\dagger a_A$ and $n_B = a_B^\dagger a_B$ take the values 0 or 1. Using Eqs. (D.10) and Eqs. (D.13), we find:

$$\begin{aligned}
|n_b = 0, \tilde{n}_c = 0\rangle &= -\frac{1}{\sqrt{2}} \left(|n_A = 1, n_B = 0\rangle \right. \\
&\quad \left. - |n_A = 0, n_B = 1\rangle\right), \qquad \text{(D.14a)} \\
&\quad (= |0\rangle) \\
|n_b = 1, \tilde{n}_c = 1\rangle &= \frac{1}{\sqrt{2}} \left(|n_A = 1, n_B = 0\rangle \right. \\
&\quad \left. + |n_A = 0, n_B = 1\rangle\right), \qquad \text{(D.14b)} \\
|n_b = 1, \tilde{n}_c = 0\rangle &= \frac{1}{\sqrt{2}} \left(|n_A = 0, n_B = 0\rangle \right. \\
&\quad \left. + |n_A = 1, n_B = 1\rangle\right), \qquad \text{(D.14c)} \\
&\quad (= |1\rangle) \\
|n_b = 0, \tilde{n}_c = 1\rangle &= \frac{1}{\sqrt{2}} \left(-|n_A = 0, n_B = 0\rangle \right. \\
&\quad \left. + |n_A = 1, n_B = 1\rangle\right). \qquad \text{(D.14d)}
\end{aligned}$$

Tracing over B is immediate, as the only vectors of the basis of B with possible non zero contributions are $|n_B = 0\rangle$ and $|n_B = 1\rangle$. In particular:

$$\begin{aligned}
&\rho_A \left(|n_b = 0, \tilde{n}_c = 0\rangle\langle n_b = 0, \tilde{n}_c = 0|\right) \\
&= \frac{1}{2} \left(|n_A = 1\rangle\langle n_A = 1| + |n_A = 0\rangle\langle n_A = 0|\right),
\end{aligned} \qquad \text{(D.15)}$$

of entanglement entropy $S_A = \log 2$. The same happens for the other ground state.

Notice that the partial trace for fermions can induce a change of sign compared to the bosonic case. For example:

$$\mathrm{tr}_B \left(|n_A = 1, n_B = 1\rangle\langle n_A = 0, n_B = 1|\right) = -|n_A = 1\rangle\langle n_A = 0|. \qquad \text{(D.16)}$$

Using Eqs. (D.14), it is possible to get the expressions of the ground states in the local basis of an arbitrary partition. Additionally, taking a partition where all sites are their own individual subsets leads to the expression of the ground states in the original basis, up to a phase. The general expression of the reduced density matrix for an arbitrary partition of the system is obtained recursively, by considering the partition $A_1, A_2, \ldots, A_n$ of connected subsets A_i that are next to each others like in Fig. D.4. Calling $A = A_1$ and $B = B_1 = \cup_{i=2}^n A_i$ allow use of Eqs, (D.14) to express the two ground states in the local basis of A and B instead of $A \cup B$. The recurrence follows. Naming c_i the link between subsets A_i and A_{i+1} and constructing the "local boundary

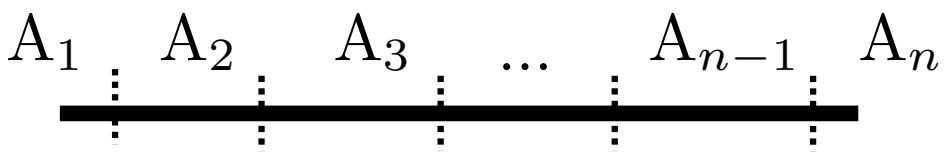

Figure D.4: A partition of the chain into n consecutive connected subsets A_1, A_2, ..., A_n.

operators" a_{A_i} and $a^\dagger_{A_i}$ for the subset A_i and a_{B_j} and $a^\dagger_{B_j}$ for $B_j = \cup_{i=j+1}^{n} A_i$ similarly to Eqs. (D.14), the recurrence can be written as ($\forall n \geqslant 2$):

$$
\begin{aligned}
& u_n\left(A_1, \ldots, A_n\right) && \text{(D.17a)}\\
& \doteq |n_b = 0, \tilde{n}_{c_1} = 0, \ldots, \tilde{n}_{c_{n-1}} = 0\rangle (= |0\rangle) && \text{(D.17b)}\\
& = \frac{1}{\sqrt{2}} \left(|n_{A_1} = 0, n_{B_1} = 1, \tilde{n}_{c_2} = 0, \ldots, \tilde{n}_{c_{n-1}} = 0\rangle \right. \\
& \qquad \left. - |n_{A_1} = 1, n_{B_1} = 0, \tilde{n}_{c_2} = 0, \ldots, \tilde{n}_{c_{n-1}} = 0\rangle \right) && \text{(D.17c)}\\
& = \frac{1}{\sqrt{2}} \left(|n_{A_1} = 0\rangle \otimes v_{n-1}\left(A_2, \ldots, A_n\right) \right. \\
& \qquad \left. - |n_{A_1} = 1\rangle \otimes u_{n-1}\left(A_2, \ldots, A_n\right) \right), && \text{(D.17d)}\\
& v_n\left(A_1, \ldots, A_n\right) && \text{(D.17e)}\\
& \doteq |n_b = 1, \tilde{n}_{c_1} = 0, \ldots, \tilde{n}_{c_{n-1}} = 0 (= |1\rangle)\rangle && \text{(D.17f)}\\
& = \frac{1}{\sqrt{2}} \left(|n_{A_1} = 0, n_{B_1} = 0, \tilde{n}_{c_2} = 0, \ldots, \tilde{n}_{c_{n-1}} = 0\rangle \right. \\
& \qquad \left. + |n_{A_1} = 1, n_{B_1} = 1, \tilde{n}_{c_2} = 0, \ldots, \tilde{n}_{c_{n-1}} = 0\rangle \right) && \text{(D.17g)}\\
& = \frac{1}{\sqrt{2}} \left(|n_{A_1} = 0\rangle \otimes u_{n-1}\left(A_2, \ldots, A_n\right) \right. \\
& \qquad \left. + |n_{A_1} = 1\rangle \otimes v_{n-1}\left(A_2, \ldots, A_n\right) \right). && \text{(D.17h)}
\end{aligned}
$$

Calling:

$$
\begin{aligned}
U_n &= u_n + i v_n, && \text{(D.18a)}\\
V_n &= u_n - i v_n, && \text{(D.18b)}\\
|+_j\rangle &= 1/\sqrt{2} \left(i |n_{A_j} = 0\rangle - |n_{A_j} = 1\rangle \right), && \text{(D.18c)}\\
|-_j\rangle &= 1/\sqrt{2} \left(-i |n_{A_j} = 0\rangle - |n_{A_j} = 1\rangle \right), && \text{(D.18d)}
\end{aligned}
$$

these relations become:

$$U_n(A_1,\ldots,A_n) = |+_1\rangle \otimes V_{n-1}(A_2,\ldots,A_n) \tag{D.19a}$$

$$= \begin{cases} |+_1 -_2 \cdots -_{n-2}\rangle \otimes U_2(A_{n-1},A_n) & \text{if n is even} \\ |+_1 -_2 \cdots +_{n-2}\rangle \otimes V_2(A_{n-1},A_n) & \text{if n is odd} \end{cases} \tag{D.19b}$$

$$V_n(A_1,\ldots,A_n) = |-_1\rangle \otimes U_{n-1}(A_2,\ldots,A_n) \tag{D.19c}$$

$$= \begin{cases} |-_1 +_2 \cdots +_{n-2}\rangle \otimes V_2(A_{n-1},A_n) & \text{if n is even} \\ |-_1 +_2 \cdots -_{n-2}\rangle \otimes U_2(A_{n-1},A_n) & \text{if n is odd} \end{cases} \tag{D.19d}$$

where:

$$u_2(A_{n-1},A_n) = \frac{1}{\sqrt{2}}\left(|n_{A_{n-1}}=0, n_{A_n}=1\rangle - |n_{A_{n-1}}=1, n_{A_n}=0\rangle\right), \tag{D.20a}$$

$$v_2(A_{n-1},A_n) = \frac{1}{\sqrt{2}}\left(|n_{A_{n-1}}=0, n_{A_n}=0\rangle + |n_{A_{n-1}}=1, n_{A_n}=1\rangle\right), \tag{D.20b}$$

so that:

$$U_2(A_{n-1},A_n) = \sqrt{2}i|+_{n-1}-_n\rangle, \tag{D.21a}$$

$$V_2(A_{n-1},A_n) = \sqrt{2}i|-_{n-1}+_n\rangle. \tag{D.21b}$$

Therefore, in a local basis of $A_1,\ldots,A_n$, the ground states become:

$$|n_b=0\rangle = u_n(A_1,\ldots,A_n) \tag{D.22a}$$

$$= \frac{i}{\sqrt{2}}\left(|+_1 -_2 \ldots\rangle + |-_1 +_2 \ldots\rangle\right), \tag{D.22b}$$

$$|n_b=1\rangle = v_n(A_1,\ldots,A_n) \tag{D.22c}$$

$$= \frac{i}{\sqrt{2}}\left(|+_1 -_2 \ldots\rangle - |-_1 +_2 \ldots\rangle\right). \tag{D.22d}$$

These states are not Néel states because they are made out of fermions. It becomes clear in the basis of the subsets $\{\otimes|n_{A_j}\rangle\}_j$ up to the global phase change:

$$|\tilde{0}_j\rangle \doteq (-1)^j i|0_{A_j}\rangle, \quad \text{and} \quad |\tilde{1}_j\rangle \doteq |1_{A_j}\rangle. \tag{D.23}$$

In that case:

$$|+_1 -_2 \dots\rangle = \left(-\frac{1}{\sqrt{2}}\right)^n \otimes_{i=1}^n \left[|\tilde{0}_i\rangle + |\tilde{1}_i\rangle\right] \tag{D.24a}$$

$$= \left(-\frac{1}{\sqrt{2}}\right)^n \sum_{\{n_{A_i}\}_{i\in[\![1,n]\!]}=0,1} |\{n_{A_i}\}_{i\in[\![1,n]\!]}\rangle \tag{D.24b}$$

$$|-_1 +_2 \dots\rangle = \left(-\frac{1}{\sqrt{2}}\right)^n \times \sum_{\{n_{A_i}\}_{i\in[\![1,n]\!]}=0,1} (-1)^{n-\sum n_{A_i}} |\{n_{A_i}\}_{i\in[\![1,n]\!]}\rangle \tag{D.24c}$$

so that:

$$S_{A_1\cup A_3\cup A_5\cup\dots} = \lfloor \frac{n+1}{2} \rfloor \log 2, \tag{D.25}$$

where $\lfloor \dots \rfloor$ is the floor function, and n the number of partition. This last equation proves the exact additivity of the entropy in this case independently of the position of the cuts, which, in addition to the non-nullity of the contribution of the individual subsets, ensure the non-nullity of S^{D} for any superposition of the ground states. Indeed, for $n = 4$:

$$S^{\mathrm{D}} = S_{A_1\cup A_2} + S_{A_2\cup A_4} - S_{A_2} - S_{A_1\cup A_2\cup A_4}, \tag{D.26}$$

becomes the net contribution of one connected subset only: $\log 2$. Alternatively, it is the contribution of two cut Bell pairs of Majorana fermions. This result is valid for both the von Neumann and the Rényi entropies.

D.4 Equivalence of the S_n^{D}

For 1D gapped systems, all S_n^{D} can be used interchangeably, with $n \geq 1$ and finite the index of the Rényi entropy:

- The property of minimum value shared by all S_n imply that if $S_{n_1} \neq 0$, then $S_{n_2} \neq 0$ and vice-versa, so both are simultaneously non-zero.
- The property of monotonicity and the fact that all gapped 1D phases have finite von Neumann entanglement entropy imposes all all S_n to also be finite for 1D gapped systems, so no S_n^{D} can diverge.
- For a given n-entropy Translation invariance further imposes that all connected entropy will have the same value for big subset size, *i.e.* if A_{i+t} is the subset translated from A_i, then $S_n(A_{i+t}) = S_n(A_i)$ up to finite size effects.
- The property of additivity is shared by all S_n.

D.5 Comparison between the topological and non-topological phases away from the phase transition

In the topological superconductor phase, away from any phase transition, both the von Neuman and Rényi entanglement entropies for large enough partitions (i.e., $L_A, L_B, L_D \gg \xi$ for the definitions of Fig. 8.1 (a), or $L_{A_i} \gg \xi$ for all i for Eq. (D.26)) are non zero and additive as demonstrated above in the stereotypical regime (in addition, see next section). If A is a simply connected subset of a partition of the chain (independent of its position), then, $S_A = 2\Gamma$, where $\Gamma = (\log 2)/2$ is the contribution of one (Majorana) Bell pair. Eq. (D.26) then gives:

$$S^{\mathrm{D}} = 2\Gamma + 2 \times 2\Gamma - 2\Gamma - 2\Gamma = 2\Gamma \tag{D.27}$$

In that regard, S^{D} is not unique: combination such as $S_{A_1 \cup A_3} + S_{A_2 \cup A_4} - S_{A_1 \cup A_4} - S_{A_2 \cup A_3}$ would have also work as detectors, but with less experimental relevance, and a more complicated interpretation in terms of mutual information. The quantitative equality $S^{\mathrm{D}} = S_2^{\mathrm{D}}$ is here coincidental and is not a generic feature for other systems.

For the band insulator phase and for large enough partitions, the contribution of each term of Eq. (D.26) is proportional to the number of boundaries of the partition, as we expect from the so called *area law*. For the 1D OBC systems, one can argue that $S^{\mathrm{D}} = 0$ by simply counting the number of boundaries of the partitions shown in Fig. 8.1 a), which gives:

$$S^{\mathrm{D}} = \Theta + 3\Theta - 2\Theta - 2\Theta = 0, \tag{D.28}$$

where Θ is the contribution for the entanglement of a single boundary. While Θ is model-parameter depending, the ratios between each terms is constant in the limit $L_A, L_B, L_D \gg \xi$, ensuring $S^{\mathrm{D}} = 0$. In the limit $\mu \to \infty$, each term is identically zero. The result $S^{\mathrm{D}} = 0$ in the non-topological phase is backed up by numerical simulations.

We also discuss the behavior of S^D for other non-toplogical phases. For the case of a gapped phase displaying ground state equivalent to *e.g.* a maximally entangled Néel state, the entanglement entropy becomes non zero for each term, but is not additive, such that (calling Θ the contribution of the only Bell pair of spin $1/2$) :

$$S^{\mathrm{D}} = \Theta + \Theta - \Theta - \Theta = 0. \tag{D.29}$$

For a critical phase, conformal field theory predicts a vanishing contribution. This is in agreement with all of our microscopic simulations. For critical, non-conformal points, we are not aware of any field theoretical prediction.

Finally, for the case of a rigorously dimerized phase, S^{D} is well-defined and can be considered additive, but is not translation invariant. More precisely, let us define ϵ_{ij}, where $i, j = 1, 2, 3, 4$,

such that $\epsilon_{ij} = 1$ if the cut between A_i and A_j is on a dimer, and $\epsilon_{ij} = 0$ otherwise. Then, if Θ is the contribution of one dimer:

$$S^{\mathrm{D}} = \Theta(\epsilon_{41} + \epsilon_{23} + \epsilon_{12} + \epsilon_{23} + \epsilon_{34} + \epsilon_{41} - \epsilon_{12} - \epsilon_{23} - \epsilon_{23} - \epsilon_{34}) = 2\Theta\epsilon_{41}, \tag{D.30}$$

which is always zero if A_1 and A_4 are subsets at both ends of the open chain. S^{D} is not translation invariant in the case of periodic boundary conditions.

Bibliography

[1] L. Amico, R. Fazio, A. Osterloh, and V. Vedral, Rev. Mod. Phys. **80**, 517 (2008).

[2] P. Calabrese and J. Cardy, J. Physics A: Math. Theor. **42**, 504005 (2009).

[3] J. Eisert, M. Cramer, and M. B. Plenio, Review Modern Physics **82**, 277 (2010).

[4] E. Fradkin, *Field Theories of Condensed Matter Systems* (Cambridge University Press, 2013).

[5] A. Hamma, R. Ionicioiu, and P. Zanardi, Physics Lett. A **337**, 22 (2005).

[6] M. Levin and X.-G. Wen, Physical Review Letters **96**, 110405 (2006).

[7] A. Kitaev and J. Preskill, Physical Review Letters **96**, 110404 (2006).

[8] X.-G. Wen, Science **363**, 3099 (2019).

[9] S. Depenbrock, I. P. McCulloch, and U. Schollwöck, Physical Review Letters **109**, 067201 (2012).

[10] H.-C. Jiang, Z. Wang, and L. Balents, Nature Physics **8**, 902 (2012).

[11] S. V. Isakov, M. B. Hastings, and R. G. Melko, Nature Physics **7**, 772 (2011).

[12] D. A. Abanin and E. Demler, Physical Review Letters **109**, 020504 (2012).

[13] A. J. Daley, H. Pichler, J. Schachenmayer, and P. Zoller, Physical Review Letters **109**, 020505 (2012).

[14] A. Elben, B. Vermersch, M. Dalmonte, J. I. Cirac, and P. Zoller, Physical Review Letters **120**, 050406 (2018).

[15] B. Vermersch, A. Elben, M. Dalmonte, J. I. Cirac, and P. Zoller, Physical Review A **97**, 023604 (2018).

[16] H. Pichler, G. Zhu, A. Seif, P. Zoller, and M. Hafezi, Physical ReviewX **6**, 041033 (2016).

[17] M. Dalmonte, B. Vermersch, and P. Zoller, Nature Physics **14**, 827 (2018).

[18] E. Cornfeld, E. Sela, and M. Goldstein, Phys. Rev. A **99**, 062309 (2019).

[19] F. Pollmann, A. M. Turner, E. Berg, and M. Oshikawa, Physical Review B **81**, 064439 (2010).

[20] L. Fidkowski, Physical Review Letters **104**, 130502 (2010).

[21] A. M. Turner, F. Pollmann, and E. Berg, Physical Review B **83**, 075102 (2011).

[22] H. Katsura, D. Schuricht, and M. Takahashi, Physical Review B **92**, 115137 (2015).

[23] A. Y. Kitaev, Physics-Usp. **44**, 131 (2001).

[24] C. Beenakker, Ann. Review Cond. Matt. Physics **4**, 113 (2013).

[25] T. Brydges, A. Elben, P. Jurcevic, B. Vermersch, C. Maier, B. P. Lanyon, P. Zoller, R. Blatt, and C. F. Roos, Science **364**, 260 (2019).

[26] S. J. van Enk and C. W. J. Beenakker, Physical Review Letters **108**, 110503 (2012).

[27] H. Casini and M. Huerta, Physics Lett. B **600**, 142 (2004).

[28] P. Fromholz, G. Magnifico, V. Vitale, T. Mendes-Santos, and M. Dalmonte, Physical Review B **101** (2020), 10.1103/physrevb.101.085136.

[29] D. Wang, S. Xu, Y. Wang, and C. Wu, Physical Review B **91** (2015).

[30] B. Zeng and D. L. Zhou, EPL **113**, 56001 (2016).

[31] I. H. Kim, Physical Review B **89** (2014).

[32] E. M. Stoudenmire, J. Alicea, O. A. Starykh, and M. P. Fisher, Physical Review B **84** (2011).

[33] M. Caraglio and F. Gliozzi, JHEP **0811**, 076 (2008).

[34] S. Furukawa, V. Pasquier, and J. Shiraishi, Physical Review Letters **102**, 170602 (2009).

[35] I. Peschel, Journal of Physics A: Mathematical and General **36**, L205 (2003).

[36] S. R. White, Physical Review Letters **69**, 2863 (1992).

[37] U. Schollwöck, Review Modern Physics **77**, 259 (2005).

[38] M. D. Caio, N. R. Cooper, and M. J. Bhaseen, Phys. Rev. Lett. **115**, 236403 (2015).

[39] L. D'Alessio and M. Rigol, Nature Commun. **6**, 8336 (2015).

[40] M. McGinley and N. R. Cooper, arXiv:1908.06875 .

[41] T. Giamarchi, *Quantum physics in one dimension*, InterNature Ser. Mono. Physics (Clarendon Press, Oxford, 2004).

[42] N. M. Gergs, L. Fritz, and D. Schuricht, Physical Review B **93** (2016).

[43] L. Levy and M. Goldstein, Universe **5**, 33 (2019).

[44] Q. Niu, D. J. Thouless, and Y.-S. Wu, Physical Review B **31**, 3372 (1985).

[45] X. Chen, Z.-C. Gu, Z.-X. Liu, and X.-G. Wen, Science **338**, 1604 (2012).

[46] J. Haegeman, D. Pérez-García, I. Cirac, and N. Schuch, Phys. Rev. Lett. **109**, 050402 (2012).

[47] F. Pollmann and A. M. Turner, Physical Review B **86**, 125441 (2012).

[48] H. Shapourian, K. Shiozaki, and S. Ryu, Phys. Rev. Lett. **118**, 216402 (2017).

[49] H. Shapourian, K. Shiozaki, and S. Ryu, Physical Review B **95**, 165101 (2017).

[50] B. Zeng, X. Chen, D.-L. Zhou, and X.-G. Wen, *Quantum Information Meets Quantum Matter* (Springer New York, 2019).

[51] A. Elben, J. Yu, G. Zhu, M. Hafezi, F. Pollmann, P. Zoller, and B. Vermersch, Science Advances **6**, eaaz3666 (2020).

[52] H. Ollivier and W. H. Zurek, Physics Revs Lett. **88**, 017901 (2001).

[53] I. Frérot and T. Roscilde, Physical Review B **94**, 075121 (2016).

[54] D. I. Tsomokos, A. Hamma, W. Zhang, S. Haas, and R. Fazio, Physical Review A **80**, 060302 (2009).

[55] G. B. Halász and A. Hamma, Physical Review A **86**, 062330 (2012).

[56] G. B. Halász and A. Hamma, Physical Review Letters **110**, 170605 (2013).

[57] X.-G. Wen, ISRN Condensed Matter Physics **2013**, 1 (2013).

[58] T. D. Stanescu, *Introduction to Topological Quantum Matter & Quantum Computation* (CRC Press, 2016).

[59] L. Fidkowski, Physical Review Letters **104** (2010), 10.1103/physrevlett.104.130502.

[60] H. Li and F. D. M. Haldane, Physical Review Letters **101** (2008), 10.1103/physrevlett.101.010504.

[61] A. M. Turner, Y. Zhang, and A. Vishwanath, Physical Review B **82** (2010), 10.1103/physrevb.82.241102.

[62] P. Fendley, M. P. A. Fisher, and C. Nayak, Journal of Statistical Physics **126**, 1111 (2007).

[63] A. Y. Kitaev, Physics-Uspekhi **44**, 131 (2001).

[64] W. P. Su, J. R. Schrieffer, and A. J. Heeger, Physical Review Letters **42**, 1698 (1979).

[65] W. P. Su, J. R. Schrieffer, and A. J. Heeger, Physical Review B **22**, 2099 (1980).

[66] F. Verstraete, J. I. Cirac, J. I. Latorre, E. Rico, and M. M. Wolf, Physical Review Letters **94** (2005), 10.1103/physrevlett.94.140601.

[67] L. Campos Venuti, C. Degli Esposti Boschi, and M. Roncaglia, Physical Review Letters **96**, 1 (2006).

[68] L. C. Venuti, S. M. Giampaolo, F. Illuminati, and P. Zanardi, Physical Review A - Atomic, Molecular, and Optical Physics **76**, 1 (2007).

[69] A. Lavasani, Y. Alavirad, and M. Barkeshli, (2020), arXiv:2004.07243 .

[70] M. McGinley and N. R. Cooper, Physical Review Letters **121**, 090401 (2018).

[71] J. Zak, Physical Review Letters **62**, 2747 (1989).

[72] M. V. Berry, Proceedings of the Royal Society of London. A. Mathematical and Physical Sciences **392**, 45 (1984).

[73] C.-K. Chiu, J. C. Teo, A. P. Schnyder, and S. Ryu, Reviews of Modern Physics **88** (2016), 10.1103/revmodPhysical88.035005.

[74] A. Altland and M. R. Zirnbauer, Physical Review B **55**, 1142 (1997).

[75] L. Fidkowski and A. Kitaev, Physical Review B **81**, 134509 (2010).

[76] E. J. Meier, F. A. An, A. Dauphin, M. Maffei, P. Massignan, T. L. Hughes, and B. Gadway, Science **362**, 929 (2018).

[77] F. Cardano, A. D'Errico, A. Dauphin, M. Maffei, B. Piccirillo, C. de Lisio, G. D. Filippis, V. Cataudella, E. Santamato, L. Marrucci, M. Lewenstein, and P. Massignan, Nature Communications **8** (2017).

[78] D. Xie, W. Gou, T. Xiao, B. Gadway, and B. Yan, npj Quantum Information **5** (2019).

[79] J. Sirker, M. Maiti, N. P. Konstantinidis, and N. Sedlmayr, Journal of Statistical Mechanics: Theory and Experiment **2014** (2014).

[80] Q. Wang, D. Wang, and Q.-H. Wang, EPL (Europhysics Letters) **124**, 50005 (2018).

[81] X. Chen, Z.-C. Gu, and X.-G. Wen, Physical Review B **83** (2011).

[82] X. Chen, Z.-C. Gu, and X.-G. Wen, Physical Review B **84** (2011).

[83] S. Ryu and Y. Hatsugai, Physical Review B - Condensed Matter and Materials Physics **73**, 1 (2006).

[84] A. Rényi, in *Proceedings of the Fourth Berkeley Symposium on Mathematical Statistics and Probability, Volume 1: Contributions to the Theory of Statistics* (University of California Press, Berkeley, Calif., 1961) pp. 547–561.

[85] X. Hu and Z. Ye, Journal of Mathematical Physics **47**, 023502 (2006).

[86] M. Müller-Lennert, F. Dupuis, O. Szehr, S. Fehr, and M. Tomamichel, Journal of Mathematical Physics **54**, 122203 (2013).

[87] R. Islam, R. Ma, P. M. Preiss, M. E. Tai, A. Lukin, M. Rispoli, and M. Greiner, Nature **528**, 77 (2015).

[88] J. K. Asbóth, L. Oroszlány, and A. Pályi, *A Short Course on Topological Insulators* (Springer International Publishing, 2016).

[89] B. C. Shin, Bull. Aust. Math. Soc. **55**, 249 (1997).

[90] V. Eisler and I. Peschel, Journal of Statistical Mechanics: Theory and Experiment **2018**, 104001 (2018).

[91] M.-C. Chung and I. Peschel, Physical Review B **64**, 064412 (2001).

[92] The OEIS Foundation Inc, "A008315," (2020), `http://oeis.org/A008315`.

[93] N. Sedlmayr, P. Jaeger, M. Maiti, and J. Sirker, Physical Review B **97**, 1 (2018).

[94] E. Abrahams, P. W. Anderson, D. C. Licciardello, and T. V. Ramakrishnan, Physical Review Letters **42**, 673 (1979).

[95] C. A. Müller and D. Delande, (2010), arXiv:1005.0915 .

[96] J. Li, R.-L. Chu, J. K. Jain, and S.-Q. Shen, Physical Review Letters **102** (2009).

[97] H. Jiang, L. Wang, Q. feng Sun, and X. C. Xie, Physical Review B **80** (2009), 10.1103/physrevb.80.165316.

[98] C. W. Groth, M. Wimmer, A. R. Akhmerov, J. Tworzydło, and C. W. J. Beenakker, Physical Review Letters **103** (2009).

[99] T. Liu and H. Guo, Physics Letters A **382**, 3287 (2018).

[100] X.-L. Qi and S.-C. Zhang, Reviews of Modern Physics **83**, 1057 (2011).

[101] P. Heinzner, A. Huckleberry, and M. Zirnbauer, Communications in Mathematical Physics **257**, 725 (2005).

[102] M. R. Zirnbauer, "Symmetry Classes," (2010), 1001.0722 .

[103] R. Verresen, R. Moessner, and F. Pollmann, Physical Review B **96**, 165124 (2017).

[104] L. Fidkowski and A. Kitaev, Physical Review B **83**, 075103 (2011).

[105] M. J. Rice and E. J. Mele, Physical Review Letters **49**, 1455 (1982).

[106] B. M. McCoy and M.-L. Yan, Nuc. Physics B **215**, 278 (1983).

[107] C. Lacroix, P. Mendels, and F. Mila, eds., *Introduction to Frustrated Magnetism* (Springer Series in Solid-State Sciences Vol. 164, 2010).

Conclusions

While we have provided conclusive thoughts for each chapter, discussing possible outlooks, we would like to give here some additional remarks.
We have started this thesis by emphasizing how entanglement has been used successfully to investigate many-body quantum systems both theoretically and experimentally. Then, the focus of this work has been bridging these two aspects. At the broader level, our results span three different lines, whose outlooks we outline below.

Mixed state entanglement - We have defined the concept of *negativity hamiltonian* for the partial transpose of a density matrix in analogy with the entanglement hamiltonian for reduced density matrices of bipartite systems. We have described its structure in the case of (1+1)-d fermionic conformal field theories and a tight-biding model of spinless fermions on a chain. In this regard, there are several topics on which we could elaborate more.
First, our results only apply to equal and adjacent intervals on a line. The generalization to more complicated geometries, as well as different models, could be an interesting topic of study. Secondly, it might be possible to engineer experimental set-ups that reconstruct the negativity hamiltonian in the laboratory and measure the negativity spectrum directly. Indeed, the full spectral resolution of the density matrix and the estimation of the spectrum of its partial transpose is a relevant topic of study in the field of entanglement detection and it has been the focus of Chap. 5. There, we have discussed approaches to entanglement detection, different from the standard PPT-criterion, and provided new conditions, enhanced by symmetry resolution, using the moment of the partial transpose of a reduced density matrix.
In this respect, the full potential of the moments of the partial transpose has not been discovered yet. Other possible routes are trying to find different combinations that can highlight other aspects of the entanglement content of the many-body quantum states or new conditions that allow the detection of entanglement with low-order momenta.

Symmetry resolved entanglement dynamics - From the post-processed data of the experiment [Brydges et al., Science 364, 260 (2019)], we have observed a new physical phenomenon, we have dubbed *symmetry-resolved dynamical purification*. We have given a theoretical explanation, employing time-dependent perturbation theory, and showed its generality with extensive numerical simulations. This work has highlighted, for the first time, the intimate connection between sym-

metry and quantum correlations in NISQ devices and the experimental tools developed could find useful implementation in contexts where symmetry-resolved contributions to entanglement may be of particular interest.
From the same data, we have also computed the operator entanglement and addressed the presence of the *entanglement barrier* for the first time in experiments. We have defined the symmetry-resolution of operator entanglement, given an explanation in terms of charge-imbalance, and devised a new experimental protocol to access highly non-trivial functionals of the density matrix. This method, we call *batch-shadows estimator*, could open up to the estimation of difficult to access quantities as it allows the computation of multi-copy observables and the post-processing of the data is highly parallelizable. We also have benchmarked our results against free fermionic and tensor networks simulations providing a simple physical intuition, in terms of the quasiparticle picture, about the dynamics of operator entanglement in the time interval investigated.
Certainly, this work may stimulate future developments in this field, as it is the first time where symmetry-resolved operator entanglement is studied and experimentally observed, and the method developed here, to access the experimental estimation, may have practical application to probe non-linear properties of quantum many-body systems, in any physical context where randomized measurements can be employed.

Entanglement topological invariants - We have proved the existence of topological invariants based solely on entanglement properties in one-dimensional topological matter. We have observed that with appropriate combinations of entanglement entropies it is possible to isolate the topological contribution to entanglement called *topological entanglement entropy*.
We have studied this both for the Kitaev p-wave superconductor and the Su-Schrieffer-Heeger model. The entanglement order parameter displays universal features at the phase transition and behaves like a topological invariant. It would be interesting to investigate whether other measures of entanglement could characterize the topological behavior of these kinds of models or display similar characteristic features. As topology in open systems is a hot topic of study, it would be interesting also to shed light on the existence of topological invariants based solely on entanglement negativity for mixed states, as in the case of pure states.

We conclude by remarking on how the investigation of entanglement could give fundamental information in several contexts ranging from time dynamics, to entanglement detection in mixed states and topological systems. The connection between symmetries and quantum correlations also opens up new ways to exploit both of them in the context of quantum information and quantum many-body physics. We believe the work of this thesis might pave the way to further investigation on this topic, in intimate connection with new experimental platforms and quantum simulators.

Acknowledgements

Here, I would like to express my gratitude to several people that have been close to me in the past four years.

First, I would like to thank my supervisor Marcello Dalmonte for his support in these difficult times, introducing me to research and teaching me the 'right way' to do physics, with passion and enthusiasm. Furthermore, I would like to mention my future supervisor Benoît Vermersch and my future colleagues, Aniket and Matteo, for their warm welcoming in Grenoble, during the coldest winter I've ever faced.

During the past years, despite social distancing and obvious restrictions that affected the whole world, I have shared lots of memories and bonding times with several people, near and far. I would like to mention Alessandro, with whom I pretended to be an independent researcher for the first time. I thank Federico, for the numerous evenings together, and for introducing me to Trieste when I first arrived. And I would like to thank Sara for sharing with me the work (and the pain) of the last year of my Ph.D. Lastly, I would like to thank Alberto for the patience he has had in listening to my rants, every time I have been feeling low.

Lots of other people have passed by during these long years; I would like to greet everyone I met who shared with me part of their life, hoping they will hold precious memories, as I do.

In this last part, I would like to thank the people that have been with me for most of my life and still believe in me and support me. In particular, my parents and my brother, and my old friends, back in my hometown, with whom I manage to spend little but high quality time.

Last, I would like to thank Silvia for having been an invaluable support at my lowest and having shared with me many joyful moments in the past years. I wish you can find your way and happiness in life.